THE CREEP PROPERTIES OF A NICKEL BASE ALLOY

by

ANDREW PETER DAVID COX, BSc(Eng), ACGI

A thesis presented for the degree of
Doctor of Philosophy
of the
University of London
and for the
Diploma of Imperial College

June 1981

Department of Mechanical Engineering
Imperial College of Science & Technology
London SW7 2BX

ABSTRACT

High temperature (0.57 T_m to 0.73 T_m) constant stress creep, cyclic stress creep and yield stress tests have been carried out on a cast nickel base alloy of composition (wt%): 19.5 Cr, 2.6 Ti, 1.4 Al, 0.06 C and balance Ni. The grain structure was either in an equi-axed form or directionally solidified by the exothermic mould technique.

The directionally solidified grain form gave improved creep rupture strain and creep rupture time properties over the equi-axed form. The improvement was greatest in the higher temperature region where strains at rupture were in excess of 10%. The improvement was a result of eliminating major grain boundaries transverse to the applied stress direction.

The constant stress creep data for the directionally solidified grain form have been analysed on an empirical basis and on equations based on a physical model of dislocation dynamics. Neither approach resulted in a unique form of relationship between the creep strain properties and applied stress, time and temperature. This was due to the basic material structure being a function of time at temperature, resulting in growth of the γ' precipitate phase, a changing mechanism for the interaction of the γ' precipitate phase with dislocations and a time-dependent yield stress.

Common γ' precipitate/dislocation interactions were found for both creep and direct yielding. The time dependence of the yield stress was related to the size of the γ' precipitate. A reasonable relationship between the creep strain rate and an effective stress (the ratio of the applied creep stress to the current material yield stress) is proposed for when the alloy is in the overaged condition.

ACKNOWLEDGEMENTS

I would like to thank my supervisor, Dr G.A. Webster, for the suggestion of the topic of creep and his continual guidance over the period of experimental work and more recent theoretical analysis.

The staff of the Mechanical Engineering Department workshop are thanked for their skill in constructing the creep machines used in this work. Particular thanks go to Mr John Miller for his stimulating discussions during the period when Mr A. Graham was working in the creep field, the latter's contribution to the philosophy of phenomenology was much appreciated.

The personal financial support of Bristol Siddley Engines, Leavesden (now Rolls-Royce Limited, Aero Engine Division) and the assistance from Dr W.J. Harris and Mr E. Tough of the Metallurgy section of the Materials Laboratory is gratefully acknowledged. The general support of the Science Research Council for equipment and materials is acknowledged.

Much credit is given to my wife, Elizabeth, for the final writing of this thesis.

Finally, the diligent typing of Mrs E.A. Hall is much appreciated.

CONTENTS

		Page
Title Page		1
Abstract		2
Acknowledgements		3
Contents		4
Notation		8
INTRODUCTION		10
CHAPTER 1:	LITERATURE SURVEY	12
1.1	Nature of Creep Deformation	12
1.2	Strengthening Methods	14
1.3	Development of Nickel Base Alloys	16
1.4	Structural Changes and Processes Occurring During Creep	22
	1.4.1 Structural changes due to creep	22
	1.4.2 Structural changes occurring during creep	24
1.5	Structural Theories	29
1.6	Phenomenological Expressions and Creep Parameters	40
1.7	Conclusions	46
CHAPTER 2:	SPECIMEN MATERIAL AND MANUFACTURE	48
2.1	Specimen Material	48
2.2	Directionally Solidified Grain Form	48
2.3	Equi-Axed Grain Form	53
CHAPTER 3:	EQUIPMENT	55
3.1	General	55
3.2	Furnaces, Temperature Control and Measurement	55

		Page
3.3	Specimen Grips and Extensometry	58
3.4	Constant Stress Compensation	60
3.5	Cyclic Loading Apparatus	63
CHAPTER 4:	EXPERIMENTAL PROCEDURE AND RESULTS	67
4.1	Experimental Procedure	67
	4.1.1 Constant stress tests	67
	4.1.2 Cyclic stress tests	72
	4.1.3 Thin foil preparation	72
4.2	Experimental Results for Directionally Solidified Material	73
	4.2.1 Constant stress creep tests	73
	4.2.2 Fracture characteristics	79
	4.2.3 Interaction of dislocations and particles during creep	89
	4.2.4 Time at temperature parameters	94
	4.2.4.1 Introduction	94
	4.2.4.2 Cyclic stress data	94
	4.2.4.3 Yield stress measurements	95
4.3	Experimental Results for Equi-Axed Grain Material	101
CHAPTER 5:	ANALYSIS OF DATA	103
5.1	Introduction	103
5.2	Physical Curve Fitting Analysis	105
	5.2.1 Discussion	109
5.3	Empirical Analysis	120
	5.3.1 Discussion	137
5.4	Equi-Axed Grain Material	142

		Page
5.4.1	Analysis of constant stress creep tests	142
5.4.2	A comparison between the properties of the directionally solidified and equi-axed cast grain structures	150
CHAPTER 6:	THE RÔLE OF STRUCTURE	158
6.1	Observation of γ' Morphology	158
6.2	Growth Laws of γ'	161
6.3	The Effects of Time at Temperature on Creep Properties	166
6.4	Relationships Between the Macroscopic Yield Stress and the γ' Particle Size for the Overaged State	178
6.5	Correlation of the γ' Effects on Mechanical Properties	186
CHAPTER 7:	GENERAL DISCUSSION	193
CHAPTER 8:	CONCLUSIONS	203
References		207
Appendix A:	Constant Stress Creep Data for Directionally Solidified Grain Form	215
Appendix B:	Cyclic Stress Creep and Elastic Data for Directionally Solidified Grain Form	233
Appendix C:	Yield Stress Data for Exposure at Temperature for Directionally Solidified Grain Form	239
Appendix D:	Constant Stress Creep Data for Equi-Axed Grain Form	241

Page

Appendix E: Convergence Criteria and Subroutines for Computer Program 246

Appendix F: Computer Derived Parameters and Comparisons Between Fitted and Experimental Data 251

Appendix G: A Relationship Between Transient and Steady-State Creep at Elevated Temperatures (Paper by G.A. Webster, A.P.D. Cox, & J.E. Dorn, *Metal Science Journal*, 3 (1969) 221)

Appendix H: Some Effects of Grain Structure on the Creep Properties of a Cast Nickel Base Alloy (Paper by A.P.D. Cox & G.A. Webster, *Jernkontorets Annaler*, 155 (1971) 349.

NOTATION

1. Common Notation:

ε	:	strain
$\dot{\varepsilon}_s$	:	steady-state creep rate
ε_R	:	strain at rupture
ε_r	:	recovered strain
t_r	:	rupture time
ε_c	:	recovered time
t	:	time
R	:	gas constant

Other parameters defined by relevant equations.

2. Precipitate Particle Morphology and Size:

λ : edge to edge

h : centre to centre

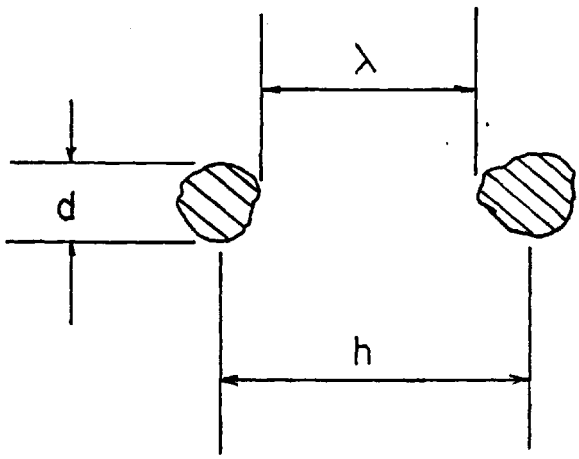

3. Common Experimental Temperatures:

Symbol	Temperature	
	°C	K
○	650	923
△	700	973
●	750	1023
□	800	1073
▲	850	1123
■	900	1173

INTRODUCTION

In the field of steam turbines, nuclear reactors, gas turbines and aircraft frames, there are many components that operate under conditions of extremes of temperatures and stresses. Many materials are used according to these conditions and, on a general basis, these range from glass fibre composites and aluminium base alloys used up to 150°C, titanium base alloys up to 400°C, steels up to 600°C to the nickel and cobalt base alloys at temperatures over 600°C.

The main desire for an increase in operating temperature is for an increase in performance and/or efficiency from the component, and it is here that the interface of engineering and metallurgy operates. The engineering approach is primarily concerned with the mechanical strength and working stresses on the component, whilst the metallurgist is primarily concerned with the material structure and damage caused by the environmental conditions.

One component of damage can be that caused by creep which is defined by time-dependent strain. This damage can accumulate and eventually lead to failure of the structure. Creep can occur over a wide range of stress and temperature, but it is at temperatures in excess of 0.5 T_m (where T_m is the melting point of the material in degrees absolute) that the creep phenomenon is predominant in practical applications. An example of this condition can be found in the gas turbine where, for reasons of efficiency and power, the inlet gas temperature to the power turbine stages are approaching 1500 K, high centrifugal stresses also being present in the rotating components.

The design criteria for safe operating conditions in the creep damage range has often been obtained on an empirical basis from data measured over a restricted range of conditions. These results have then been used

to predict data for conditions outside the experimental range by parameters thought to contain the relevant variables, e.g. for the Larson-Miller parameter, P, at a constant value of stress $P = f[T(C + \log t_R)]$, where T is the operating temperature, t_R is the rupture time, and C is a constant. In this case, it would be assumed that the parameter holds for all values of t_R and T.

For applications in the field of gas turbines, the above criteria have been successfully used for some of the nickel base alloys. The nickel base alloys have been primarily used because of their high strength and corrosion resistance properties. However, under certain conditions, the structure of the alloy varies with time of use and the above analysis is found not to accurately predict data. The grain structure of the alloy can also radically affect the properties, and a good example of this is the development of directional solidification in the cast form. This form of the cast nickel base alloy was introduced to enhance the creep life and ductility of an alloy with the same composition by the elimination of grain boundaries transverse to the applied stress.

Whilst there can be a wide variation in metallurgical structure, there can also be a wide range and variation of conditions under which these structures operate. In the gas turbine, conditions of stress and temperature are not necessarily constant and the cyclic loadings can affect both the structure and the mechanical properties.

Such is the complexity of the mechanical and metallurgical conditions that components operate under that a rational approach to the problems of strength and structure is required. The work in this thesis is on the most simple of precipitation hardened nickel base alloys, additionally strengthened by directional solidification and tested under conditions of constant high stresses and temperatures. With the basic mechanical properties known, predictions of behaviour under cyclic stress and temperature conditions may then be possible.

CHAPTER 1

LITERATURE SURVEY

1.1 NATURE OF CREEP DEFORMATION

Creep, being defined as time dependent strain, can be demonstrated in a generalised form of creep strain versus time in Figure 1.1 [1]. These

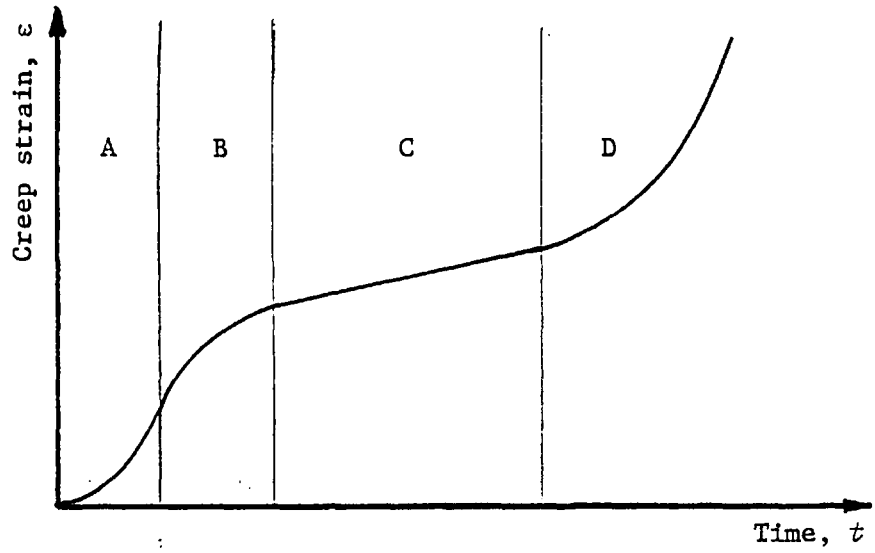

Figure 1.1: Generalised form of creep curve

Region A: Incubation period, accelerating creep rate
Region B: Primary creep, decelerating creep rate
Region C: Secondary creep, constant creep rate
Region D: Tertiary creep, accelerating creep rate leading to failure

four regions do not necessarily all occur for all materials under all conditions. A further classification can be made by considering the temperature under which the stress is being applied. Based on the melting point of the material in degrees absolute (T_m), the following classifications have been made:

$0.1 - 0.2\ T_m$ - logarithmic creep

$0.4 - 0.7\ T_m$ - recovery creep

$0.8 - 0.9\ T_m$ - diffusion (Herring-Nabarro) creep

These descriptions are partly descriptive of the mechanical effects and the metallurgical processes occurring, i.e. in the 'logarithmic creep' range, there is a relationship between the creep strain and time of the form:

$$\varepsilon = A \log t + B$$

which corresponds just to section B in Figure 1.1, and in the 'recovery creep' range, the microstructure of the material is changing under the influence of recovery processes.

The above divisions are still not absolute and there is an overlap of descriptions which can be further illustrated by the influence of the applied stress, as shown in Figure 1.2 [2]. Figure 1.2 incorporates the

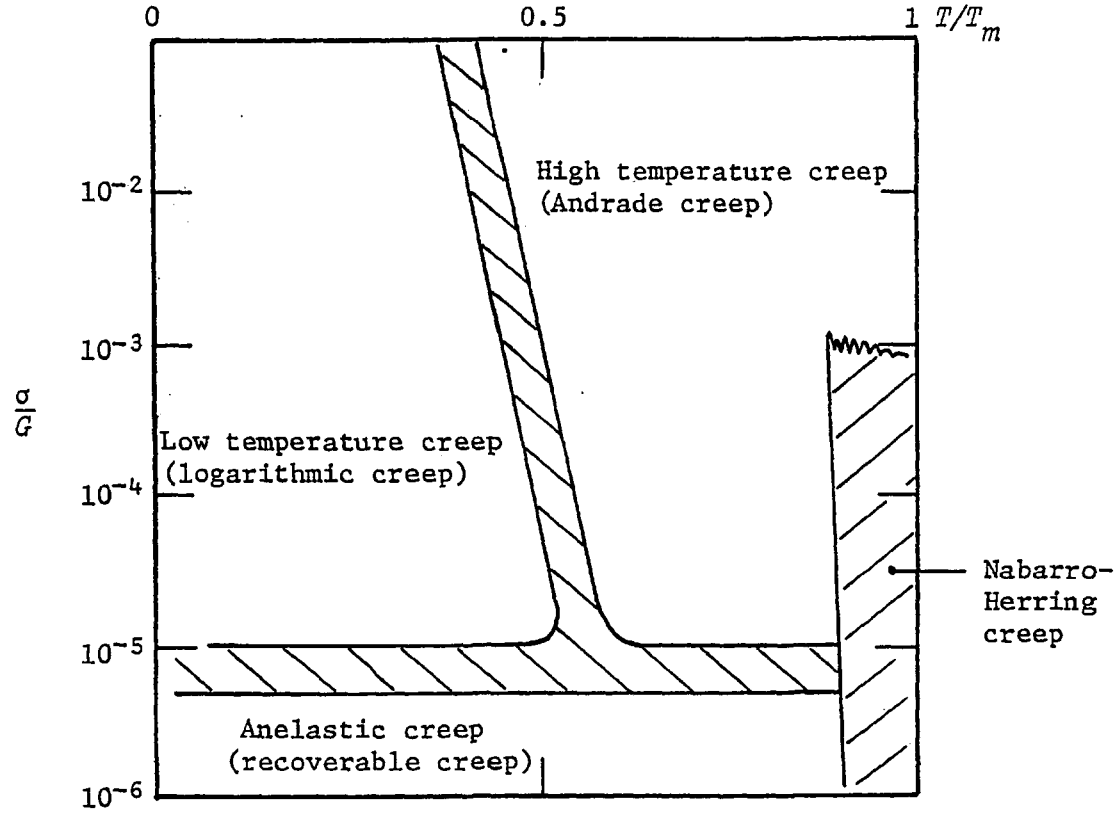

Figure 1.2: Stress and temperature dependence of creep mechanisms

main mechanical parameters, T/T_m and σ/G, which can be used to define the operating conditions, although the dimensionless stress factor is rarely used.

The effects of creep, i.e. a time dependent strain, on the material are numerous. One of these is the microscopic dislocations which occur in the lattice. The mechanisms of dislocation motions have been used by Klahn et al [3] to classify creep behaviour and four divisions are given: diffusion controlled, thermally activated, athermal, and viscous drag. Usually one of these mechanisms is dominant in the particular temperature range considered but, again, there is an overlap when two, or even three, mechanisms can be operating, as shown in Figure 1.2 on a descriptive basis.

The groupings so far given have their own sub-divisions and for the temperature range of prime interest in this experimental study, greater than 0.5 T_m, some of the diffusion controlled mechanisms which might be controlling the strain rate are listed by Conrad [4] as:

(a) the climb of dislocations over second phase particles;
(b) the non-conservative motion of jogs in screw dislocations;
(c) the dragging of a solute atmosphere;
(d) the healing of the disruption of a cluster of solute atoms or of short range order as a dislocation moves through the lattice;
(e) the dissolution or agglomeration of precipitates opposing the motions of dislocations.

Thus, the creep phenomenon cannot be described in a simple manner but may be summarised by the fact that the application of a stress to a material at certain temperatures will result in a time dependent strain, causing strain rate changes and various structural and micro-structural changes in the material.

1.2 STRENGTHENING METHODS

As the work of this thesis is primarily concerned with the practical

applications of materials in the temperature range greater than 0.5 T_m, a short review of materials and strengthening methods essential for this regime is given below.

The materials used in this temperature range are primarily steels, nickel base alloys, cobalt base alloys, ceramics and composites. All of them rely for strength to some extent on their chemical composition with the basic strengthening mechanism of solid solution hardening.

Solid solution hardening can be related to the atomic diameter oversize of the constituents, as measured by lattice expansion, while an additional superimposed effect can be attributed to position in the periodic table or N_v, the electron vacancy number. The latter effect may result from a lowering of the stacking fault energy which would make cross-slip more difficult in the solid solution [5]. Solid solution hardening persists to high temperatures, but above 0.6 T_m the strengthening is diffusion dependent.

Examples of solid solution elements are cobalt, iron, chromium, molybdenum, tungsten, vanadium, titanium and aluminium in metal base alloys, where these elements differ from nickel by 1% to 13% in atomic diameter and 1% to 7% in N_v [6].

To add to the effect of a solid solution hardened matrix, most complex high strength alloys have a hard dispersed second phase which adds to the basic strength in several ways. Some of the mechanisms by which hardening occurs due to the coherent particles are [5]:

(a) coherency strains;

(b) differences in elastic moduli between particle and matrix;

(c) existence of order in the particles;

(d) differences in the stacking fault energy of particle and matrix;

(e) energy to create additional particle-matrix interface;

(f) increases in lattice resistance of particles with temperature;

(g) particle-dislocation interactions.

Of these, it is considered that mechanisms (a), (c) and (g) are the major strengthening processes and they will be discussed further in Section 1.5.

1.3 DEVELOPMENT OF NICKEL BASE ALLOYS

Nickel base alloys were originally developed for creep resistant components in the early gas turbine engines. The basic constituents were Ni and Cr in a ratio 80/20, the chromium being a solid solution strengthener and an aid in corrosion resistance. With the addition of aluminium and titanium, a second phase precipitate, γ' ($Ni_3(Ti,Al)$), was formed providing high temperature creep resistance. Carbon was also added to form grain boundary carbides.

The major phases present in all nickel base alloys are the FCC austenite, γ (the matrix), γ', the major precipitate phase and carbides. The most basic alloy containing these is Nimonic 80A* with a volume fraction of γ' of approximately 20% and a chemical composition of 20% Cr (for solid solution hardening), 2% Ti, 1.5% Al (γ' precipitate components), balance Ni with trace elements Si, Cu, Fe, Mn, Co, B and S. This alloy has a γ' solubility temperature of 850°C to 880°C [7], which is then regarded as an operating temperature limit. To increase this limit, cobalt was added to formulate Nimonic 90. From then on, alloying ingredients were added to stabilise the γ' phase, increase the volume fraction of γ' and control the carbides.

The simple alloys were easily forged. With greater complexity and an increase in strength, it then became impossible to forge by available

---

* Trade name of Henry Wiggin Company Limited.

methods. A series of investment cast alloys were then developed. When the maximum strength was being reached with complex compositions in the cast form, attention was turned to the refinement of the casting techniques to improve the mechanical strength and creep properties.

One source of weakness under creep conditions in these materials is the grain boundary in a plane perpendicular to the applied stress axis. To eliminate these grain boundaries, a series of directionally solidified alloys have been developed. In 1960, Ver Snyder & Guard first described a technique for the unidirectional solidification of ingots with a cooled copper base exothermic mould [8], as illustrated in Figure 1.3.

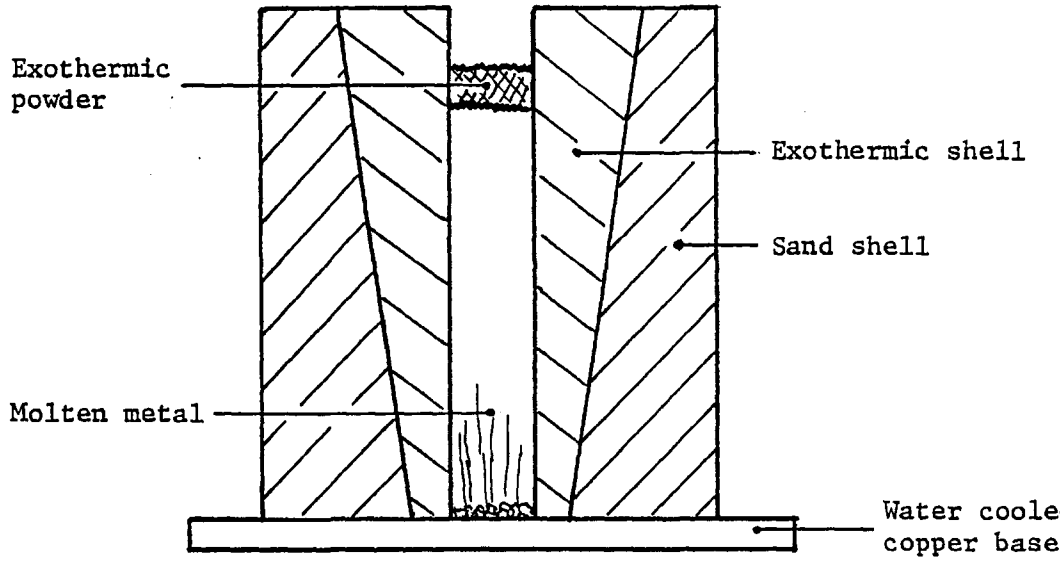

Figure 1.3: A method for producing directionally solidified ingots

An alloy of composition 75.5% Ni, 21% Cr, 3.5% Al was tested under creep conditions in the columnar grained form produced by the unidirectional solidification. It was found that the rupture life and ductility obtained in the columnar grained form was greater when the tensile axis was in the direction of solidification than when the axis was transverse to the

direction of solidification, and also greater than conventionally cast ingots having an equi-axed grain structure. The elimination of transverse grain boundaries was considered to be the major reason for the increased performance.

Piearcey & Terkelson [9] used the above technique to evaluate the effect of directional solidification on the properties of the nickel base alloys B1900, IN100, TRW1900 and Mar M-200. Tested with the tensile axis in the direction of solidification, all alloys had better stress rupture and thermal shock resistance properties than the equivalent equi-axed grained alloys. The latter improvement being due to the reduced elastic moduli. The degree of improvement in creep rupture life of the alloy through directional solidification was found to depend mainly on the intrinsic strength of the alloy, which was a function of composition, heat treatment and crystallographic orientation. The improvement in properties was typically from 5% to 20% in creep rupture ductility and an order of magnitude in creep rupture life. The latter effect was more prominent at a test temperature of 1400°F (760°C) than at the higher test temperature of 2000°F (1093°C). The least ductile in the conventionally cast condition, Mar M-200, benefited most in increased stress rupture life from directional solidification.

The material Mar M-200 (composition (wt%) 0.15 C, 9 Cr, 10 Co, 5 Al, 2 Ti, 12 W, 1 Nb, 0.15 B, 0.05 Zr, balance Ni) has been tested in a directionally solidified form (often designated DS200) in engine components as the guide vanes and turbine blades in Pratt & Whitney gas turbine jet engines [10].

The influence of the crystallographic orientation of the columnar grains with the tensile axis was evaluated for the material DS200 by Kear & Piearcey [11] under creep and tensile test conditions. Tensile yield stress measurements indicated that in the temperature range 70°F to 1400°F

(21°C to 760°C), the plastic behaviour depends strongly on orientation, whereas at 1800°F (982°C) there is little orientation effect. This was attributed to single slip systems operating at the lower temperatures and multiple slip occurring at the high temperature. A similar effect was noticed under creep conditions. The resistance to deformation should be greatest at <100> owing to a minimum in the Schmid factor and the tendency to maximise work hardening. From the creep data, the optimum orientation for a single crystal turbine blade was deduced to be either with the tensile axis parallel to [001] or [111]. However, the [001] orientation may be preferred due to its minimum elastic modulus value, a factor which increases the resistance to thermal shock.

An absence of transverse grain boundaries has also been shown to improve the low cycle fatigue life of DS200 over Mar M-200 [12], the usual intergranular crack propagation process being eliminated. An improvement of one or two orders of magnitude was found at the temperatures 1400°F (760°C) and 1700°F (927°C).

From a theoretical standpoint, Northwood & Homewood made an experimental comparison of the creep and tensile properties of the nickel base alloy 713C (composition (wt%) 0.12 C, 12.5 Cr, 6.1 Ti, 0.8 Al, 4.2 Mo, 2.2 Nb, 2.5 Fe, 0.12 B, 0.10 Zr, balance Ni) in the conventionally cast and directionally solidified (columnar grained in [001]) forms [13]. Initially, the exothermic mould technique, as described in Figure 1.3, was used. To investigate the casting parameters of the directionally solidified form, a modified Bridgman technique was developed, i.e. a mould on a cooled base with a moving furnace, withdrawal rate being 4 in/h to 40 in/h (102 mm/h to 1020 mm/h). The furnace withdrawal rate affected the grain size and, to a small extent, the morphology of the γ' particles. The withdrawal rate had no significant effect on the tensile properties of the material at 750°C but, under a tensile stress of 11 ton/in^2 (170 MN/m^2)

at 950°C, the mean creep life of three tests increased from 110 h for a withdrawal rate of 4 in/h (102 mm/h) to 201 h at 15 in/h (381 mm/h). The optimum stress rupture properties were associated with finer dendrite arm spacing and γ' cuboid distribution.

A comparison between the stress rupture properties at 950°C of the unidirectionally and conventionally solidified air-cast ingots again showed the improvement for the directionally solidified form when the tensile axis is parallel to the columnar grains. This is shown in Figure 1.4. No direct metallurgical reasons were given for the improvement in life for the longitudinal DS structure.

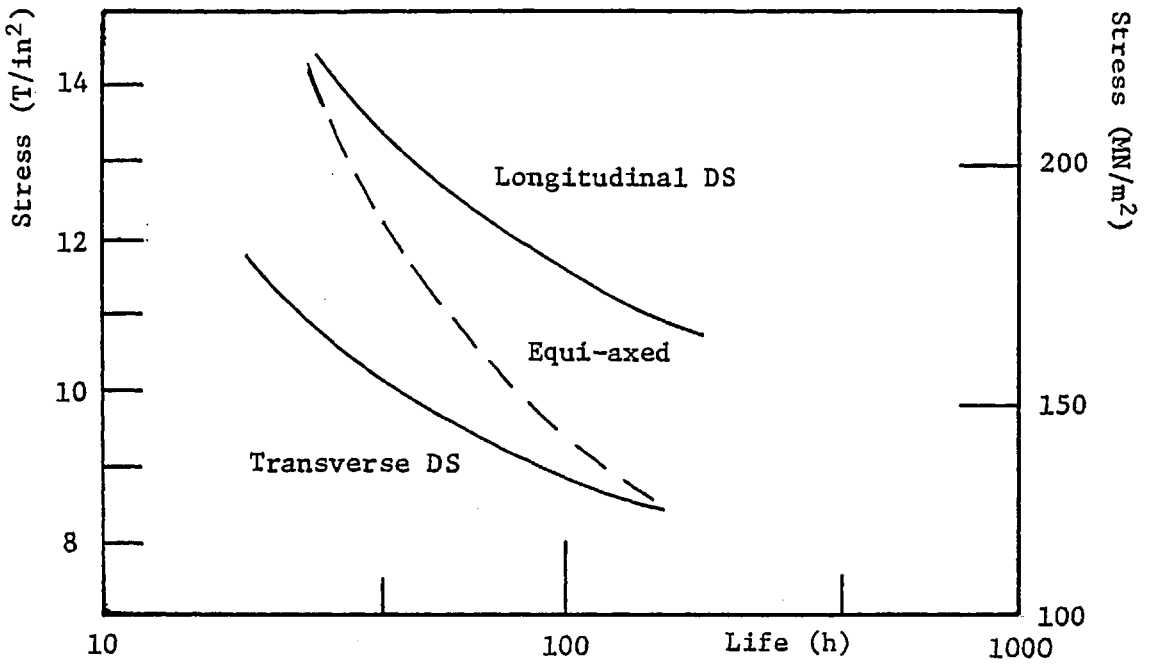

Figure 1.4: Effect of structure on creep life of Inco 713C at 950°C

The directionally solidified alloys so far mentioned all have a basic dendritic structure which means that there are still small sections of transverse grain boundary where the grains are aligned with the tensile axis. These areas of transverse grain boundary have been shown as a weakness under creep conditions [9]. To eliminate this effect, recent

developments [14] have been towards monocrystals and the refinement of directional solidification with a cellular or plane front structure. These structures are obtained by controlling the growth rate and thermal gradient of the cast.

As the directional solidification processes are comparatively expensive on a commercial scale, there have also been developments on the composition of the nickel base alloys. Lund has carried out a comparison between the manufacture and properties of DS200 and a comparable alloy developed to improve the stability and properties - Mar M-246 (composition (wt%) 0.15 C, 9.0 Cr, 10 Co, 10 W, 2.5 Mo, 1.75 Ta, 5.5 Al, 1.5 Ti, 0.15 B, 0.05 Zr, balance Ni) [15]. The results are summarised in the table below.

	Directionally Solidified	Conventionally Cast - Composition Modified
Advantages	(a) Superior resistance to thermal shock (b) Somewhat better overall stress rupture properties	(a) Lower cost (b) Uses conventional casting equipment
Disadvantages	(a) Difficult processing (b) Higher creep rates at intermediate temperatures (c) Lowered modulus of elasticity	(a) Does not equal the inherent exceptional resistance to thermal thermal fatigue

The gap in the thermal fatigue properties can be reduced by coating components (usually with an aluminide). However, even the alloy Mar M-246 is being superseded by Mar M-002, which has 1.5% Hafnium added to change the Chinese-script MC carbide morphology to a more equi-axed

morphology, and hence improve intermediate stress rupture properties [17].

Thus, the development of the nickel base alloys is still progressing and will continue to with the ever increasing temperatures that components are being operated at, e.g. the introduction of thermomechanical processes where work hardening and heat treatments are used to improve high temperature properties [16].

1.4 STRUCTURAL CHANGES AND PROCESSES OCCURRING DURING CREEP

1.4.1 Structural Changes Due to Creep

Besides the macroscopic observable phenomenon of an increasing strain during creep, there are many microscopic and structural changes occurring within the material.

During the secondary creep stage (Region C, Figure 1.1), the material structure is often regarded as being constant [18] and as that formed during the incubation period and primary creep stages (Regions A and B, Figure 1.1). For example, Mukherjee et al [19] have suggested that transient creep involves:

(a) sub-grain formation;

(b) sub-grain misorientation;

(c) a change in density and disposition of dislocations in sub-grains.

Barrett et al [20] observed the above changes for a Fe - 3% Si alloy. The sub-grain formation did not occur immediately on loading but developed during the primary creep stage until the secondary creep stage was reached, when no further changes occurred.

Creep occurs both within the grains and at the grain boundaries. The amount of deformation within either structure is dependent on both the

stress and the temperature. Garofalo [21] found that for a type 316 stainless steel, the ratio of grain boundary sliding to total strain was as high as 0.5 in the low creep stress region, 6000 lb/in^2 (41.4 MN/m^2), but decreased to a constant value of 0.1 at stresses greater than 15000 lb/in^2 (103 MN/m^2). These tests were in the temperature range 704°C to 830°C.

McLean [22] studied grain boundary sliding in aluminium after 10% strain and found that the amount of sliding increased with test temperature up to 300°C and then remained constant. There was also a variation in the amount of sliding with the grain size; the larger the grain size, the greater the sliding distance and hence strain.

Threadgill & Wilshire [23] have observed grain boundary deformation in a two-phase copper-cobalt alloy. It was found that at creep stresses below the yield stress, only limited deformation takes place in the grains and creep is a result of grain boundary sliding and accommodating deformation. In the high stress region, creep occurs by deformation of both the grains and the grain boundary regions.

Thus, the grain boundary has an important effect on deformation over a wide range of stresses and temperatures for the primary and secondary creep stages, as illustrated by the statement of McLean [24]: "In engineering creep grain boundary sliding seems to account for a substantial fraction of the total strain." The effects of the grain boundary on creep fracture have already been described in Section 1.3, where the transverse sections of grain boundary in a tensile creep test were found to be a considerable source of weakness [25].

For an equi-axed structure, creep fractures are predominantly intergranular, originating from either triple point grain boundaries or cavities. However, cavities have also been shown to exist in Nimonic 80A, under creep conditions of 90 MN/m^2 to 400 MN/m^2 and 750°C, throughout the

creep life [26]. The number of cavities per unit area was directly proportional to the strain, the proportionality constant being a function of the applied stress. The grain size for these tests was only 20 μm, which may explain why so little grain boundary sliding could be accommodated. Hence the formation of cavities.

Dislocations play a fundamental part in the structural changes taking place during creep and their influence on creep deformation and second phase structures will be formulated in Section 1.5.

1.4.2 Structural Changes Occurring During Creep

The nickel base alloys reviewed in Section 1.3 are mainly used for components operating at temperatures greater than 0.5 T_m. At these temperatures, the second phase precipitation hardening phase, γ', changes in size and morphology whilst the grain boundary areas may become denuded of γ'. Also, changes occur in the carbide structures and morphology.

The γ' morphology can be either spherical or cuboid, depending on the misfit parameter of the γ' with the γ matrix [27]. When the misfit is less than approximately 0.5% spheres are likely, whilst in the range 0.5% to 1.0% cubes are formed, there being no precipitation when the misfit is greater than 1%. This is not always obeyed as for the alloy Nimonic 80A (misfit 0.5%) the particles can be either spherical or cuboid, depending on the temperature at which the γ' is precipitated. Another anomaly is Nimonic 115 where the γ' particles are cuboid (misfit 0.08%) [28]. The volume fraction of γ' must also have some influence on these results, it being nominally 15% for 80A and 60% for 115.

The presence of a creep stress has been shown to have little effect on precipitate coarsening (Mitchell [29], Rowe & Freeman [30]) when the volume fraction is low (< 33%), but in contrast Tien & Copley [31,32] have found significant effects for the alloy Udimet-700, where the volume

fraction is 35%. In the latter case, monocrystals with the applied stress parallel to <100>, <110> and <111> were tested. Stress annealing resulted in oriented cuboidal, plate or parallel-piped shaped precipitates, the basic γ' morphology being <100> cuboids. The morphology changes were related to the orientation of the stress axis, the changes in bulk precipitate strain and the elastic constraints of the matrix with the precipitate phases. Only if the elastic constants of the matrix and precipitate are equal can stress-induced morphological changes be completely precluded.

Above 0.6 T_m, the coarsening rate of the γ' phase is pronounced and it is in this range that many gas turbine components are operating.

The basic process occurring in the coarsening of the γ' is diffusion. From Wagner's basic Ostwald ripening theory [33], Fleetwood [5] and Oriani [34] have derived that the γ' particle size grows according to the relationship:

$$d^3 = \left(\frac{64\ \gamma_e\ D\ C_o\ V_m^2}{9\ R\ T}\right) t \qquad (1.1)$$

where d = particle diameter

γ_e = the particle/matrix interface energy

D = coefficient of diffusion of γ' solutes in γ

C_o = concentration of solute in equilibrium with an infinitely large particle

V_m = molar volume of γ'

R = gas constant

The original Wagner theory assumed that the particles were: (a) in an equilibrium state, (b) spheroid, and (c) in a constant volume fraction. The form of equation (1.1) has been used by many people to represent the

growth rates of nickel base alloys, despite the above criteria clearly not being met. For example, Ardell & Nicholson [35] successfully used the above expression for a Ni - 6.7% Al where the particles were cuboid. In this case, the particle diameter parameter was replaced by the length of the cube side.

The predominant temperature factor in equation (1.1) has been found to be the diffusion coefficient, D, with a temperature dependence of the form [35]:

$$D = A \exp^{-Q_{SD}/RT} \tag{1.2}$$

where A = constant

Q_{SD} = activation energy of self diffusion

The value of the activation energy for the diffusion of Al in Ni is 64 kcal/mol (268 kJ/mol) and for Ti diffusion in a 75 wt% Ni, 20 Cr, 5 Mo alloy is 65 kcal/mol (272 kJ/mol) [36]. These values are close to those found experimental for the growth of γ' in the nickel base alloy PE16 of 64 kcal/mol (268 kJ/mol) [36], and in the Ni - 6.7% Al alloy of 64.4 kcal/mol (270 kJ/mol) [35]. However, Mitchell [29] has analysed the series of nickel base alloys PE16, Nimonics 80A, 90 and 115 collectively and found a value of 86 kcal/mol (360 kJ/mol). The different value found to that for the Al and Ti diffusion may be due to the wide range in morphology of the γ' precipitate, from spheres to cubes, and the variable volume fraction, from 15% to 50%, giving rise to individual values of activation energy for each alloy which cannot be agglomerated.

Not all creep is carried out under conditions of constant stress and temperature and the cyclic nature of these parameters can affect the deformation and structural characteristics. Rowe & Freeman [37] studied cyclic overheating above 1600°F (871°C) for the nickel base alloys

Mar M-252 and Inconel 700. Mar M-252 has a low volume fraction of γ' and the creep properties with cyclic overheating were sensitive to the size and spacing of the γ' particles. The higher volume fraction of γ' in Inconel 700 resulted in a virtual insensitivity of creep properties to size and spacing. Complications arose in the analysis in that during the overheating cycle, some of the γ' resolutionised and a fine γ' reformed at the lower temperature.

It is thus certain that there will be some change in the γ' phase morphology and size during service conditions in gas turbine applications. One of the methods by which the γ' phase increases the strength of nickel base alloys is the particle/dislocation interaction (Section 1.2). However, the increase in strength is dependent upon the particle size and volume fraction. Upon reaching a critical size, there can be a decrease in strength due to a change in the dislocation/particle interaction process. This is illustrated in Figure 1.5 [38].

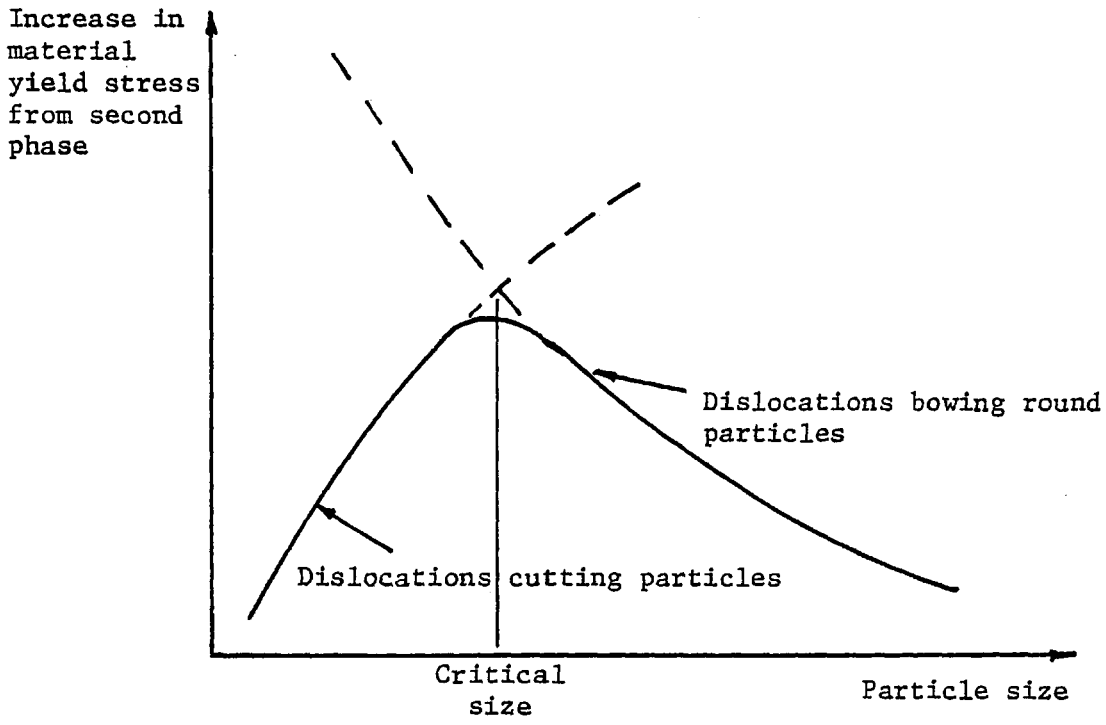

Figure 1.5: The relationship between particle size and increase in yield stress

For small particle sizes, and hence small interparticle spacing for a constant volume fraction, it is easier for the dislocations to cut through the particles, creating anti-phase boundaries. This dislocation/particle strengthening process has been studied theoretically by Gleiter & Hornbogen [39] and observed by Copley & Kear [40].

The transition from the cutting mechanism to the by-passing, or looping mechanism, would appear to be dependent on the volume fraction of the γ' and cannot be readily predicted [5]. Once past the critical particle size, it then becomes easier for dislocations to by-pass the particles by bowing between them or by climb. Bilsby [36] has illustrated the effects for the alloy PE16 and also experimentally related the particle size to the steady-state creep rate, as shown in Figure 1.6. From

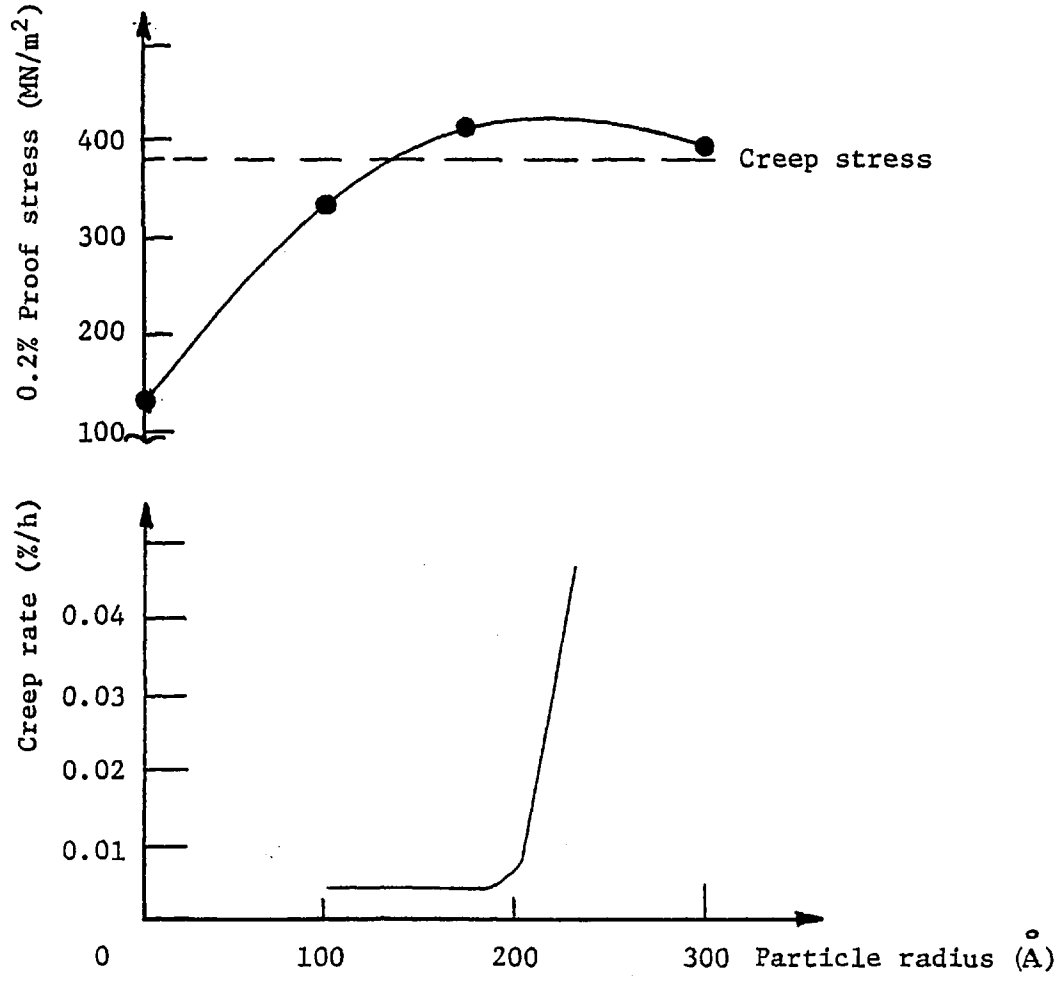

Figure 1.6: Steady-state creep rate at stress of 381 MN/m^2 and 0.2% proof stress at 650°C as a function of particle radius

Figure 1.6, it can be deduced that for the alloy PE16, the critical particle size for the change in dislocation deformation mechanisms is of the order of 200 Å (0.02 μm).

Concentration in this survey has been made on the primary second phase, γ', in nickel base alloys but decomposition of other phases can occur with exposure to temperature and stress. The σ phase (Ni_3Ti in TCP form) is particularly detrimental to strength in that the plate-like morphology provides an excellent source for crack initiation [6]. The σ phase can precipitate in the temperature range 650°C to 925°C, especially under stress, depending on the average electron-vacancy number [5].

The individual effects of composition, precipitate morphology and size, exposure to stress and temperature on material properties cannot be considered in isolation and the illustrations given in this section show the complex interactions that take place.

1.5 STRUCTURAL THEORIES

The simplest of structural theories is that derived by Cottrell [63] and is the basis of dislocation dynamics theories:

$$\dot{\varepsilon}_p = \phi\, b\, \rho\, v \tag{1.3}$$

where $\dot{\varepsilon}_p$ ≐ plastic strain rate

ϕ = an orientation factor

b = Burgers vector

ρ = mean dislocation density

v = mean dislocation velocity

The above equation was derived purely from geometric considerations of a

single dislocation moving one Burgers vector in the material lattice, either in the form of a screw dislocation or an edge dislocation.

The difficulty in applying equation (1.3) directly to experimental data arises from the experimental determination of the dislocation density and velocity. Johnston & Gilman [41] were amongst the first to observe deformation due to dislocations by the use of the etch pit technique on LiF crystals. Relationships between stress, temperature, strain, dislocation velocity and density were found.

The dislocation velocity has a maximum value of the velocity of sound in the material. Experimentally, the dislocation velocity was found from the duration of the stress pulse in a compression test. For low stresses and in a temperature range $25°C < T < -50°C$, a relationship was found between the velocity, v_s, stress and temperature of the form:

$$v_s = \sigma^n \exp^{-E/kT} \tag{1.4}$$

where σ = resolved shear stress

n = stress exponent of between 15 and 25

E = an activation energy ($\simeq$ 93 kJ/mol) independent of stress

The dislocation density was found to be linearly related to the plastic strain and it was proposed that a time rate dependence existed in the form:

$$\dot{\rho} = \alpha \rho - \beta \rho^2 \tag{1.5}$$

where α and β are constants. This is similar to relationships used in later theories.

Using equations (1.3) and (1.4) and the experimental linear strain dependence of the dislocation density, the experimental results for the

compression test were compared with:

$$\dot{\varepsilon} = 2 \times 10^9 \times \varepsilon \times v_s \qquad (1.6)$$

Deviations occurred at high strains due to neglecting the effects of work hardening.

On a purely qualitative basis, Barrett & Nix [20] observed dislocations under creep conditions in an Fe - 3 wt% Si alloy. Both etch pit and electron microscopy techniques were used, the former method being proposed as being an accurate relative measure of true dislocation density. The dislocation density in areas not associated with sub-grain boundaries was found to decrease by a factor of 3 for approximately 0.2% creep strain in the primary creep region.

The observations of Barrett & Nix highlight the fact that equation (1.3) is derived assuming all dislocations are mobile and does not take into account any dislocation interactions. Gilman [42] introduced a mobility factor into the total dislocation density. The mobile fraction, m, was given by:

$$m = exp^{-(H.\varepsilon_p)/\sigma_s} \qquad (1.7)$$

where H = strain hardening coefficient

ε_p = plastic strain

σ_s = applied shear stress

A similar analysis to that for the LiF results of Johnston & Gilman was performed, including the mobile fraction given by equation (1.7), and the resulting equation was:

$$\dot{\varepsilon}_p = g\, b\, (\rho_o + M\, \varepsilon_p)\, v^*\, exp - \frac{(D + H\, \varepsilon_p)}{\sigma_s} \qquad (1.8)$$

where g = geometric factor that depends on the direction of the plastic strain

ρ_o = initial dislocation density

M = dislocation multiplication rate

v^* = terminal velocity at high applied shear stress

D = characteristic drag stress

Equation (1.8) gives a relatively simple relationship for the plastic strain rate dependence on strain but needs numerical integration to find the dependence of strain with time for a creep test.

In the diffusion-controlled range of creep, the steady-state creep rate is closely related to the size and morphology of the dispersed second phase and its interaction with dislocations. A good example of this is the analysis of Ansell & Weertman [43] for the climb of dislocations round particles. Here, the climb dislocation mechanism was the rate controlling process. The dislocations originate at Frank-Read sources, whose lengths are much greater than the distance between particles. The analysis is split into two stress regions; in the first, the dislocations remain as loops and in the second the loops are pinched off. This is illustrated in Figure 1.7.

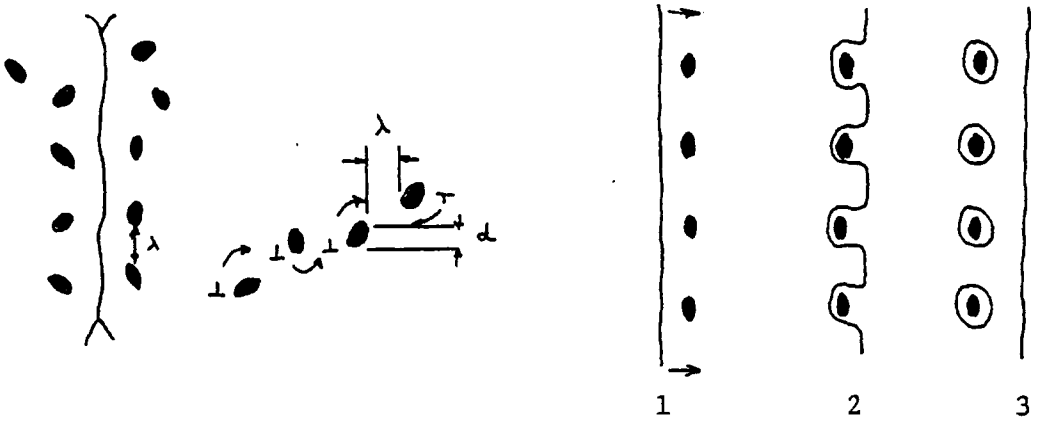

A - Low stress B - High stress

Figure 1.7: Dislocation-particle interaction mechanisms

For the low stress region, defined by Ansell & Weertman as $(\mu b)/L < \sigma < (\mu b)/\lambda$, where μ is a shear modulus, L is the length of a Frank-Read source, and λ is the interparticle spacing, the creep strain rate is given by:

$$\dot{\varepsilon} = \frac{\pi \sigma b^3 D}{4\sqrt{2}\, d^2 k T} \tag{1.9}$$

In the high stress region, the rate controlling process is the climb of the pinched off loops which leads to:

$$\dot{\varepsilon} = \frac{\pi \sigma^4 \lambda^2 D}{\sqrt{2}\, d\, \mu^3 k T} \tag{1.10}$$

At stresses when $(n \sigma b^3)/kT > 1$ (n is the number of loops piled up in the distance λ), the velocity term of dislocations is changed and the creep rate now becomes:

$$\dot{\varepsilon} = \frac{\pi \sigma^2 \lambda D}{2\sqrt{2}\, \mu^2 b^2 d} \exp\left(\frac{2\sigma^2 \lambda b^2}{\mu k T}\right) \tag{1.11}$$

Sherby & Burke [44] illustrated the above relationships for various particle sizes in a constant volume fraction, as shown in Figure 1.8.

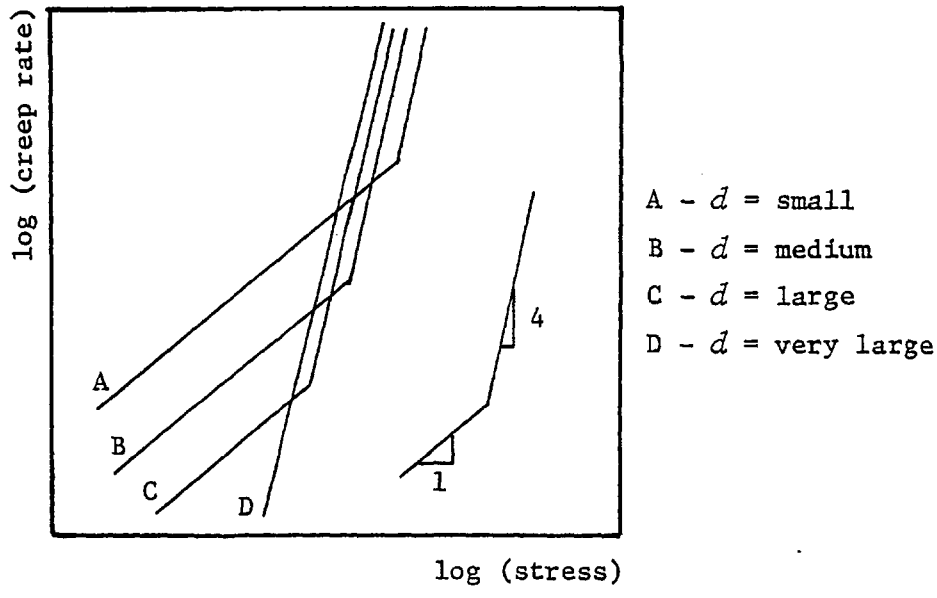

Figure 1.8: Influence of particle size on the creep rate-stress relationship

McLean [45] has also reviewed the creep rate dependence on the particle size with similar conclusions but splits the particle size relationships into three regions, as shown in Figure 1.9.

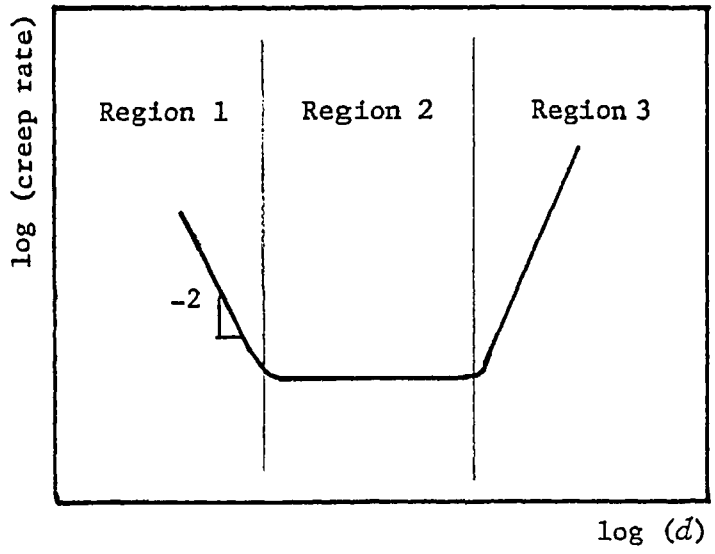

Figure 1.9: Influence of the particle size, d, on the creep rate

In Region 1, the dislocations move by pushing the particles ahead, with the rate controlling process being that of vacancy migration from the tension side of the particle to the compression side. The creep rate is then inversely proportional to the diffusion distance squared, i.e. $\dot{\varepsilon} \propto 1/d^2$.

In Region 2, the dislocations alternatively climb over particles and then glide a certain distance, λ, before another particle is met. Thus, for a glide distance, λ, the time taken is proportional to d and the creep rate is proportional to λ/d. For a constant volume fraction, λ/d is a constant and the creep rate is then constant.

Bowing of dislocations becomes important in Region 3 but no specific creep rate - particle size is given. However, from equation (1.10) a relationship $\dot{\varepsilon} \propto d$ is expected for a constant volume fraction when the looping mechanism is operating (since λ is proportional to d).

Regions 2 and 3 are similar to those observed by Bilsby, as was shown

in Figure 1.6, but no critical value of particle size is offered for the change from Region 2 to Region 3.

Most of the above analysis has been applied purely to the secondary steady-state creep rate stage of creep. However, structural theories have been extended to other regions.

From the simple equation of state, $\sigma = f(\varepsilon, t)$, it can be shown, for a creep test, when $d\sigma/dt = 0$, that:

$$\dot{\varepsilon} = \frac{r}{h} \tag{1.12}$$

where r is the rate of recovery $= -(\partial\sigma/\partial t)_{\varepsilon}$, and h is the strain hardening rate $= (\partial\sigma/\partial\varepsilon)_{t}$.

Experiments have shown that during the primary stage of creep (Region B, Figure 1.1), the values of r and h are different functions of time and approach their constant secondary creep rate values at different rates [46,47]. The strain hardening rate, h, quickly rises to its steady secondary creep rate value but the recovery rate, r, only decreases slowly, leading to a slowly reducing creep rate being predicted from equation (1.12).

The rate of approach of the creep rate, $\dot{\varepsilon}$, during primary creep to its steady-state secondary value, $\dot{\varepsilon}_s$, has been proposed as following unimolecular reaction kinetics by Webster, Cox & Dorn (Appendix G). This is summarised by the relationship:

$$\frac{d\dot{\varepsilon}}{dt} = -\frac{(\dot{\varepsilon} - \dot{\varepsilon}_s)}{\tau} \tag{1.13}$$

where τ is the relaxation time for rearrangements of dislocations during transient creep; which, on integration, gives:

$$\varepsilon = \varepsilon_o + \varepsilon_T \{1 - exp\ (\frac{-t}{\tau})\} + \dot{\varepsilon}_s\ t \qquad (1.14)$$

where ε_o = the instantaneous strain at $t = 0$ arising from application of the stress

$\varepsilon_T = (\dot{\varepsilon}_i - \dot{\varepsilon}_s)\ \tau$

$\dot{\varepsilon}_i$ = creep rate at $t = 0$

Equation (1.14) was successfully used to fit creep data for an austenitic iron based alloy and type 316 stainless steel and is similar to that used by Garofalo et al [21] for the analysis of similar material. Sidey & Wilshire [47] and Evans & Wilshire [46] have also used an equation of the form of (1.14) for the analysis of the creep of Nimonic 80A.

The formulation of equation (1.13) was made without a specific dislocation deformation mechanism. Evans & Williams [48] have used equation (1.12) and a similar form of equation (1.13) to reach equation (1.14).

Assuming that in (1.12) the value of the work hardening rate, h, is constant for a given value of stress and temperature, then $\dot{\varepsilon} \propto r$. A relationship for r is proposed in the form:

$$r = B\ D\ (exp\ \frac{F}{k\ T} - 1) \qquad (1.15)$$

where B = constant

D = a diffusion coefficient

F = driving force on dislocations

The analysis of Webster, Cox & Dorn is followed in assuming that the driving force, favouring a change $F - F_s$ (F_s is the value of F during

steady-state secondary creep), follows first order kinetics, i.e.

$$-\frac{dF}{dt} = k\,(F - F_s) \tag{1.16}$$

Using equations (1.12), (1.15) and (1.16), the time dependence of the creep strain is found to be of similar form to (1.14) with the following equivalencies:

$$\varepsilon_T \equiv \frac{\varepsilon_o - \varepsilon_s}{k} \quad \text{and} \quad k \equiv \frac{1}{\tau}$$

For a three-dimensional network of dislocations, Evans & Williams proposed that the driving force, F, was related to the dislocation density, ρ, by $F \propto \rho^{\frac{1}{2}}$. The dislocations are only those not associated with grain boundaries or sub-boundaries. Using (1.16), the time dependence of dislocation density is found to be:

$$(\rho^{\frac{1}{2}} - \rho_s^{\frac{1}{2}}) = A\,exp\,(-k\,t) \tag{1.17}$$

where A is a constant, and ρ_s is the value of dislocation density during steady-state secondary creep. Experimental evidence was presented for a stainless steel creep tested at 129 MN/m^2 and 750°C, where the dislocation mesh size was measured. The mesh size is proportional to $\rho^{\frac{1}{2}}$. It was found that the values of k in (1.17) and $1/\tau$ from equation (1.14) were identical, giving confirmation of the first order kinetics approach to primary and secondary creep.

Equation (1.14) has also been applied to the transient creep of metals by Amin et al [49]. In the high temperature diffusion controlled region of creep, they came to the conclusion that the prime deformation mechanism operating is the climb of dislocations.

The structural theories so far presented have concentrated on the

transient and secondary stages (B and C of Figure 1.1) and mainly for constant values of work hardening rates.

To cover the Regions A, B and C of Figure 1.1, Webster [1] used the basic dislocation dynamics equation (1.3) but also took into account a variable work hardening rate and the multiplication and annihilation of dislocations.

The change in dislocation density, ρ, was presented as:

$$\dot{\rho} = a_1 + a_2 v \rho - a_3 \rho^2 \tag{1.18}$$

where a_1, a_2 and a_3 are constants. The dislocation velocity, v, was given by:

$$v = V_o - k \rho \tag{1.19}$$

where V_o and k are constant at a constant stress and temperature. Thus, equation (1.19) predicts work hardening as the dislocation velocity decreases with an increase in dislocation density. Both the above equations are similar to those presented by Johnston & Gilman (equations (1.4) and (1.5)), but differ by the inter-relationship of dislocation velocity and density which is essential to incorporate the work hardening phenomenon.

Combining equations (1.18) and (1.19) gives:

$$\dot{\rho} = n + \alpha \rho - \beta \rho^2 \tag{1.20}$$

which, on integration, gives the time dependence of the dislocation density as:

$$\rho = \frac{\alpha_1 - \alpha_2 \theta \exp(-\phi t)}{[1 + \theta \exp(-\phi t)]} \tag{1.21}$$

Substituting equation (1.18) into (1.3), and omitting the orientation factor, gives:

$$\dot{\varepsilon} = b\,(V_o - k\,\rho)\,\rho \qquad (1.22)$$

and using the time dependence relationship for dislocation density in equation (1.21), this can be integrated to give:

$$\varepsilon = A\,t + D\,ln\,[B + (1-B)\,exp\,(-\phi\,t)] + \frac{C\,(1-B)(1-exp\,(-\phi\,t))}{[B + (1-B)\,exp\,(-\phi\,t)]} \qquad (1.23)$$

where $A = b\,\alpha_1\,(V_o - k\,\alpha_1)$ and α_1 is the steady-state dislocation density

$B = 1/(1+\theta) = (\alpha_2 + \rho_o)/(\alpha_1 + \alpha_2)$ and ρ_o is the initial dislocation density

$C = (b\,k)/\beta\,(\alpha_2 + \rho_o)$

$D = b/\beta\,(V_o - k\,(\alpha_1 - \alpha_2))$

$\phi = \beta\,(\alpha_1 - \alpha_2)$

The condition for an incubation period, i.e. Region A, Figure 1.1, is simply found from equation (1.22) by putting $\ddot{\varepsilon} = 0$, from which $\rho_o = V_o/2k$. The conditions for the Regions A, B and C on their own, or in combination, is similarly found to depend on the initial dislocation density.

Experimental evidence for the use of equation (1.23) was shown for creep data on the Ni base alloy Mar M-200, aluminium oxide and lithium fluoride.

Equation (1.23) may be simplified by eliminating individual dislocation mechanisms, e.g. if multiplication occurs from mobile dislocations only ($n = 0$) and if the dislocation velocity remains constant, i.e. no work hardening and $k = 0$, then the reduced equation becomes:

$$\varepsilon = \frac{b V_o \alpha t}{\beta} + \frac{b V_o}{\beta} ln [B' + (1-B') exp (-\alpha t)] \qquad (1.24)$$

As expected, this is identical in form to that derived by Li [50] on the basis of equations (1.3) and (1.5) and a constant dislocation velocity. Li's equation is given as:

$$\varepsilon = \varepsilon_o + \dot{\varepsilon}_s t + \frac{\dot{\varepsilon}_s}{k_1} ln \left[1 + \frac{\dot{\varepsilon}_i - \dot{\varepsilon}_s}{\dot{\varepsilon}_s} (1 - exp (-k_1 t))\right] \qquad (1.25)$$

Equations (1.23) to (1.25) provide useful relationships between creep strain and time but do not include any stress and temperature functions as compared with equation (1.8), which did not have an explicit time function.

Lagneborg has made experimental observations of dislocation changes during creep of a 20% Cr - 35% Ni stainless steel [51,52] and derived a recovery based model for a complex three-dimensional network of dislocations with a distribution of link sizes in the network [53]. The resulting equation for the variation in link size with time, and hence dislocation density, is complex and involves terms accounting for the recovery of the dislocation distribution, the realise of links due to thermal activation and the supply of links through the multiplication of dislocations. The creep rate is presented as an integration of the deformation due to the dislocations but is not in a form that can be readily compared with other data.

1.6 PHENOMENOLOGICAL EXPRESSIONS AND CREEP PARAMETERS

By definition, phenomenological expressions are obtained by direct observation of experimental data and the fitting of a curve, or curves. They are sometimes in agreement with physically based equations.

Some examples of these equations are listed by Kennedy [54] and are

grouped together in (a) strain-time equations, (b) temperature dependence of strain and strain rate, and (c) stress dependence on strain and strain rate.

Classical examples in group (a) are those of Andrade, which is:

$$\varepsilon = a\,(1 + b\,t^{1/3})\,exp^{kt} \tag{1.26}$$

and has been used for the analysis of data of many material, and that of McVetty which is:

$$\varepsilon = a + b\,t + c\,exp^{-dt} \tag{1.27}$$

Equation (1.27) is similar in form to that derived from first order reaction rate theory by Webster, Cox & Dorn (Appendix G).

Perhaps the most complex of phenomenological expressions is that originally presented by Graham [55] and more fully by Graham & Walles [67]. The creep strain is a summation of one or more terms in the form:

$$\varepsilon = \sum C\,\sigma^{\beta}\,t^{\kappa}\,(T' - T)^{-20K} \tag{1.28}$$

In each term, the constants κ and the ratios κ/β take one of a limited number of standard values, viz:

$$\left.\begin{aligned} \kappa &= 1/3,\ 1,\ 3,\ \ldots. \\ \text{and:}\quad \kappa/\beta &= \ldots.,\ 1/16,\ 1/8,\ 1/4,\ 1/2,\ 1 \end{aligned}\right\} \tag{1.29}$$

The parameters C, T', κ and β are determined to give the best possible fit to the experimental data. This has been successfully done for nickel base alloys [70] and stainless steels over a wide range of temperatures

and stresses. With experience, the technique can be used to extrapolate data on a time, stress or temperature basis.

It is noted that the temperature term, $(T'-T)^{-20K}$, has a zero value when $T = T'$ and the particular term cannot then be used. However, it is often found that the T' value has some metallurgical significance, e.g. for nickel base alloys it can be the solution temperature of the precipitate phase and for some aluminium alloys the T' coincides with a value of temperature when the activation energy approach produces a discontinuity in values as a function of temperature.

The analysis is capable of covering all the Regions A, B, C and D of Figure 1.1 individually but incapable of operating when the incubation period, A, is followed by the normal primary and secondary creep stages, B and C. However, the usefulness in covering the tertiary part is important.

Starting from a phenomenological approach, the work of Dorn [56] has encompassed the metallurgical approach. Early analysis of the steady-state creep rate for pure metals was made to find a temperature parameter. It was then found that using an activation energy term, the energy values found were identical to those for self diffusion. Thus, a link between diffusion and creep was established.

Proceeding from the activation energy, a time-temperature parameter was developed of the form:

$$\theta = F(\sigma) = t \exp - \frac{\Delta H}{R\,T} \qquad (1.30)$$

where ΔH = an activation energy

and was successfully used for many pure metals and simple alloys over the complete creep strain range.

Others have developed time-temperature parameters from a purely phenomenological viewpoint and examples of these are the Larson-Miller:

$$P = F(\sigma) = T\,(C + \log t_R) \tag{1.31}$$

and the Manson-Haferd:

$$P = F(\sigma) = \frac{T - T_a}{\log t_R - \log t_a} \tag{1.32}$$

where t_R = creep rupture time, and C, T_a and t_a are constants.

The parameters in equations (1.31) and (1.32) have been predominantly used for creep rupture data and its extrapolation.

Goldhoff [57] has reviewed the use of the parameters in equations (1.30) to (1.32) for extrapolating the rupture data of several high temperature alloys to determine long time rupture stresses. The three parameters gave better values than those obtained by a pure visual extrapolation of the data. This latter method can produce gross errors and Lubahn & Felgar [58] summarise these by showing the dependence on personal choice and viewing of data points.

So far in this section on creep strain/creep strain rate-time relationships, no specific stress functions have been given. Recent developments in creep analysis have been to consider the applied stress as a summation of active stresses and internal stresses.

For many materials over a wide range of stress and temperatures, the dependence of the steady-state creep rate, $\dot{\varepsilon}_s$, on the applied stress, σ, can be expressed as:

$$\dot{\varepsilon}_s = A\,\sigma^n \tag{1.33}$$

where A and n are assumed to be constant. However, the value of n varies

enormously from 4 to 6 for pure metals and many single phase alloys to up to 40 for two phase alloys.

Wilshire & Threadgill [59] have rationalised these different values by proposing that:

$$\dot{\varepsilon}_s \propto (\sigma - \sigma_o)^4 \tag{1.34}$$

where σ_o is some internal stress. A measure of σ_o can be determined by arresting the crosshead during a constant strain rate test and noting the level to which the stress decays. An alternative method whereby the stress is reduced by small increments during a creep test until a zero creep rate is sustained produces another value for σ_o and has been shown to be similar to that found by the above method [71].

Williams & Wilshire [72] presented data for measurements of σ_o for Nimonic 80A creep tested at 750°C and showed that equation (1.34) held. They also suggested, but did not confirm, that the internal stress, σ_o, was affected by sub-grain size, the size and distribution of particles and other microstructural aspects.

Nix & Barrett [66] have also used a structural approach to the concept of internal stress, but in this case considered that creep takes place under an effective stress, σ_e, such that:

$$\sigma_e = \sigma - \sigma_i \tag{1.35}$$

where σ_i is their interpretation of internal stress. In this case, there was a rapid reduction in applied stress during creep such that when σ was reduced to σ_i, the effective stress on the dislocations, σ_e, was zero and the creep rate should also be zero. However, Wilshire & Threadgill [59] showed that an incubation period of zero creep rate occurred for all stress reductions during creep of pure metals, single phase and two phase

alloys. Thus, the total internal stress opposing deformation during creep must be equal to or even slightly greater than the applied stress. When the applied stress is reduced, the structure must change by recovery processes before creep can recommence at the lower stress.

The data for σ_o for the γ' hardened austenitic steel presented by Wilshire & Threadgill [59] showed that the internal stress values determined were themselves a function of the applied stress. Up to a value of creep stress close to the yield stress for the material, the value of n in equation (1.33) was approximately 4.5, whilst for values above the exponent was approximately 13. The experimental values of σ_o up to creep stresses close to the yield stress were linearly related to the applied stress, whilst for applied stresses above the yield stress the value of σ_o was the yield stress. With these values of σ_o, equation (1.34) was found to apply.

The above approaches to internal stress was criticised by Lloyd & McElroy [68], who considered that, although the answers were right, the fundamental reasoning was in error. They considered that the internal stress as measured is a complicated function of anelastic strain, strain rate, creep rate and applied stress, and consequently unlikely to correspond to any real material parameter. Their hardening and recovery rates were both proportional to anelastic strain and the creep model presented was based on the statistical distribution of dislocation segment lengths in crept material.

Harrison [69] has more recently studied the empirical and theoretical aspects of internal stress for the nickel base alloys Nimonic 90 and M-246. The internal stress was presented as a friction stress, with two components, and measured experimentally. The work was intended to be used for prediction of creep data, especially under thermal fatigue and of interest is the presentation of a stress parameter of the form $(\sigma - \sigma_o)/\sigma_p$, where σ_p

is the proof stress. This approach has been expanded by Evans & Harrison [92,94] and will be discussed in Section 7.

1.7 CONCLUSIONS

This literature survey has covered the nature and analysis of creep and creep strain data, the strengthening mechanisms and development of creep resistant materials and the metallurgical and microstructural aspects of high temperature creep deformation.

Section 1.1 showed that complex interactions between stress, strain, temperature and time exists and, in most cases, studies are confined to a small area. The above parameters of stress, temperature and time are all externally applied and the resultant strain is the sole description of the result. The material aspect was introduced by the effect of internal diffusion.

To reduce the large scope of creep, the temperature region above the dimensionless value of 0.5 T_m was concentrated on, which is the area at which many stressed components in gas turbines operate. This practical area of operations is primarily concerned with Ni base alloys and the industrial search for high creep strength was highlighted in Section 1.3. The search for better materials never ceases but the results presented in Section 1.3 represent some of the major developments in the last two decades. The next stage will probably involve ceramics and fibre composites which will use completely different theories and ideas. However, there is still a need to fully understand the operational characteristics of Ni base alloys.

Section 1.4.2 highlighted the importance of research into the main strengthening component of Ni base alloys, the γ' precipitate phase. The microstructural aspects of the γ' phase and dislocations were shown to be highly complex and even the morphology of the phase itself was in dispute.

For example, the work of Mitchell and Rowe & Freeman indicated that stress had no interaction with the γ' phase, whilst Tien & Copley presented evidence to the contrary. Simple growth laws for the γ' phase were shown to be based on assumptions which clearly did not apply in many cases.

In the structural theories presented in Section 1.5, dislocations play an important part from both the theoretical and empirical viewpoints. No one equation could be fully justified from either standpoint but each have merits. In a descriptive way, both Figures 1.8 and 1.9 illustrate the result of interaction between the precipitate particle size and dislocations, but neither can be described as the complete answer. In both figures, the actual mechanism of dislocation/particle interaction was not experimentally verified and this must be borne in mind when considering their accuracy. This can also be a criticism of the theoretical models resulting in equations (1.8) and (1.23). However, the five parameter model proposed in equation (1.23) is a relatively plain expression for the time dependence of creep strain which may be able to be verified experimentally. This will be attempted in the work presented in Section 5.2.

The phenomenological expressions in Section 1.6 have their greatest merit in being derived purely from experimental data and as such must fit well. The major criticism is that, although the expressions fit very well in a particular regime, there is rarely any guidance as to their use in other areas.

There is thus a great need for the microstructural, metallurgical, theoretical and empirical viewpoints to be rationalised and this was the main philosophy of the research project on the time, temperature, stress dependence of creep, of which this thesis is a part.

CHAPTER 2

SPECIMEN MATERIAL AND MANUFACTURE

2.1 SPECIMEN MATERIAL

The material used for all tests was a cast nickel base alloy with an equi-axed or a directionally solidified grain form supplied by Henry Wiggin Company Limited. The chemical composition of the tested alloy and the comparable commercial alloy, Nimonic 80A to BS.2HR.1:1973, are given in Table 2.1.

TABLE 2.1

Composition of Experimental Alloy and Commercial Nimonic 80A

Element	Experimental Alloy (wt%)	BS.2HR.1:1973 (wt%)
Cr	19.4 - 19.6	18.0 - 21.0
Ti	2.4 - 2.7	1.8 - 2.7
Al	1.3 - 1.5	1.0 - 1.8
C	0.05 - 0.07	0.04 - 0.10
Ni	Balance	Balance + trace elements

Thus, the experimental tested alloy differs from the commercial alloy in that the trace elements Cu, Si, Fe, Mn, B, S and Co are absent and the carbon content is much reduced, resulting in fewer complications from carbide formation.

2.2 DIRECTIONALLY SOLIDIFIED GRAIN FORM

The directionally solidified material was cast in 16 batches, two ingots in each batch, using the exothermic mould technique. This produced

ingots 50 mm in diameter with an aligned columnar grain section for approximately 75 mm of the 125 mm cast (see Figure 2.1). All batches were checked for chemical composition and were within the tolerances given in Table 2.1. A visual check on the grain orientation was made by etching the half sectioned ingots with an acid ferric chloride solution. The crystal orientation of the grains was checked on two ingots using the Laue back reflection X-ray technique and was found to be within ±5° of the [001] axis.

From the half ingots, blanks 13 mm × 20 mm × 121 mm were machined so that the axis of the specimens would be aligned with the axis of the directionally solidified columnar grains. After cutting, the blanks were solution heat-treated in air at 1080°C ±5°C for 8 hours and air cooled. Blanks were then fully machined to the specimen dimensions, as shown in Drawing ME/A496 (Figure 2.2), before finally ageing in air at 700°C ±2°C for 16 hours and air cooled. The form of the finished specimen, etched with the acid ferric chloride solution, is shown in Figure 2.3, where the alignment and size of the columnar grains can be seen.

An indication of the effect of the heat treatment and machining process is given by the Vickers hardness figures taken on the flat areas of the specimen ends and summarised in Table 2.2.

TABLE 2.2

Vickers Hardness Values

Material Condition	Hardness Value (VPN with 50 kg load)
As-received	280 - 300
Solution treated	240 - 260
Machined	270 - 310
Aged	320 - 380

Figure 2.1: Acid ferric chloride etch of as-received directionally solidified ingot

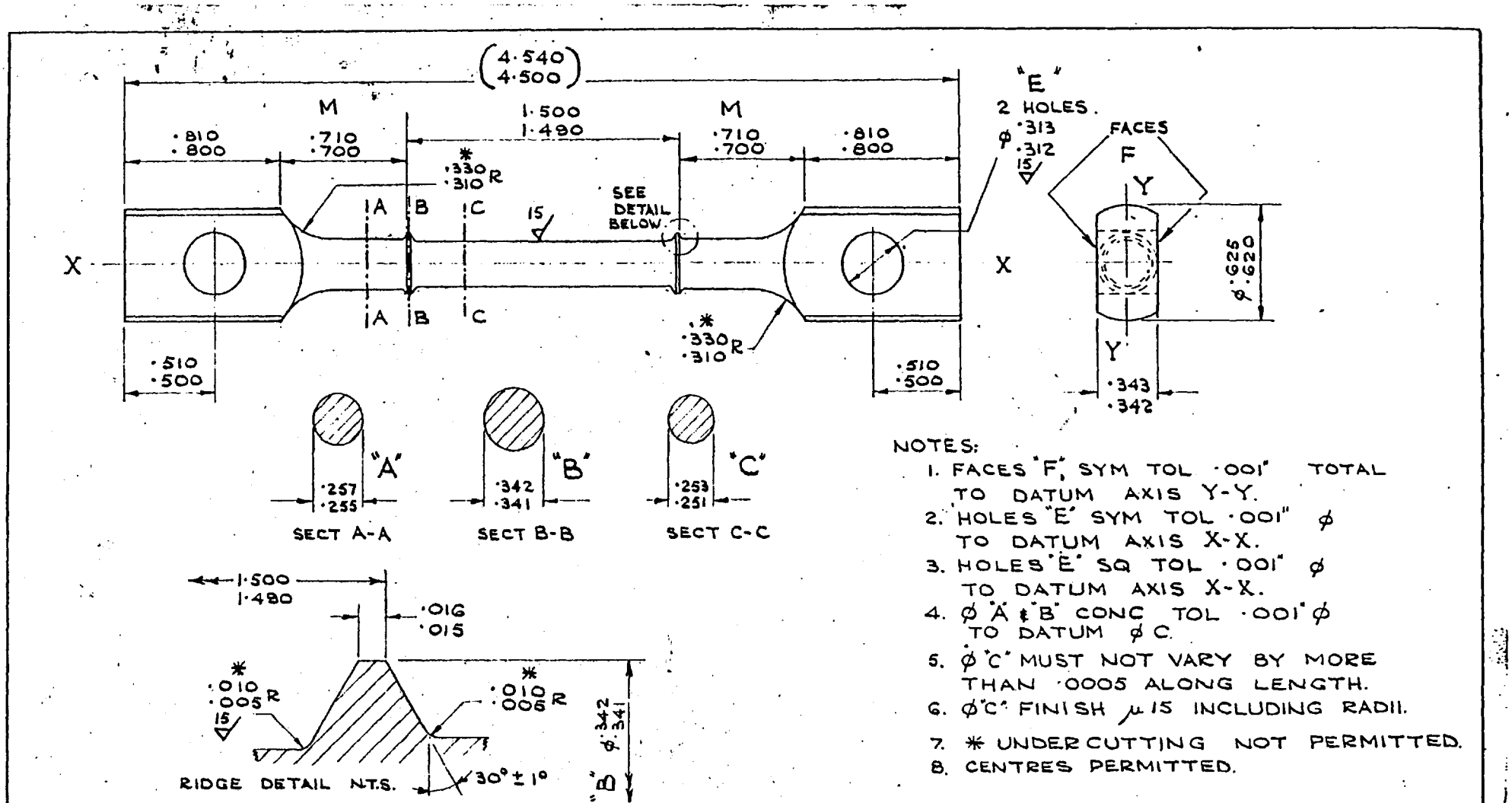

Figure 2.2: Drawing for manufacture of all test pieces

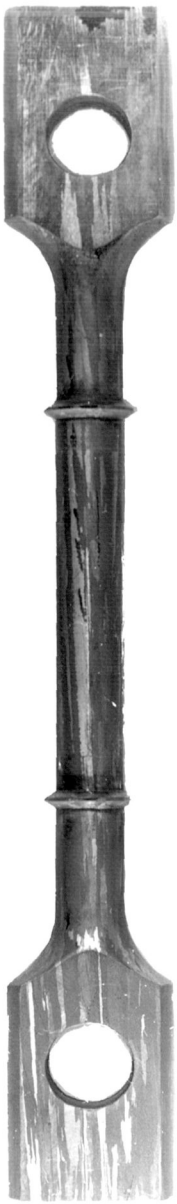

x 1.4

Figure 2.3: Macro-etched creep test piece

The specimen material identification system used was by means of the last two digits of the batch cast number, as provided by Henry Wiggin, the batch ingot letter, either A or B, and the specimen number from the batch, e.g. 67A4 signified batch number 1067, ingot A, number 4 specimen.

2.3 EQUI-AXED GRAIN FORM

The as-cast equi-axed grain material was received in half ingots of dimension 125 mm diameter × 150 mm with a structure as shown in Figure 2.4. It can be seen that only the inner section, approximately 50 mm diameter, has a true equi-axed grain structure.

The procedure for heat treatment and machining of specimens was as for the directionally solidified material with one exception. Due to an error by the firm machining the specimens, blanks were cut with dimensions 18 mm × 20 mm × 146 mm and the dimension M on Drawing ME/A496 (Figure 2.2) was increased to 1.0" (25.4 mm).

On testing, this increased length of specimen created suspected problems with temperature distributions and the gauge length section was reduced in diameter by centreless grinding to approximately 0.248" (6.30 mm).

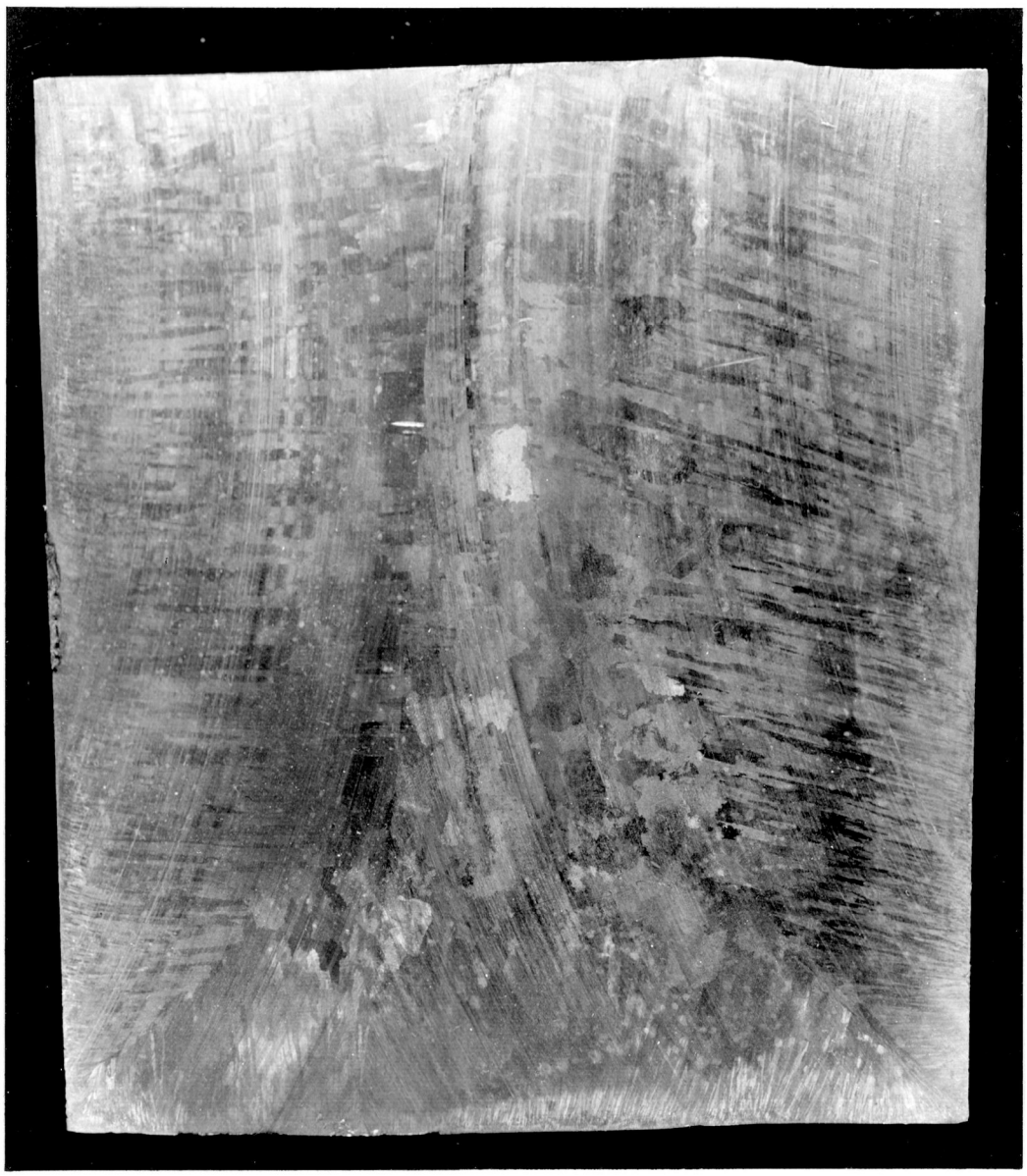

Figure 2.4: Acid ferric chloride etch of a cast equi-axed grained ingot

CHAPTER 3

EQUIPMENT

3.1 GENERAL

All constant stress creep tests, cyclic stress creep tests and tensile yield stress tests were carried out in five constant load, 10:1 lever ratio, 5 ton (50 kN) capacity creep machines. A general view of a machine is shown in Figure 3.1. The machines were all mounted on a sprung floor to reduce the influence of vibrations transmitted from the rest of the building. To ensure the thermal stability of the machines and strain measuring equipment, the laboratory air temperature was controlled to 68°F ±2°F (20°C ±1°C) by continual air-conditioning.

The exact lever ratio of all the machines was measured using a Clockhouse 3 ton capacity proving ring to measure the load between the universal joints in the specimen loading section to an accuracy of 3.3 lbs/division (14.7 N/division). A section of the bottom pull rod was strain gauged to form a permanent load cell (see Figure 3.6). Two active and two compensatory 500 Ω gauges were used in a bridge network, with an applied voltage of 24 dc to give a sensitivity of approximately 50 lbs/mV output (222 N/mV).

3.2 FURNACES, TEMPERATURE CONTROL AND MEASUREMENT

Furnaces were of the three-zone type wound on a ceramic core and wired as shown in Figure 3.2. The variation in temperature along the specimen gauge length could be adjusted to less than 1°C and for most cases was within 0.5°C, or the errors in the temperature measurement.

Temperatures along the gauge length were measured by three Pt/Pt - 13% Rh thermocouples made by resistance welding, followed by annealing and calibration. The temperature on the flat ends of the

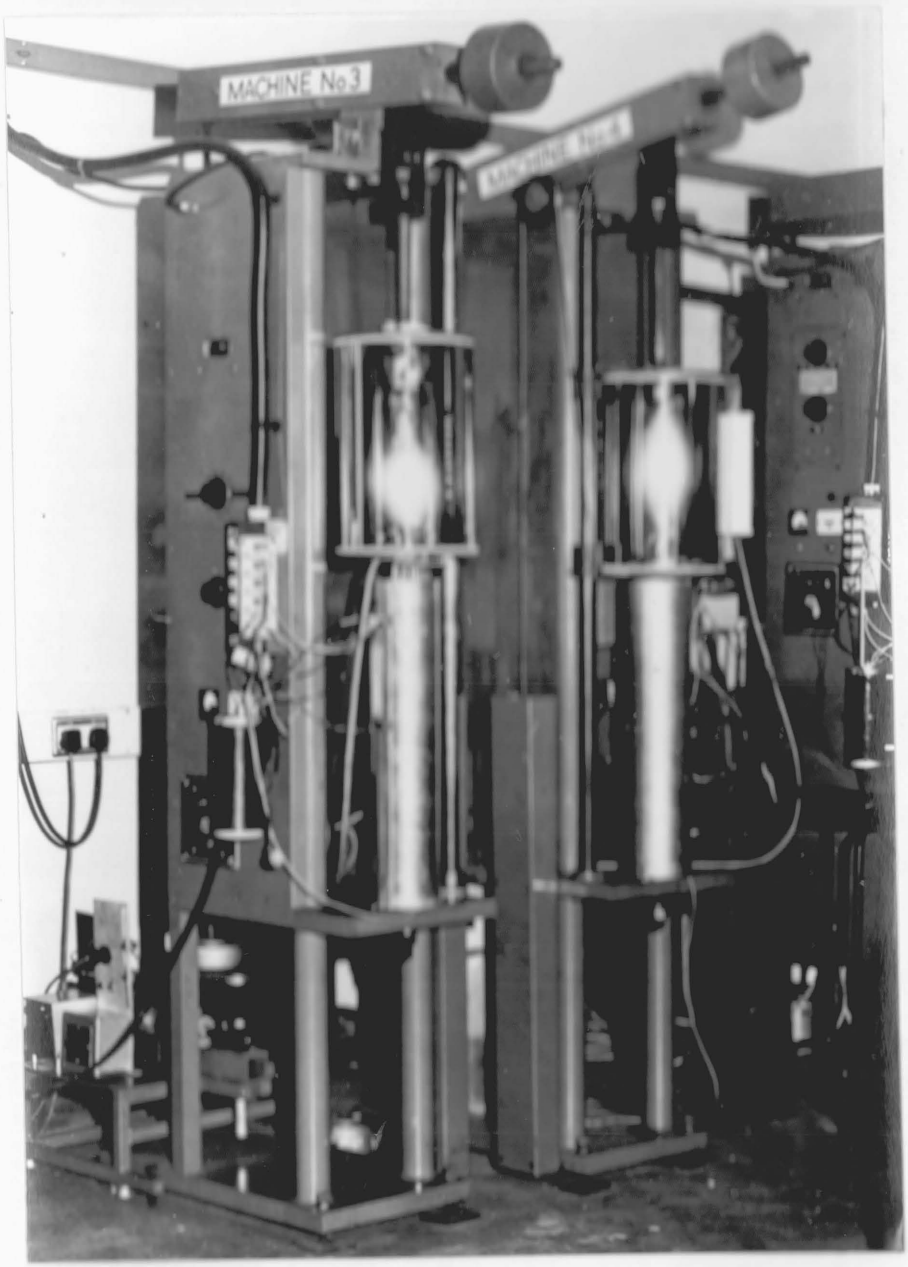

Figure 3.1: General view of creep machines in test mode

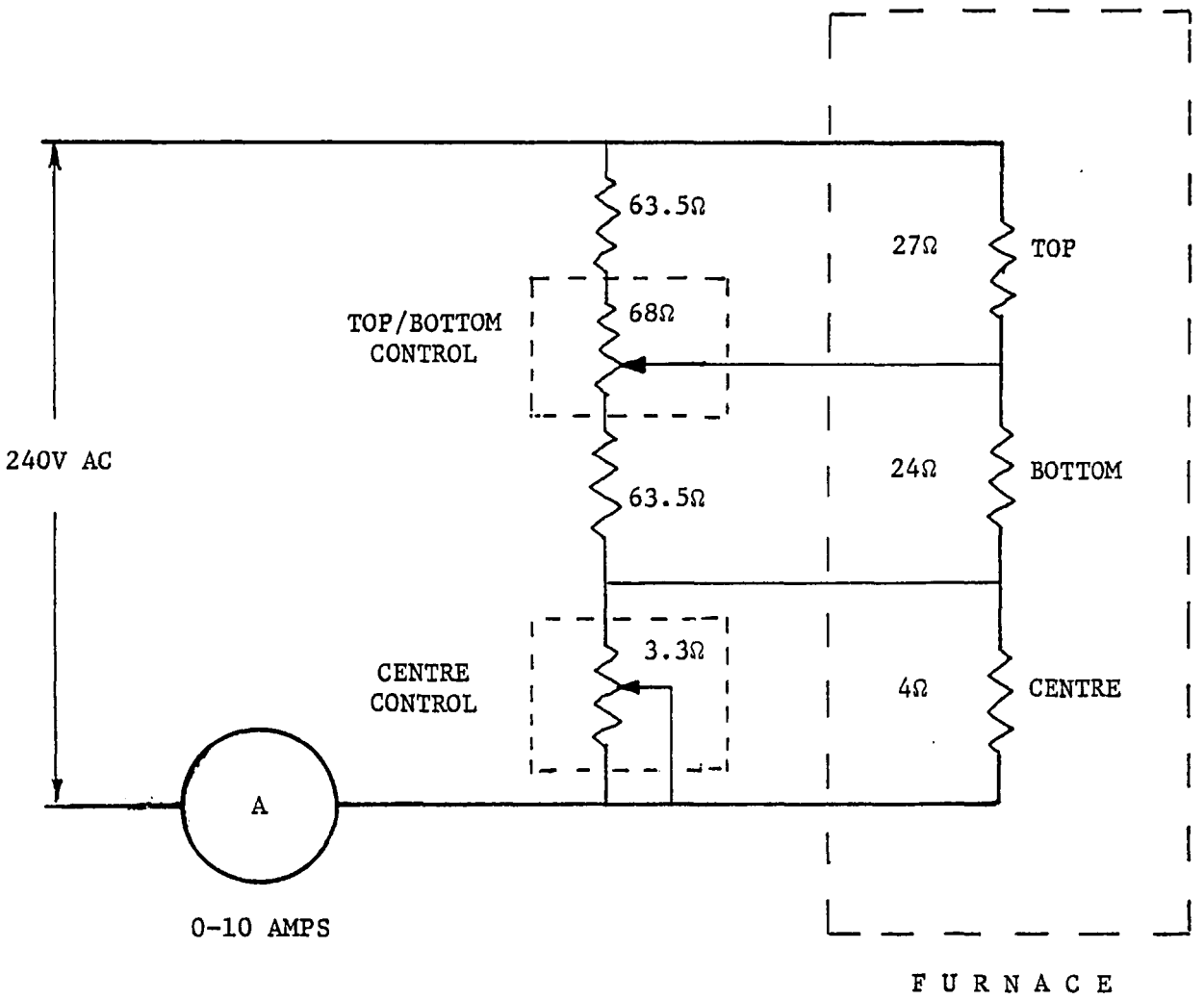

Figure 3.2: Power control circuit for creep machine furnaces

specimen in the shackles was measured by two Chromel-Alumel thermocouples and was found to be up to 5°C above the gauge length temperature. Calibrated Sunvic cold junctions were used as a reference point on each machine and the output from thermocouples read on a Cropico dc potentiometer, type P9, to within ±0.001 mV. This corresponds to a temperature of approximately ±0.1°C at 750°C for the Pt/Pt - 13% Rh thermocouples.

Temperature stability was achieved by Emec solid state thyristor powered temperature controllers coupled to a platinum resistance thermometer (PRT). Initially, the furnaces had a mat form of PRT on the outside of the furnace windings but, due to repeated burn-outs of the windings, a modified furnace was used with a stick type PRT located in a tube between the ceramic core and the windings. Both types could control the specimen temperature to within ±1°C but the modified furnace had a much faster response and coupled with a reduced heat loss, the heat-up time to test temperature was greatly reduced. The temperature overshoot on heating was controlled by an overall current limit and was kept to a minimum, generally being not more than 10°C over the test temperature. A run-up to a test temperature of 900°C could be achieved in 3 h with a corresponding reduction in time for lower temperatures.

3.3 SPECIMEN GRIPS AND EXTENSOMETRY

The specimen, universal blocks and extensometry arrangement, as shown in Figure 3.3, was that as described by Penny et al [60] and Tishler & Wells [61]. Bending in the specimen is less than 2%. This was checked using a strain-gauged specimen and the spacing between the universal blocks and the test specimen calibrated to give a minimum bending load.

The test piece gauge length extension was measured by a single LVDT (linear variable differential transformer), clamped centrally between

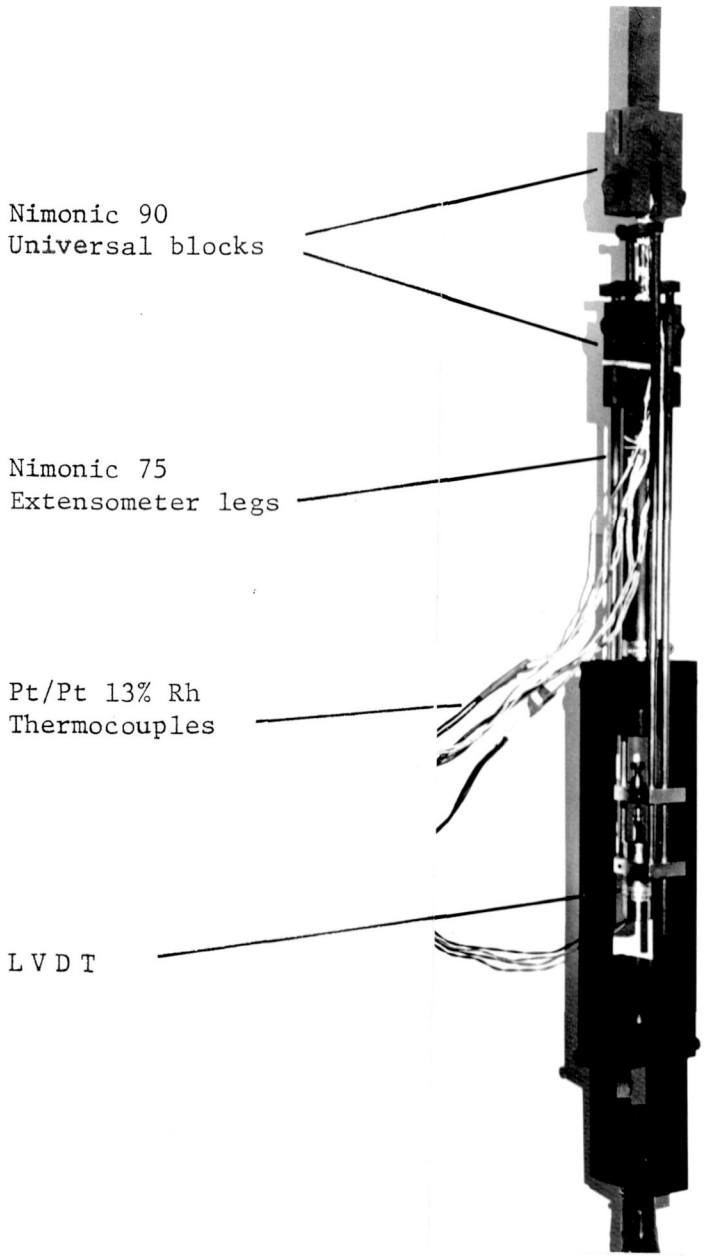

Figure 3.3: Specimen clamps, extensometry and temperature measuring systems

aluminium plates attached to the end of Nimonic 75 extensometer legs.

A circuit diagram for the LVDT and sensitivity controller is shown in Figure 3.4. This gave a maximum sensitivity calibration of 10 mV output for 0.008" (0.20 mm) travel of the armature which had a total displacement range of ±0.2" (51 mm). Most strain measurements were made from records on a Rikadenki dc voltage pen recorder. On a 1 mV full scale setting, a resolution of 8×10^{-7}" (0.02 μm) was theoretically possible but electrical noise and slight transducer instabilities through temperature variations made this setting impractical. A resolution used for most tests corresponded to ±0.002% strain.

The drift of transducers over a period of 500 h were measured to be less than 4×10^{-5} in (1.0 μm).

For some tests, a Honeywell type Electronik 194 dc recorder was used which enabled strains of ±0.0001% and times down to one second (0.000278 h) to be resolved for the early stages of creep.

3.4 CONSTANT STRESS COMPENSATION

For long time creep tests, a constant stress condition was approximated by removing weights from the loading rod to accommodate the reduction in cross-sectional area. Assuming all the creep deformation is plastic strain and a constant volume condition exists, i.e. Poisson's ratio is 0.5, the reduction in area can be easily calculated from the axial strain. Using 0.5 lb (2.2 kN) and 1 lb (4.4 kN) weights, a correction for approximately every 0.2% creep strain was possible.

However, for short term creep tests (in the order of 0.1 h), this method was impracticable and a lever mounted jockey compensating arrangement was designed (see Figure 3.5). The screwed rod is driven by a DC receiver motor coupled to a commutator transmitter driven by the Honeywell recorder pen drive motor which was recording the creep strain.

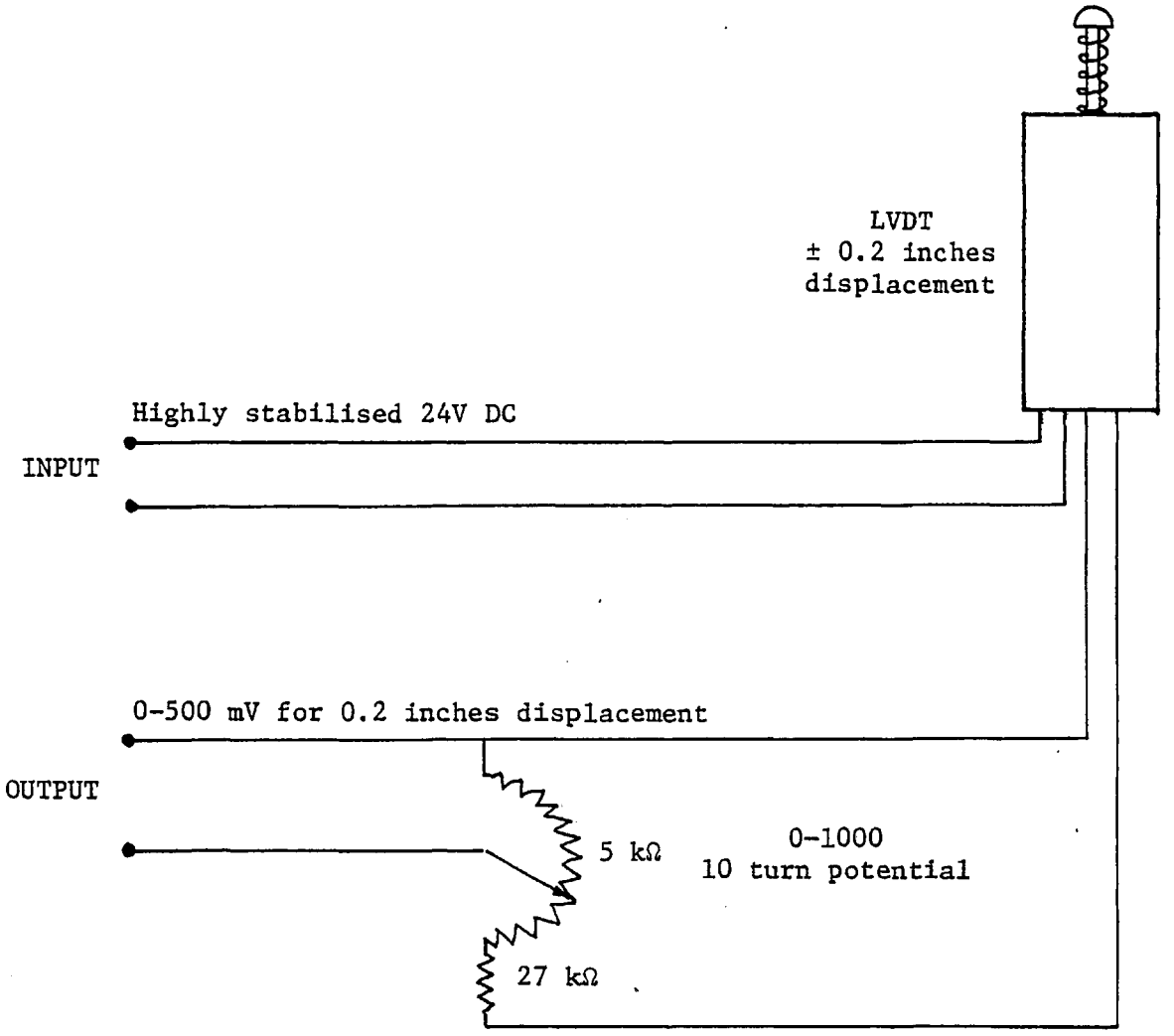

Figure 3.4: Input and output circuits for extension measuring transducer

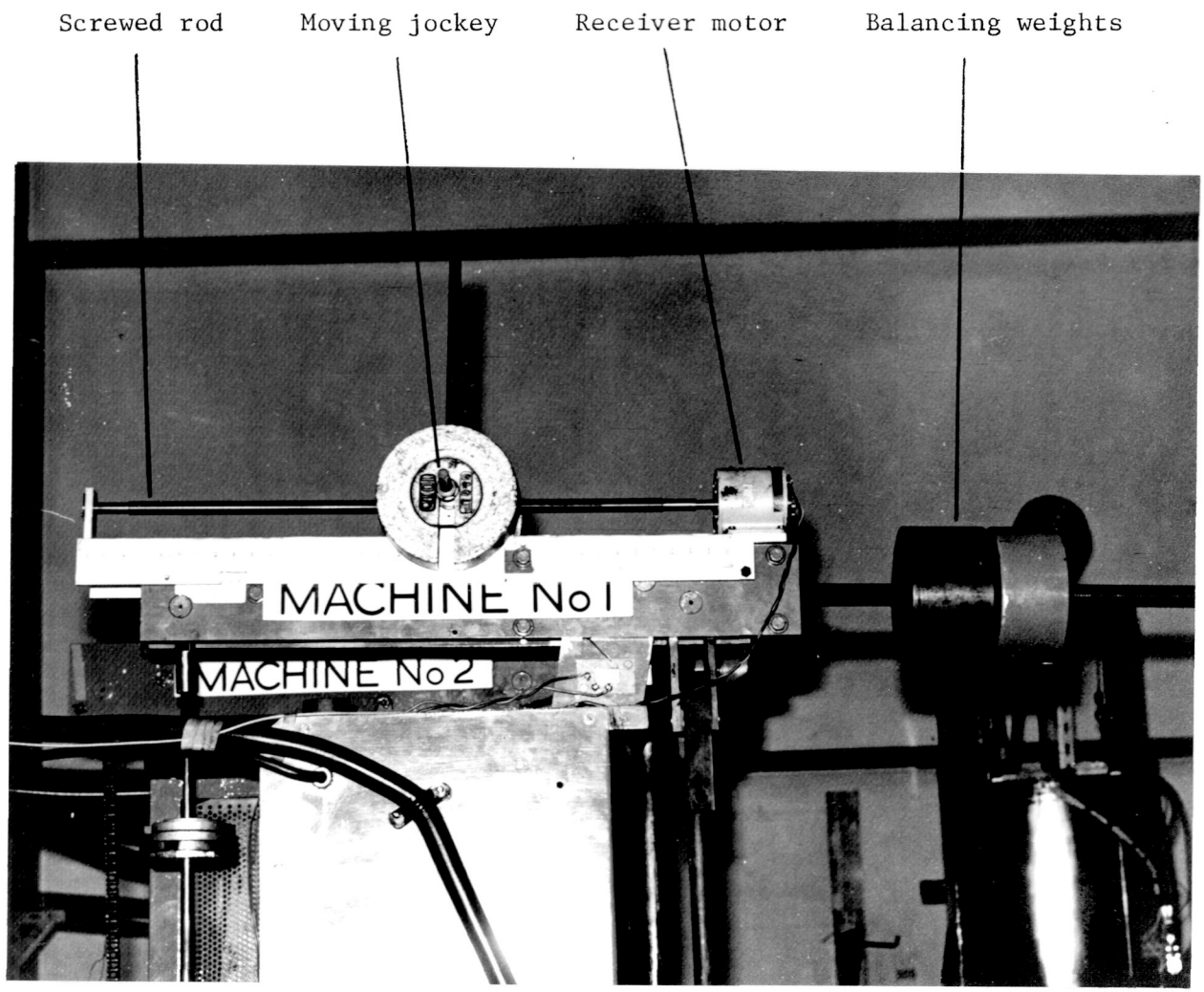

Figure 3.5: Rapid constant stress compensation mechanism

This gave a linear movement of the jockey, and hence a reduction in specimen load, directly proportional to the axial creep strain. Thus, a continual load compensation was made while the specimen was deforming uniformly, compared with the Chalmers type of compensating cam where the load compensation is dependent on the total deformation of specimen and pull rods at the front of the machine.

The gearing used gave the jockey a travel of 16 cms for full scale deflection of the recorder pen, leaving as variables the full scale strain and the jockey weight. The maximum jockey load used has been 100 lbs (445 N) but the receiver motor had difficulty in following rapidly with this load.

During short term tests, problems also arose when high ductilities, in the order of 30%, materially changed the level of the lever, causing the lever to come into contact with the safety stops and altering the effective lever ratio (nominally 10:1). This was overcome by using a self-levelling system, as shown in Figure 3.6. The $\frac{1}{4}$ hp dc motor was activated by a micro-switch mounted close to the rear of the lever arm on the top platform and drove the worm and pinion arrangement which relevelled the lever arm. There was no shock loading from the motor and the lever arm was kept horizontal to within $\pm 2°$.

The self-levelling and jockey load compensation systems were only fitted to one machine which was primarily used for the short time creep tests.

3.5 CYCLIC LOADING APPARATUS

Although this apparatus was not used to give a constant cycle of load, it was used during the overageing tests for removing and applying the loads and its design is worthy of mention. A $\frac{1}{4}$ hp reversible dc motor was attached to the underneath of the top platform with the drive to the

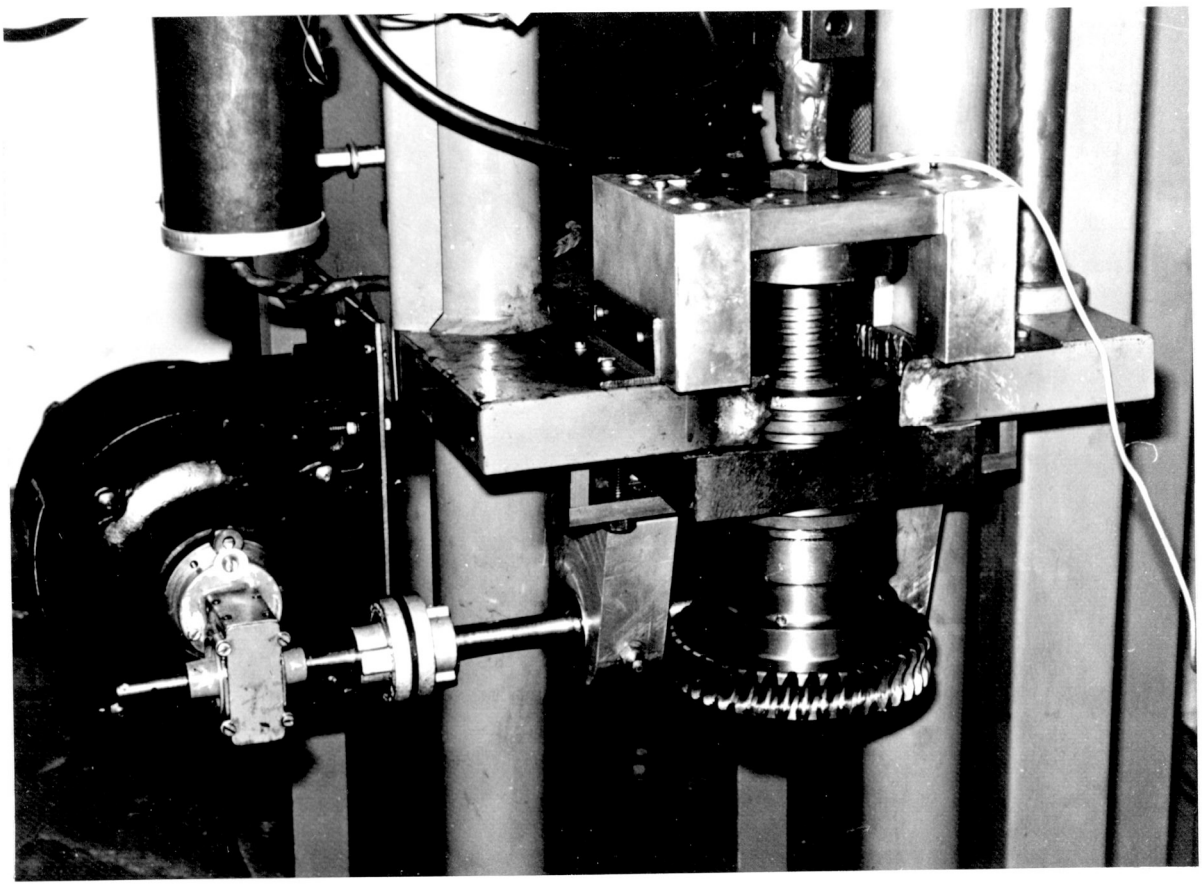

Figure 3.6: Automatic lever levelling system for Machine No. 1

lifting mechanism being taken by a sprocket and chain. The lifting mechanism runs on roller bearings on angle sections bolted to the rear of the machine, making the set-up simple and adaptable for any of the machines. The power supply to the motor was governed by two Crouzet timers and limit micro-switches on the machine. As the loading rod tube was now in two sections, any percentage of the load may be cycled with a large variation in the ratio of time-on load/time-off load available. A circuit for the apparatus is shown in Figure 3.7.

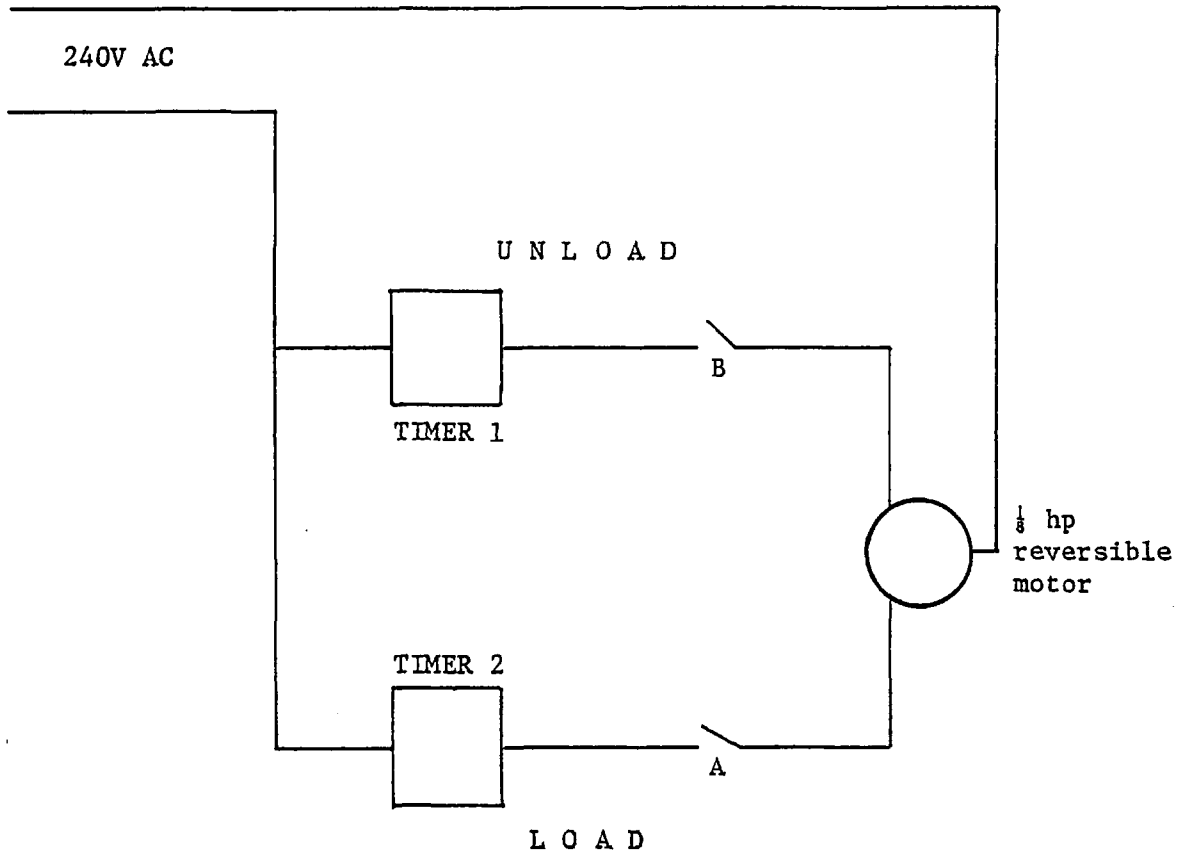

TIMER 1 : Controls off-load period. Activated by microswitch B between loading rig and creep machine frame.

TIMER 2 : Controls on-load period. Initially manually started. Receives pulse from Timer 1 at end of off-load period. Microswitch A between loading rig and loading rod prevents excess travel and trips when all load applied.

Figure 3.7: Cyclic loading arrangement

CHAPTER 4

EXPERIMENTAL PROCEDURE AND RESULTS

4.1 EXPERIMENTAL PROCEDURE

4.1.1 Constant Stress Tests

Each specimen was checked for grain alignment with the tensile axis by etching the flat ends with acid ferric chloride (see Figure 2.3 for complete specimen etch) or by observing the gauge length structure enhanced by oxides from the ageing treatment. Two hardness readings on each end were taken using a Vickers indenter with a 50 kg load and recorded. The gauge length diameter was measured at three sections using a micrometer to an accuracy of 0.0001 in (0.0025 mm). An occasional check was made on the specimen gauge length using a Shadograph measuring to 0.0001 in (0.0025 mm). The readings at all times were within the tolerances specified on the specimen drawing (Figure 2.2).

Particular care was taken to heat treat all specimens from one ingot casting at the same time in order to eliminate possible variations between heat treatments. Most of these specimens were then tested at a particular temperature to minimise possible batch to batch variations.

After the preliminary measurements had been taken and recorded, the specimen was set up in the testing machine as described in Section 3.3. Three Pt/Pt - 13% Rh thermocouples were tied to the gauge length with asbestos string or Refrosil ceramic fibre and two Chromel-Alumel thermocouples were similarly attached to the specimen in the area of the bolt holes. The extensometry and transducer mechanisms were then attached and the transducer dial-pot set to give the requisite value of strain for 10 mV output (see Figure 3.4).

A load-extension test was then carried out using the motorised jack arrangement shown in Figure 4.1.

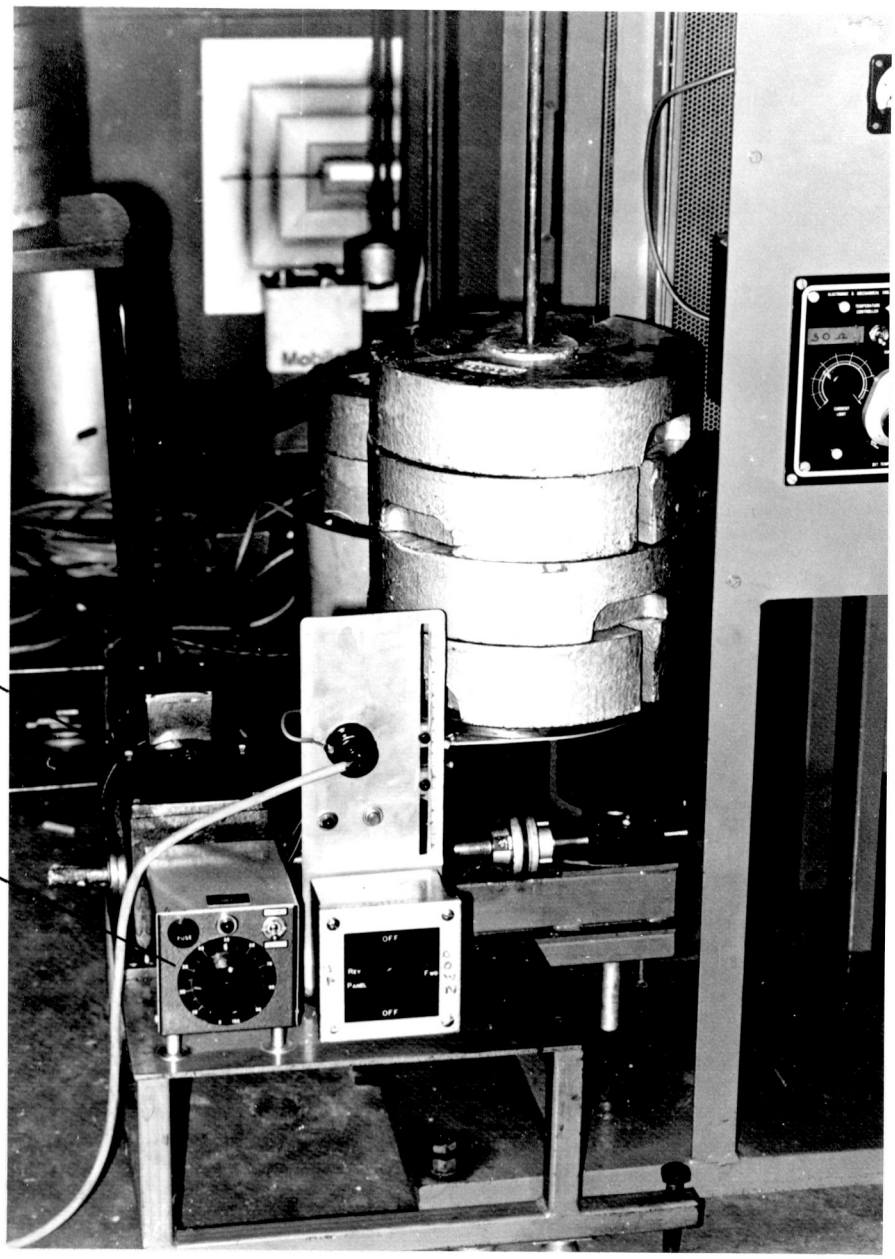

Figure 4.1: Constant rate weight lowering apparatus

The load and extension readings were recorded on a Bryans X-Y recorder where an instant assessment could be made of the alignment of the specimen. If necessary, adjustments in the extensometry grips were made until a satisfactory load-extension plot was obtained, an example being as in Figure 4.2. For these tests, a load of 150 lbs (666 N) was applied, unless this corresponded to the applied stress in the creep test (207 MN/m^2). In this case, the load was reduced to give either a stress of 20,000 lb/in^2 (138 MN/m^2) or 10,000 lb/in^2 (69 MN/m^2). The readings from this load-extension test were used later to evaluate the room temperature Young's modulus.

The furnace was then lowered to a position so that the specimen was in the centre in both the axial and longitudinal directions and the ends were lightly packed to a depth of no more than 1" (25 mm) with Kaowool ceramic fibre. The load-extension test was then repeated to ensure that the extensometry was still moving freely.

After recording the initial time and hour meter reading, the furnace was switched on with a deadweight stress in the specimen of 400 lb/in^2 (2.8 MN/m^2) to keep the universal block settings and extensometry aligned. By using the run-up procedure as described in Section 3.2, the desired test temperature and distribution were obtained. From the time the specimen first reached the test temperature, a 24 h soak was given to fully stabilise the specimen, grips and extensometry temperature.

The load to be applied for the desired stress was calculated using the average of three specimen gauge length diameter readings to determine the area.

After the soak time at temperature, the load was applied by lowering the weights onto the rear loading rod by the motorised jack. The motor speed was kept constant for all tests but the actual loading

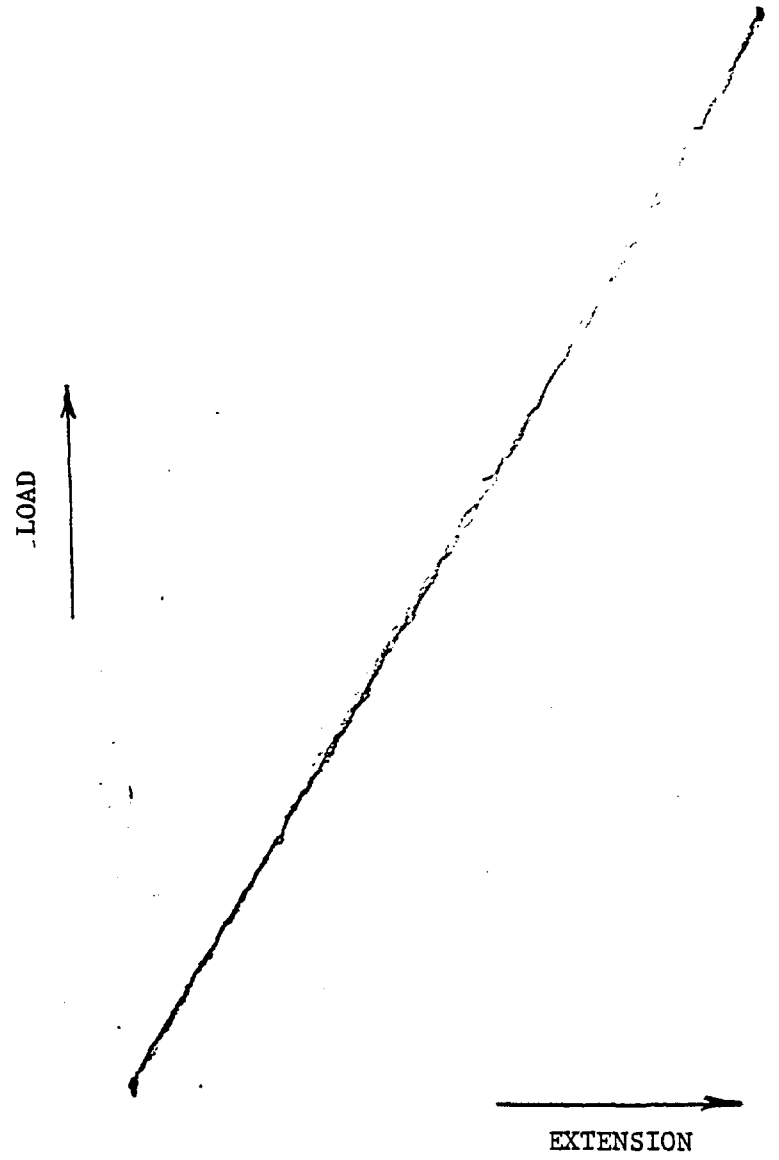

Figure 4.2: Typical load versus extension record on X-Y plotter at room temperature. Two consecutive loadings shown.

stress rate on the specimen would depend on the relevant elastic modulus and, to some extent, the weight on the loading pan. To give some indication of the values, at a test temperature of 650°C the stress rate was 25 MN/m^2sec and at 850°C the stress rate was 15 MN/m^2sec. When the specimen yielded, this stress rate would reduce considerably and the time of loading was subsequently increased.

During the loading, the load, extension and temperature were continually monitored on the Rikaden i or Honeywell dc millivolt recorders, the settings being adjusted to give the greatest sensitivity possible for the strain values. The chart speed was run at a maximum during the loading which, for the Rikadenbi recorder, corresponded to 200 mm/min and, for the Honeywell Electronik 194, 20 mm/sec. Once all the load was applied, the chart was left at this speed to give enough resolution over the first 0.1 h for a logarithmic time scale and thereafter the chart speed was reduced to a value depending on the length of the test and the time resolution required.

For the duration of the test, the strain and temperatures were continually monitored and slight adjustments made to keep the temperature within ±1°C of the test temperature. A continual up-date of the strain record was made and the load reduced in units of 0.5 lbs (2.2 N) to keep the stress constant, or the constant stress unit used as described in Section 3.4.

On failure of the test specimen, the falling action of the lever arm activated a micro-switch which switched off power to the furnace and hour meter. Whenever possible, the furnace was raised after fracture and the specimen air cooled, otherwise the specimen was furnace cooled. The former method was used for all interrupted tests where the rapid air cooling was used to freeze the strained microstructure in the specimen, the specimen remaining under stress during the cooling period.

After extraction from the test machine, care was taken to note any surface effects, especially oxide colours and cracks. The ends where the pre-test hardness measurements were made were then re-polished to remove any surface oxide and the hardness measurements repeated. The relevant gauge length dimensions were then recorded and the specimen placed in a protective envelope.

4.1.2 Cyclic Stress Tests

A similar procedure to that described in Section 4.1.1 was used, except that the load was periodically removed and re-applied. The load was applied at predetermined times for long enough to give a steady-state creep rate. The load was then removed with the motorised jack set at the same speed as for loading or the cyclic stress arrangement described in Section 3.6. The load and extension was recorded continuous continuously. Care was taken to set the strain recording channels and chart speed to a high as possible sensitivity (a maximum of 0.1% strain full scale for the Rikaden i recorder and a maximum of 0.01% strain full scale for the Honeywell Electronik 194) in order to measure the small subsequent recovery strain and exact point of unloading.

4.1.3 Thin Foil Preparation

A selection of the tested specimens were prepared for transmission electron microscopy in an AEl EM6G 100 keV electron microscope.

A representation section of the gauge length with uniform strain was removed using a high speed 0.020 in (0.5 mm) thick slitting wheel. All sections taken were transverse to the stress axis, i.e. in the [001] plane. The thickness of the slices varied from 0.015 in to 0.025 in (0.38 mm to 0.52 mm) and any slices cut thinner were discarded due to any possible damage induced by the cutting. The slices were then

mechanically thinned, in a specially made holder, to approximately 0.005 in (0.13 mm) using a wet and dry grade 320 SiC paper on a water lubricated wheel. Where possible, two 3 mm discs were then spark machined from each slice.

The discs were prepared for transmission microscopy using the jet polishing technique as illustrated in Figure 4.3. The initial rough polish to produce a bi-concave section was obtained with a solution of 50% HCl at 20 volts applied for approximately 10 seconds each side. The final polish to produce the thin section was carried out with the specimen held stationary in a solution of:

20% perchloric acid
80% acetic acid
} at -5°C

or:

10% perchloric acid
90% ethanol
} at -40°C

The voltage was applied to give a fine polish and switched off when a hole appeared in the centre of the foil, the area surrounding the hole being suitable for transmission microscopy. The specimen was then carefully washed in methanol, dried and stored in a protective container.

4.2 EXPERIMENTAL RESULTS FOR DIRECTIONALLY SOLIDIFIED MATERIAL

4.2.1 Constant Stress Creep Tests

Constant stress creep tests were carried out as described in Section 4.1.1 in the temperature range 650°C to 900°C. This corresponds to a range of 0.57 T_m to 0.73 T_m. Figure 4.4 indicates the range of stresses covered for each temperature. In order to carry out a full as possible programme of tests, the stresses used were limited to these,

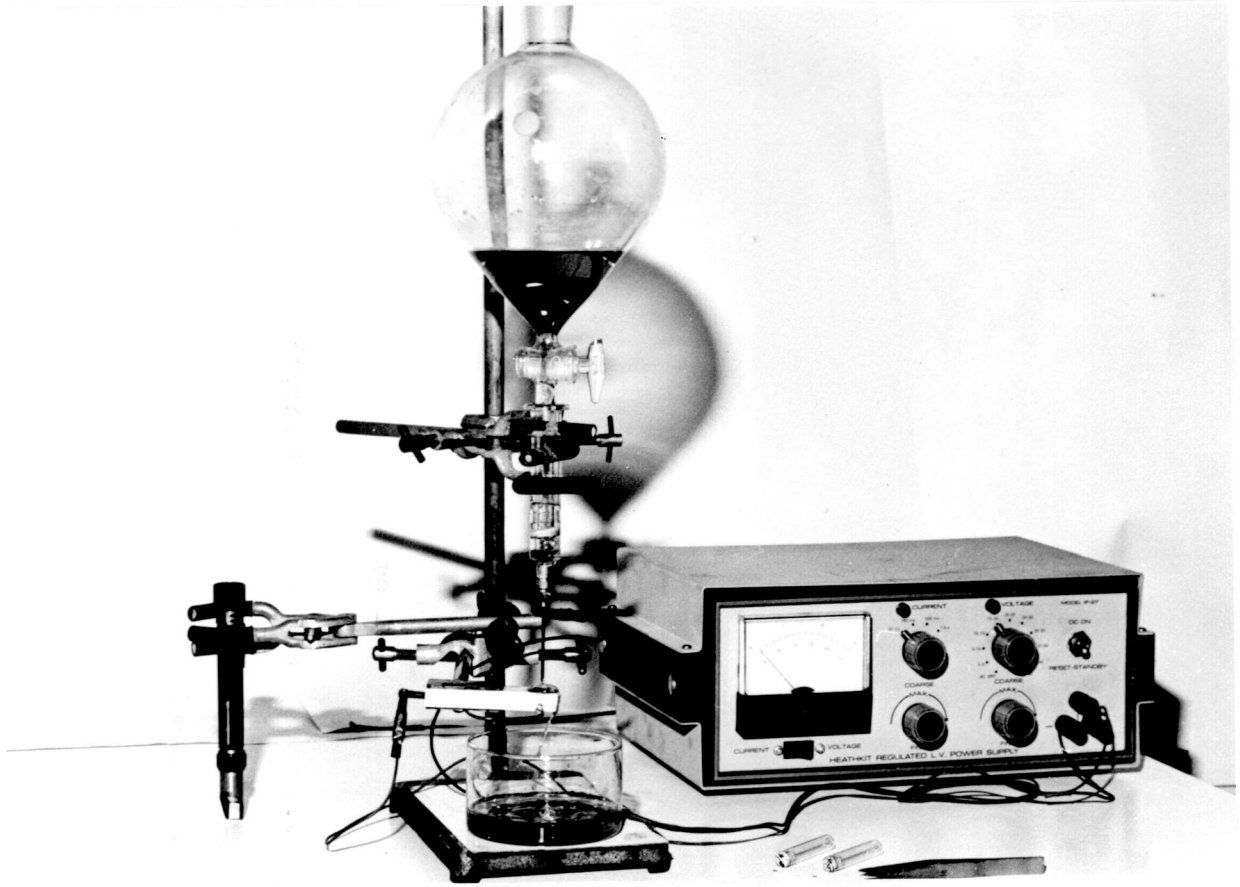

Figure 4.3: Jet polishing apparatus to prepare electron microscope samples

Nominal Stress (MN/m^2)	Test Temperature (°C)					
	650	700	750	800	850	900
138					42	52 , 54
207				23	40	51
241			8			
276			4	22	41	
310			32 , 36	21	39 , 44	
345			9 , 37		45 , 46	
379			31	25		
414		13	30	27	38	
448		11 , 34	10	28		
483		15	33			
517	47	14 , 18 , 56				
552	26 , 29	16 , 17	6 , 49			
586	50	12 , 67				
621		55	5			
655	24					
689	35 , 48					

All test numbers prefixed by letter N

Figure 4.4: Temperature and stress ranges of constant stress creep tests

giving rupture times of less than 5000 h. The shortest creep test duration was 0.1 h.

Mechanical data (creep rupture strain, time, reduction in area and elastic moduli) for the constant stress tests are listed in Appendix A (Figures A.1 to A.5). Creep strain-time data is presented in a logarithmic form in Figures A.6 to A.11, and in a linear form in Figures A.12 to A.17. It must be emphasised here that the creep strain was defined as that strain after all the load had been applied, i.e. all initial plastic and elastic strains have been neglected in these plots. Actual stress values given, where different from nominal stress values, have taken into account any reduction in area due to plastic strains through initial yielding on loading.

Considering the general shape of the creep strain-time curves (Figures A.6 to A.17), it is seen that no geometrically similar curve can be applied to all the data on either the logarithmic or linear plots. In Figure 1.1, a general plot of creep strain versus time indicated four distinct areas but no particular emphasis was given to any area. The present data has been catagorised into five basis forms of curves, as shown in Figure 4.5, and Figure 4.6 tables the classification of the curve for each test condition. Strain has now also been used to quantify the relevant areas of the creep strain-time curve.

Significant primary creep only occurs at stresses above 550 MN/m^2, where the yield stress level is in the range 400 MN/m^2 to 500 MN/m^2, and for temperatures less than 800°C.

When the stress was just above the yield stress at the temperatures 650°C and 700°C, then an incubation period occurred, i.e. there was an initial period with a low creep rate followed by an accelerating rate before a reduced level of steady-state creep was reached (curve type 4). This effect is not clearly pronounced in the linear plots

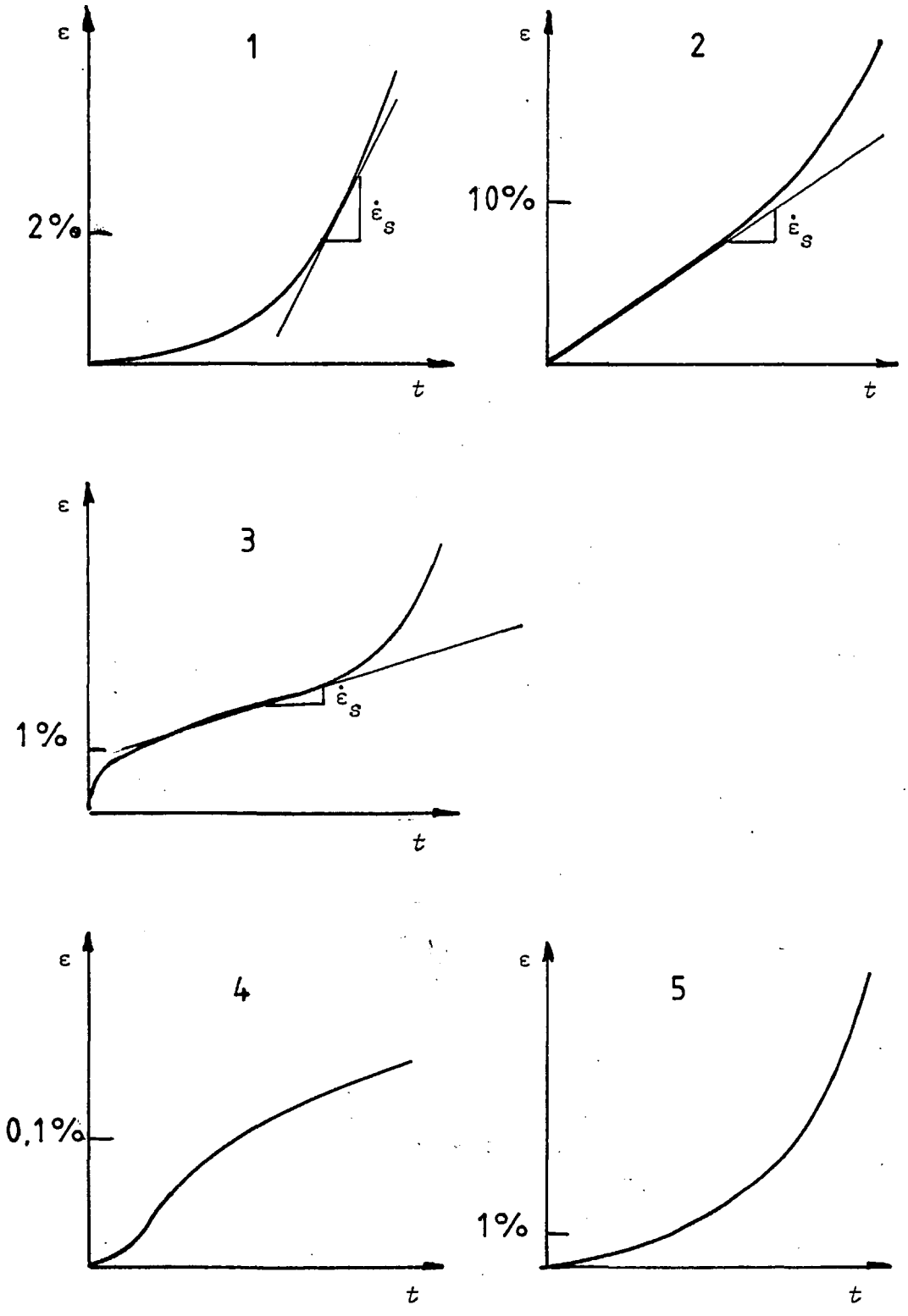

Figure 4.5: Basic types of linear creep strain versus linear time curves

Nominal Stress (MN/m^2)	Test Temperature (°C)					
	650	700	750	800	850	900
138					1	2
207				1	1	2
241			-			
276				1	1	
310			5 , 5	1	1 , 2	
345			5 , 5	-	2	
379				1		
414		5	5	1		
448		5 , 5	5			
483		5	5			
517	5	5 , 5				
552	4 , 4	4 , 4	5			
586	3	3				
621		3	3			
655	3					
690	3 , 3					

Figure 4.6: Classification of creep strain versus time curves for each test, as defined in Figure 4.5

but on the logarithmic plots is very noticeable, e.g. tests N16 and N17 in Figure A.7.

In the intermediate stress and temperature range, 300 MN/m^2 to 500 MN/m^2 and less than 800°C, the typical curve for nickel based precipitation hardened alloys occurred, i.e. a continual increase in creep rate with time with no pronounced steady-state secondary creep rate (curve type 5).

At 800°C and above, a secondary steady-state creep rate occurred which was not the minimum creep rate. After a variable period of time, the creep rate accelerated to an almost constant value until final fracture resulted in an increasing creep rate (curve type 1). It is noted that tests were carried out under constant stress conditions but creep strain has been defined by engineers strain (change in original length/original length) and not true strain (change in current length/ current length). The difference in values up to 5% is negligible but tests at 800°C and above involved strains of the magnitude 10% to 40%. Conversion of the creep strain values to true strain values would accentuate the above phenomenon.

For the shorter time tests at 850°C and for both tests at 900°C, there was an almost constant steady-state creep rate from the initial loading up to approximately 10% creep strain before an accelerating creep rate led to a high ductility fracture.

4.2.2 Fracture Characteristics

For all tests, a note was made of the surface colour, texture and uniformity of deformation at fracture.

A surface oxide was present after all creep tests, the thickness and composition being a function of time at the test temperature. For long time tests at 650°C and 700°C, a heavy white oxide, possibly

Cr_2O_3, was formed preferentially on the dendrites in the grains. For short time tests at these temperatures, a thin layer of a light green oxide was formed. At test temperatures of 800°C and above, a heavy green oxide, NiO, was formed with the thickness dependent on the time at temperature. The thickness would be of the order of 1000 Å.

The colour of the actual fracture surface was associated with the type of fracture. For sheared surfaces, a golden colour was noticed whilst for direct tensile failure areas, the colour was typically dark blue. An example of a mixed failure is seen in Figure 4.7a. Assuming that these colours are the first order interference colours from the oxide films, the shortest time of exposure is associated with a golden colour (shear failure area) and the longest the blue colour (tensile failure area area). This gives some idea of the fracture mechanism, an initial tensile failure followed by a final shear failure. These mixed modes of failures predominated at the lower test temperatures, where rupture strains were less than 10%.

Average strains at fracture are plotted on a temperature basis in Figure 4.8, where it is seen that a ductility trough appears around 700°C. Some idea of the fracture characteristics can also be obtained from the reduction in area at fracture and this is plotted in Figure 4.9 as a function of the total plastic strain. This plastic strain includes the plastic strain on loading where yielding occurred, the value being determined from a cross-plot of the load and strain readings and the deviation from the linear elastic line. Results from constant stress creep tests where failure occurred outside the gauge length or where the test was interrupted for investigation of structure are included. For these results, it is seen that the plastic strain-reduction of area relationship closely follows that for the constant volume condition, i.e. $\nu = 0.5$, up to a total plastic strain of 18%. Voids, especially on

A

B

Figure 4.7: Creep fracture modes for directionally solidified grain form

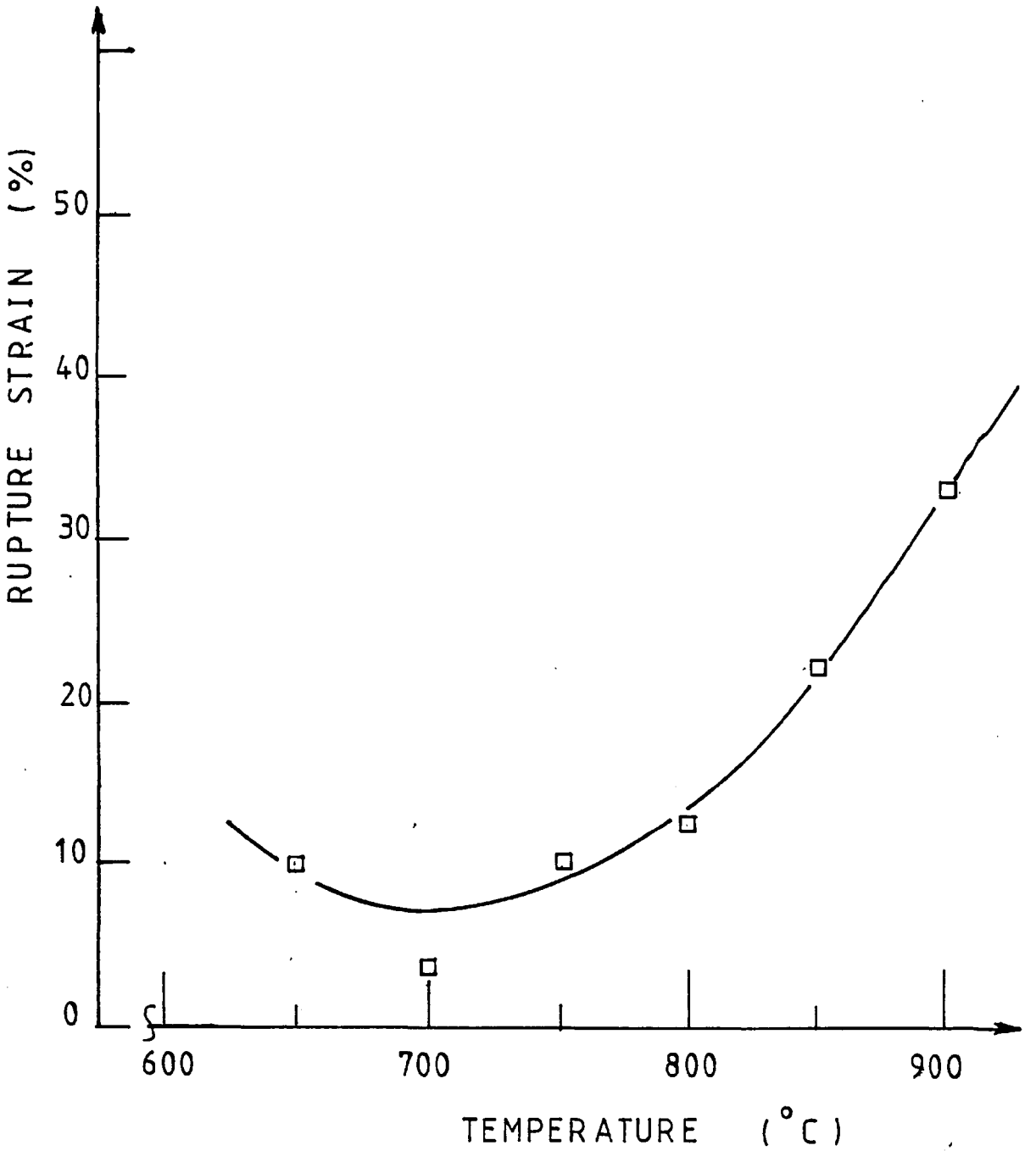

Figure 4.8: Mean creep strain at rupture versus temperature

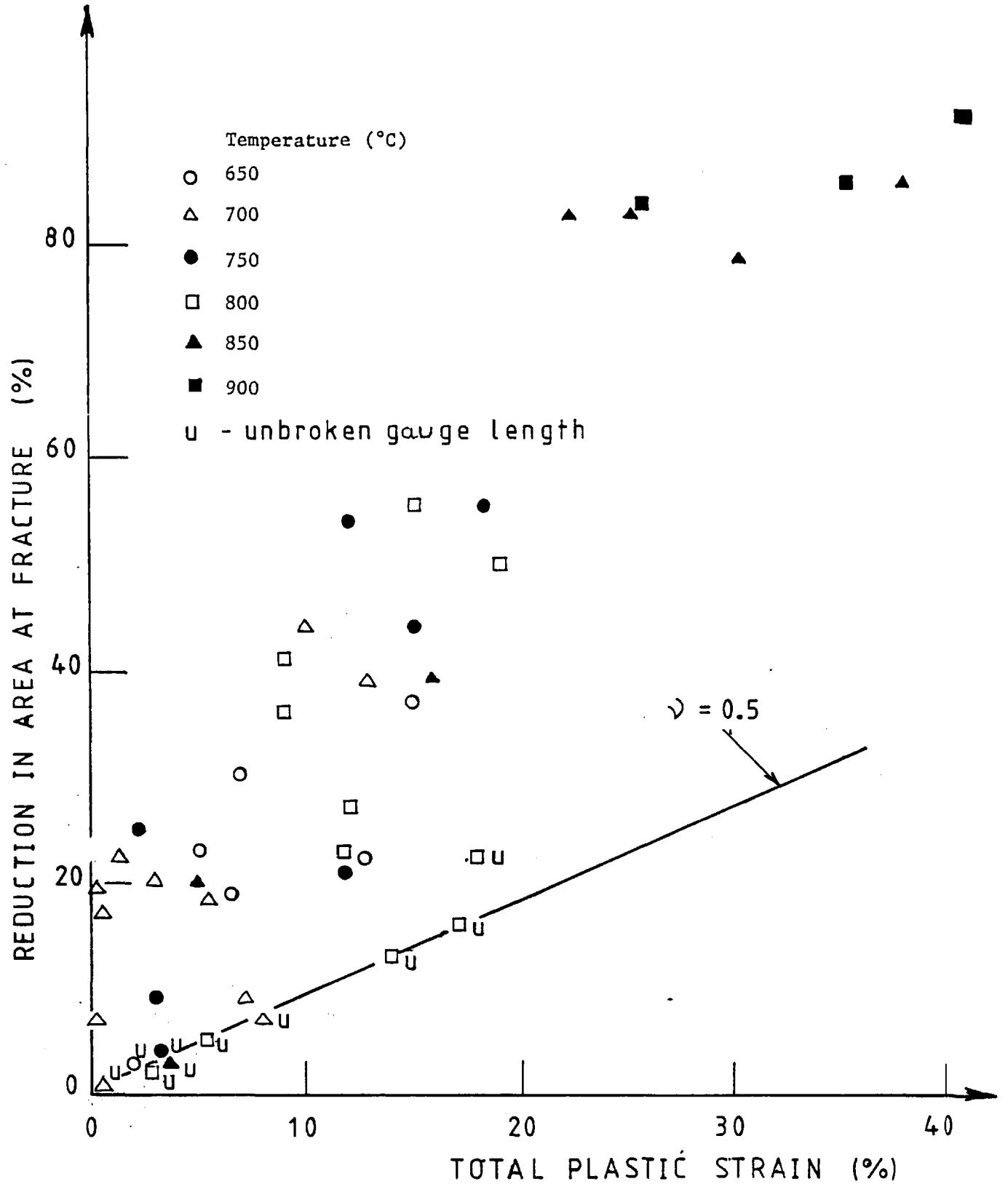

Figure 4.9: Reduction in area at fracture point versus total plastic strain (total creep strain plus yield strain on loading)

grain boundaries, can contribute to creep strain [83] but the experimental results on reduction in area are not of sufficient accuracy to calculate a possible void density. With a columnar grain structure and grain boundaries predominantly in the tensile axis direction, a high void density would not be expected. Creep strain voids are predominantly associated with grain boundaries at right angles to the applied stress.

Low ductility fractures occurred at all temperatures but it is seen from Figure 4.9 that large reduction in areas at fracture (greater than 50%) only occurred at test temperatures 800°C and above.

Figure 4.10 shows a variety of high ductility fractures compared with an untested specimen. Specimens A and C are typical of creep tests at 800°C and above in that, with high strains, a double neck appeared which had some influence in the final position of the fracture. Specimen A had a rupture strain of 41.2% and a reduction in area of 95%, the highest value recorded. Test conditions were a stress of 207 MN/m^2 and a temperature of 900°C. Specimen C is typical of tests at 800°C where reduction in areas at fracture ranged from 20% to 55%. Specimen B was tested at 650°C and 690 MN/m^2 which resulted in 14.6% plastic strain on loading followed by 12.4% creep strain. The surface of this specimen showed non-uniform transverse straining where ripples were produced around the circumference, some of which can be seen in the photograph.

As was mentioned earlier, fracture surfaces indicated shear and/or direct tensile failure areas. The example shown in Figure 4.7a had areas of both types as is indicated. The direct tensile areas show the dendrite nature of the structure. For a directionally solidified structure, it may be expected that the structure would influence the final mode of fracture in that a pure intergranular fracture is impossible. For one case only, there was a vertical shearing of the longitudinal grain boundary, shown in Figure 4.7b. The vertical sheared boundary was over

Specimen	Test Number N	Creep Stress (MN/m^2)	Temperature (°C)	ϵ_R (%)	t_R (h)
A	51	207	900	41.2	0.4
B	48	736	650	12.4*	9.1
C	25	379	800	18.3	10.1

* Additional strain of 14.6% on yielding during loading

Figure 4.10: Necking modes for creep tested directionally solidified grain form

approximately 3 mm. It is possible that a transgranular failure started at two sections in a direct tensile mode with the final failure occurring. by the shear of the longitudinal boundary joining the two transverse planes. Several of the fractured specimens were sectioned in the longitudinal plane to the stress axis and prepared for microscopic observation. An example is shown in Figure 4.11 of a specimen tested at 700°C and 552 MN/m^2 for 32.3 h. Evidence is seen of the weakness of the transverse grain boundaries sections in the interdendritic areas, an enlarged view is also shown in Figure 4.11 at the fracture point. The separations also occurred at areas well away from the fracture, but whether these are as a result of the final fracture is not clear. This specimen had a reduction in area of only 9% at fracture with a rupture strain of 7.2%.

A comparison is made in Figure 4.12 with a rupture at a higher test temperature. Test conditions were 379 MN/m^2 and 800°C with a rupture strain of 18.3% and a reduction in area of 50% (specimen C in Figure 4.10). The double neck is seen, together with separation of transverse sections of the longitudinal grain boundary. However, most of the longitudinal and transverse strain is accommodated purely within the grains and the voids at the grain boundaries are not contributing significantly to the strain. It is noted that there are only four to five grains across the section and that the alignment of the grains with the tensile axis were within specification.

It is seen in Figure A.7 that there is a variation in rupture strains for repeated constant stress tests. An unsuccessful attempt was made to find any structural reasons for this for the test conditions of 552 MN/m^2 and 700°C. The fracture section for test N17 has been shown in Figure 4.11, where the ductility was 7.2% after 32.3 h. Test N16 lasted for only 0.2 h with a rupture ductility of 0.2%. A comparison between the fracture surfaces showed little difference except for a much reduced

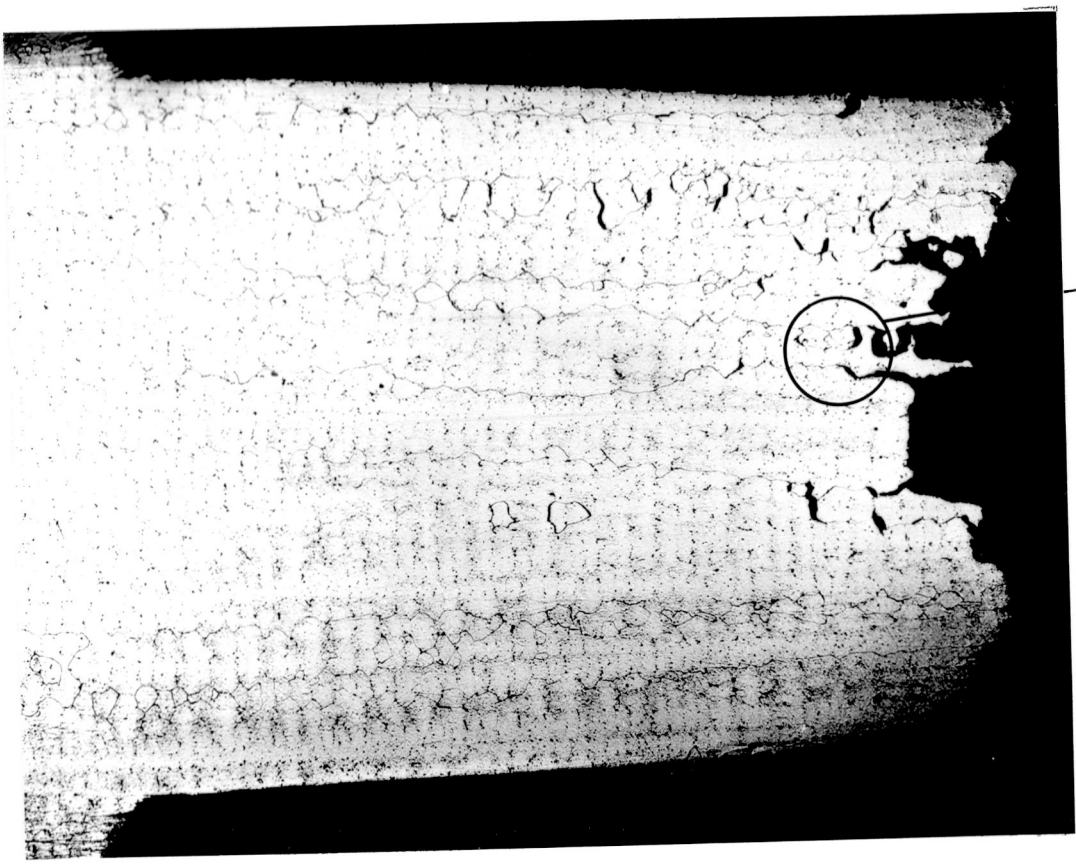

x 15

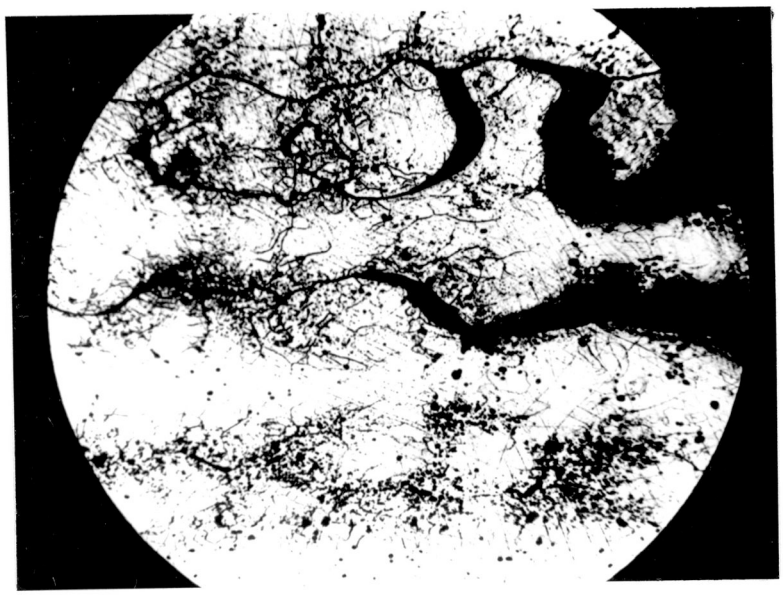

Enlarged view of area A

x 125

Figure 4.11: Longitudinal section of test N17 showing interdendritic separation and failure mode

x 10

Figure 4.12: Longitudinal section of test N25 showing double neck

shear area for test N16. For test N16, the specimen had fewer grains across the gauge length section, including one very large grain, and there was no indication of any interdendritic separation.

Figures A.1 to A.5 show that some specimens failed outside the gauge length. This was primarily due to high temperature gradients outside the gauge length with the original EMEC furnaces. Temperatures could be greater than 10°C above the gauge length test temperature and failures resulted from the reduced creep strength rather than any structural effects. For the rewound Donaldson furnaces, this difference was less than 5°C.

4.2.3 Interaction of Dislocations and Particles During Creep

Experimental evidence of the dislocation mechanisms under creep conditions can be found from transmission electron micrographs. Specimens from failed constant stress creep test specimens were taken in the transverse plane of the gauge length at sections away from the fracture surface. Sections suitable for insertion in the electron microscope were prepared as described in Section 4.1.3.

A section from a fully prepared test specimen was also taken and the initial test condition is shown in Figure 4.13 at magnifications of ×80 K, ×100 K and ×120 K, together with a diffraction pattern. Photograph A indicates the pre-test dislocation-free structure, whilst Photograph C indicates the very fine nature of the γ' precipitate, approximatley 100 Å (0.01 μm) in diameter. The morphology and time-temperature dependence of the γ' phase will be studied in greater depth in Section 6.1.

Figure 4.14 characterises the dislocation structure under various conditions at a creep test temperature of 700°C. Photograph A shows the low number of single dislocations associated with a rupture strain of 0.5%, the time at temperature was 119 h. At a higher rupture

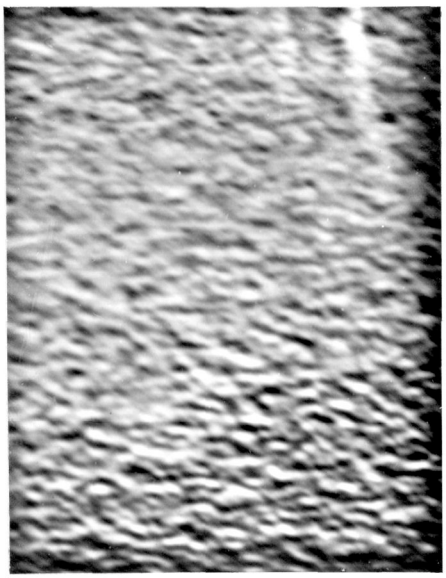

A ×80 K

B ×100 K

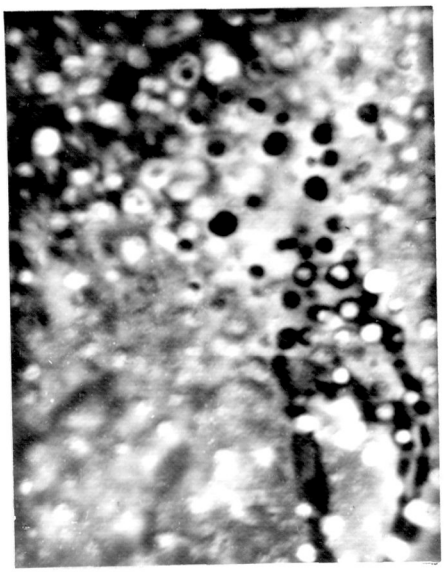

C ×120 K

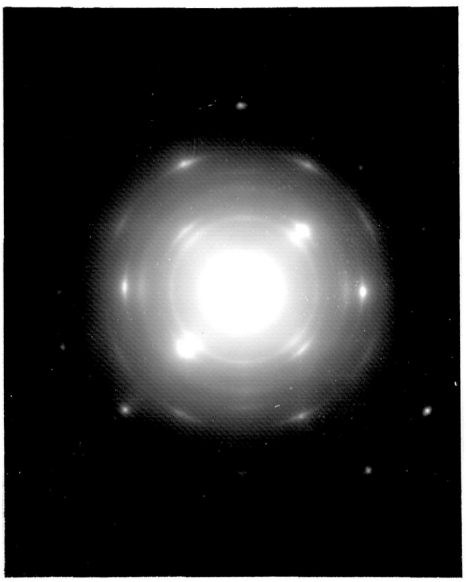

D

Figure 4.13: Transmission electron micrographs of untested specimen in fully heated condition

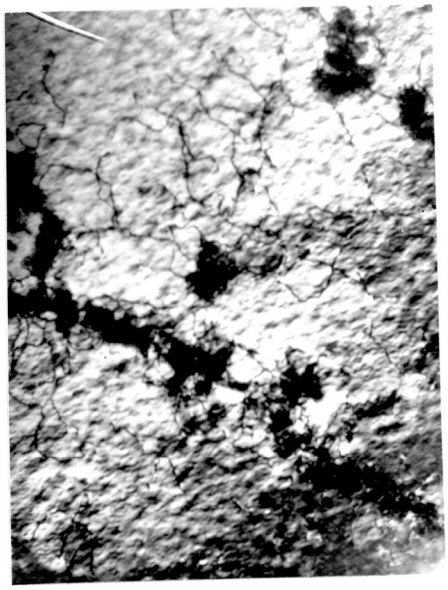

A N15 ×50 K

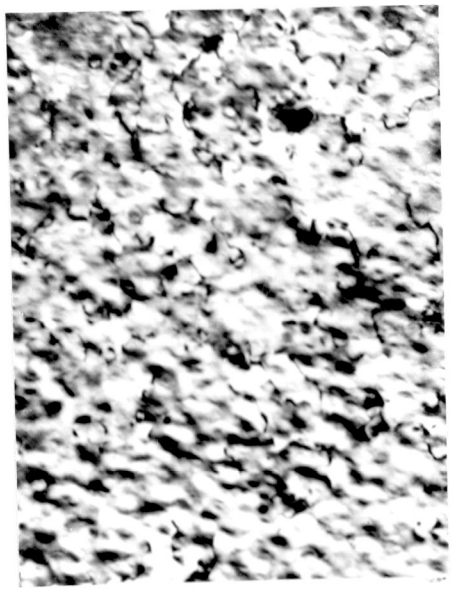

B N18 ×55 K

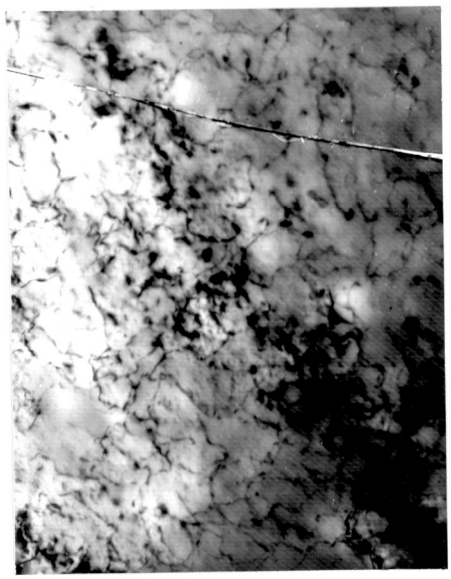

C N12 ×60 K

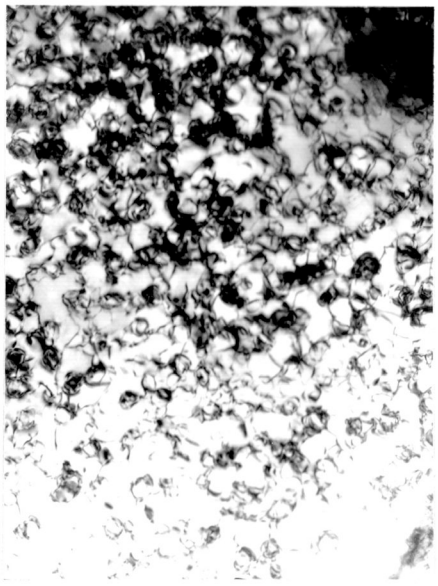

D N13 ×50 K

Figure 4.14: Transmission electron micrographs of creep tested specimens at 700°C. Test numbers are indicated.

strain level, 3.3%, the dislocation density is increased (Photograph B), but again evidence of dislocation pairs is absent. Tangled dislocations are shown in Photograph C where the rupture strain was approximately 5% after only 5.5 h on load and with a time of 30 h at the test temperature. After 2700 h at temperature and stress, the particle size has grown considerably and from Photograph D some evidence of a looping mechanism is evident as well as tangled dislocations. The rupture strain was approximately 10% and the measured particle size is approximately 1050 Å (0.105 μm).

At higher test temperatures, no suitable thin foils were prepared for short time tests. However, some indication of structure can be obtained from tests carried out by M.A. Abdel Hameed on identical test specimens creep tested under induction heating conditions [95]. These are shown in Figures 4.15A and 4.15B, where the stress level was 210 MN/m^2 and the temperature was 838°C for Photograph A and for Photograph B the temperature was 789°C. The looping dislocation mechanism is clearly evident with a measured particle size of 550 Å for Photograph A and 570 Å for Photograph B.

For long time tests at 800°C and above, the particle size increases rapidly and at large particle sizes, the dislocation structure is not so clearly evident, as is seen in Figures 4.15C and 4.15D. The dislocations observed in Figure 4.15D are both in the matrix and around the particles, but the looping mechanism is not so clear. Here, the time at temperature was 688 h, the strain 3.54% and the measured particle size 1292 Å (0.1292 μm).

Thus, for creep deformation, it would appear that there is a change in dislocation deformation mechanisms with the growth of the γ′ precipitate, the change over point being estimated to be for a particle size of between 200 Å and 500 Å (0.02 μm and 0.05 μm).

A ×40 K

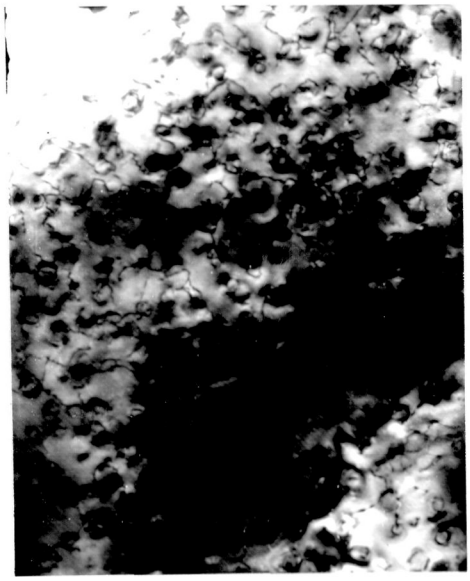

B ×40 K

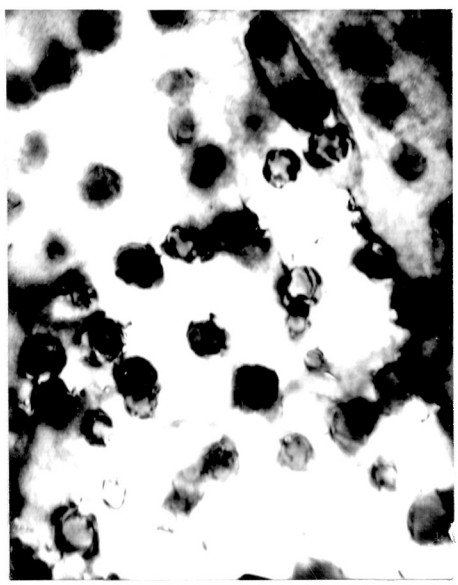

C N42 ×40 K

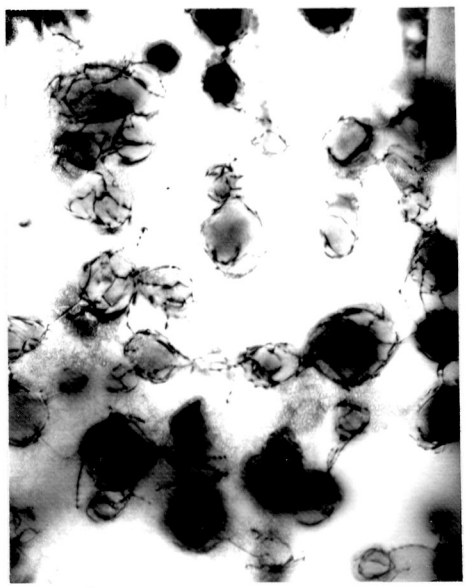

D N77 ×55 K

Figure 4.15: Transmission electron micrographs of creep tested specimens. Test N77 was an interrupted creep test at 800°C and 207 MN/m^2 (t = 688 h, ε = 3.54%).

4.2.4 Time at Temperature Parameters

4.2.4.1 Introduction

The previous three sections of results and studies were being performed at the same time and it became evident from early analysis of the results that the microstructure could be having a significant effect on the mechanical behaviour. An example is the many different shapes of creep curves (Figure 4.5). The electron microscopy revealed the effect of the γ' precipitate on the dislocation structure but, at this stage, no quantitative evidence was at hand of the effect on mechanical properties.

The most significant changes in the γ' precipitate were occurring at temperatures of 800°C or greater and for this reason several cyclic stress tests were performed to investigate the effect of time, and hence γ' particle size, on the parameter 'steady-state creep rate'. To try and eliminate any strain effects, a low value of stress was chosen for the tests at 800°C, 207 MN/m^2, with a single comparison for a higher stress, 276 MN/m^2.

For a comparison of test conditions where the material was not ageing significantly, or being overaged, a cyclic stress test was performed at 700°C.

Associated with the above tests, a possible reduction in yield stress with time was observed for the tests at 800°C and another series of tests was then carried out to measure purely this phenomenon at 800°C and 850°C.

4.2.4.2 Cyclic stress data

Four cyclic stress tests at 800°C and one at 700°C were carried out as described in Section 4.1.2. At 800°C, three tests were with an intermittent stress of 207 MN/m^2 and with different values of

α, the ratio of the time on load to the total cycle time (defined in Figure 4.16). The desired value of α only applied during the initial loading periods when a small accumulated strain occurred. On the advent of an increasing level of creep rate, the on-load time was reduced to keep the incremental creep strain as small as possible for a measurement of the creep rate. A single test was carried out at an intermittent stress of 276 MN/m^2.

For the comparison test at 700°C, an intermittent stress of 448 MN/m^2 was applied, this stress being below the yield stress and sufficient to cause a measurable creep rate over a period on-load of 24 h.

A definition of the parameters used to describe the cyclic stress tests is shown in Figure 4.16. Tables B.1 to B.5 (Appendix B) give the values of these parameters for each of the cyclic stress tests.

All tests showed an increasing creep rate with time at temperature, both at 700°C and at 800°C. A full interpretation of these tests will be given in Section 6.3.

4.2.4.3 Yield stress measurements

During the loading section of all constant stress creep tests, a record of load and strain was made and yield points were determined by a cross-plot of load and strain. However, during the cyclic stress tests, reported in Section 4.2.4.2, it was noted that for tests N75 and N76 at 800°C, there was a possible yielding on loading after long exposure times. To investigate this possibility, and also to determine the basic matrix yield stress, a series of tests was carried out purely to measure yielding parameters.

All specimens used were the standard creep test

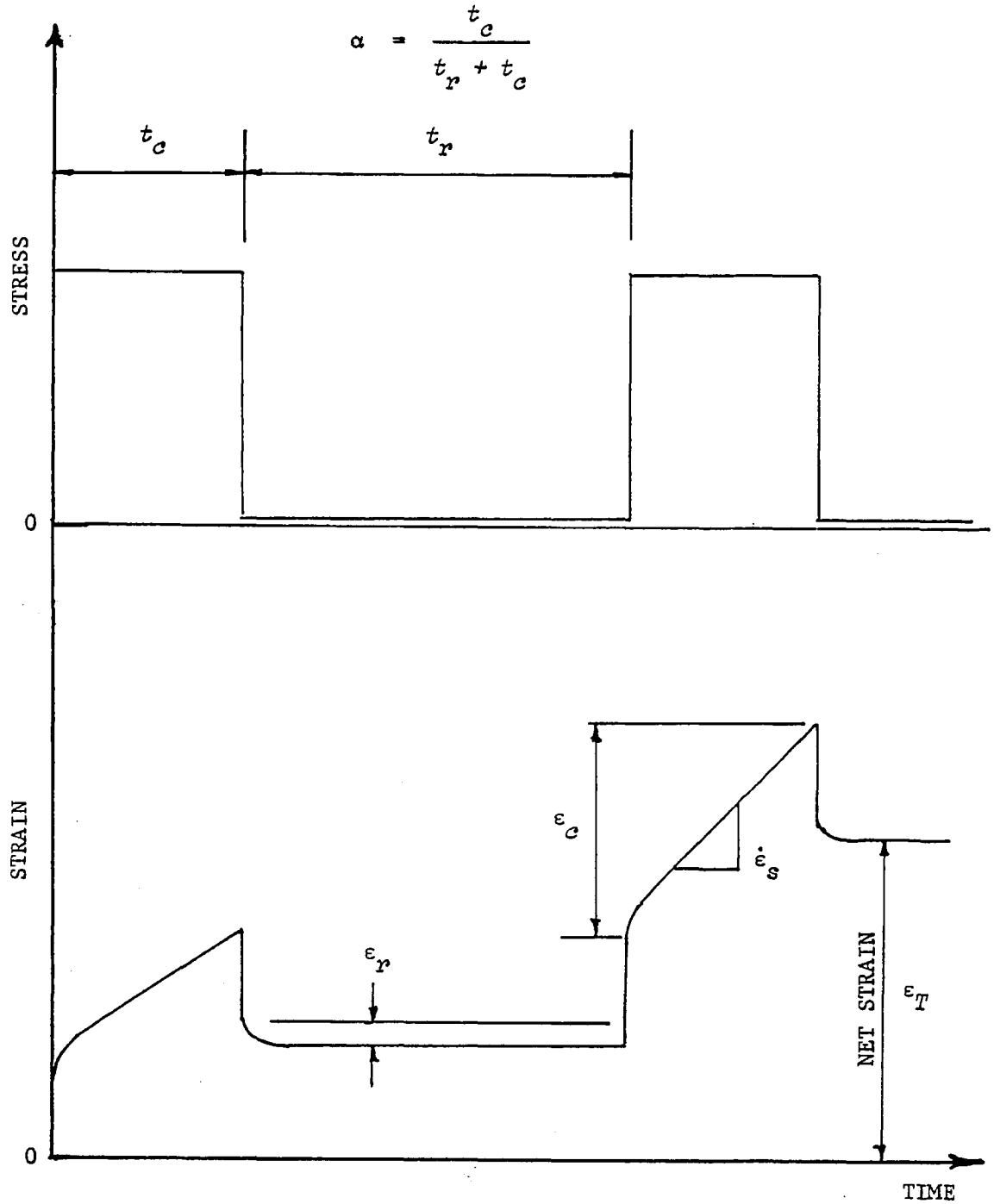

Figure 4.16: Definitions of terms for cyclic stress creep tests

specimens, as shown in Figure 2.2, and the tests carried out in the creep machines, as described in Section 4.1.3. The specimens were set up as for a constant stress creep test as described in Section 4.1.1. The load was applied by weights lowered on the motorised jactuators at the constant rate of 100 mm/min, the same as that used for the creep tests. No change in rate was made on yielding, although there would be an effective change in strain rate for the specimen.

To determine the basic yield stress of the matrix, a specimen in the solutionised heat-treated condition, i.e. no γ' present (this is debatable in that it is considered that some γ' forms during the air cooling from the solution heat treatment temperature, 1080°C), was first tested at room temperature, 68°F (20°C). A value of the yield stress was obtained as 138 MN/m^2. The yield point was defined as that load when a deviation occurred in the load extension plot made on the Bryans X-Y plotter. In this first loading, there was a deviation from linearity at a stress of 138 MN/m but also on the unloading cycle when a marked deviation towards the origin occurred with the stress at a value of 28 MN/m^2. A plastic strain of 0.0097% was recorded. This initial value of yield stress was considered to be on the low side on comparison with with published data (a value of 276 MN/m^2 being given for the 0.2% flow stress of γ at room temperature by Beardmore et al [82]) and the consideration that the directional solidification should increase the tensile properties. The specimen was reloaded several times to low values of stress with the repeated deviations being observed. A final loading was then made, the previous loadings giving a total plastic strain of 0.113%, and yielding occurred at a stress of approximately 321 MN/m^2 and gross yielding at 462 MN/m^2.

Because of the difficulty of defining the exact yield stress in the above test, the value of the 0.01% proof stress was then

used to define the yield point for further tests at elevated temperatures.

A second specimen in the solution heat-treated condition was then yielded at room temperature to give a value of the 0.01% proof stress of 416 MN/m^2 with 0.0384% plastic strain and an elastic modulus of 126 GN/m^2. The specimen was then rapidly heated to 675°C and, on application of the load, a definite yield occurred at a stress of 440 MN/m^2, with 0.0508% plastic strain and an elastic modulus of 93.2 GN/m^2. Further heating was then made to 804°C and the loading repeated to give a 0.01% proof stress of 415 MN/m^2 associated with a sudden yield point producing a plastic strain of 0.421% with an elastic modulus of 126 GN/m^2. The specimen was then rapidly cooled to room temperature by raising the furnace and a final loading made after the specimen and extensometry had stabilised. This loading produced another 0.01% proof stress of 517 MN/m^2 closely associated with a sudden yield at a stress of 565 MN/m^2 and an elastic modulus of 185 GN/m^2.

This latter value is considerably higher than the initial value measured at the beginning of the test. The plastic strain in the specimen before the final loading was 0.510%, but such was the yielding characteristics of this specimen, a yield followed by very little work hardening, that this plastic strain cannot have contributed to the higher value of room temperature proof stress or account for the non-reduction in value with temperature. Hardness measurements were then made on the flat, unstressed, ends of the specimen and an increase of 30 Hv was found over the pre-test values. This suggests that some ageing, or precipitation of the γ' phase, had occurred during the brief spells at temperature and the material was not in a constant metallurgical condition approximating to the matrix composition. Thus, doubt must be cast on the values of the 0.01% proof stress for the temperatures 675°C and 804°C as representing those of the matrix γ phase.

It would thus be preferable to test a separate alloy of the matrix composition in the directionally solidified form to determine the true matrix tensile yield and modulus properties.

A study was then made of the yield stress of the material in the directionally solidified aged condition at the temperatures 800°C and 850°C.

In the first of these, test N81T, an initially solution heat-treated specimen was used for the tests at 800°C, the basic ageing to full hardness taking place in the 27.5 h before the first loading. Table C.1 (Appendix C) gives the values of the measured 0.01% proof stress, the elastic modulus and the plastic strain for each loading cycle in the 796.5 h at the test temperature. Figure 4.17 shows the changing nature of the direct load (converted to stress units) versus extension (converted to strain units) plots associated with time at temperature. Plot A is after 47.6 h at temperature and shows a fairly sudden yield, whilst plot B, after 120 h at temperature, shows a more gradual yield and a non-linear plot on the initial unloading. This latter effect was possibly caused by a creep process occurring simultaneously with the tensile loading and unloading. The small amounts of plastic strain accumulated during each cycle were taken into account by a change in the cross-sectional area used to calculate the stress. Otherwise, the strain was considered to have no work hardening effect due to the long periods of recovery between cycles.

For the test N82T at 850°C, an already aged specimen (16 h at 700°C) was used and the cycles performed as above over a time span of 646.3 h. Table C.1 again gives values of the 0.01% proof stress, elastic modulus and the plastic strain for each cycle. It will be noted that there were two loading cycles after 44.9 h at temperature. This was because a sudden change in slope of the load versus extension plot occurred in the early stage of the first cycle, probably due to a slight

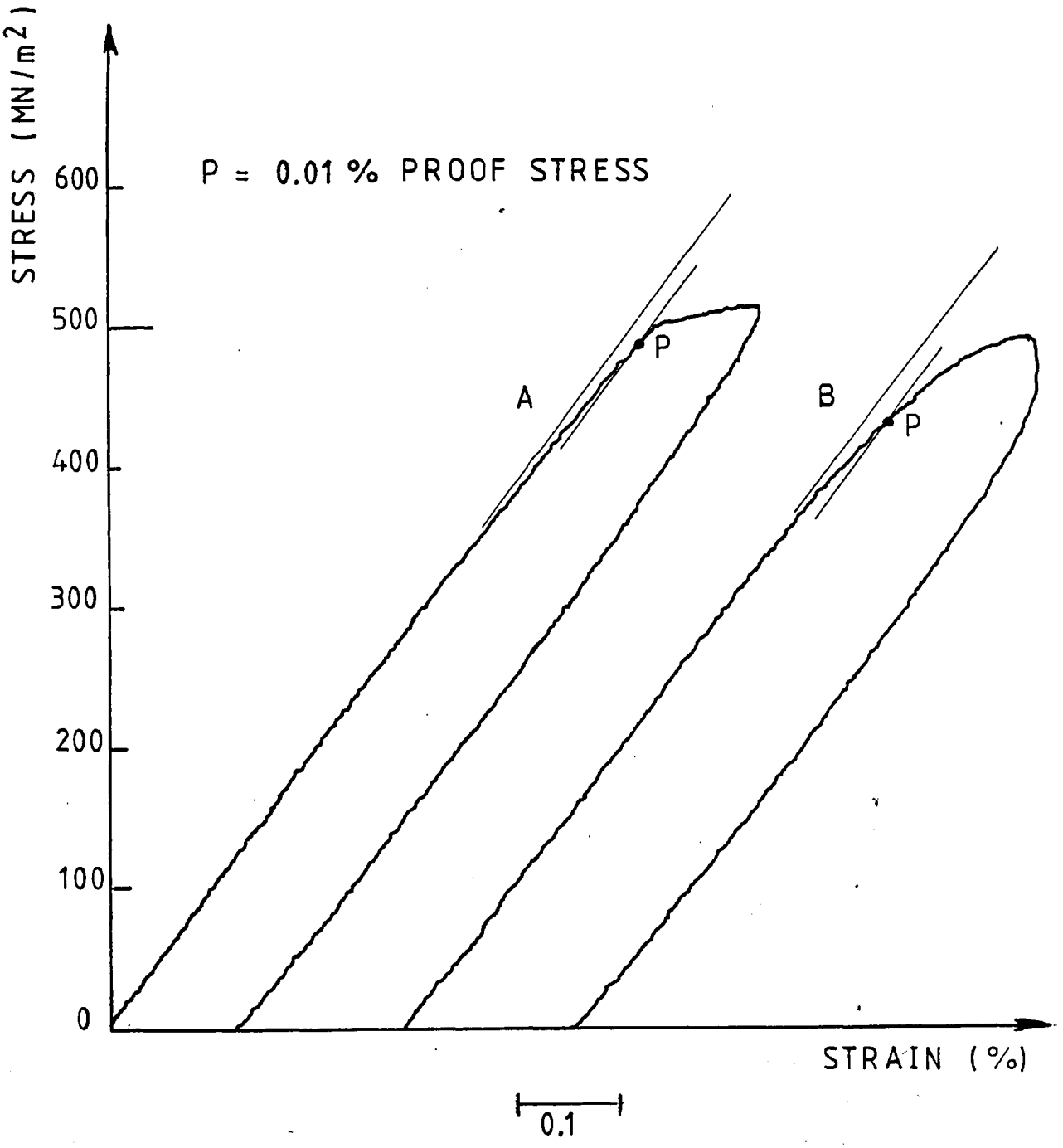

Figure 4.17: Load (converted to stress units) versus extension (converted to strain units) for the 3rd (A) and 4th (B) loadings for test N81T. Slopes are elastic moduli.

realignment of the extensometry. The second loading produced identical values of the 0.01% proof stress and the elastic modulus, after the initial change.

Figure 4.18 shows a typical plot of the direct load (converted to stress units) versus extension (converted to strain units) for the tests at 850°C. It is noted that the plot is in some way similar to plot B in Figure 4.17 but with a more pronounced non-linearity in the unloading cycle. This is due to the greater recovery rates associated with the higher temperature, a fact which was also shown by the recovery strain observed at the base load after a period of several minutes.

4.3 EXPERIMENTAL RESULTS FOR EQUI-AXED GRAIN MATERIAL

It was intended that a full programme of constant stress creep tests comparable to that for the directionally solidified form of the alloy should be carried out. As mentioned in Section 2.2, an error by the manufacturer machining the test pieces resulted in an extended length between the end of the gauge length and the locating holes. This resulted in the creep machine furnaces being re-calibrated to what was thought to be a uniform temperature throughout the test section.

Fifteen constant stress creep tests were then carried out in a manner as described in Section 4.1.1. The results are listed in Table D.1 (Appendix D). It is seen that for only six of the tests did fracture occur within the gauge length. At this point, the test programme was halted.

Plots of creep strain versus time for the three test temperatures of 700°C, 750°C and 800°C are shown in Figures D.2 to D.4.

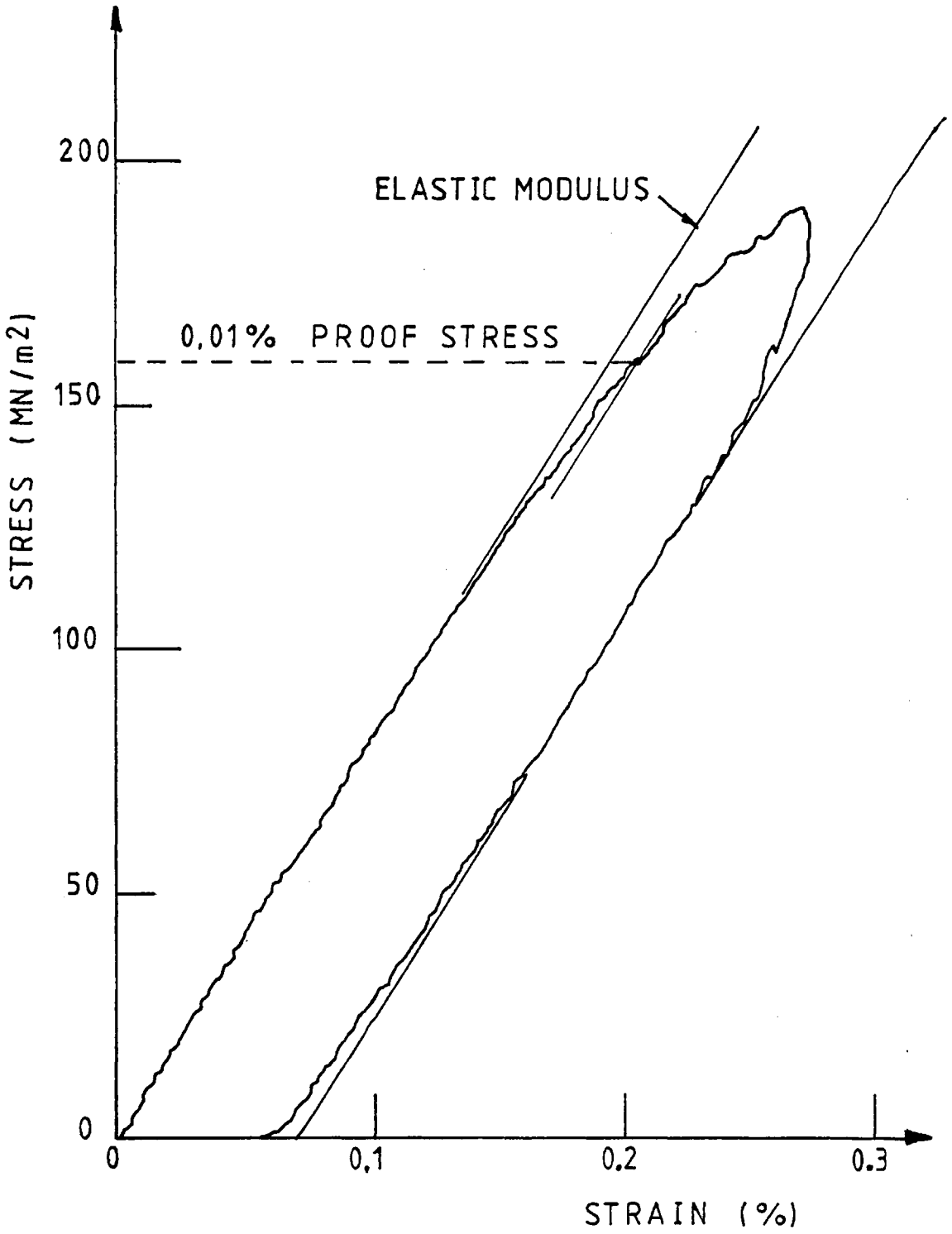

Figure 4.18: Typical load (converted to stress units) versus extension (converted to strain units) for test N82T. 9th loading cycle.

CHAPTER 5

ANALYSIS OF DATA

5.1 INTRODUCTION

Before a critical review can be made of the experimental creep and tensile data, the possible effects of variations in material composition and structure should be considered.

The initial monitoring of the chemical composition of the alloy, by Henry Wiggin Company Limited, during the 10 melts that were required to produce the test pieces showed a smaller variation in the weight percentage of the constituents than is required by the BS specification for the commercially equivalent alloy (see Table 2.1). In particular, the low carbon content, 0.05 wt% to 0.07 wt%, closely controlled the amounts of grain boundary carbide, these carbides can play an important part in creep rupture and the formation of denuded zones.

As far as was possible, all test pieces received the same heat treatment cycles, the treatment being carried out in batches of each cast melt. For most creep test temperatures, specimens were taken from the same batch. Thus, it is hoped that any effects of chemical composition and heat treatment history have been minimised.

During the manufacture of the test pieces, close control of the alignment of the directionally solidified grains was kept and the limit of $\pm 5^{\circ}$ alignment of the <001> crystal axis with the tensile test axis reduced the possible effects of alignment, the yield stress and elastic modulus of directionally solidified nickel base alloys being strongly dependent on the crystal axis.

The number of grains across the sections of the directionally solidified ingots varied along the length of the case but in the gauge length of the test pieces, the number remained almost constant. The

actual value varied from three to ten across the gauge length transverse section from test pieces sectioned.

Richards [62] has evaluated the effects of gauge length and the number of grains across the gauge length diameter on the creep properties of equi-axed cast and wrought nickel base alloys. A relationship between the time to fracture and the number of grains across the specimen diameter for a cast alloy was found as shown below in Figure 5.1.

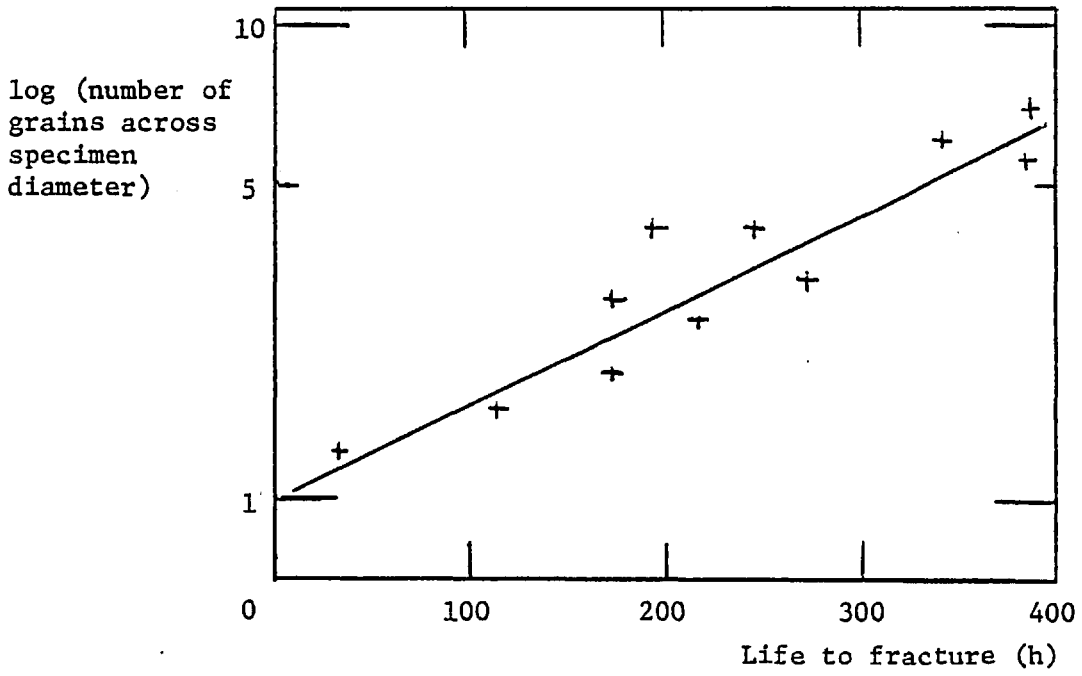

Figure 5.1: Effect of number of grains across creep test specimen

From the large scatter obtained in the creep data for the experimental material in the equi-axed grain form, the above relationship may hold but in the case of the directionally solidified material the effects of grain boundary deformation are minimal due to the absence of transverse grain boundaries. These effects will be discussed later.

In the same analysis [62], the specimen gauge length had negligible influence on the life to fracture and creep rate, although the elongation at fracture increased from approximately 8% to 12% when the gauge length

was reduced by one third. This is surprising as the influence of extensometer ridges at the ends of the gauge length would be expected to be large for the small gauge lengths of 12.7 mm. In the present work, the extensometer ridges had some constraining effect on lateral deformation which probably gave rise to the double neck phenomenon as was shown in Figure 4.10. However, their influence on deformation up to the fracture point is considered small.

There is no absolute certainty that all specimens were in an identical metallurgical and physical condition at the start of the creep tests but it is hoped that any significant variations would be noticed by the monitoring of the parameters, hardness and elastic modulus, and the physical dimensions of the gauge length. No significant variations were found in these parameters.

The repeatability of the creep data was generally good, e.g. the incubation period being observed for tests at 552 MN/m^2, and identical initial creep strain-time relationships for tests N14 and N18. Some anomalies did occur, e.g. the difference in rupture strains in tests N16 and N17 (possibly due to structural differences in grain size), and the cross-over of some creep strain-time data at small strains and times. This latter effect could be due to the definition of creep strain used, i.e. strain from when all the load is applied. When there was yielding in the specimen on loading, the load application rate reduced considerably and the increased loading time could then allow creep strain to occur and the recorded creep data will be an underestimate of total creep strain.

5.2 PHYSICAL CURVE FITTING ANALYSIS

The physical equations considered were those based on a model of dislocation dynamics as proposed by Webster and described in Section 1.5.

The first equation was the final solution considering the

immobilisation and multiplication rates of all dislocations and a variable dislocation velocity, the solution being:

$$\varepsilon = A\,t + D\,ln\,[B + (1-B)\,exp^{(-\phi t)}] + \frac{C\,(1-B)\,(1-exp^{(-\phi t)})}{B + (1-B)\,exp^{(-\phi t)}} \qquad (5.1)$$

By assuming that multiplication occurs from mobile dislocations only and that the dislocation velocity remains constant, equation (5.1) can be reduced to a much simpler three-parameter equation:

$$\varepsilon = A'\,\alpha\,t + A'\,ln\,[B' + (1-B')\,exp^{(-\alpha t)}] \qquad (5.2)$$

Equations (5.1) and (5.2) are the two equations that have been compared by curve fitting and hereafter are referred to as the five-parameter model and the three-parameter model, respectively.

As can be seen, both equations contain non-linear terms in time, t, and the five-parameter equation cannot be suitably solved graphically for the values of the parameters. For this reason, all curve fitting was carried out using the IBM 7094 computer installed at Imperial College during 1967 to 1970.

The technique for solving parameters in non-linear equations was that of non-linear regression, the basic method being that described by Scarborough [89]. The first program tried using this technique applied to computing originated from the United States Steel Corporation [61]. After converting to Fortran IV language, from the original Fortran II, several sets of creep strain-time data were tried using the simple three-parameter model and the more complicated five-parameter model. Little success was achieved due to the very slow convergence of the parameters to give the "best" solution. Convergence occurred when the sum of the square of the errors between the experimental and predicted values of creep strain

```
N =  20      K =  5       P =  6       M =  1
FF =  0.4300E 01      I =  0.2000E 01      B =  0.5000E-04      TAU =  0.1000E-02
                        A                    B                    C                    D                    Φ
( 421 PARAMETERS      0.1574331?E 01    0.52584166E-01   -0.96403459E-02    0.10435034E 01    0.1566946CE 01
 0.10E-02                                                                                          0.41E 01
*
Y
Y
Y
Y
Y
Y
Y
Y
PO
  PO
    OP
       JP
          OP
                Y
                  Y
                        Y
                              OP
                                 O P
                                    O P
                                       O >
( 421 PARAMETERS      0.1574331?E 01    0.52584166E-01   -0.96403459E-02    0.10435034E 01    0.1566946CE 01
                 STRAIN                STRAIN                                PRNT (1)          PRNT (2)          PRNT(3)
                  OBS                   PRED                 DIFF             PRNT (4)
          0.1060000E-02     0.1402095+E-04     0.9859790+E-03     0.1306694E-02    -0.1260833?E-02    -0.1184CC55E-04
                                                                  0.8330000?E-03
          0.2060000E-02     0.2825043+E-04     0.1971709+E-02     0.2629133?E-02    -0.2577CC59E-02    -0.2383676?E-04
                                                                  0.1670000?E-02
          0.4060000E-02     0.8559312?E-04     0.3914404?E-02     0.7871656?E-02    -0.7714526?E-02    -0.7153356?E-04
                                                                  0.5330000?E-02
          0.5060000E-02     0.1441617?E-03     0.5355030?E-02     0.1211942?E-01    -0.1265515?E-01    -0.1195012?E-03
                                                                  0.8333300?E-02
          0.1560000E-02     0.2664543?E-03     0.7203545?E-02     0.2629133?E-01    -0.2575395?E-01    -0.2406166?E-03
                                                                  0.1670000?E-01
          0.1160000E-01     0.5793424?E-03     0.1102063?E-01     0.7871659?E-01    -0.7655654?E-01    -0.7352456?E-03
                                                                  0.5000000?E-01
          0.1560000E-01     0.8245434?E-02     0.1305456?E-01     0.1574331?E 00    -0.1536552?E 00    -0.1525356?E-02
                                                                  0.1000000?E 00
          0.3460000E-01     0.1451703?E-01     0.2538296?E-01     0.4722993?E 00    -0.4563534?E 00    -0.5286656?E-02
                                                                  0.3000000?E 00
          0.3160000E-01     0.3540203?E-01     0.3139796?E-01     0.9916287?E 00    -0.9561777?E 00    -0.1404846?E-01
                                                                  0.6300000?E 00
          0.1256000E 00     0.1051693?E 00     0.2431467?E-01     0.1574331?E 01    -0.1441451?E 01    -0.2664141?E-01
                                                                  0.1000000?E 01
          0.2356000E 00     0.2566781?E 00    -0.1717815+E-01     0.3228278?E 01    -0.1571544?E 01    -0.5415536?E-01
                                                                  0.1450000?E 01
          0.4636000E 00     0.5031254?E 00    -0.3991549+E-01     0.2954742?E 01    -0.2372518?E 01    -0.8406653?E-01
                                                                  0.1880000?E 01
          0.6836000E 00     0.7171234?E 00    -0.3382360?E-01     0.3384812?E 01    -0.2564737?E 01    -0.1025506?E 00
                                                                  0.2150000?E 01
          0.9786000E 00     0.9743587?E 00     0.2401292?E-02     0.3899811?E 01    -0.2712304?E 01    -0.1201177?E 00
                                                                  0.2420000?E 01
          0.1356000E 01     0.1372424?E 01     0.2257154?E-01     0.4360897?E 01    -0.2850119?E 01    -0.1383626?E 00
                                                                  0.2770000?E 01
          0.2736000E 01     0.2324035?E 01     0.1496049?E-01     0.5478677?E 01    -0.2954333?E 01    -0.1402595?E 00
                                                                  0.3480000?E 01
          0.2760000E 01     0.2792352?E 01    -0.3239294?E-01     0.4988245?E 01    -0.3024741?E 01    -0.1453246?E 00
                                                                  0.3850000?E 01
          0.3156000E 01     0.3274088?E 01    -0.8308833?E-01     0.6486244?E 01    -0.3043634?E 01    -0.1488214?E 00
                                                                  0.4120000?E 01
          0.3716000E 01     0.3856867?E 01    -0.1460074?E 00     0.7084449?E 01    -0.3056884?E 01    -0.1761962?E 00
                                                                  0.4500000?E 01
          0.4116000E 01     0.4296079?E 01    -0.1737584?E 00     0.7525303?E 01    -0.3062732?E 01    -0.1716122?E 00
                                                                  0.4780000?E 01
                 PHI                 S C              LAMDA          ANALYTIC PARTIALS USED
          0.6606196?E-01     0.6634349?E-08     0.1000E-01

PTP INVERSE
    1     0.1252?97?0E 02     0.2311179?E-03    -0.1342381?E 01     0.5765143?E 01     0.6501054?E-02
    2     0.2113?082E-03     0.4644564?E-08    -0.1066258?E-04     0.1055022?E-03     0.1326745?E-06
    3    -0.1342?915E 01    -0.1866261?E-04     0.1648300?E 00    -0.4096656?E 00    -0.5574552?E-03
    4     0.5765?431E 01     0.1055023?E-03    -0.4096656?E 00     0.3067524?E 01     0.3170711?E-02
    5     0.6501?054E-02     0.1326746?E-06    -0.5974588?E-03     0.3170711?E-02     0.2751612?E-05

PARAMETER CORRELATION MATRIX
        1         1.0000     0.8617    -0.9196     0.9155     0.9285
        2         0.8617     1.0000    -0.6744     0.9838     0.9846
        3        -0.9196    -0.6744     1.0000    -0.6886    -0.7557
        4         0.9155     0.9838    -0.6886     1.0000     0.9297
        5         0.9285     0.9846    -0.7557     0.9297     1.0000

              STD                ONE - PARAMETER                              SUPPORT PLANE
   B          ERROR          LOWER                UPPER                LOWER                UPPER
   1     0.2166311E 00     0.1577?89E 01     0.2051573E 01     0.5071849?E 00     0.2641477E C1
   2     0.4423?011E-05     0.5257511E-01     0.5259321E-01     0.5256393?E-01     0.5260435E-01
   3     0.2654?11E-01    -0.6332545?E-01     0.4424593E-01    -0.1301337?E 00     0.1108535E CC
   4     0.1160?15E 00     0.8110443?E 00     0.1275970E 01     0.5237041?E 00     0.1563310?E 01
   5     0.1292?346E-03     0.1560?715E 01     0.1561210E 01     0.1560382?E 01     0.1561537E C1

 NONLINEAR CONFIDENCE LIMITS

PHI CRITICAL =  0.1541445?E 00

 PARA       LOWER B          LOWER PHI          UPPER B          UPPER PHI
   1     0.1552?445E 01     0.3210?82?E-01     0.1580911?4E 01     0.1541446?E 00
   2 NONE FOUND
   3    -0.1519?46?E-01     0.4452344?E-01    -0.5083219?E-02     0.1541445?E 00
   4     0.1056?787E 01     0.2720454?E 00     0.1099561?E 01     0.1541445?E 00
   5 NONE FOUND
```

Figure 5.2: Typical final solution print-out

was not being reduced by more than 0.05% of the sum for the previous iteration. As the distribution of experimental points covered a strain range of 0.001% to 10%, this meant that the sum of squared errors was more influenced by the data in the high strain range. Several weighting methods were applied but none succeeded in producing a good fit between the models and the creep strain data.

A second, more advanced program was then used. This was Program No. SDA 3094 from the Share Program Library and was also a least squares estimate of parameter improvement using the maximum neighbourhood method of iteration. The criterion for convergence could now be one of five and these are listed and explained in Appendix E. The program could use either finite difference estimates or analytical values of the parameter partial derivatives, but for both models the analytical values were used, as described in Appendix E.

Twenty six sets of creep strain-time data were analysed covering the temperature range 650°C to 850°C. Each set of data contained at least twenty points distributed on a semi-log and linear basis, and Figure 5.2 shows a typical set of computer output for the final solution. The visual plot indicates the degree of fit on a linear scale of strain (the horizontal axis) but the vertical axis (time) is simply a new line for each set of data. During the initial testing of the program, negative values of B and ϕ for the five-parameter model were produced. These values do not relate to the physical representation of the model and a constraint on negative values was made (see Appendix E and subroutine FCODE).

The best fit for each set of data is shown for each temperature in Figures F.1 to F.5 on a logarithmic basis, and in Figures F.6 to F.10 on a linear scale. Tables F.1 and F.2 list the parameters for the best fit for both the three- and five-parameter models. The value of the maximum

strain reading is included in these tables as this will influence the magnitude of the sum of the squared errors. These parameters, marked *, indicate that the parameters did not change from the original estimate. This only happened with the five-parameter model.

5.2.1 Discussion

From Tables F.1 and F.2, it is seen that of the twenty six sets of data fitted, the three-parameter model gives the best fit for seventeen sets of data and the five-parameter model the best fit for nine sets of data. However, for many cases, the difference in the sum of the errors squared is insignificant and it is better to consider the possible physical significance of the parameters and the shape of the predicted curves.

There is little significance in the final criteria for fitting between the models. Both had the same total number of ε and γ-ε fits. The γ-λ test was not the criterion for any of the sets of data.

From the linear plots of creep strain-time (Figures F.6 to F.10), it would appear that both models give a very good fit to the data, but on the logarithmic plots (Figures F.1 to F.5), then a large discrepancy is found in strain values in the early part of the creep curve.

This may be explained by investigating the form of the equations (5.1) and (5.2). Consider first equation (5.1) for small values of time. With t small and $\phi t \ll 1$, the following approximations can be made:

$$exp^{(-\phi t)} = (1 - \phi t)$$

$$ln\ (1 \pm \phi t) = \pm \phi t$$

$$(1 \pm \phi t)^{-1} = 1 \mp \phi t$$

The second and third terms may then be reduced as follows:

(i) Second term: $D\ ln\ [B + (1-B)\ exp^{(-\phi t)}]$

$$= D\ ln\ [B + (1-B)\ (1-\phi t)]$$

$$= D\ ln\ [1 + (B-1)\ \phi t]$$

$$= D\ (B-1)\ \phi t$$

(ii) Third term: $\dfrac{C\ (1-B)\ (1-exp^{(-\phi t)})}{1 + (B-1)\ exp^{(-\phi t)}}$

$$= \frac{C\ (1-B)\ \phi t}{1 + (B-1)\ \phi t}$$

$$= C\ (1-B)\ \phi t$$

Thus, equation (5.1) approximates to:

$$\varepsilon = A\ t + D\ (B-1)\ \phi t + C\ (1-B)\ \phi t$$

$$= [A + (B-1)\ (D-C)\ \phi]\ t \qquad \text{for} \qquad \phi t << 1 \tag{5.3}$$

The creep rate for all values of time is given by differentiating equation (5.1) with respect to time and this gives:

$$\dot{\varepsilon} = A - \frac{D\ \phi\ (1-B)\ exp^{(-\phi t)}}{B + (1-B)\ exp^{(-\phi t)}} + \frac{C\ (1-B)\ \phi\ exp^{(-\phi t)}}{[B + (1-B)\ exp^{(-\phi t)}]^2} \tag{5.4}$$

Thus, when $t = 0$, the initial strain rate is given by:

$$\dot{\varepsilon}_i = A - D\,\phi\,(1-B) + C\,(1-B)\,\phi$$

$$= A + (1-B)\,(C-D)\,\phi \tag{5.5}$$

Comparing equations (5.3) and (5.5), it is now seen that the model predicts a linear relationship between strain and time with the same rate of increase from time equals zero. This is shown in the logarithmic plots of the curves as the initial slopes have a value of unity.

A similar analysis holds for the three-parameter model. For small values of time, equation (5.2) reduces to:

$$\varepsilon = A'\,B'\,\alpha\,t \tag{5.6}$$

The creep rate is given by:

$$\dot{\varepsilon} = A'\,\alpha - \frac{A'\,(1-B')\,\alpha\,exp^{(-\alpha t)}}{B' + (1-B')\,exp^{(-\alpha t)}} \tag{5.7}$$

When $t = 0$, $\dot{\varepsilon} = \dot{\varepsilon}_i$, where:

$$\dot{\varepsilon}_i = A'\,\alpha - A'\,\alpha\,(1-B')$$

$$= A'\,B'\,\alpha \tag{5.8}$$

Again, there is a linear relationship between strain and time with the same rate of increase from time equals zero. Thus, both models will give rise to an error in the predicted strain value for the

experimental material for small values of time. This error is more pronounced for the tests in the low stress range at each temperature where there are several decades of primary creep on the logarithmic scale. For all temperatures, however, the difference in the time to 0.1% creep strain between the experimental and predicted value from the models is small, less than a factor of two in most cases.

For strains above 0.1%, there is very good fit and the various shapes of creep curve are all fitted. It will be noted, however, that the maximum value of creep strain used was decided on a visual basis as the end of the "secondary" creep stage. The secondary creep stage was that as defined at the end of the "steady-state creep rate" regions of the linear creep strain-time plots shown in Figure 4.5.

For the five-parameter model, the second and third terms represent an increasing function of strain with time which reaches a constant value. The relative magnitudes of these values depends on the sign and magnitude of the parameters B, C and D.

The value of the predicted secondary creep rate can be found from equations (5.4) and (5.7) by putting t large. For the five-parameter model, this gives:

$$\dot{\varepsilon}_s = A \tag{5.9}$$

and for the three-parameter model:

$$\dot{\varepsilon}_s = A' \alpha \tag{5.10}$$

Thus, for the five-parameter model, the secondary creep rate involves only one parameter, but for the three-parameter model two parameters are involved. It is interesting to note that by comparing equations (5.8) and (5.10), the ratio between the initial and secondary

creep rates is now given by the parameter B' and by looking at Tables F.1 and F.2, it can be deduced which shape of curve in Figure 4.5 is represented by the models by considering whether $B' > \text{or} < 1$. The only anomaly in this analysis is test N4 at 750°C where the value of B' (18.86) would indicate that the curve for that particular stress has a pronounced primary component. However, the maximum value of experimental strain for test N4 was only 0.1%, the specimen breaking outside the gauge length. The above analysis would suggest that the major part (the secondary and tertiary stages) of the creep curve was not reached.

The values of the parameters B and B' have been plotted on a stress and temperature basis in Figure 5.3. It is seen that for values of B, $B' < 1$, there is little dependence on temperature and for values of B, $B' > 1$, there is no obvious relationship with temperature. In this latter range, the stress function is not clear but for B, $B' > 1$, a power-law relationship with stress could apply with an exponent of 35.

The values of the secondary creep rates predicted by equations (5.9) and (5.10) are plotted in Figure 5.4. These computed values are compared with the values predicted from Section 5.3 by the stress law fits to the experimental data and it is seen that there is very good agreement between the computed and experimental values. The experimental values were decided on after considering the whole of the creep curve up to fracture but for the models, no such criterion is set. The value of the secondary creep rate is also derived in physical terms from equation (1.3), which gives:

$$\dot{\varepsilon}_s = A = b\,\alpha_1\,(V_o - k\,\alpha_1)$$

where α_1 is the steady-state value of dislocation density, V_o and k are constants, and b is the Burgess vector.

As was explained in Section 4.2.3, the dislocation densities

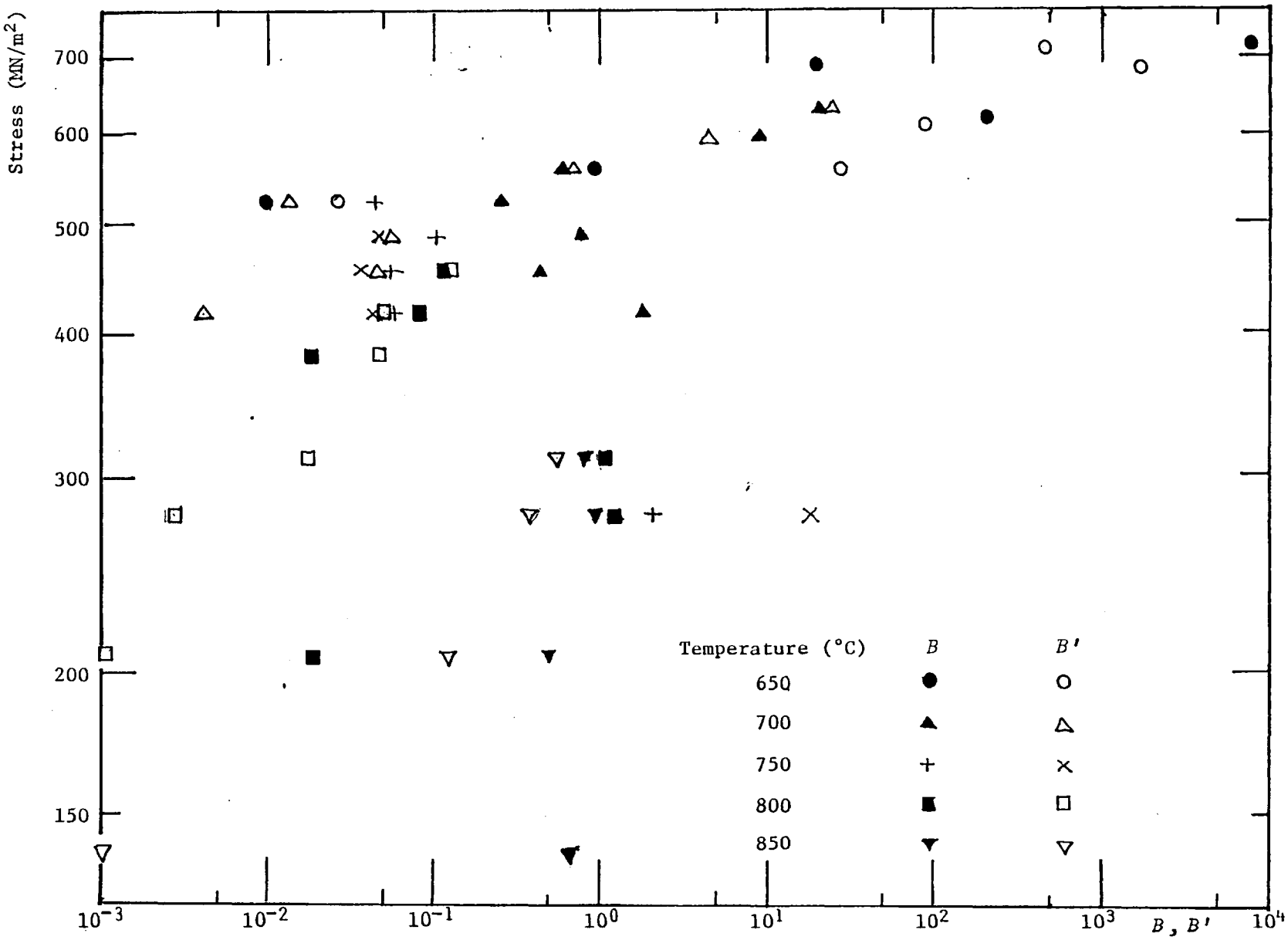

Figure 5.3: Stress dependence of parameters B and B'

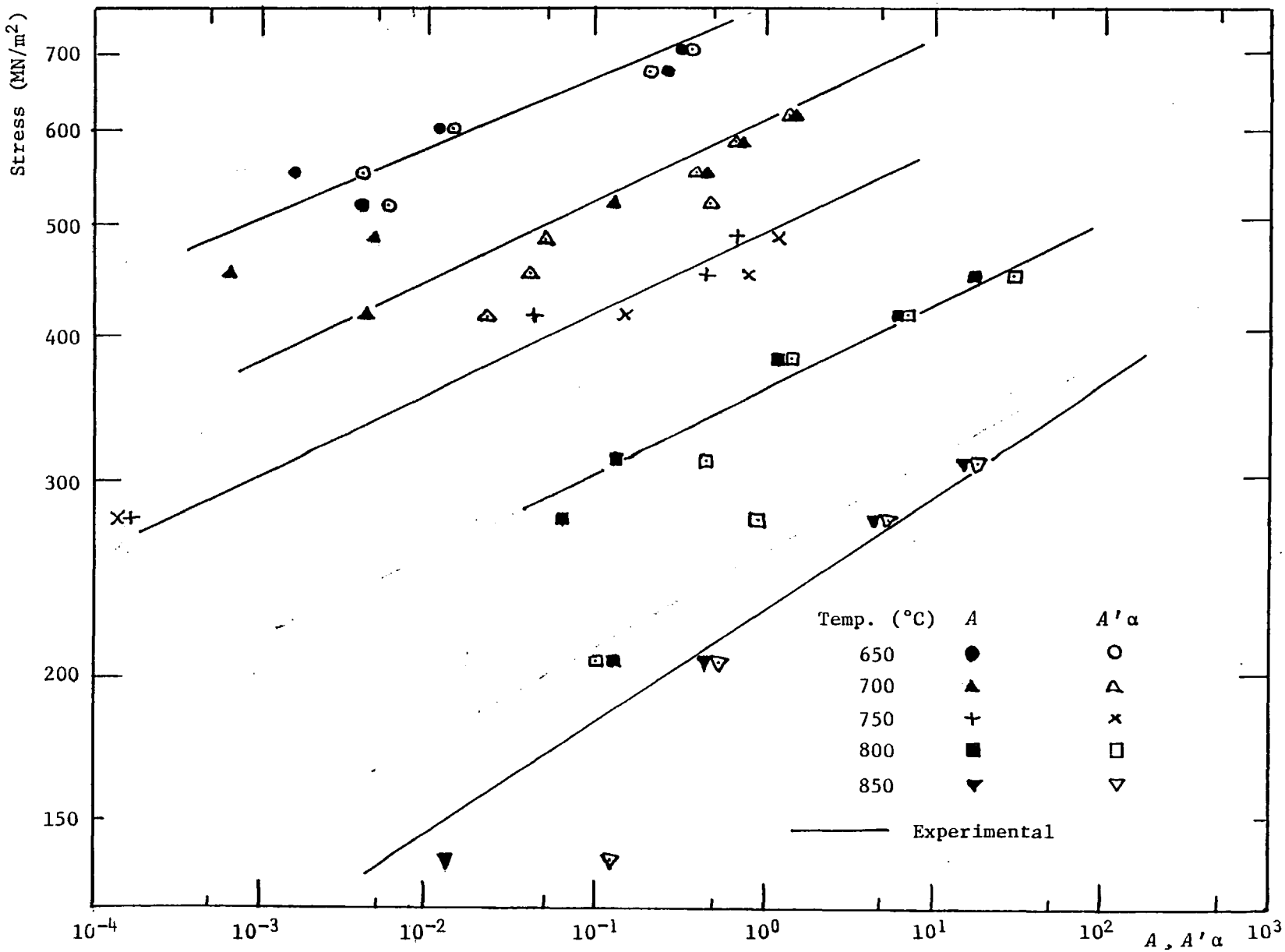

Figure 5.4: Stress dependence of the predicted steady-state creep rate A , $A'\alpha$

could not be measured experimentally but the above analysis could well be used to derive predicted values of dislocation density once the stress and temperature functions of A are substituted.

From Tables F.1 and F.2, it is also seen that the parameters ϕ and α, the rate of exhaustion of primary creep, show distinct trends with stress and temperature, and these are plotted in Figure 5.5. There is very little difference between the values of ϕ and α, and for each temperature it would appear that a power-law function applies for the stress dependence. However, the value of the exponents varies slightly with temperature ranging from a value of 10 at 850°C to a value of 15 at 650°C.

Some comment can be made on the choice of the parameters by considering the parameter correlation matrix produced by the program. Typical examples are:

(a) For the five-parameter model (test N25):

	A	B	C	D	ϕ
A	1.0000	0.8617	-0.9196	0.9155	0.9285
B	0.8617	1.0000	-0.6744	0.8838	0.9846
C	-0.9196	-0.6744	1.0000	-0.6886	-0.7557
D	0.9155	0.8838	-0.6886	1.0000	0.9297
ϕ	0.9285	0.9846	-0.7557	0.9297	1.0000

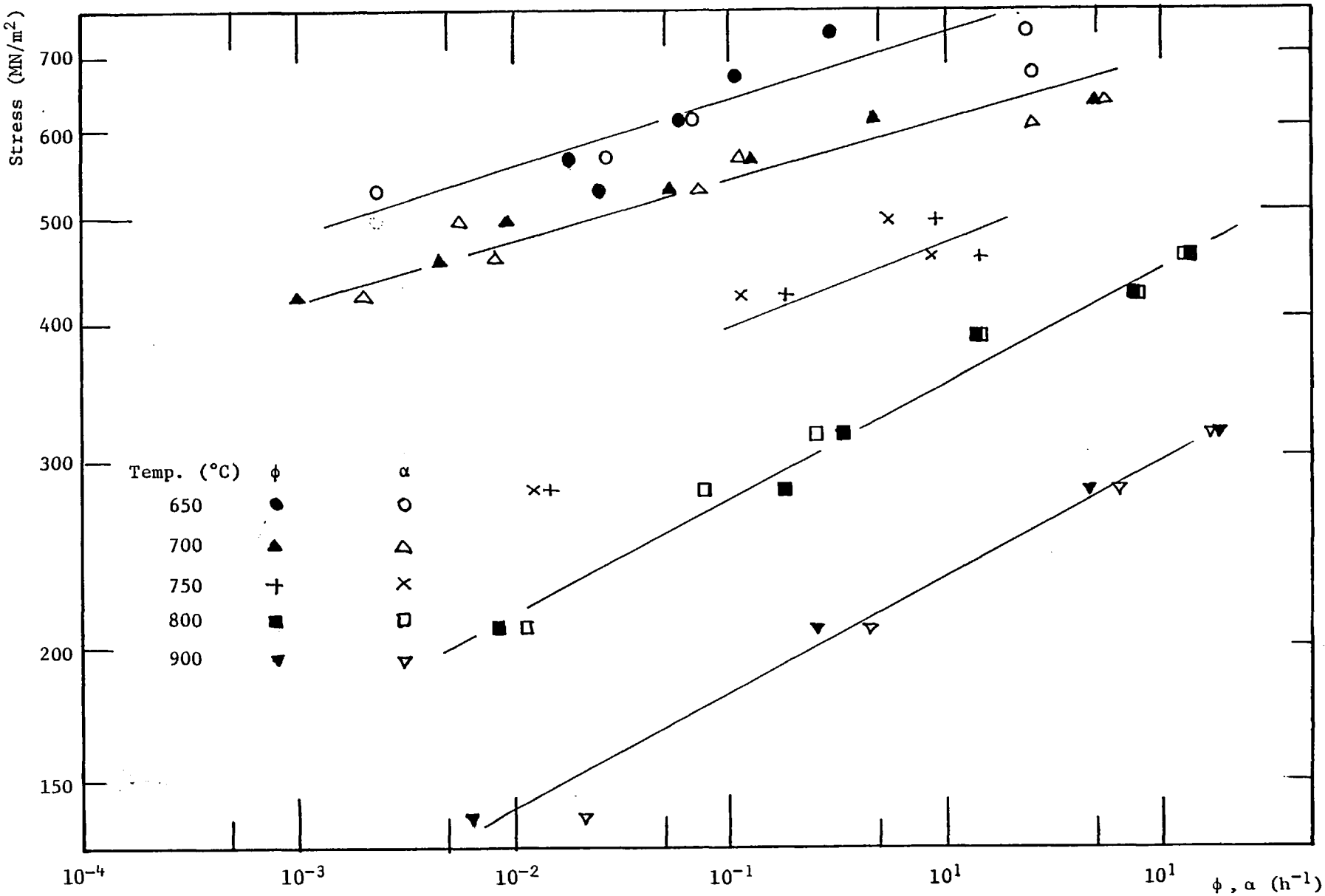

Figure 5.5: Stress dependence of parameters ϕ and α

(b) For the three-parameter model (test N47):

	A'	B'	α
A'	1.0000	0.9984	-1.0000
B'	0.9984	1.0000	-0.9986
α	-1.0000	-0.9986	1.0000

The high correlation values suggest that the final solution is dependent on the initial estimates and indeed this was so for the five-parameter model. Also, there may well be an excess of parameters and that some are interrelated.

The relationship between the parameters A and ϕ is shown in Figure 5.5A for the five-parameter model. It is seen that there is an approximate linear relation between the two parameters which represent the steady-state creep rate and the rate of exhaustion of primary creep. This may suggest that both the primary and secondary stages have the same deformation mechanism, as has been suggested by Webster, Cox & Dorn (Appendix G) and further expanded by Amin, Mukherjee & Dorn [49]. On this basis, for the three-parameter model, the value of A', effectively the ratio of the secondary creep rate ($A'\alpha$) to the rate of exhaustion of primary creep (α), should be a constant. However, the computed values show a spread in values from 0.01 to 29.5. The three-parameter model assumes that the dislocation velocity is constant throughout the primary and secondary stages but this analysis infers that this may not be true and that the material structure may not be constant.

It would be useful if values of dislocation densities and other deformation parameters could be deduced from the values of the

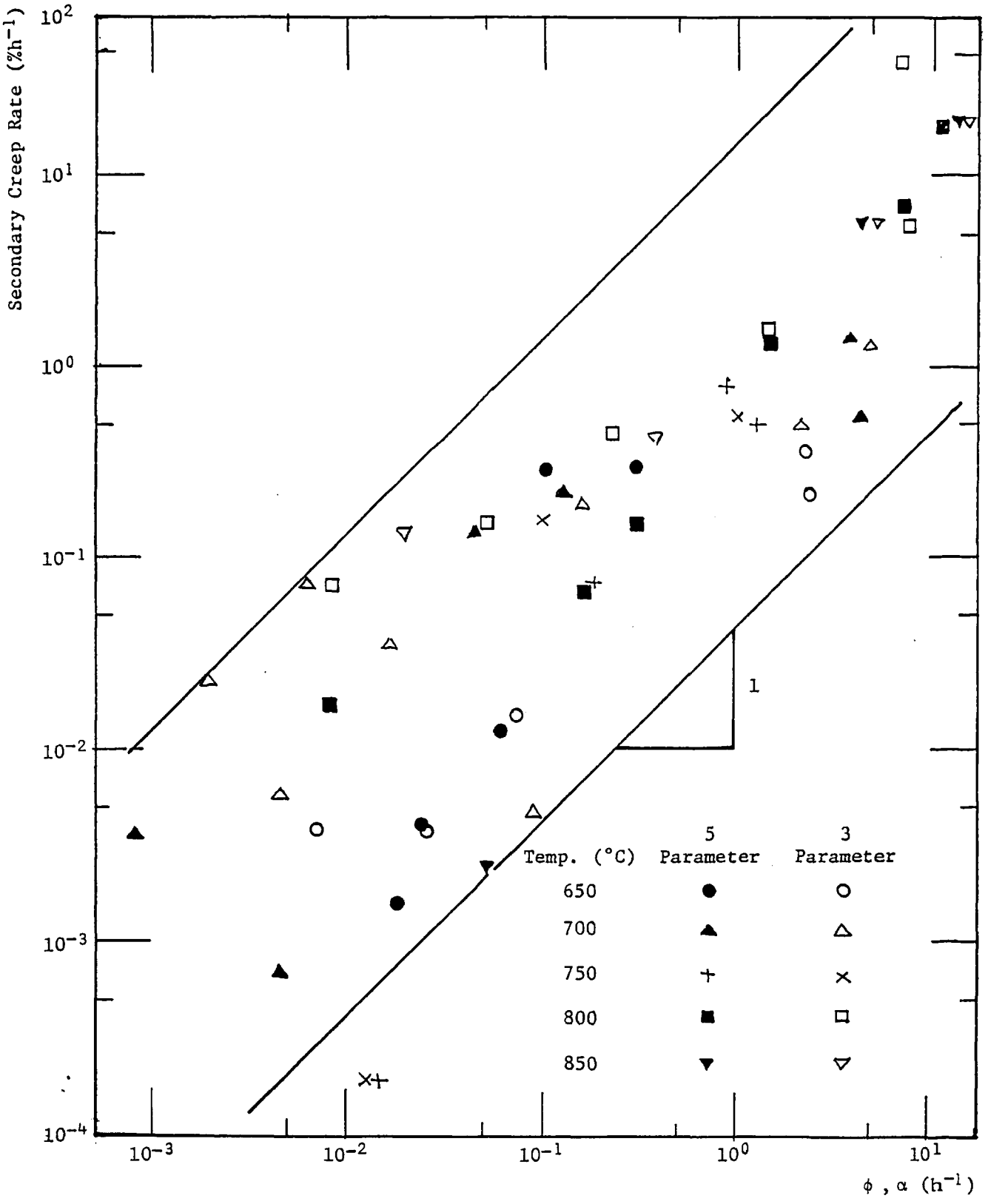

Figure 5.5A: Predicted relationship between secondary creep rate $\dot{\varepsilon}_s$ (A , $A'\alpha$) and rate of exhaustion of primary creep (ϕ , α) for 3 and 5 parameter models

parameters. Whilst the value of A is linked with the value of the steady-state dislocation density, the other parameters are not amenable to deformation parameters.

Of particular use would be an insight into the behaviour of the parameters C and D which, from Tables F.1 and F.2, showed a random variation. No simple mathematical relationship was found. Examples are:

$$D = \frac{C\,(A\,\beta + b\,k\,(\beta\,\rho_s^{\,2} - \alpha\,\rho_s))}{b\,k\,\rho_s\,B\,\phi}$$

or:

$$= \frac{C\,(A + b\,k\,\alpha_1\,\alpha_2)}{b\,k\,\alpha_1\,(\alpha_2 + \rho_o)}$$

A, B and ϕ are themselves all functions of the other parameters and no guidance can be given as to the reasonable values of C or D from the above relationships.

5.3 EMPIRICAL ANALYSIS

Empirical analysis is based on the overall impression gained from a complete set of data. For any set of data, care must be taken that the data are representative. For this reported experimental work several of the constant stress creep tests were repeated under identical physical test conditions but with not necessarily identical material, there being 16 batches of material cast. An example of this is shown in Figure A.7 for a creep stress of 517 MN/m^2. The creep strain-time data are identical up to 0.3% when the specimen in test N14 failed. In this case, creep strain-time data is repeatable but creep rupture times are unreliable.

Several test conditions were repeated with specimens from different casts and, in general, there was good repeatability in the shape of the creep strain-time curves plotted on a linear basis. However, on a logarithmic basis, there was an overlap in some cases at the very low

strain levels (< 0.01%), as shown in Figure A.8. In this particular case the material for the tests at 750°C came from seven different casts. In the very low creep strain range, there is also the possibility of some experimental error as the creep strain has been defined as the strain after the total load was applied. Thus, some anomalies may appear from the initial visual inspection of the data but only more detailed analysis will show whether these are regular or not.

Most phenomenological approaches to curve fitting rely on the experimental creep curves having some basic geometric similarity, or in the case of the Graham-Walles analysis (see Section 1.6), the summation of geometrically similar terms.

In Section 4.2.1 it was shown that for the directionally solidified material there was no geometric similarity to cover all the creep strain-time data. However, some individual parameters may be amenable to empirical analysis, such as the time to a specific strain, the time to rupture or the steady-state creep rate. These types of parameters are often given stress and temperature functions, as was discussed in Section 1.6.

The prime one used in the present analysis is the Dorn parameter, θ. This is defined by:

$$\theta = F(\sigma) = t \exp \frac{-Q}{R\,T} \qquad (5.11)$$

where t = a time

Q = an activation energy

R = gas constant

T = absolute temperature (in K)

$F(\sigma)$ = function of the applied stress

The stress function is not specifically defined and two simple

functions have been compared for the experimental data. These are the power-law and exponential stress functions, as defined by:

Power-law: $$F(\sigma) = a_1 \sigma^n \tag{5.12}$$

Exponential law: $$F(\sigma) = a_2 \exp(b\sigma) \tag{5.13}$$

where a_1, a_2 and b are constants independent of temperature.

The first experimental parameter considered is the time to rupture as this may be of prime importance in practical engineering applications. Figures 5.6 and 5.7 show, respectively, the experimental data plotted on a power-law and an exponential stress basis. Both applications show a good fit, although there is some scatter. This is to be expected as the point of fracture was at different stages of the general creep curve.

For the power-law fit (Figure 5.6), it is seen that there is not a unique value for n but varies from 8 in the low stress region to almost 20 in the high stress region. For the experimental stress function (Figure 5.7), a constant value of 0.029 $(MN/m^2)^{-1}$ is found for b with the exception of tests at 650°C.

As the shape of the curves for both stress law fits appears to be independent of temperature, then all individual curves should be capable of being superimposed onto one master curve. This is shown for the power-law fit in Figure 5.8.

Using the temperature function described in equation (5.11), the value of the activation energy, Q, may be obtained from the gradient of the natural logarithm of the time to rupture against $1/T$ at constant stress levels. As experimental data was not obtained at all stress values, the times to rupture used have been found from smooth curves drawn through the experimental data. These are indicated in Figure 5.9, together with the

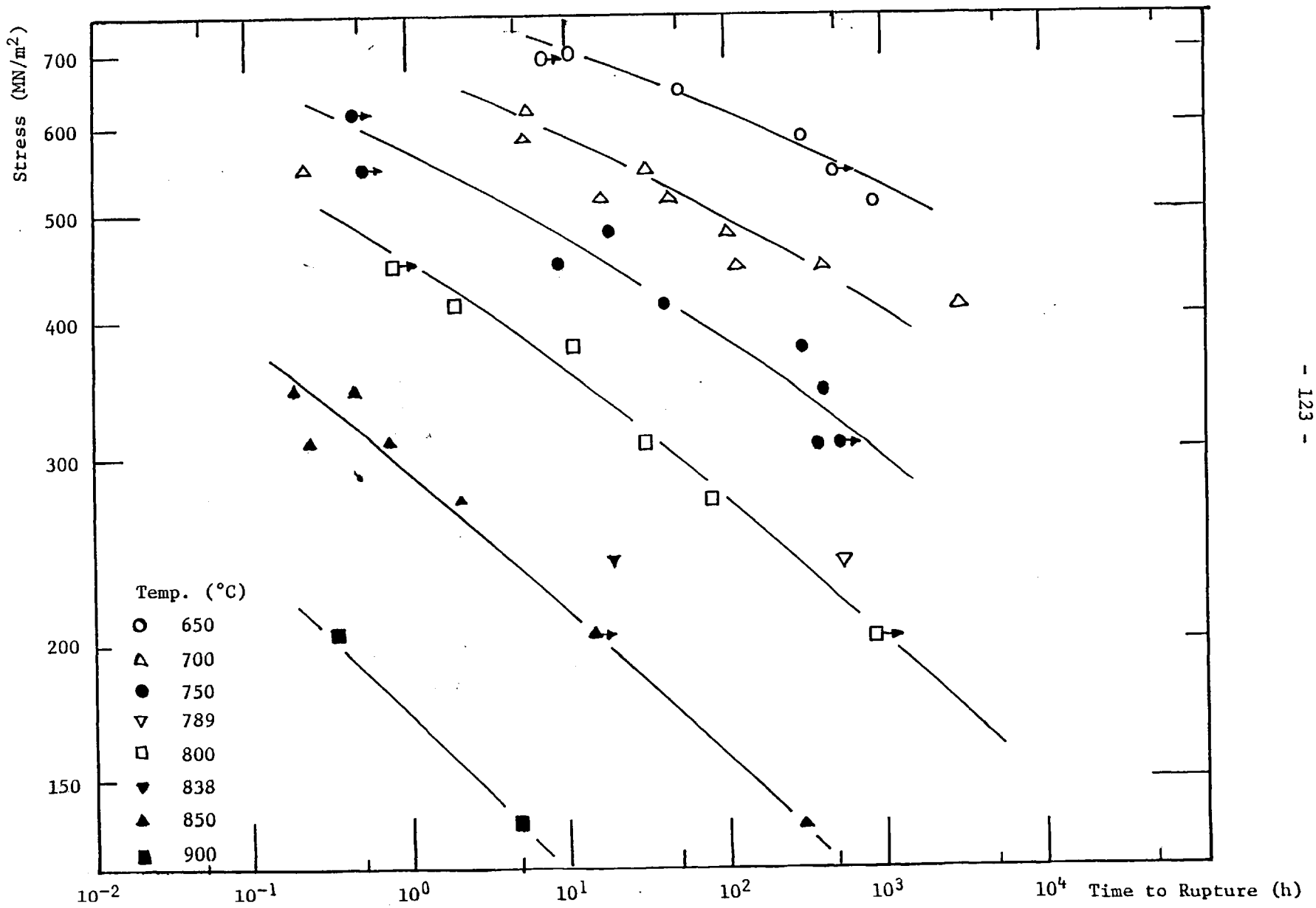

Figure 5.6: Stress dependence of time to rupture, t_R. Arrows indicate unbroken specimens.

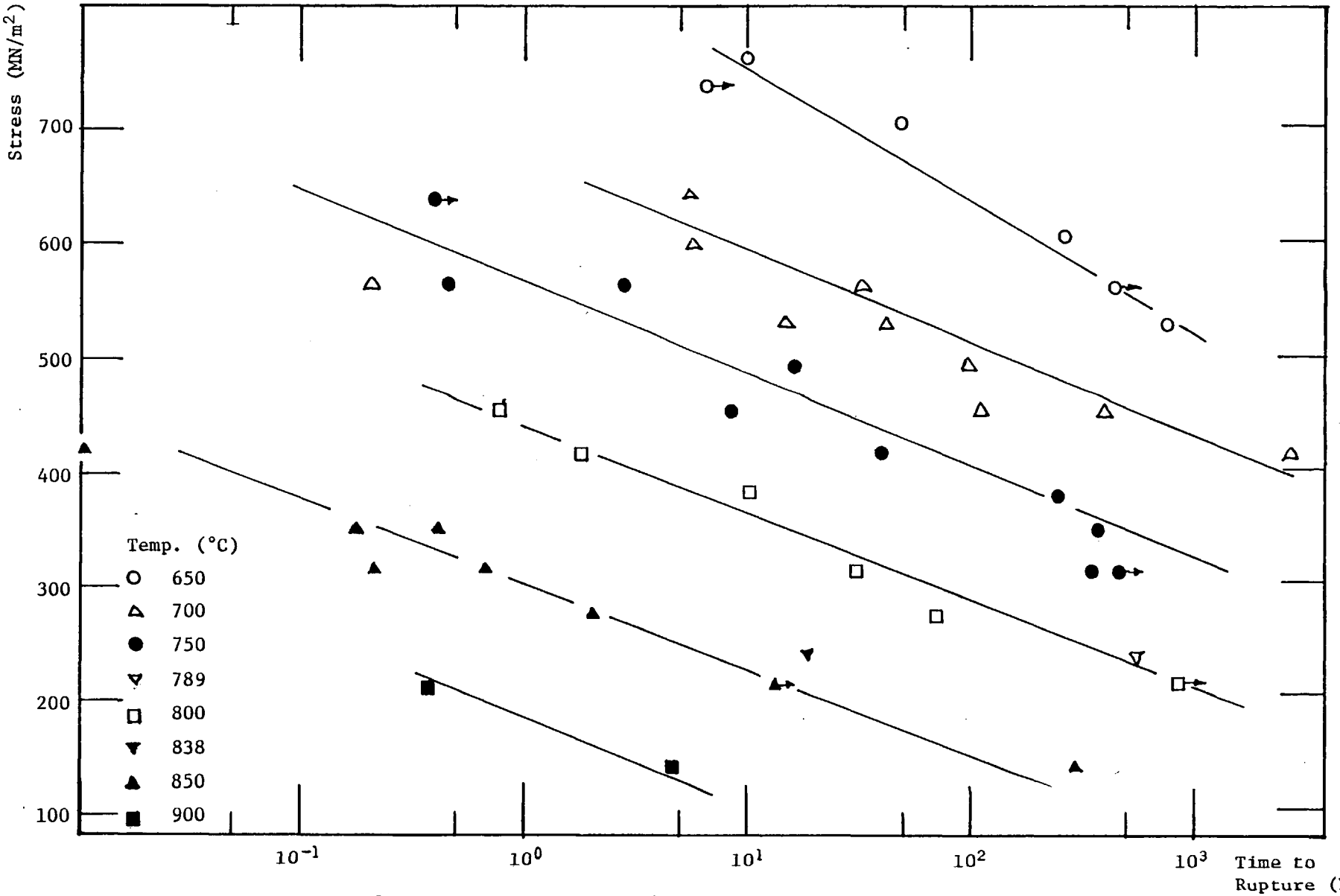

Figure 5.7: Stress dependence (exponential law) of time to rupture, t_R

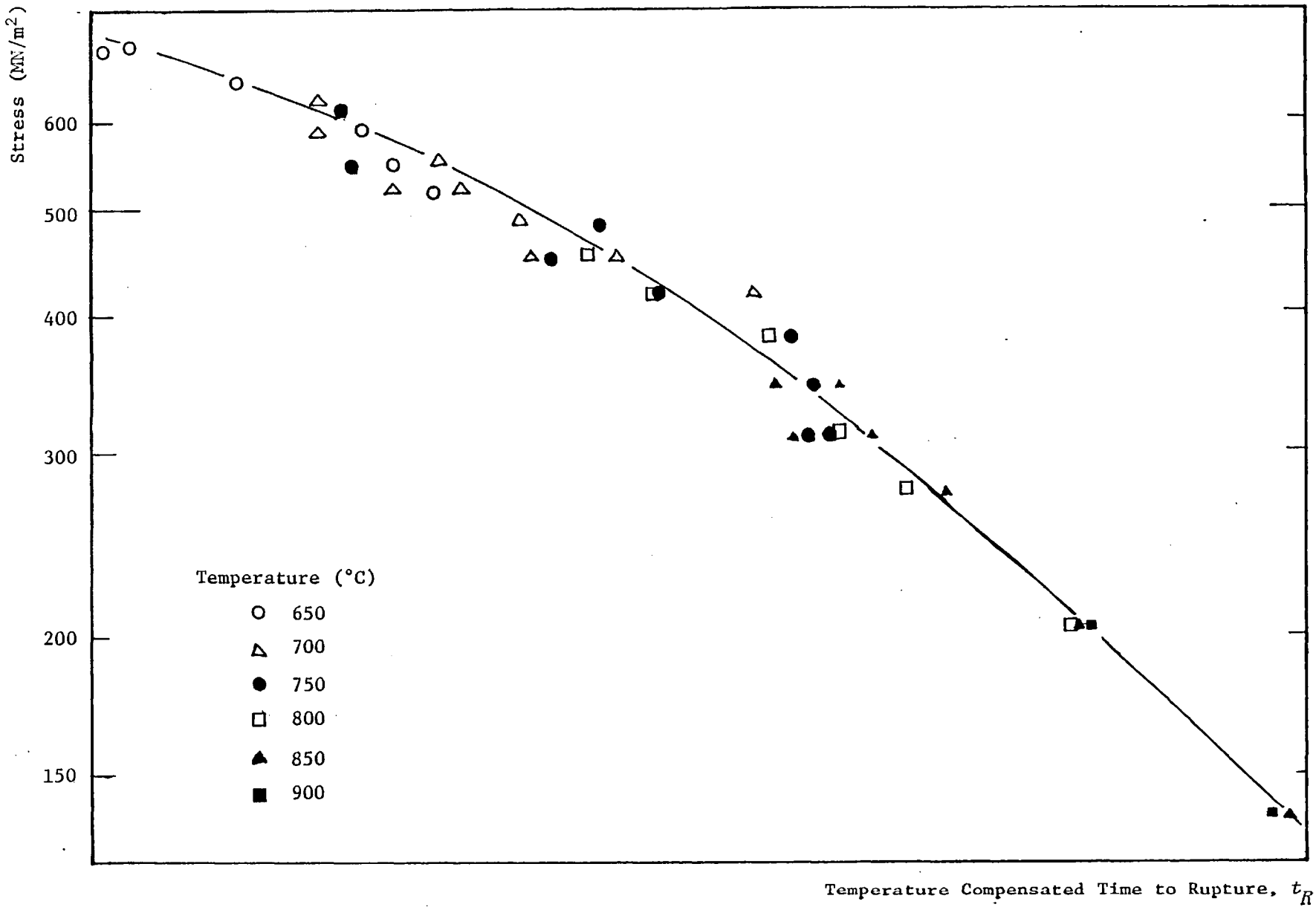

Figure 5.8: Unification of time to rupture functions

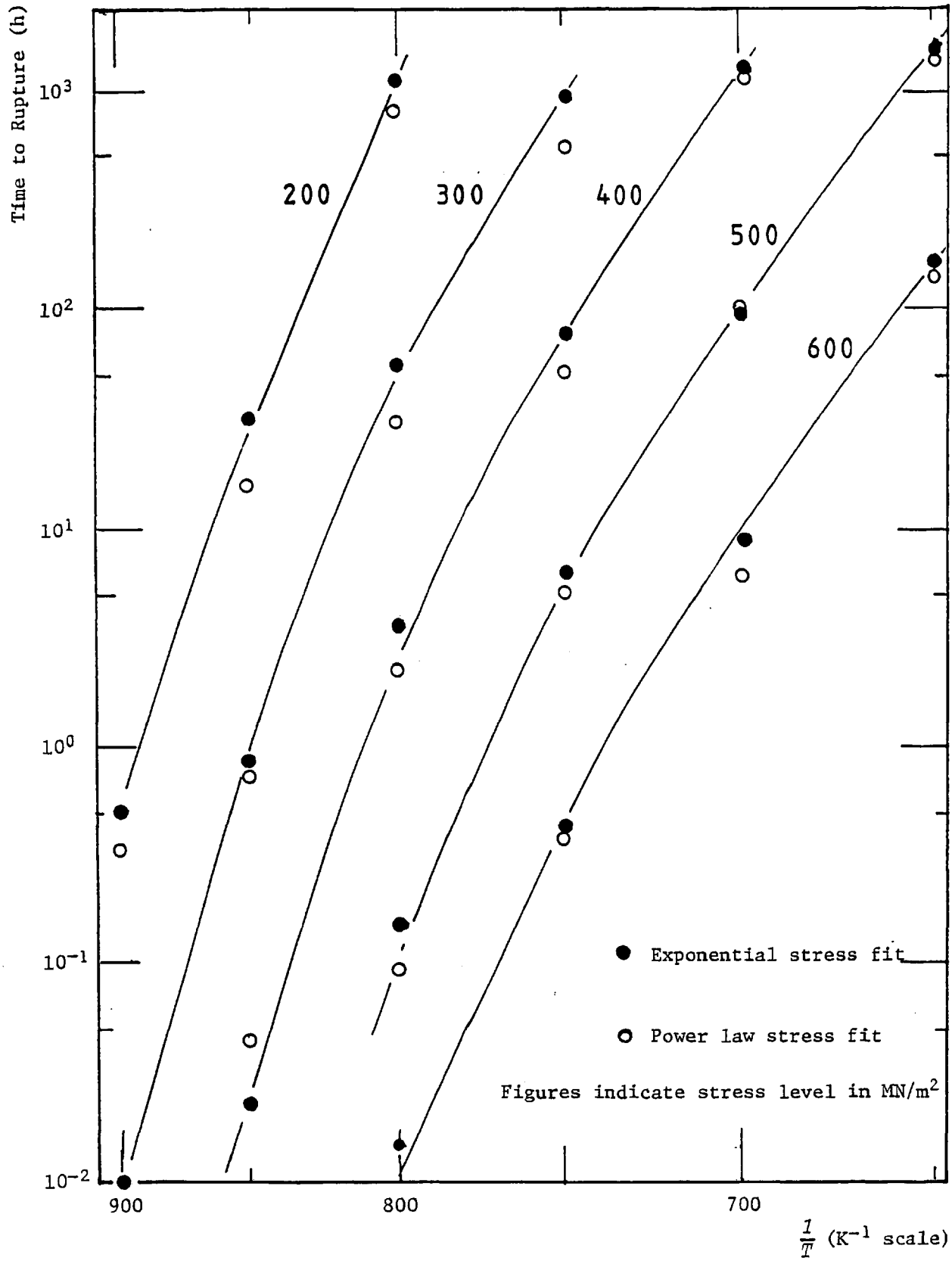

Figure 5.9: Arrhenius plot of time to rupture fitted by exponential and power stress laws

stress level. It is seen that the gradients are not constant over the complete temperature range tested but over the range 650°C to 800°C almost constant values occur. The value of the activation energy, Q, is derived from the gradient and thus a least squares analysis has been used to find the value of the best slope through the predicted points. In Figure 5.9, only a single smooth curve for each stress level has been shown. Values of Q so obtained are listed in Table 5.1.

TABLE 5.1

Activation Energy, Q, for the Time to Rupture over the Temperature Range 650°C to 800°C

Stress Level (MN/m^2)	Q (kJ/mol)	
	Power-Law Fit	Exponential Law Fit
350	489	533
400	482	533
500	488	533
550	511	532
600	521	533
650	-	519
Mean	498	530

It is seen that there is no significant stress dependence for the value of Q and the difference in mean values for the two stress functions is small.

A similar analysis has been performed for the time to 0.1% creep strain and the time to 2% creep strain. The 0.1% value was chosen as this is a frequently used limit of creep strain to be accumulated in

practical engineering applications under high stress conditions, e.g. gas and steam turbines. The 2% value was chosen as this was a strain level reached in the majority of the creep tests before fracture and yet was still in the "secondary" stage of creep (area C of Figure 1.1).

The power-law stress fit is shown in Figure 5.10 for the time to 0.1% creep strain. Below the yield stress, which lies in the range 400 MN/m^2 to 500 MN/m^2, there is now much less scatter in the data compared with the time to rupture data. However, above the yield stress range, it is difficult to determine a temperature and stress dependence. This may well be due to the fact that the total plastic strain on loading for stress levels which exceeded the yield stress was, in many cases, in excess of 0.1%. Creep strain has been defined as strain accumulated after all the load was applied and thus may exclude some creep strain which occurs during the loading period. This would suggest that the plotted values are over-estimates of the time to 0.1% creep strain. If this is so, then a very high value of the stress exponent will be operating at the higher stress levels. Below the yield stress, a value for the stress exponent of 7.3 is found.

The same deviation at high stress levels occurs when the time to 0.1% creep strain is plotted on an exponential stress law basis. In this case, the value of the gradient, b, also is a function of the stress level.

A similar temperature dependence analysis as for the time to rupture has been carried out but only for the test temperatures 700°C, 750°C and 800°C at stresses below 500 MN/m^2, the yield stress level. Values are given in Table 5.2.

The time to 2% creep strain provides a set of data covering the whole test range of stress and temperature. For the power-law stress fit (Figure 5.11), it would appear that the same stress function can be fitted to each temperature. This was confirmed in a similar plot to Figure 5.8,

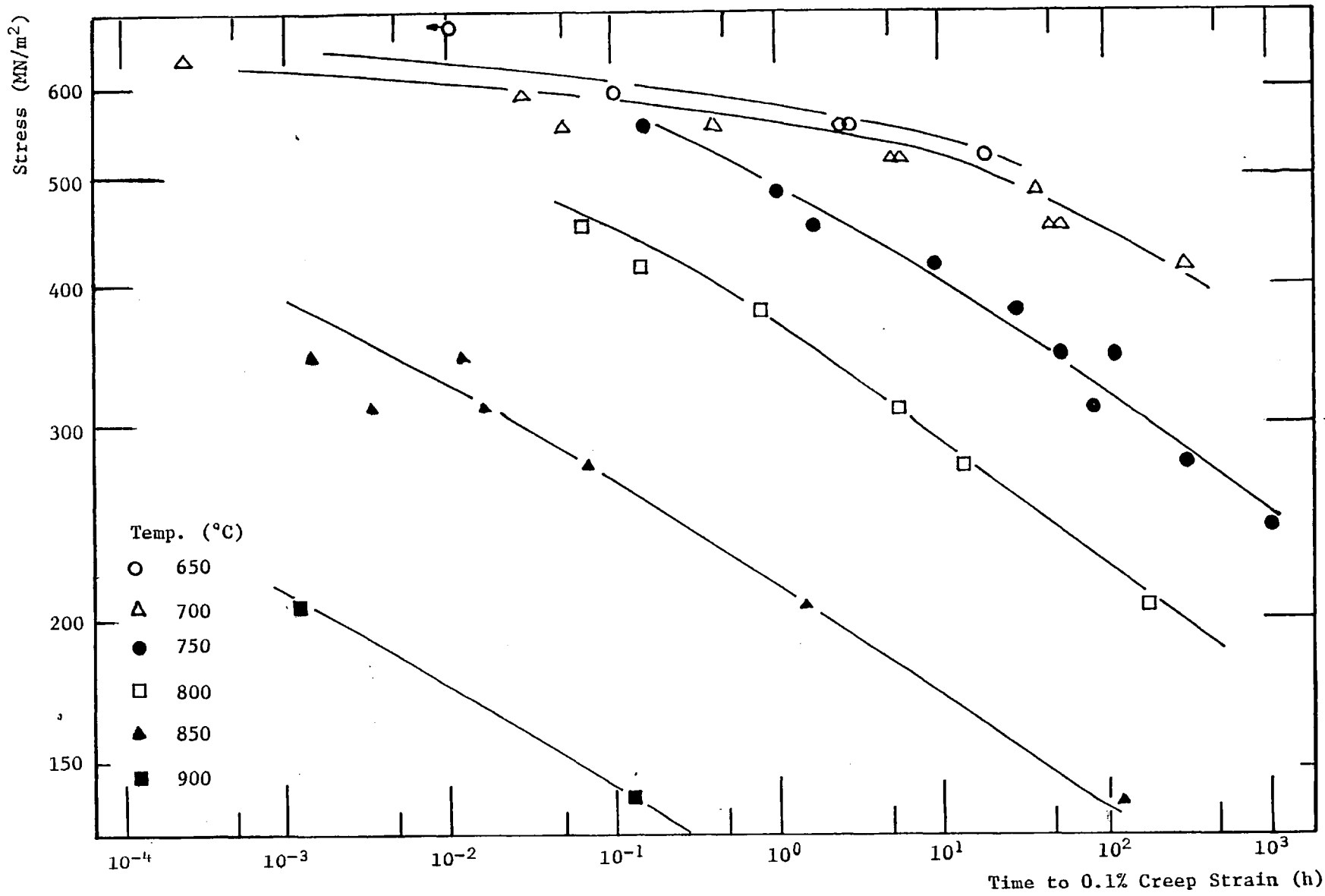

Figure 5.10: Stress dependence of time to 0.1% creep strain

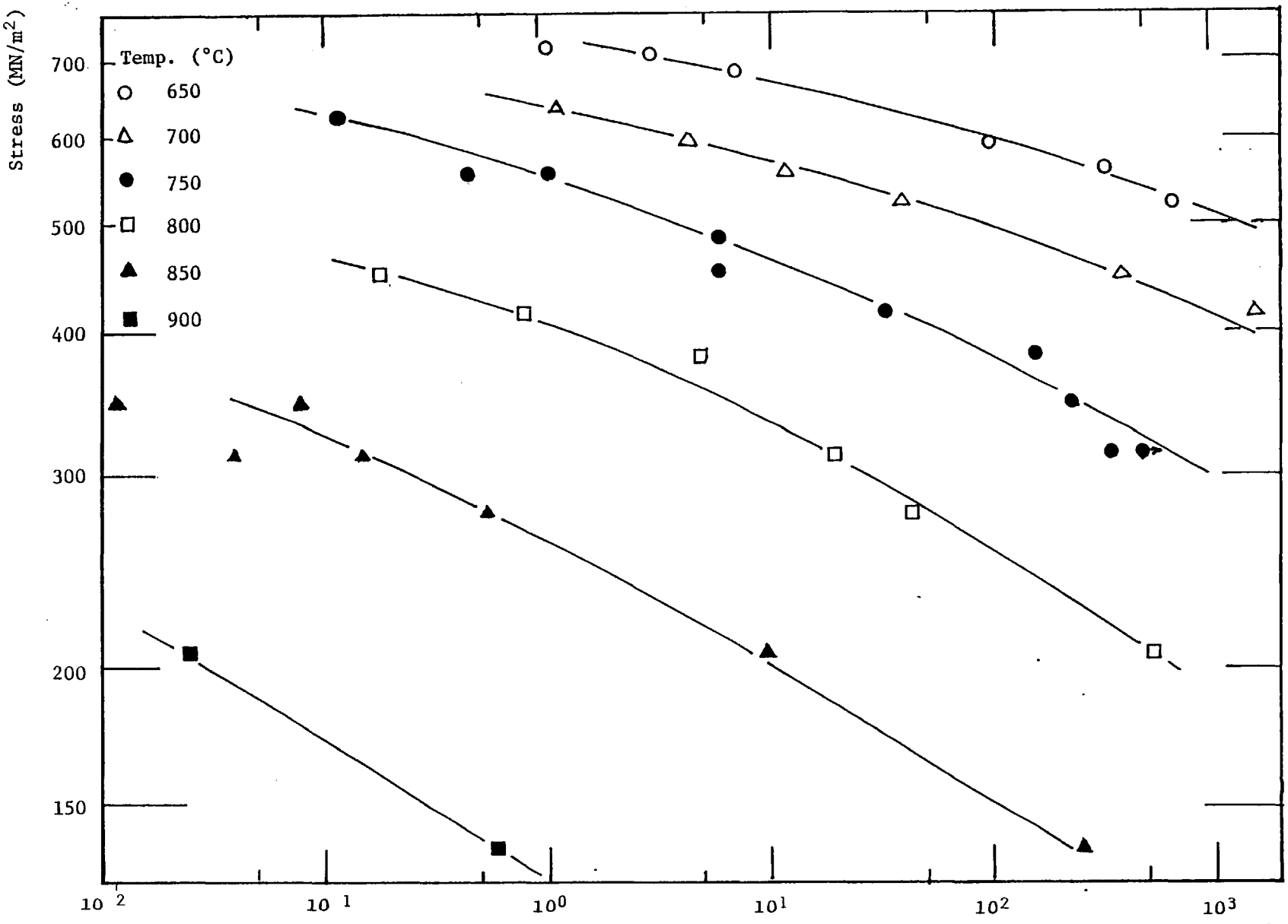

Figure 5.11: Stress dependence of time to 2% creep strain

TABLE 5.2

Activation Energy, Q, for the Time to 0.1% Creep Strain in the Temperature Range 700°C to 800°C

Stress Level (MN/m^2)	Q (kJ/mol)	
	Power-Law Fit	Exponential Law Fit
300	606	574
350	610	589
400	612	599
500	641	622
Mean	617	597

although the small degree of overlap at the same stress level makes this task difficult. The value of the stress exponent, n, in Figure 5.11 varies from 4 at stress levels below the yield stress to 12 at stress levels above.

On an exponential stress law basis (Figure 5.12), a good fit is found for all temperatures. However, at the temperatures 850°C and 900°C, a much higher value of b occurs.

The temperature dependence for the time to 2% creep strain has been analysed as before and the values are given below in Table 5.3.

A parameter often used to describe the creep phenomenon is the minimum creep rate, $\dot{\varepsilon}_s$, commonly called the secondary creep rate. Indeed, the stress and temperature functions used so far in this analysis were primarily developed for this parameter. For the experimental creep tests on the directionally solidified material, however, the secondary creep rate was not necessarily the minimum creep rate. Instead, it would be more useful to refer to a steady-state creep rate. The various shapes of creep strain-

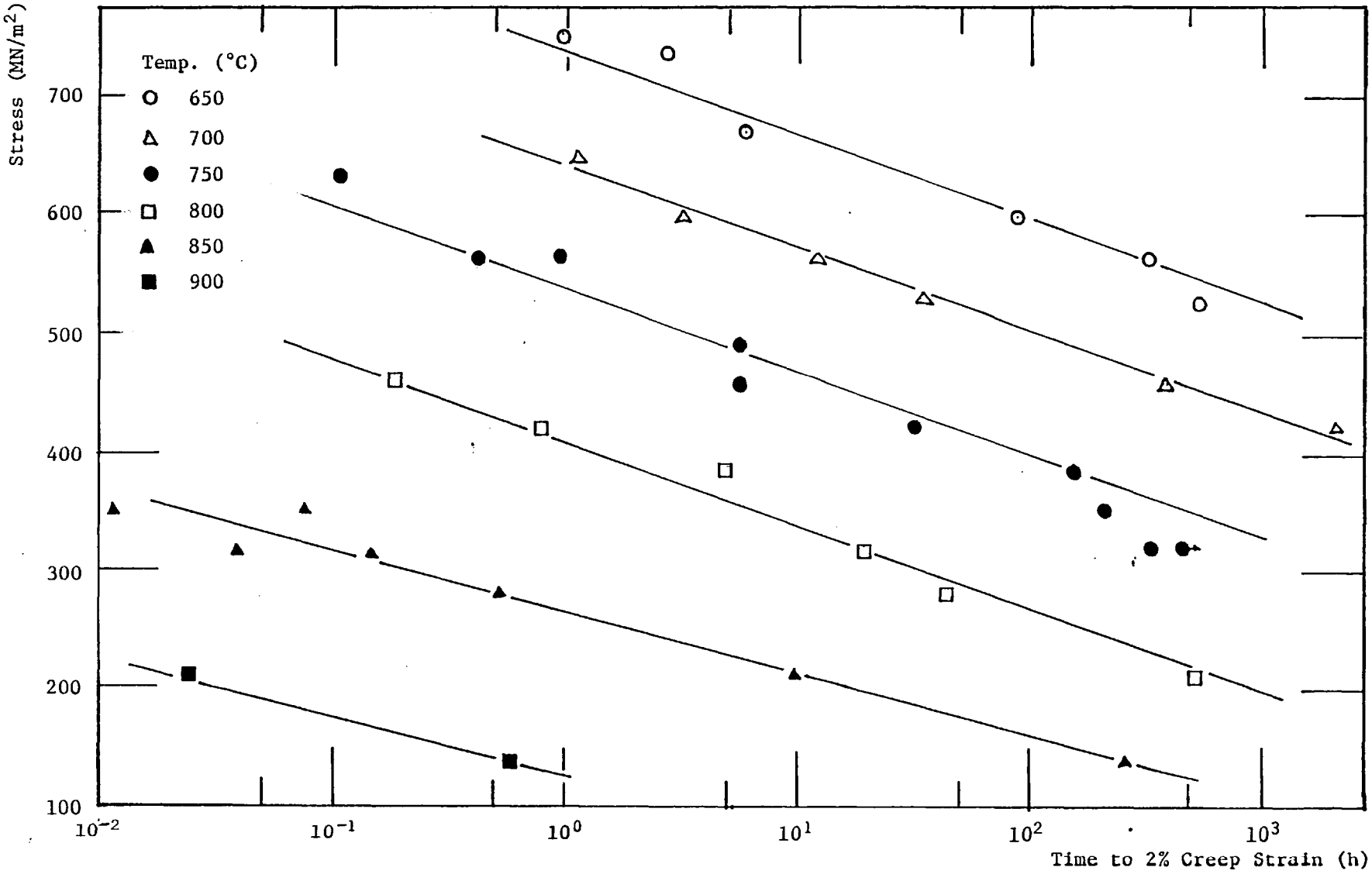

Figure 5.12: *Stress dependence (exponential law) of time to 2% creep strain*

TABLE 5.3

Activation Energy, Q, for the Time to 2% Creep Strain in the Temperature Range 650°C to 900°C

Stress Level (MN/m^2)	Q (kJ/mol)	
	Power-Law Fit	Exponential Law Fit
300	611	628
350	551	639
400	601	637
500	513	578
600	484	551
Mean	552	606

time plots have steady-state creep rates at different parts of the curve and these were indicated in Figure 4.5. It is noticed that for the tests at 800°C when curves of type 1 predominated the steady-state creep rate has been defined as the constant rate covering the creep strain region 1% to 6%. This region was the dominant area in both time and strain.

The values of $\dot{\varepsilon}_s$ so defined are plotted in Figures 5.13 and 5.14 on a power-law and an exponential stress law basis, respectively.

The power-law fit (Figure 5.13) indicates that a value of the exponent n of 10 covers the whole of the data at 650°C, 700°C and 750°C, but at 800°C, 850°C and 900°C no fixed value can be found. The two low stress level points for the data at 750°C appear to fit very well but the values for these two conditions were taken at a very low strain level, approximately 0.1%, due to premature failure of the specimens outside the gauge length. Thus, it could well be that the true steady-state creep rate, as defined

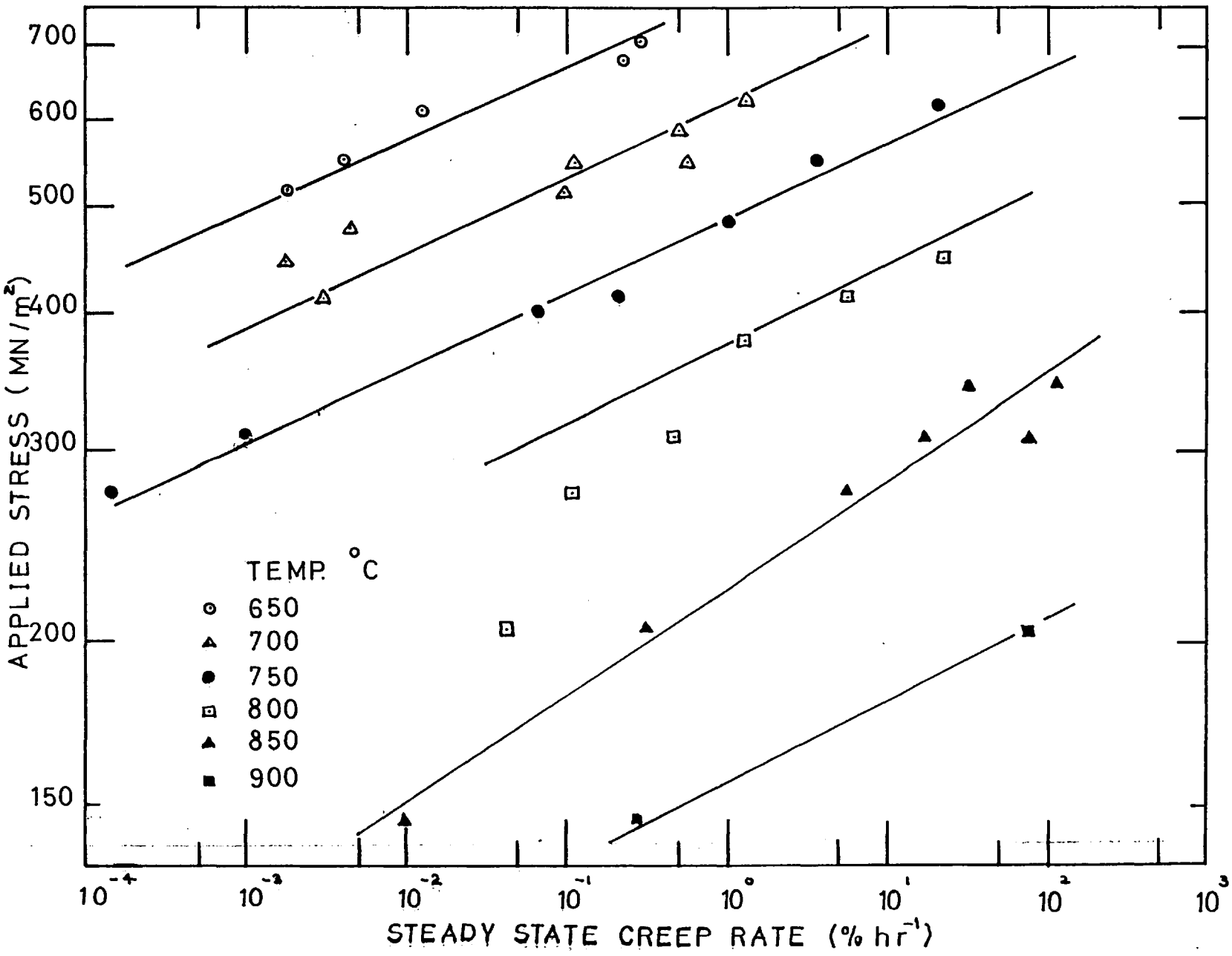

Figure 5.13: Stress dependence of steady-state creep rate

above, is higher than the values plotted. This indication was also found from the analysis in Section 5.2.

The exponential stress law fit (Figure 5.14) tends to confirm the above suggestion as it is now seen that the two tests at 276 MN/m^2 and 310 MN/m^2 do not give a constant value for the slope at 750°C. The plotted values would appear to be underestimates. The data for 650°C gives a very good linear relationship with a value for b of 0.028 $(MN/m^2)^{-1}$. However, there is difficulty in fitting this value of slope to the data at 800°C. Values of b for the data at 850°C and 900°C are also higher, approximately 0.036 $(MN/m^2)^{-1}$ and 0.083 $(MN/m^2)^{-1}$, respectively.

Because of the variation in the value of the exponential stress law parameter, b, the temperature dependence analysis has been made for two ranges of temperature, 650°C to 800°C and 650°C to 750°C. Activation energies found are listed below in Table 5.4.

TABLE 5.4

Activation Energy, Q, for the Steady-State Creep Rate in the Temperature Ranges 650°C to 800°C and 650°C to 750°C

Stress Level (MN/m^2)	Q (kJ/mol)			
	Temperature Range 650°C to 800°C		Temperature Range 650°C to 750°C	
	Power-Law Fit	Exponential Law Fit	Power-Law Fit	Exponential Law Fit
300	-	683	-	-
400	659	682	533	-
500	601	614	536	549
550	593	-	527	-
600	591	-	534	545
Mean	610	661	533	547

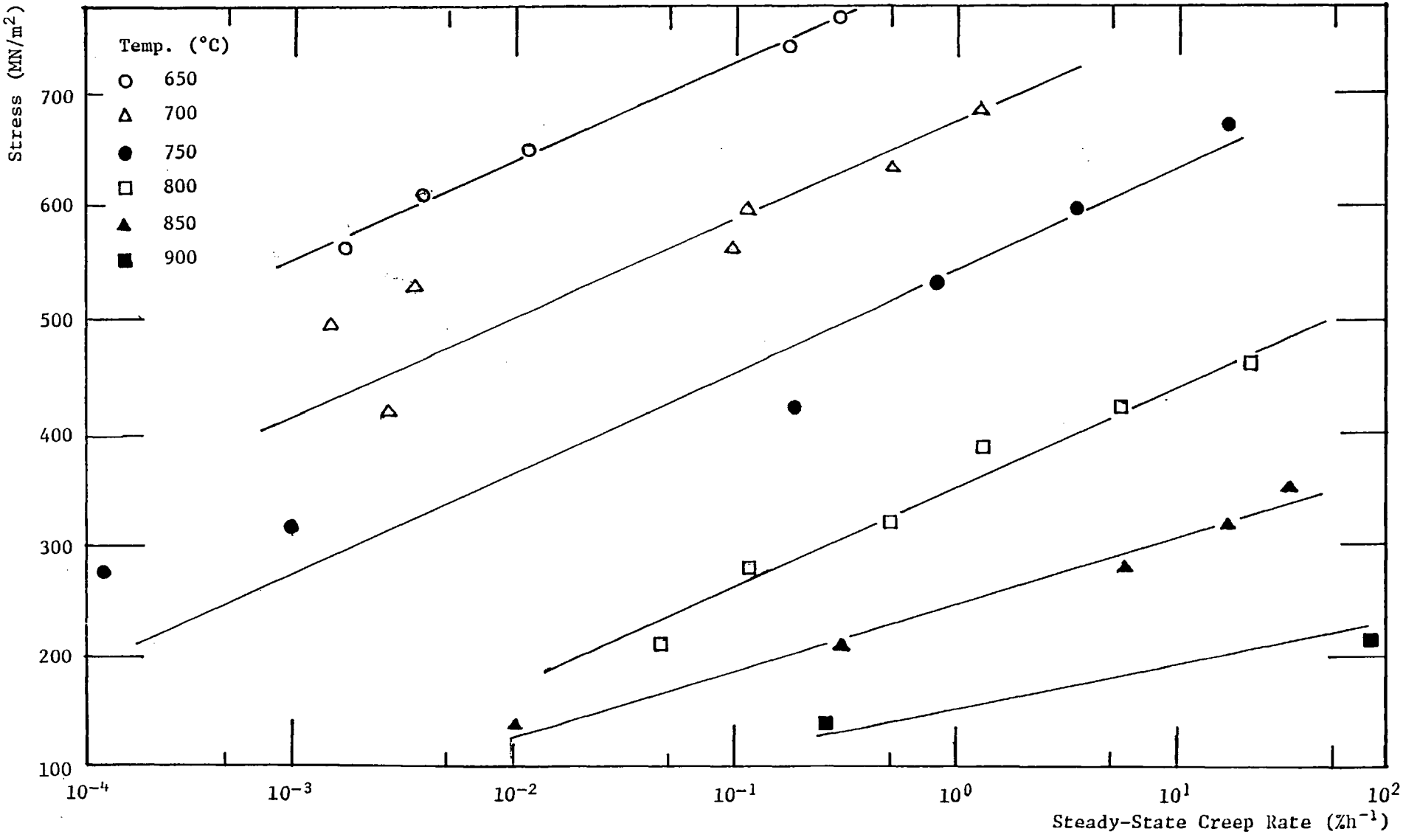

Figure 5.14: Stress dependence (exponential law) of the steady-state creep rate

5.3.1 Discussion

A summary of the mean values for the stress and temperature function parameters found from the analysis in Section 5.3 are given below in Table 5.5.

TABLE 5.5

Values of Activation Energies and Stress Parameters

Experimental Parameters	Power Stress Law Fit		Exponential Stress Law Fit	
	Activation Energy (kJ/mol)	n	Activation Energy (kJ/mol)	b $((MN/m^2)^{-1})$
Time to 0.1% creep strain	617	7-35	597	0.033
Time to 2% creep strain	552	4-12	606	0.033
Time to rupture	498	8-20	530	0.029
Steady-state creep rate*	610	10	661	0.028
Steady-state creep rate†	533	10	547	0.028

* Temperature range 650°C to 800°C
† Temperature range 650°C to 750°C

Thus, there is not a constant value of an activation energy for each stage of the creep deformation. This could suggest that more than one deformation process is operating. However, the fact that the value of activation energy is also a function of the stress law fitted may suggest that the true value has not been found, but lies in the range 480 kJ/mol to 630 kJ/mol.

The activation energy for creep in simple metals is often linked to the activation energy for the self-diffusion in the metal. For the experimental alloy the predominant base element is nickel and the value of the self-diffusion of nickel is 278 kJ/mol. Thus, the activation energy for creep found from the above analysis is approximately

twice the self-diffusion value for nickel.

Webster & Piearcey [64] found a similar effect for the creep properties of the directionally solidified alloy Mar M-200. The activation energy found for the steady-state creep rate of that alloy was 557 kJ/mol. This value, being approximately twice that for the self-diffusion of nickel, was explained by the suggestion that both the dislocation velocity and the dislocation density each had a temperature dependence similar to that for self-diffusion. The steady-state creep rate is a function of the product of the dislocation density and velocity and hence the temperature dependence found.

A similar reasoning could be applied to the values of the activation energies found for the creep parameters of the experimental directionally solidified material, as both the dislocation density and the dislocation velocity are predicted to change during the creep process.

The choice between the two simple stress laws, the power-law and the exponential law, has been shown to be very dependent on the parameter being represented. For example, for the parameter "time to rupture" the exponential stress law gives a unique value of b, but for the parameter "time to 2% creep strain" the value of b changes for temperatures greater than 800°C.

For the power-law approach, it would appear that a temperature dependence of the stress exponent n does not exist but, in this case, the value is dependent on the stress level, changing values at a test stress of approximately 350 MN/m^2.

Thus, it is difficult on an experimental basis to completely verify either form of approach. Some justification may then be made for the more difficult approach of Garofalo [65] where the two stress functions are combined to give:

$$const = f(\varepsilon, t, T) \times \sigma^{n-1} \sinh b\sigma \tag{5.14}$$

The values of the parameters n and b in the above are those obtained from the power-law and exponential law approaches in the low and high stress ranges, respectively.

Taking the parameter "time to 2% creep strain", the values for n and b, obtained as above, are 7.3 and 0.033 $(MN/m^2)^{-1}$, respectively. The expected stress function will then be in the form:

$$P(\sigma) = \sigma^{6.3} \sinh (0.033\ \sigma) \tag{5.15}$$

As both the power-law and exponential law approaches fitted in the appropriate stress ranges, it would be expected that the above stress function would adequately cover the complete range. However, for lower values of experimental stress, the hyperbolic sine function does not approximate to the value of $b\sigma$, i.e. for the lowest experimental stress, σ = 138 MN/m^2, $b\sigma$ = 4.2, and $\sinh b\sigma$ = 64.7.

Thus, the stress parameter as described by the above equation would not adequately cover the complete stress range. A similar reasoning is found using the other parameters, time to rupture and steady-state creep rate. As a result of this, difficulty would arise in predicting intermediate temperature and long time data. It would be of interest to conduct some longer term, i.e. greater than 1000 h, constant stress creep tests to evaluate these complications on an empirical basis.

Some similarity in the stress and temperature dependencies shown in Table 5.5 could suggest that combined parameters may be formed. One pair of parameters that has been linked in this manner is the steady-state creep rate and the time to rupture. The relationship used is:

$$\dot{\varepsilon}_s \times t_R = constant \qquad (5.16)$$

The constant is assumed to be independent of stress and temperature.

Figure 5.15 shows the results for the experimental alloy. Individual experimental points are shown, together with the curve-fitted lines produced from the stress law fits. Both the power-law and the exponential stress law fits gave identical lines for the individual temperatures. The predicted data for tests at 650°C and 700°C coincided. Each of the lines drawn has a slope of -1. However, the constant in equation (5.16) is a function of the test temperature, as is shown below.

Test Temperature (°C)	Constant (% strain)
650 and 700	2.4
750	4.2
800	13.0

These values of the constant could be some measure of the predicted values of the strain at rupture. Experimental values are listed below.

Test Temperature (°C)	Rupture Strain (%)	
	Range	Mean
650	5 - 15	10
700	0.2 - 13	4
750	3 - 19	10
800	9 - 18	13
850	5 - 38	23

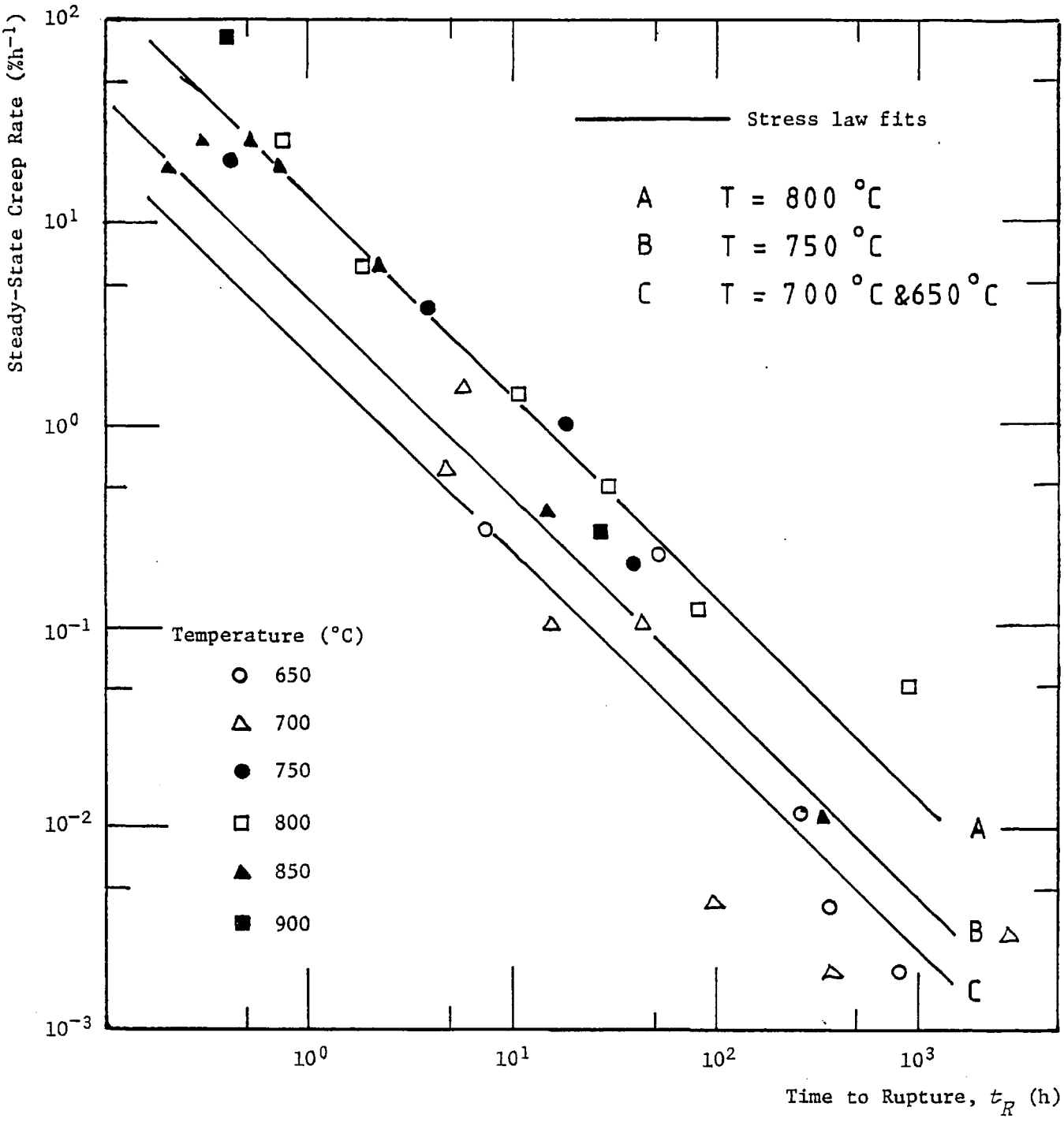

Figure 5.15: Relationship between experimental and fitted steady-state creep rate and time to rupture

The predicted values are thus generally lower than the experimental values. However, the trend in magnitudes is similar. It would be expected that predicted values are lower if the steady-state creep rate was the minimum creep strain rate since equation (5.16) takes no account of the "tertiary" or accelerating creep stage before fracture. This may be a significant part of the creep rupture strain. The values of the constant could be considered as the minimum strain at fracture. This is borne out by the experimental results, with the exception of the odd low ductility result at 700°C. The minimum values of rupture strain may then be used as a design criteria for components made from the experimental alloy.

5.4 EQUI-AXED GRAIN MATERIAL

5.4.1 Analysis of Constant Stress Creep Tests

In Section 4.3, it was noted that in only six out of the fifteen constant stress creep tests did fracture occur in the gauge length. In Section 2.3, the different geometry of the equi-axed grain test pieces was given and it was thought that the problem was either that of temperature distribution or of too small a difference in the diameters of the gauge length and the sections just outside.

Temperature control was more of a problem with the longer sections and temperatures outside the gauge length could be up to 10°C higher than the gauge length. (There was a smaller difference for the directionally solidified test pieces and only the odd test resulted in fracture outside the gauge length.)

To check on possible gauge length geometry effects, a test piece was centreless ground along the gauge length, reducing the diameter by 0.005 in (0.13 mm) and keeping within the tolerance of ±0.0005 in (±0.013 mm). This operation was carried out with the specimen in the

fully aged state. No additional heat treatment was given. Fracture still occurred outside the gauge length.

Examination of the fractures outside the gauge length showed intergranular fractures with the initiation on grain boundaries in almost a transverse plane to the stress axis. This corresponds to areas on the edge of the cast ingot, as shown in Figure 2.4. As grain boundaries are a weakness in creep, it is not unexpected that failures would occur in this manner.

The grain size in the equi-axed areas was comparatively large at approximately 3 mm diameter and may explain the low ductility at fracture, the maximum strain recorded at rupture being 0.87%. A longitudinal section of the gauge length for test N63E is shown in Figure 5.16, which confirms the intergranular failure and some large grains.

For commercial cast nickel base alloys used in gas turbine components, the grain size is dependent on the area of application. For aerofoil sections, the limit is set at 2 mm, whereas for discs the grain size can be 5 mm to 10 mm. Creep ductilities are not generally high but in the range 2% to 5%.

The form of the creep strain-time plots for most tests followed the normal primary and secondary stages (sections B and C of Figure 1.1) but at the failure point a sudden increase in creep strain and strain rate sometimes occurred. An example of this is shown in Figure 5.17, where for test N65E a creep strain of 0.017% was reached after 4.5 h and a sudden failure occurred at 4.95 h with a rupture strain of 0.30%. A repeat of this test, number N66E, did not show this sudden failure but after 20 h under stress, the recorded extension level began to reduce and failure occurred outside the gauge length at the top of the specimen after 30.6 h under stress. A large crack was also found outside

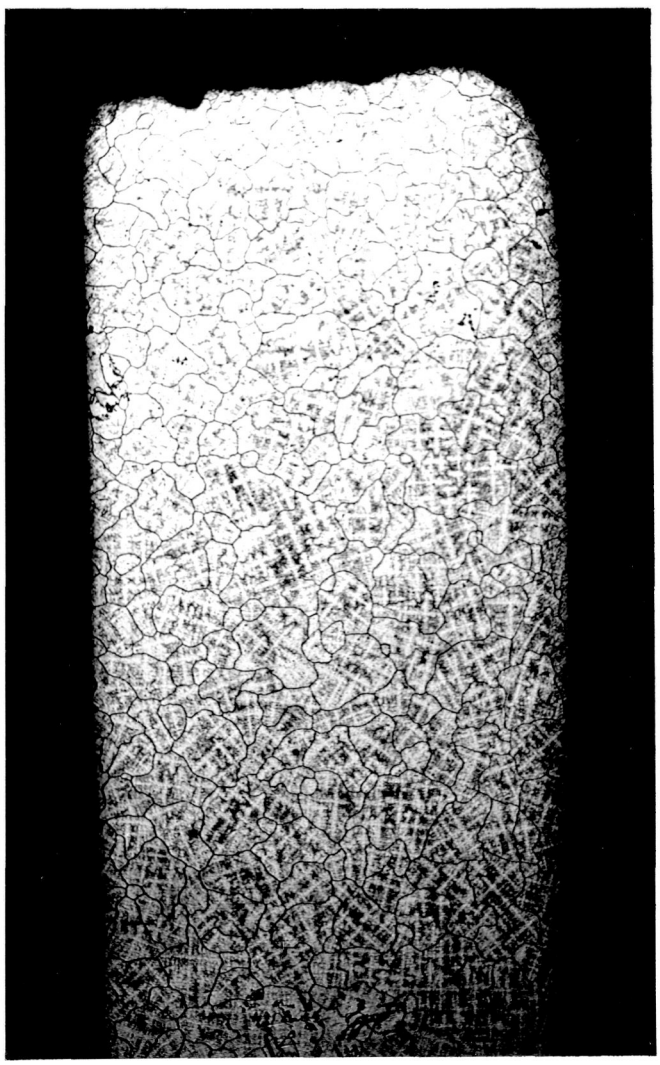

x10

Figure 5.16: Longitudinal section for test N63E

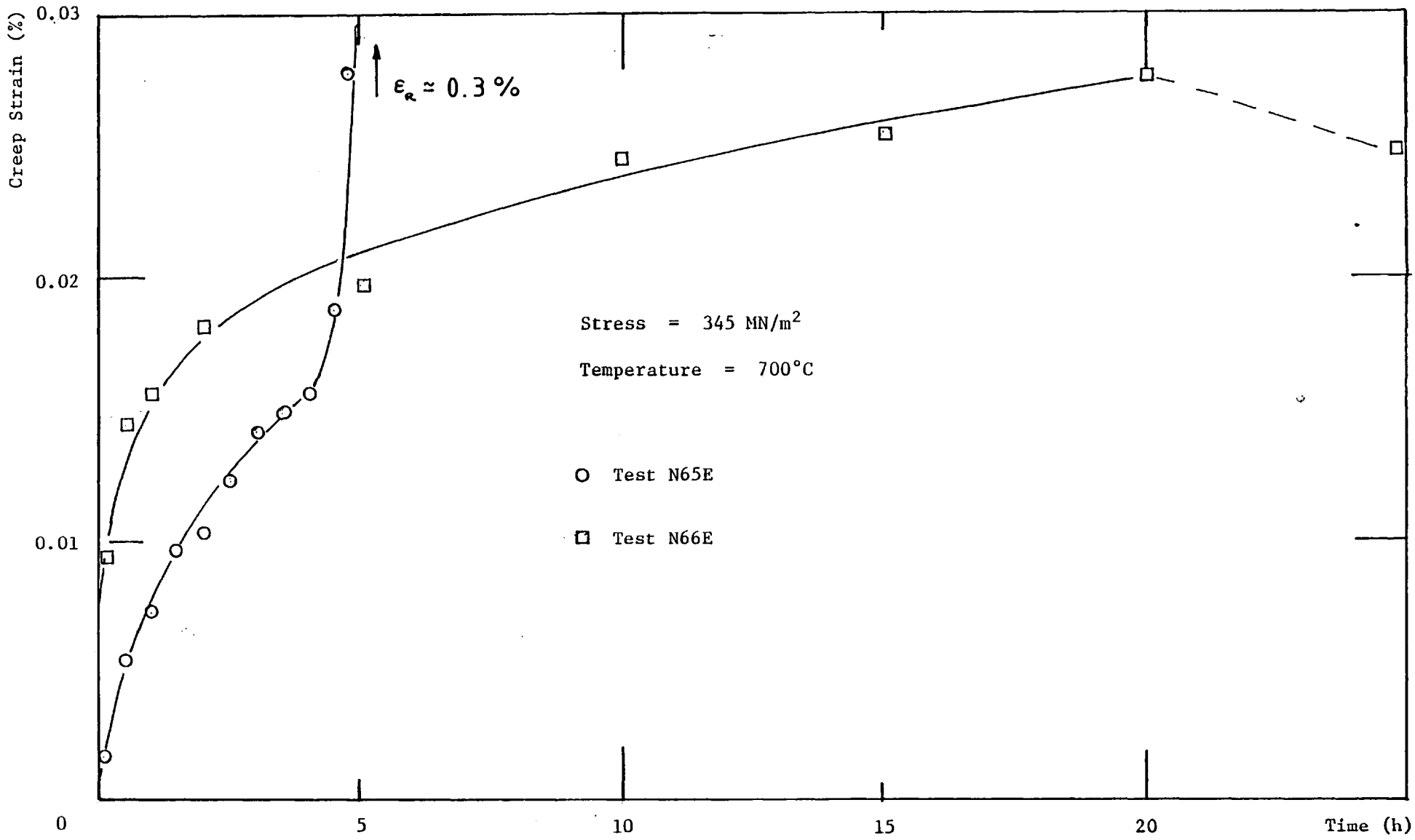

Figure 5.17: Creep strain versus time for equi-axed grain material

the gauge length at the bottom end of the specimen which had caused a rotation of the clamping shackles and interference with the extensometry. This would explain the apparent reduction in strain level being read from the single displacement transducer.

Another example of a sudden increase in creep strain rate is shown in Figure 5.18, where the creep stress was 483 MN/m^2. In this case, the rapid increase in creep strain occurred after approximately six minutes under stress, followed by a period of reduced creep strain rate before another rapid increase resulted in failure. The fracture surface suggested that for this particular test piece, there were only two or three grains across the transverse section. The initial failure was intergranular at two different points transverse to the stress axis before a final transgranular failure on a 45° shear plane. This could possibly explain the two-stage nature of the failure.

The general repeatability of the early stages of the creep strain curve was good, as is shown in Figure D.3 for the creep tests at 750°C.

Due to the premature ending of most of the creep tests, there are insufficient data for a complete analysis of the creep strain-time relationship. However, from the logarithmic plots in Appendix D, a power-law exponent of 1/3 would appear to be appropriate for the initial stages at the test temperatures 700°C, 750°C and 800°C.

A cross-plot of the time to 0.03% creep strain is shown in Figure 5.19. This may indicate an increase in the stress exponent at high stresses but, as for the directionally solidified material, at these high stresses yielding occurred on loading and some creep strain may have occurred in this stage which has not been accounted for.

The time to rupture data are plotted in Figure 5.20. Due to the few tests which failed inside the gauge length, no meaningful

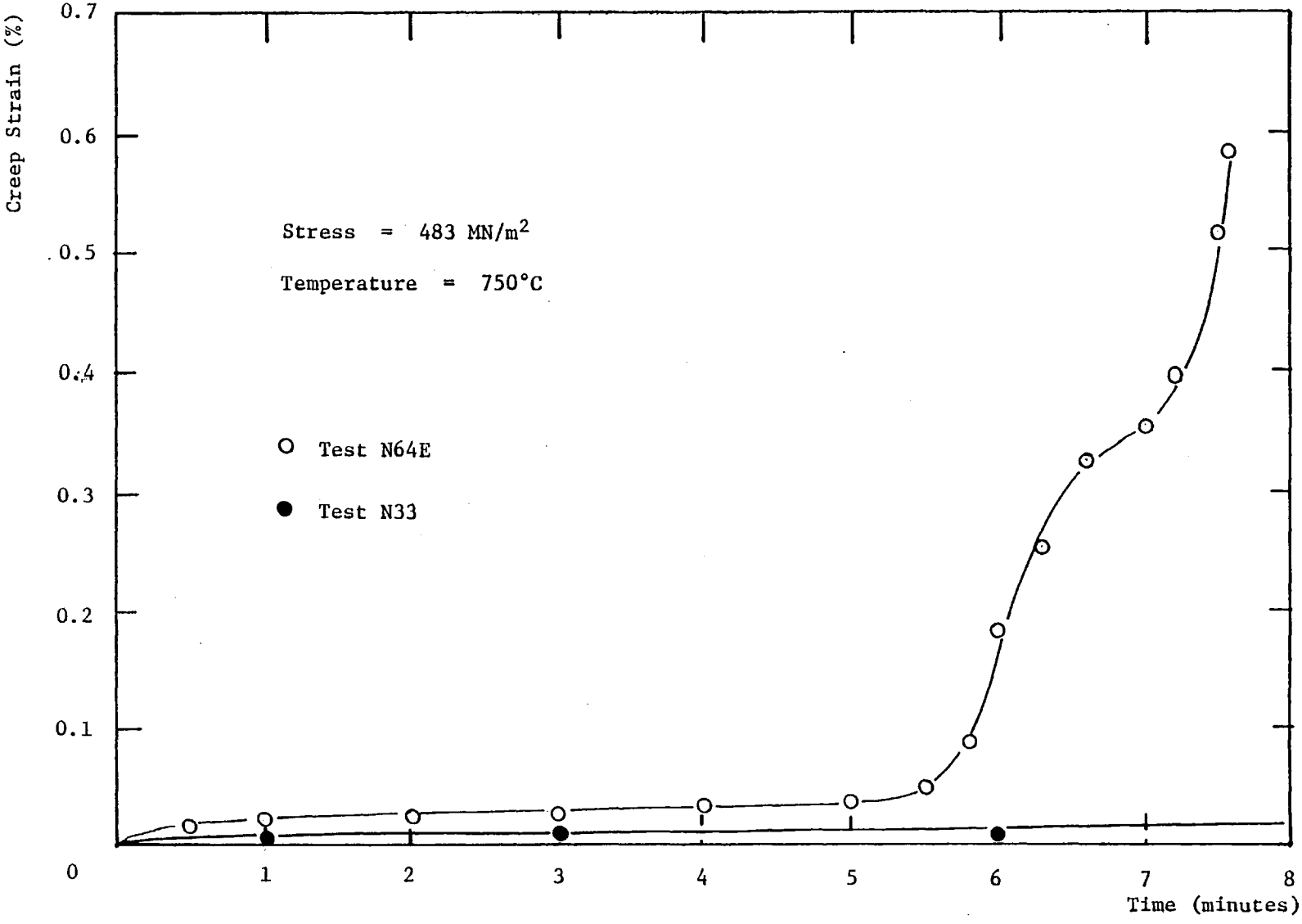

Figure 5.18: Creep strain versus time for equi-axed and directionally solidified grain forms

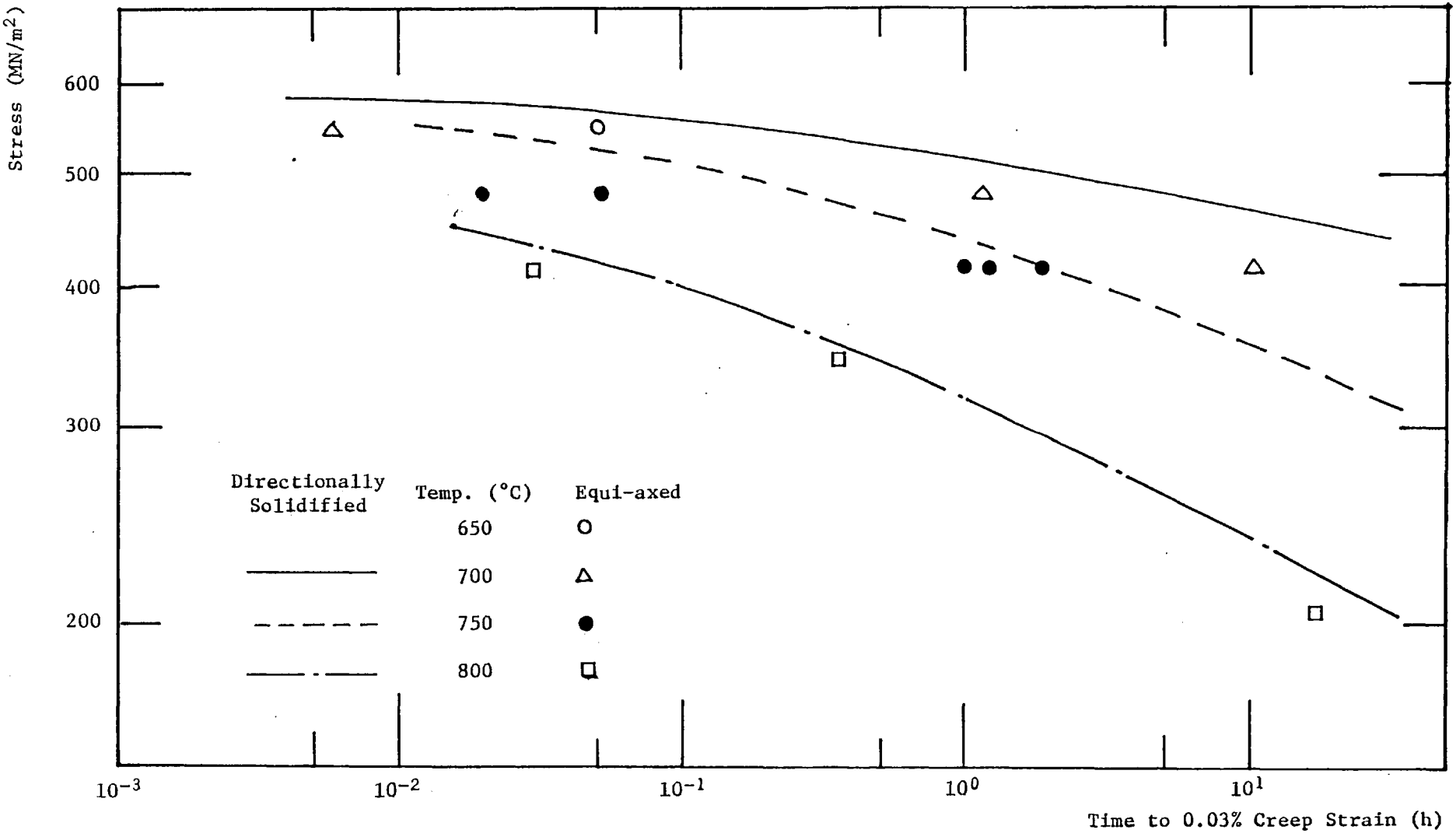

Figure 5.19: Stress dependence of time to 0.03% creep strain for directionally solidified and equi-axed grain forms

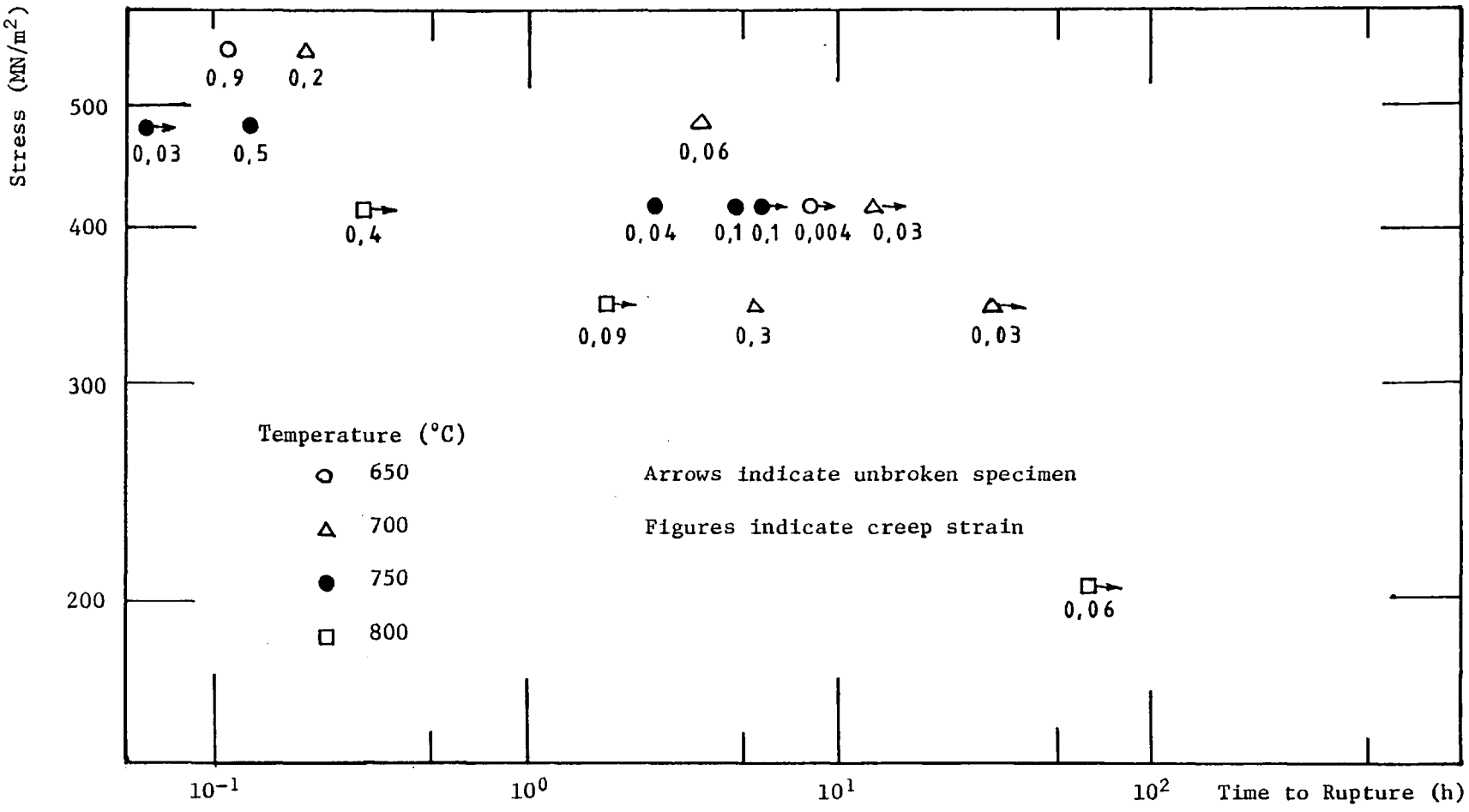

Figure 5.20: Stress dependence of time to rupture for equi-axed grain form

relationships between time, temperature and stress can be found.

5.4.2 A Comparison Between the Properties of the Directionally Solidified and Equi-Axed Cast Grain Structures

The main macro-structural features of the experimental alloy in its two forms have been featured in Sections 2.2, 2.3, 4.2.2 and 5.4.1. From these, it is seen that the reduction of predominant transverse grain boundaries to the applied stress axis, through direction solidification, clearly affected the creep fracture characteristics. For the directionally solidified form the short sections of almost transverse grain boundaries in the interdendritic areas were seen as initiators of final failure, whereas for the equi-axed form the grain boundaries were a main cause of failure. The actual grain size would appear to have had some influence on the failures for the equi-axed form but not for the directionally solidified form. For the equi-axed form, the low number of grains in the transverse section may have resulted in reduced creep lives and rupture strains.

As was explained in Section 4.3, a full set of creep data was not obtained for the equi-axed grain form. Thus, a direct full comparison between the properties of the experimental alloy in the equi-axed and directionally solidified forms cannot be made. However, there are sufficient data for the commercial wrought alloy Nimonic 80A to give some reasonable comparison.

Figure 5.21 shows the experimental creep rupture data for the cast material in both forms plus data for the wrought alloy from several sources [70,84,85,86,87]. The spread in data for the wrought alloy at 700°C and 750°C is due to the different sources presenting data in various forms. In references [84], [85] and [86], the rupture data are given in the form of the Larson-Miller parameter which does not allow for any

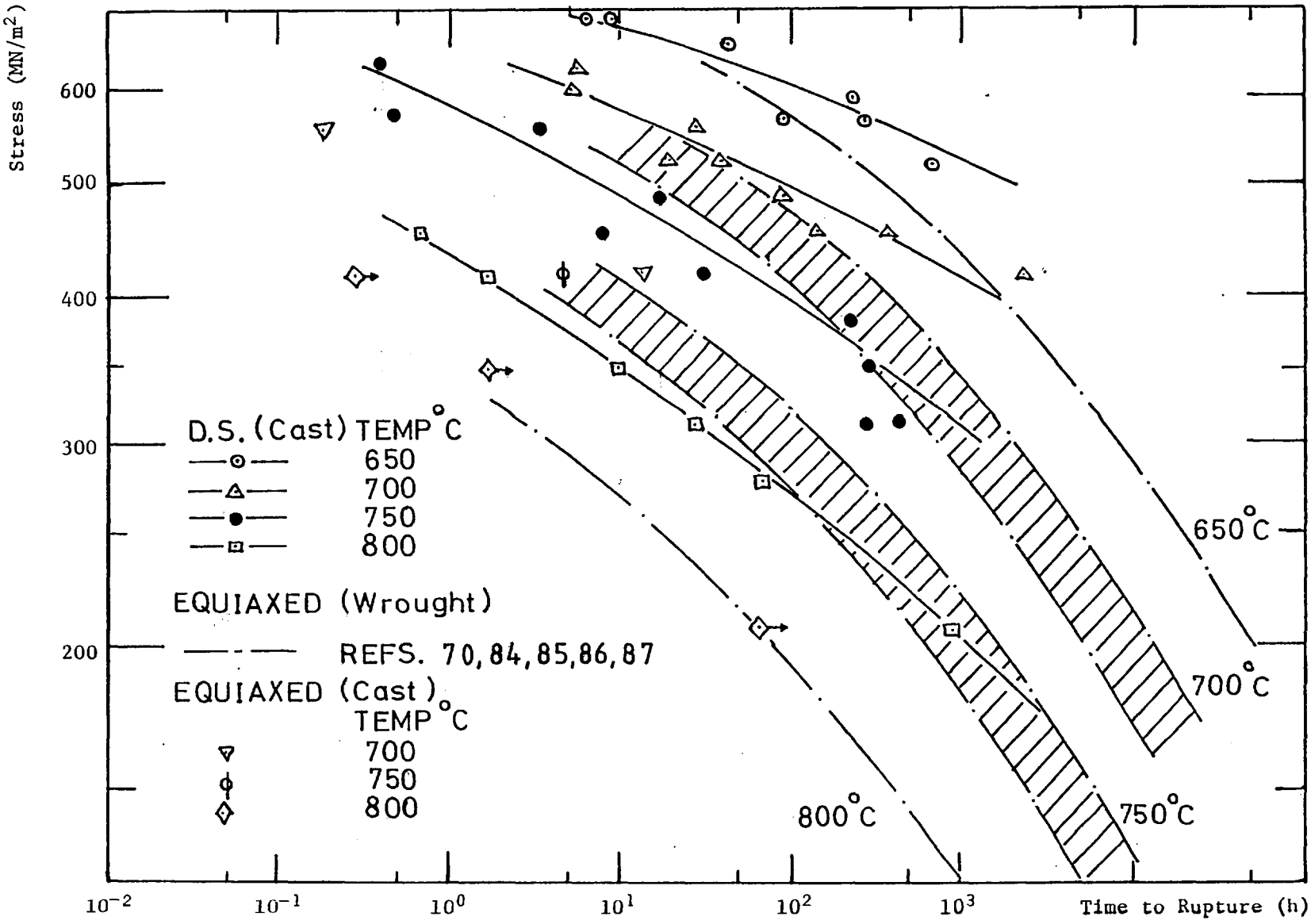

Figure 5.21: Times to rupture for experimental alloys and commercial wrought alloys. All points experimental.

differences in creep rupture strain with temperature. There are also variations from cast to cast. In reference [86], average values obtained from 16 to 18 casts are used to determine the single Larson-Miller parameter ($T(20 + \log t)$) but in the log stress versus log time to rupture plot, 98% confidence limits are presented for the temperatures 700°C, 750°C and 815°C. For example, at a stress level of 300 MN/m^2 at 700°C, the range of rupture times is 1500 h to 5200 h and at 750°C the range is 100 h to 400 h. Thus, the range in rupture times plotted in Figure 5.21 would appear to be fully representative of the data for the commercial alloy in the wrought form.

For the temperatures 650°C and 700°C, there is some overlap in the data for the experimental cast directionally solidified form and the wrought form at the higher stress levels. However, at the lower stress levels, the improvement in creep life for the directionally solidified form is over a decade. For the other tested temperatures, it would appear that the directionally solidified form is superior at all stress levels.

This improvement in life at the lower stress levels is similar to that observed by Northwood & Homewood for the alloy 713C (see Figure 1.4). This paper [13] dealt mainly with the effects of casting variables on properties and did not fully cover the reasons for the improvement in life for the directionally solidified form. The improvement in life was attributed to the prolongation of the secondary creep stage and greater ductility in the tertiary stage. However, in the examples given, the tertiary stage was of the same duration for the equi-axed and directionally solidified forms. Comment was made that the interdendritic and matrix intermetallic phases, mainly primary carbides, tended to be more uniform and finely dispersed in the directionally solidified material. Also, the fracture for the directionally solidified material tended to

follow an interdendritic path.

These points are not all applicable for the data in Figure 5.21 as there are many different casts represented and also the composition of the experimental alloy differs in the carbon content and hence carbide structure. It is evident from Section 4.3 that, for the experimental alloy in the equi-axed grain form, the grain boundaries had a pronounced effect on the failure mode and that the intergranular fractures resulted in reduced creep lives and ductilities.

Mention has already been made of creep rupture strain. Experimental values were obtained for the experimental alloy in both forms but data from the commercial alloy Nimonic 80A is not prevalent. Reference [70] gives creep rupture strain data for the temperatures 700°C, 750°C and 815°C and average values are compared in Figure 5.22. Data for the experimental equi-axed alloy is not included as the maximum recorded rupture strain was only 0.58%. It is seen that the directionally solidified form has greatly superior rupture strain values, except at the test temperature 700°C, where there is a distinct ductility trough. In fact, there is an overlap in some of the rupture strain values which reflects the similarity in rupture times shown in Figure 5.21.

For industrial applications, the rupture properties are not always the limiting criteria and often there is a creep strain limit in a certain time. Due to the early failures of the experimental alloy in the equi-axed grain form, a sensible limit value of creep strain was not obtained for all tests. However, Figure 5.19 showed the data for the time to 0.03% creep strain where it is seen that there is little improvement in time for the experimental alloy in the directionally solidified form. A more common value of creep strain limit is 0.1% and values for the time to this strain are compared in Figure 5.23 for the experimental alloy in the directionally solidified form and the commercial wrought alloy data

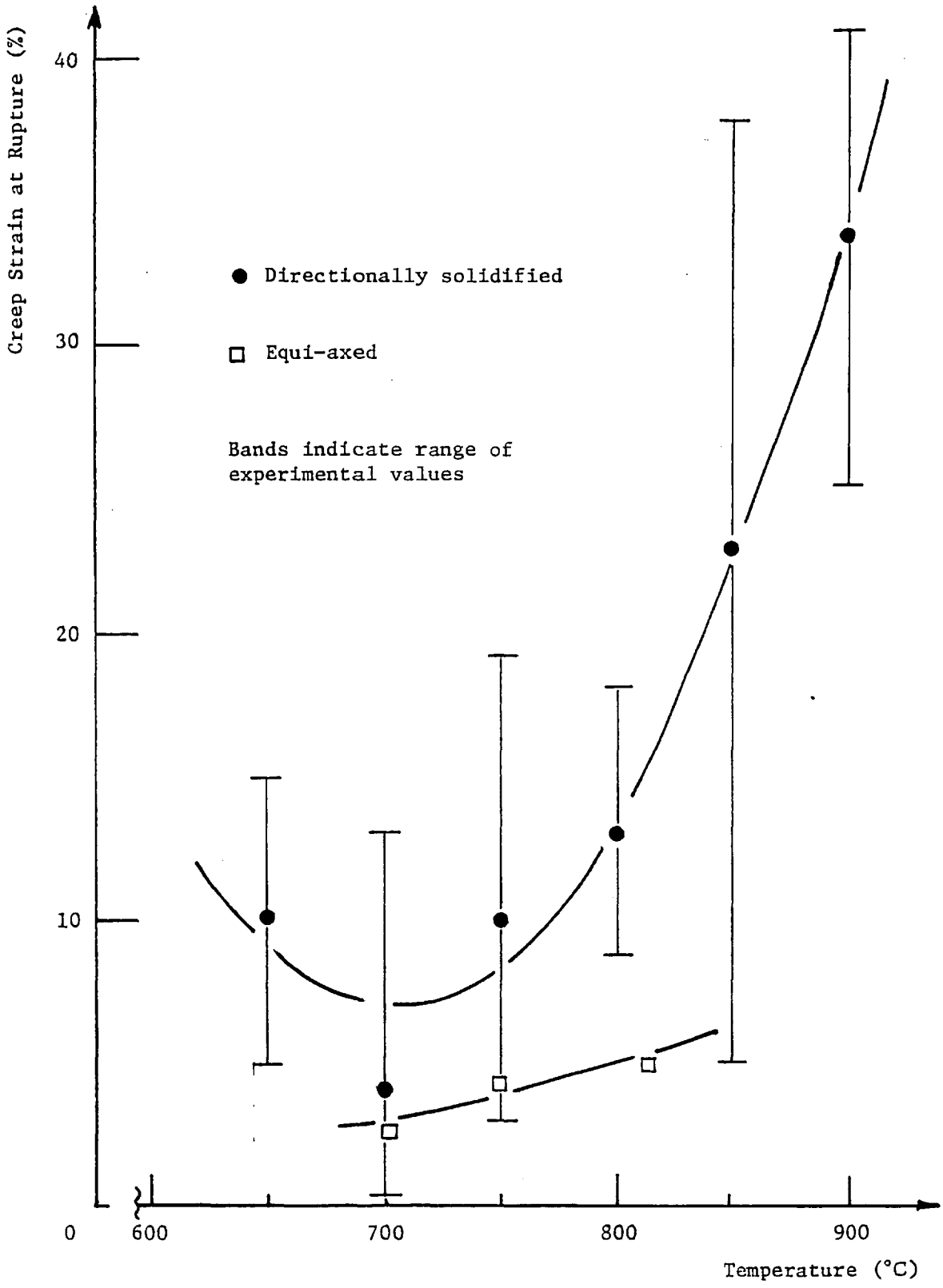

Figure 5.22: Creep strain at rupture for the directionally solidified and equi-axed grain forms

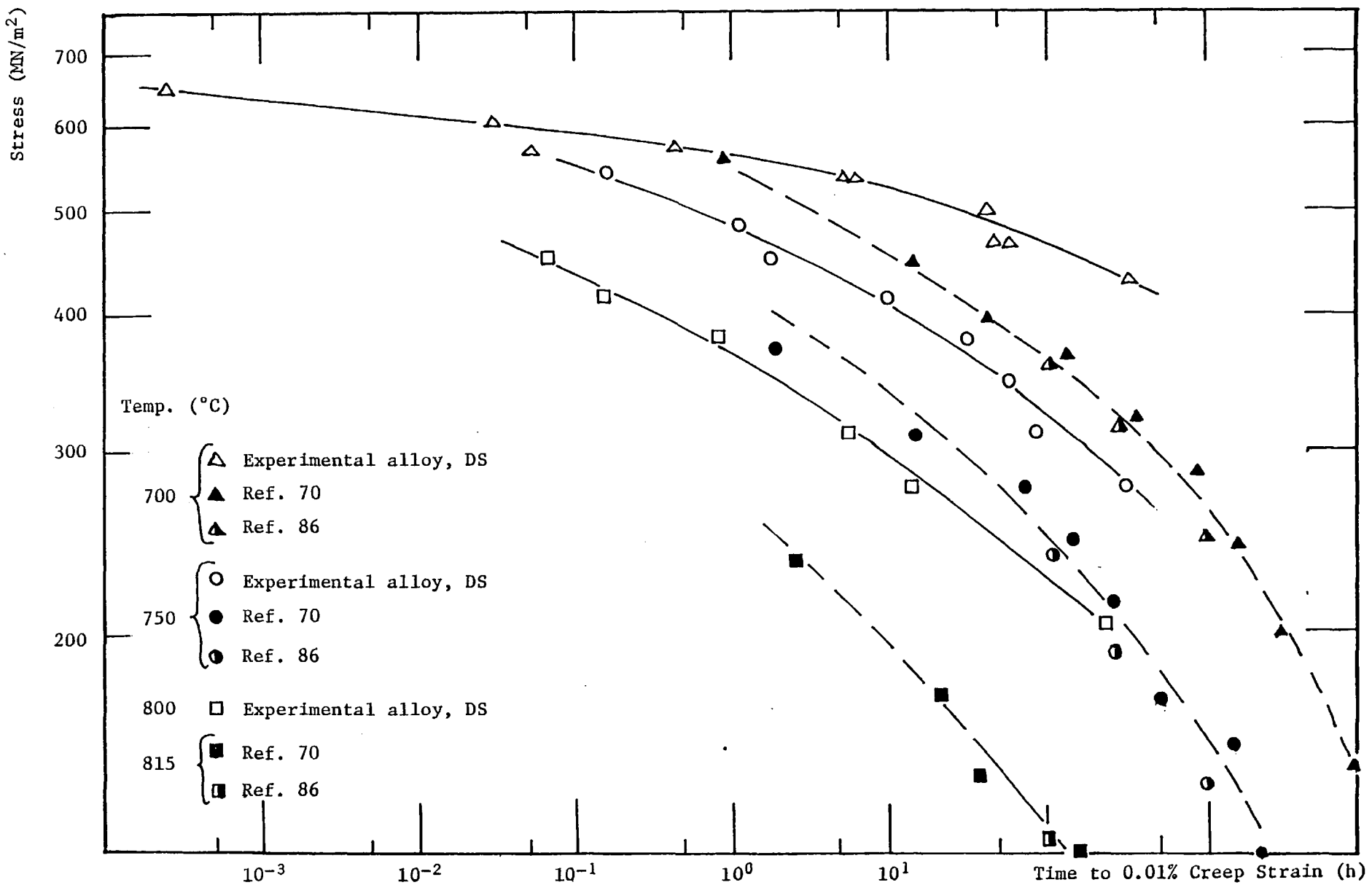

Figure 5.23: Stress dependence of time to 0.01% creep strain for experimental directionally solidified grain and other wrought alloys

from references [70] and [86]. There is a similar pattern to the rupture data shown in Figure 5.21 but, unfortunately, there is not a big overlap in stress values at the same test temperature. If anything, it would be predicted that the improvement in times through directional solidification is equivalent to an increased in operating temperature of around 50°C. This is a significant improvement.

The much reduced value of the elastic modulus for the experimental alloy in the directionally solidified form is shown in Figure 5.24 when compared with the equi-axed form. On the basis of the dynamic modulus figures [85,86], it would appear that the difference between the moduli for the two grain forms is almost constant with temperature but the experimental results of Betteridge [88] would indicate that at temperatures greater than 800°C, the difference is greatly reduced. As was shown in Section 1.3, this reduction in elastic modulus can be a benefit in gas turbines when large temperature differences can exist in components resulting in high thermal stresses.

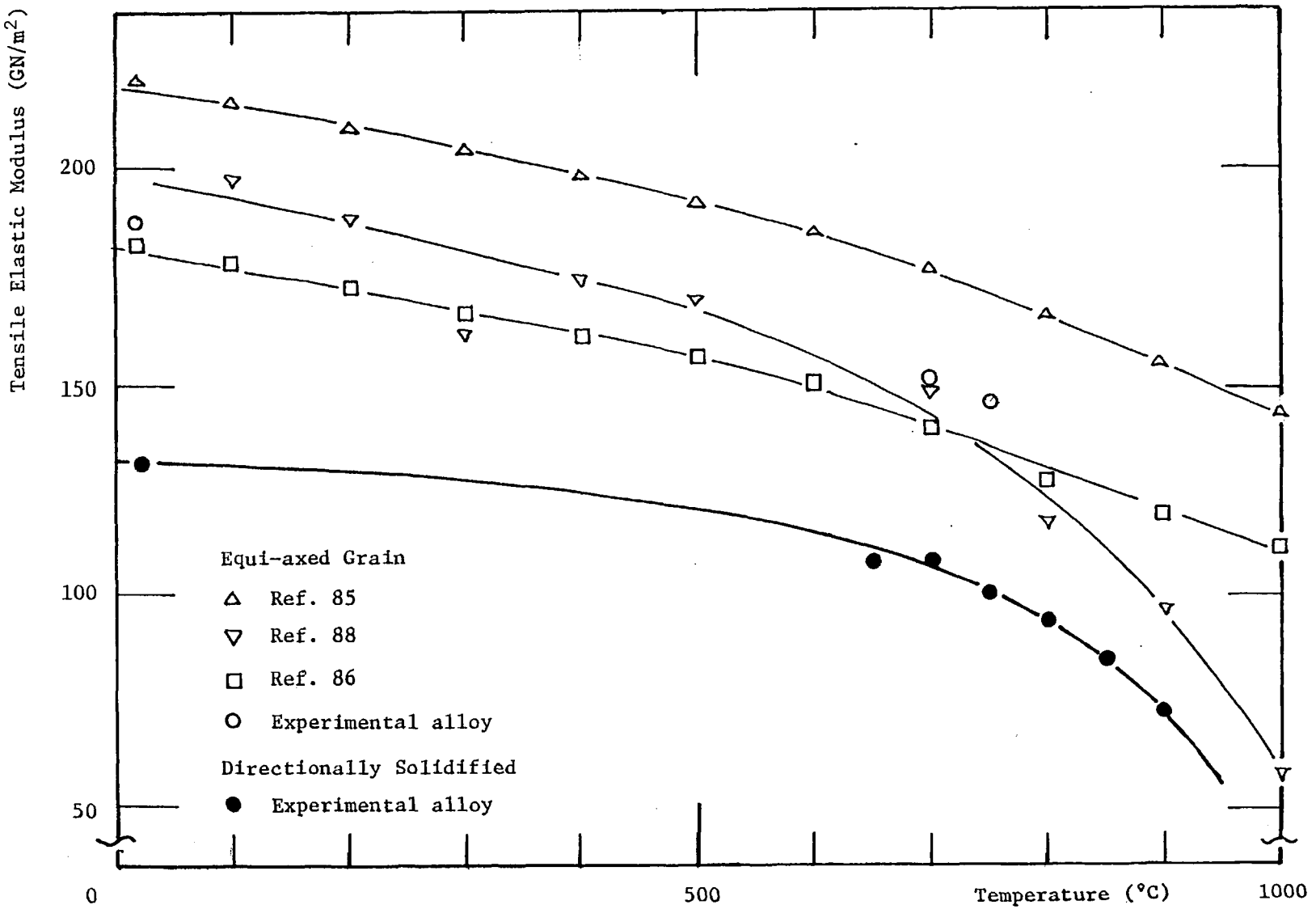

Figure 5.24: Tensile elastic modulus versus temperature for equi-axed and directionally solidified grain forms

CHAPTER 6

THE RÔLE OF STRUCTURE

6.1 OBSERVATION OF γ' MORPHOLOGY

A general survey of the properties of the dispersed phase γ' ($Ni_3(Al,Ti)$) in nickel base alloys has been given in Sections 1.3 and 1.4 with the general conclusions that the γ' phase morphology was a function of time, temperature and stress.

For the experimental directionally solidified alloy, the morphology was studied by transmission electron microscopy of thin foils prepared from tested specimens by the methods described in Section 4.1.3.

For all the constant and cyclic stress creep tests, the material was tested in the fully aged condition, i.e. solution treated at 1080°C for 8 h, AC and aged at 700°C for 16 h. Figures 4.13 A, B and C showed the material in this condition in bright field images and it is seen that even at the maximum magnification of the AEI EM6G electron microscope (×120 K), the γ' particles are barely resolvable. The shape is difficult to distinguish but suggests, together with the random distribution, a spherical morphology. Figure 4.13D showed the corresponding diffraction pattern where the γ' reflection required to resolve the γ' in a dark field image is weak. If this had been stronger than a better view of the γ' in the dark field image could have been obtained. A similar lack of γ' reflections was found by Bilsby in his study of nickel base alloys, including Nimonic 80A [36].

With time at the creep test temperature, an increase in particle size was observed in all thin foils from stressed and non-stressed areas of test specimens. As the commercial alloy Nimonic 80A has a high misfit parameter between the γ' phase and the matrix, it may be expected that a cuboid shape would develop with time at temperature [27]. The application

of a stress has also been shown to have some effect on morphology during growth [31,32] but, on the other hand, Mitchell [29] found no difference in particle shape, even with a creep strain of 33%.

Examples of a spherical morphology after testing at the temperatures 700°C, 789°C, 800°C, 838°C and 850°C have been shown in Figures 4.14 and 4.15 and are also shown in Figures 6.1A, B and C. Only one exception to the spherical morphology was observed and this is shown in Figure 6.1D. This occurred in only one section of one of several foils taken from a creep tested specimen at 850°C. The cuboid morphology is not distinct but some alignment of the grown particles is evident.

The cuboid form of γ' can be obtained in Nimonic 80A within a duplex structure [73]. An intermediate ageing treatment of 24 h at 850°C (which is near the solvus temperature of the γ' phase) is given which allows some of the fine γ' formed on air cooling from the solution temperature of 1080°C to grow easily to large proportions, approximately 900 Å (0.09 μm) mean cube edge. The remaining γ' is taken back into solution and, on ageing at 700°C for 16 h, produces a secondary spherical γ' of mean diameter approximately 70 Å (0.007 μm). On exposure to higher temperatures and growth conditions, the spherical particles remain spherical.

The non-appearance of a true duplex γ' in Figure 6.1D would indicate that the initial specimen ageing treatment fully precipitated the γ' phase, and that the unique area of cubic γ' form observed may possibly have been due to a unique stress state acting on that particular grain.

The solubility temperature of the γ' phase in Nimonic 80A has been given as in the range 840°C to 880°C by Heslop [28], but more recently this has been increased to the range 960°C to 980°C by Henry Wiggin data [77], this latter range being in doubt experimentally [91]. The first range given is close to the higher experimental creep test conditions and it may be expected that denuded zones of γ' would appear adjacent to the

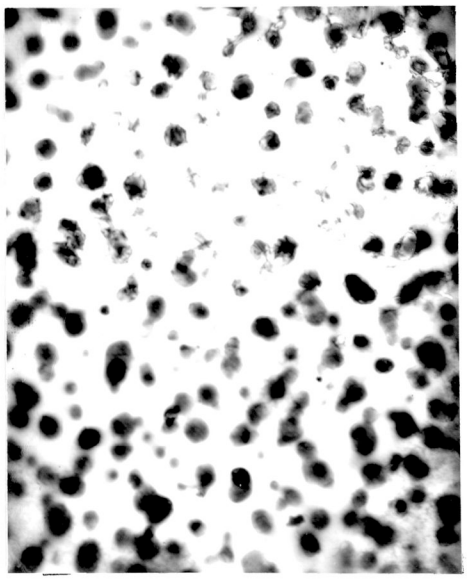

A N76 ×20 K

B N76 ×50 K

C N45 ×30 K

D N42 ×20 K

Figure 6.1: Transmission electron micrographs of creep tested specimens. Test N76 was a cyclic load test.

grain boundaries in the experimental alloy, creating a zone of weakness. Mitchell & Wakeman [78] have observed denuded zones on the grain boundaries of Nimonic 80A but this was associated with the growth of large chromium carbide particles which reduced the chromium content and increased the solubility of nickel in the grain boundary zones. Probert [79] has also produced denuded zones in Nimonic alloys, but only after an initial ageing heat treatment at 900°C.

No direct observations of denuded zones have been seen in the experimental alloy, even at the test temperature of 850°C. Also, the grain boundary carbide is not of a size as seen in the commercial alloy. This reduction in size can be attributed to the reduced carbon content of the experimental alloy.

Due to the time involved in preparing thin foils for electron microscopy, a complete survey from all creep tested specimens was not possible. From the observations made, the conclusion reached has been that the γ' phase retained the spherical morphology of its initial aged condition during subsequent growth at creep test conditions.

Measurements of γ' particle diameters were then made from the bright field images. At least ten particles were measured from each photomicrograph and true diameters determined from the calibrated magnification of the electron microscope used.

6.2 GROWTH LAWS OF γ'

The elementary growth laws for precipitate particles have been reviewed in Section 1.4.

One of the prime considerations for growth laws is that the volume fracture of the particles remains constant. Experimental determination of this parameter from electron photomicrographs depends on the assumptions made regarding the viewed particles being plane or full sections. Ashby

[74] gives the following expressions for the volume fraction, f, assuming the former:

$$f = N_v \frac{4}{3} \pi r_v^3 = N_s \pi r_s^2 = N_L \frac{4}{3} r_v \qquad (6.1)$$

where N_v = number of particles per unit volume

N_s = number of particles intersecting unit area

N_L = number of particles intersecting a random straight line of unit length

r_v = particle radius

r_s = mean planar particle radius

The second of these relationships is then simply the area of particles in a photomicrograph divided by the area covered by the film, if the assumption can be made that the photomicrographs are of plane sections of particles. Without any full experimental guidance available at this point, this assumption was made. Fullman [75] has also given a similar form of equation for determining f as:

$$f = N_L \bar{l} \qquad (6.2)$$

where N_L is as defined for equation (6.1), and $\bar{l}$ is the mean lineal transverse length.

Using experimental values of N_s, r_s, N_L and $\bar{l}$ from photomicrographs, the volume fraction was determined for various creep test temperatures. Equation (6.2) gave higher values for the volume fraction but with much greater scatter due to the small number of particles intersected in many photomicrographs. The average values using equation (6.1) are listed below.

Creep Test Temperature (°C)	Volume Fraction, f (%)
650	18.6
700	20.6
800	17.2
850	19.9

A full survey of the effects of time at temperature on the volume fraction could not be made but after an exposure of 1500 h at 800°C there was no significant change in the value of f.

Thus, within the experimental accuracy of measurement, and regarding the assumptions made, the condition of a constant volume fraction of γ' for the experimental alloy in the directionally solidified form during creep testing is met.

The growth law for the size of the γ' precipitate presented in Section 1.4.2 can be represented as:

$$d^3 = k\,t \quad , \qquad \text{from (1.1)}$$

where: $$k = A\,exp\,(-\frac{Q}{R\,T}) \quad , \qquad \text{from (1.2)}$$

although it is more commonly used in the form:

$$d = k_1\,t^{1/3} \tag{6.3}$$

Graphical data in the form of equation (6.3) has been presented by Henry Wiggin [73] for the Nimonic alloys 80A, 90, 105 and 115. The parameter, d, in equation (6.3) was defined as a particle diameter but for

the alloys 105 and 115, the γ' morphology is cubic. However, the graphical data were still presented on a mean particle diameter basis. Values of k_1 have been determined from the above data at each temperature. Activation energies may then be deduced from Arrhenius plots for each alloy. Values so obtained are given below, together with a mean value obtained from all the data.

Alloy	Activation Energy (kJ/mol)
Nimonic 80A	286
Nimonic 90	297
Nimonic 105	431
Nimonic 115	318
Mean for all data	337

It would be expected that the activation energy for the growth of the γ' phase would be independent of the alloy in the nickel base series and the scatter in the above values would throw some doubt on the applicability of equation (6.3).

All the above analysis has assumed a zero value of particle size when time is at zero. This was not the case at the start of the experimental creep tests presented in this thesis. The γ' particles were already in the aged condition. The analysis of Greenwood [76] for growth of solid particles dispersed in a liquid solution is also based on a diffusion process but derives a fastest growth rate of already formed particles. The size-time relationship was:

$$a_f^3 - a_I^3 = 3\,D\,S\,\frac{2M\sigma}{R\,T\,\rho^2}\,t \qquad (6.4)$$

where a_I = initial particle size

a_f = final particle size

D = diffusion coefficient of solute in liquid

S = solubility

ρ = density of the solid of molecular weight M

σ = interfacial tension between solid and liquid

This is similar in form to the equation presented in Section 1.4.2, where the temperature dependence of the diffusion coefficient, D, was considered to be the dominant temperature parameter.

For the experimental alloy, it is now proposed that the growth law for the γ' particles for the creep test conditions can be represented by:

$$d^3 - d_o^3 = k_2 t \tag{6.5}$$

where d_o = initial particle size in the fully heat-treated state

t = time at creep test temperature

k_2 = constant

The constant, k_2, can then be represented by:

$$k_2 = A_2 \exp\left(-\frac{Q}{R T}\right) \tag{6.6}$$

where A_2 = constant

Q = an activation energy for the growth of γ' particles

T = creep test temperature

The experimental γ' particle diameter sizes measured, with a correction factor to determine the true particle diameter of 1.25 for

particle sizes over 1000 Å (0.1 μm) diameter, have been plotted on the basis of equation (6.5) in Figure 6.2. These plots do show the scatter than can arise in such an exercise and, whilst the points do not conclusively show the validity of equation (6.5), some confirmation may be found by considering the temperature dependence of the parameter, k_2. This is plotted in Figure 6.3 on an Arrhenius temperature basis and a linear relationship is seen to exist. The activation energy obtained from the slope is 302 kJ/mol. This is in good agreement with the value found from the analysis of Henry Wiggin data on Nimonic 80A [73], but differs from that found by Bilsby [36] and Ardell & Nicholson [35]. This difference of approximately 29 kJ/mol is considered to be within the range of experimental errors. Thus, the growth law as formulated in equation (6.5) can be considered as adequate for the experimental alloy.

6.3 THE EFFECTS OF TIME AT TEMPERATURE ON CREEP PROPERTIES

The cyclic stress tests reported in Section 4.2.4.2 were performed to study the relationship between any changes in the γ' phase due to exposure at test temperatures and creep properties. Tests N68, N74, N75 and N76 were all carried out at 800°C when it was expected that the material would overage, whilst test N78 was carried out at 700°C when no rapid overageing was expected.

Tests N68, N74 and N75 were at a constant stress value of 207 MN/m^2 but with differing values of α, the ratio of the time on load to the total cycle time, as defined in Figure 4.16. On a creep strain basis, the result is shown in Figure 6.4. The net creep plastic strain (the total permanent strain accumulated during the cycles) is seen to have a different time under stress relationship and appears to be a function of α. The values of α were, however, not kept constant for the complete duration of each test. The time on load was reduced once an acceleration in the

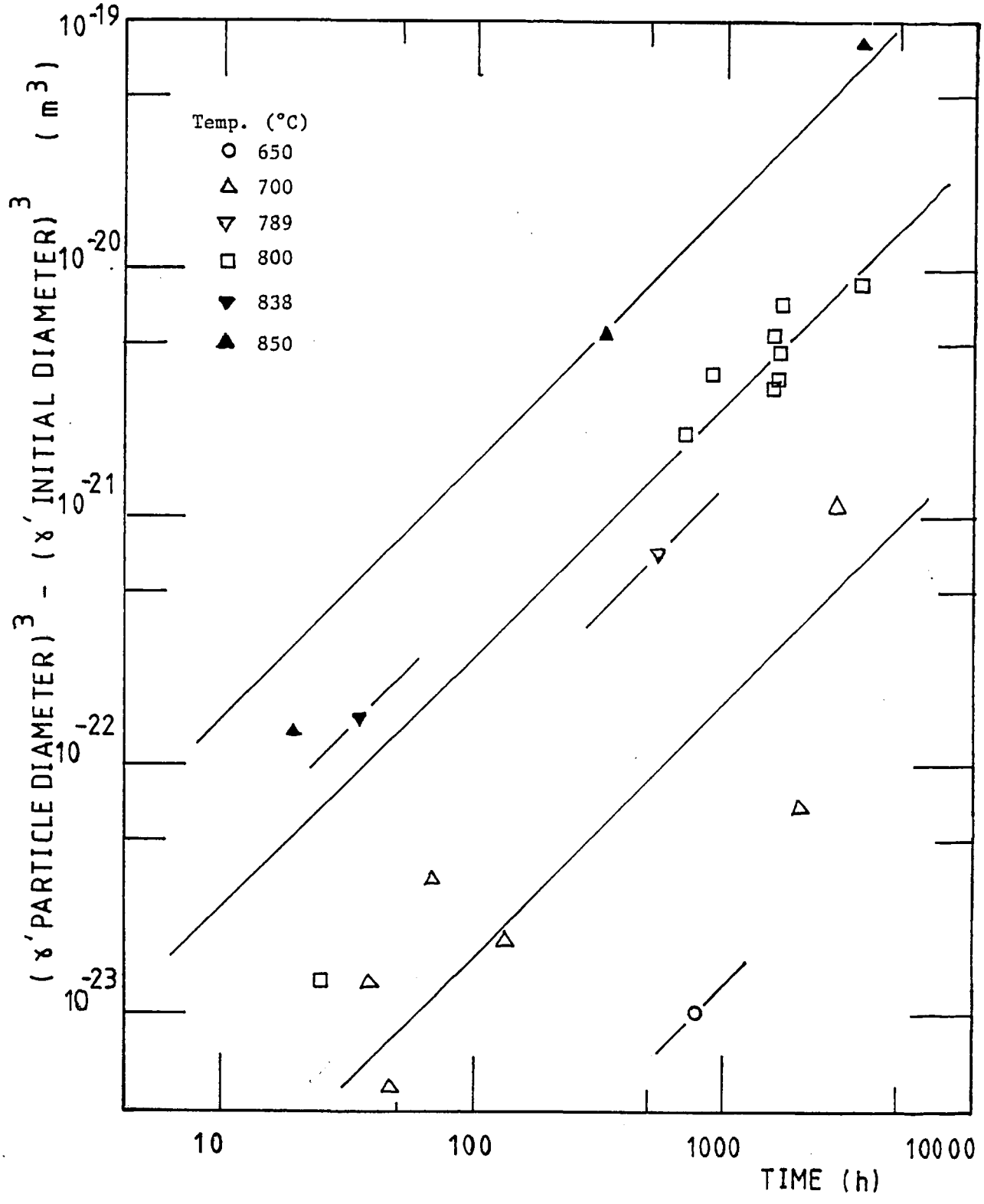

Figure 6.2: Growth law relationship for γ' precipitate particles according to equation (6.5)

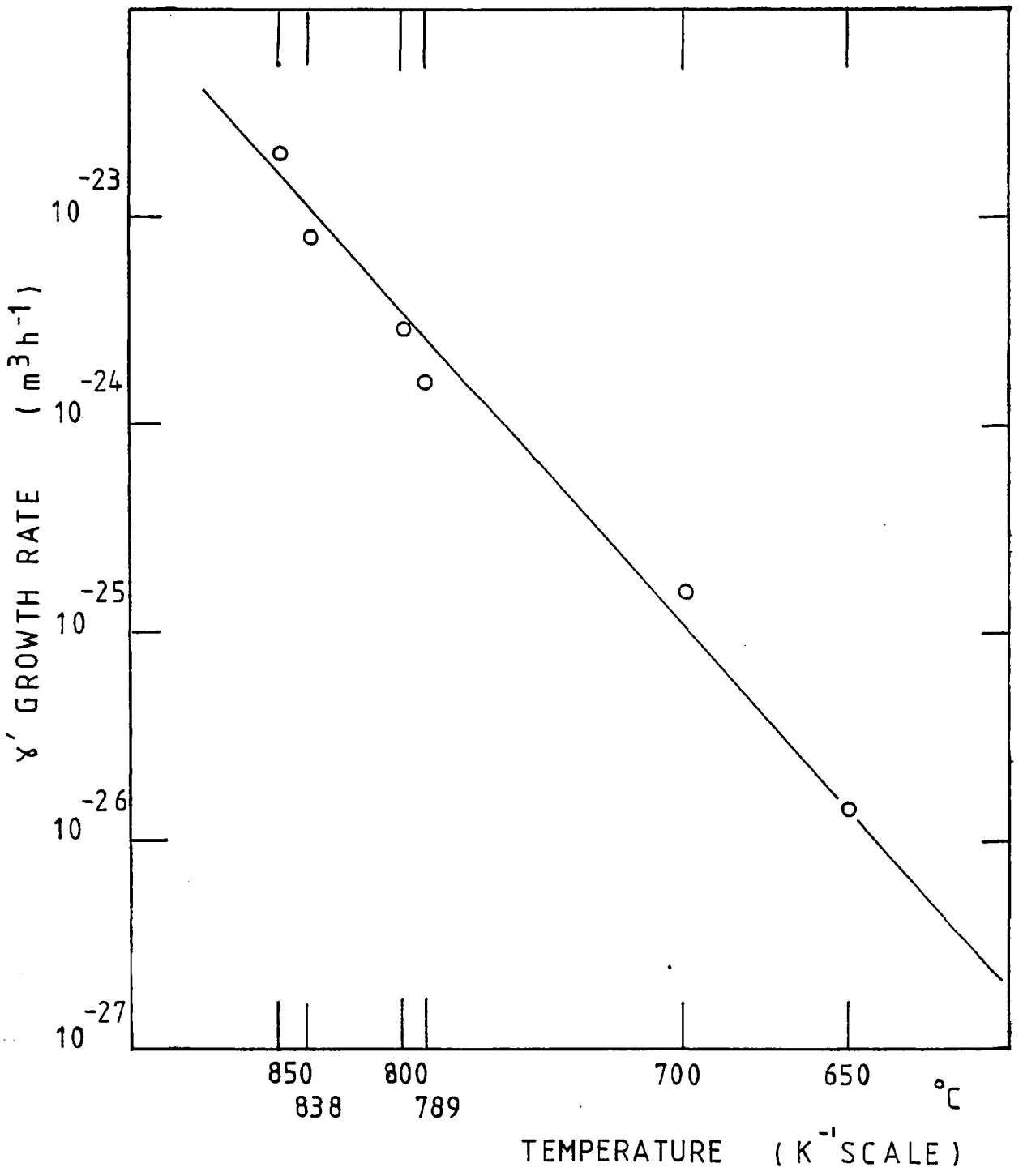

Figure 6.3: Arrhenius plot for growth rate of γ' precipitate particles according to equation (6.5)

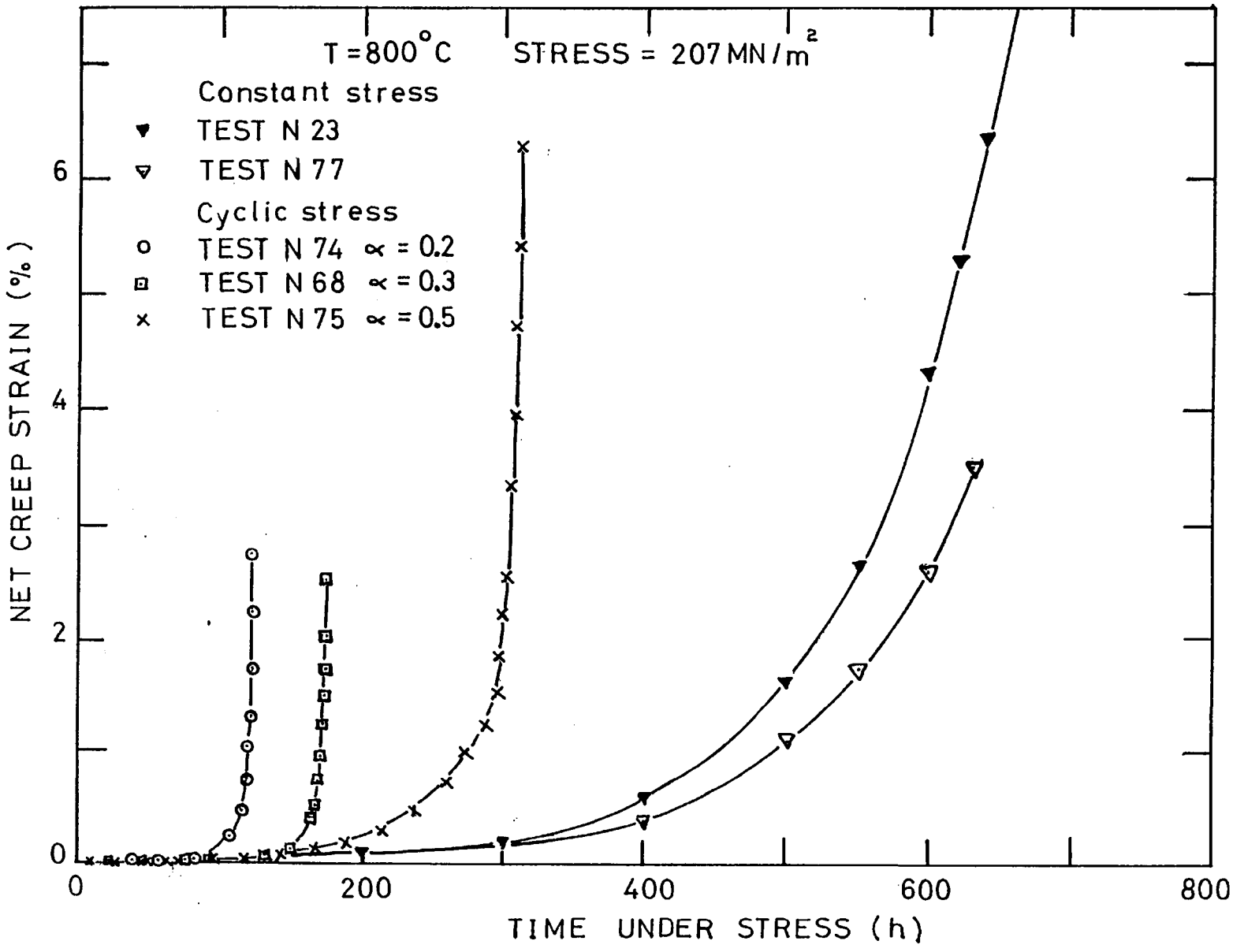

Figure 6.4: Net creep strain as a function of time under stress at 800°C

creep strain per cycle occurred to prevent any possible fracture. Hence, the value of α decreased considerably, e.g. for test N74, the initial value of α was 0.2 for the first 500 h whilst at 1300 h the value was of the order of 0.01.

The period between loadings allowed for a recovery of the deformed structure through dislocation annihilation and diffusion processes. Recovery strain data taken for all the loading cycles showed that approximately 80% of the recovered strain per cycle was obtained within one hour of unloading (see Figure 6.5). The lowest cycle time was 24 h. Thus, the associated time off load allowed full time for recovery and the relevant creep properties should be only a function of time. Thus, the parameters net strain and time under load do not adequately represent the behaviour of the material associated with time at temperature in this overageing condition.

A more meaningful parameter may then be the steady-state creep rate for each cycle. This is plotted in Figure 6.6 on a basis of total time at temperature. Data for the strain rate in constant stress tests, N23 and N77, at 207 MN/m^2 are included. It is now seen that all the cyclic stress tests have a unique relationship between the steady-state creep strain rate and time at temperature. The initial decrease in strain rate for the constant stress creep tests was in the short period of primary creep. For test N23, there was a period of almost constant strain rate after 600 h but the creep strain was high in this region, between 5% and 18%, and was accumulating rapidly enough to balance some of the recovery processes.

Some effects of recovery are also shown for the constant and cyclic stress tests at 276 MN/m^2 and 800°C, tests N22 and N76, respectively. Again, there is a difference in the net creep strain-time under stress relationships (Figure 6.7), but there is also a difference in the strain

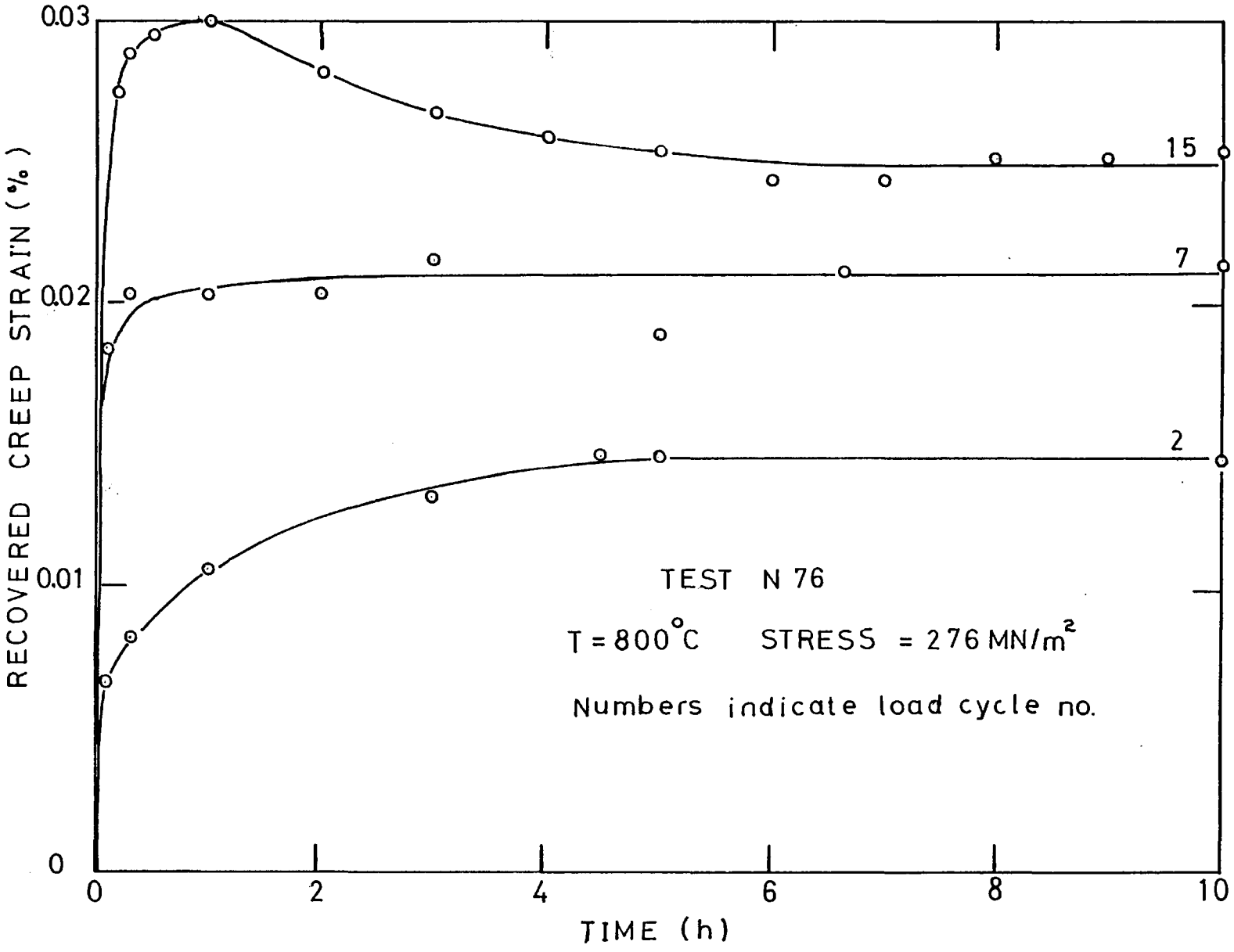

Figure 6.5: Recovered creep strain-time relationships for test N76

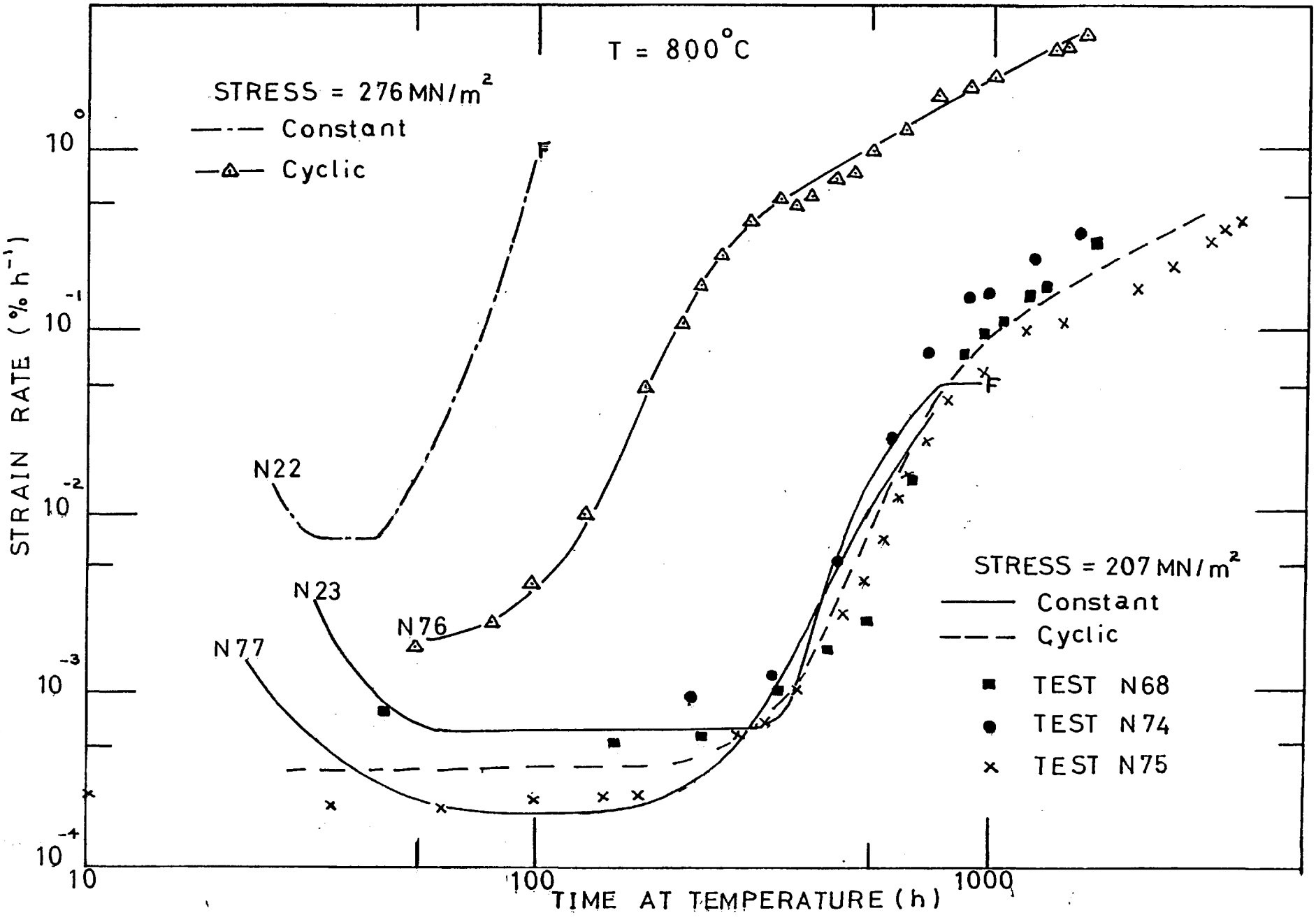

Figure 6.6: Strain rate, under creep conditions, dependence on time at test temperature of 800°C

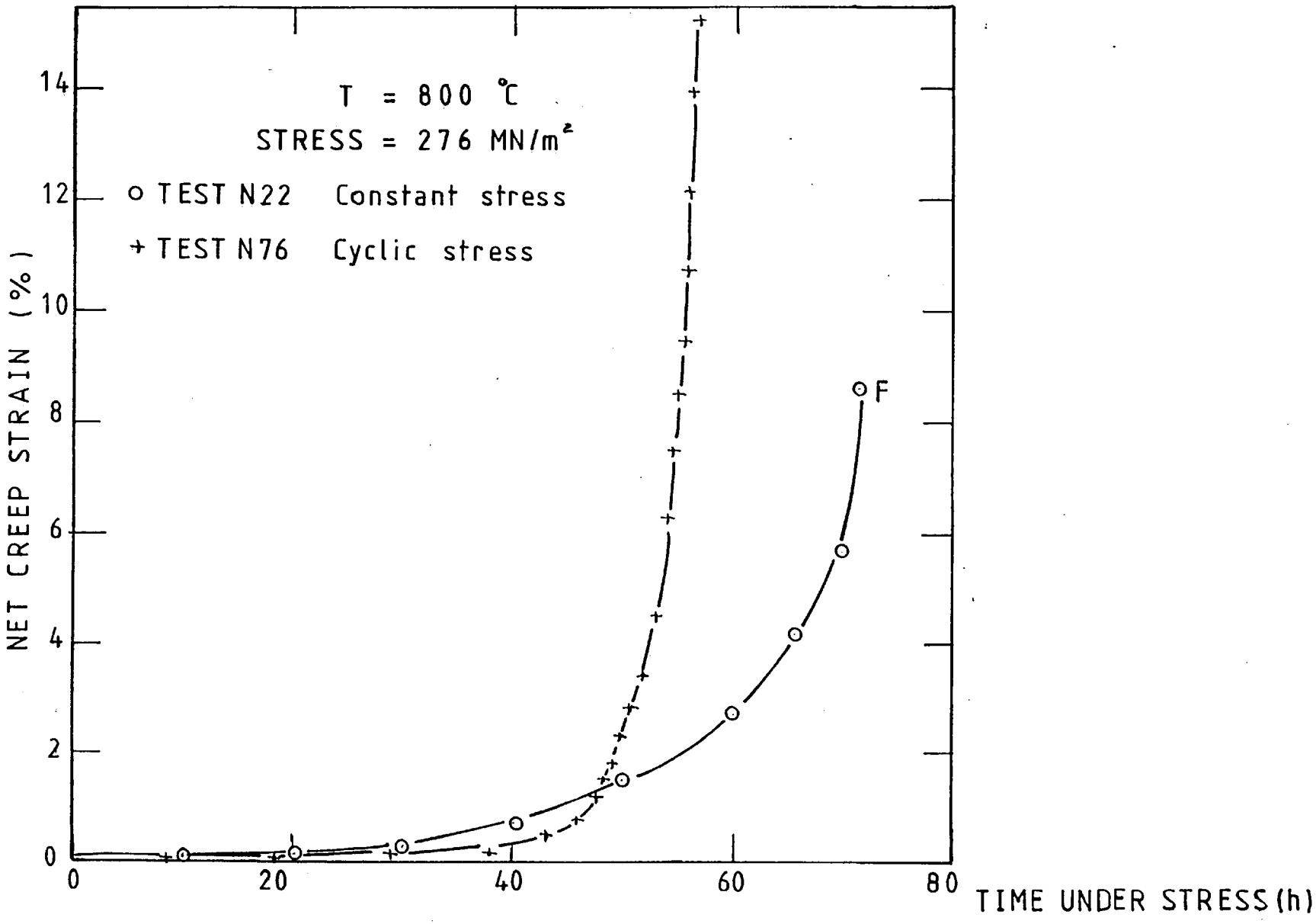

Figure 6.7: Net creep strain versus time under stress for tests N22 and N76

rate-time at temperature relationship (Figure 6.6). The net creep strain accumulates faster on a time under stress basis for the cyclic stress conditions than for the constant stress conditions. However, on a time at temperature basis, the steady-state creep rate for the cyclic stress test was considerably lower. This is partially predictable in that the rupture time for the constant stress tests was only 71.3 h with a rupture strain of 8.7%. Under the cyclic stress conditions, the specimen underwent 22 loading cycles with a total time under stress of 56.7 h. An accumulated strain of 15% was obtained with only two slight necks developing. During the final three loading cycles the normal primary and secondary steady-state creep stages were observed with the steady-state creep rate constant over at least 1% creep strain. There was no sign of any accelerating rate. Thus, the high dislocation density associated with large plastic strains must have been partially, or fully, annealed during the off load recovery periods. The high creep strain rate for the constant stress test would not then be fully compensated by recovery processes and would finally lead to fracture.

The cyclic stress tests at 800°C may thus be considered as producing the steady-state creep strain rate purely as a function of the stress level and exposure time at temperature.

The cyclic stress test at 700°C was carried out to determine the characteristics for the material in the fully aged condition where no overageing was taking place within the time limit of the cyclic test. The stress level chosen, 448 MN/m^2, had produced low ductility fractures, approximately 0.5% and 1.6%, with rupture times of 111.7 h and 386.1 h, respectively.

For the cyclic stress test, test number N78, the specimen underwent 28 loading cycles during 2179 h at temperature and accumulated 8.03% plastic strain. Figure 6.8 shows the results plotted on a net creep

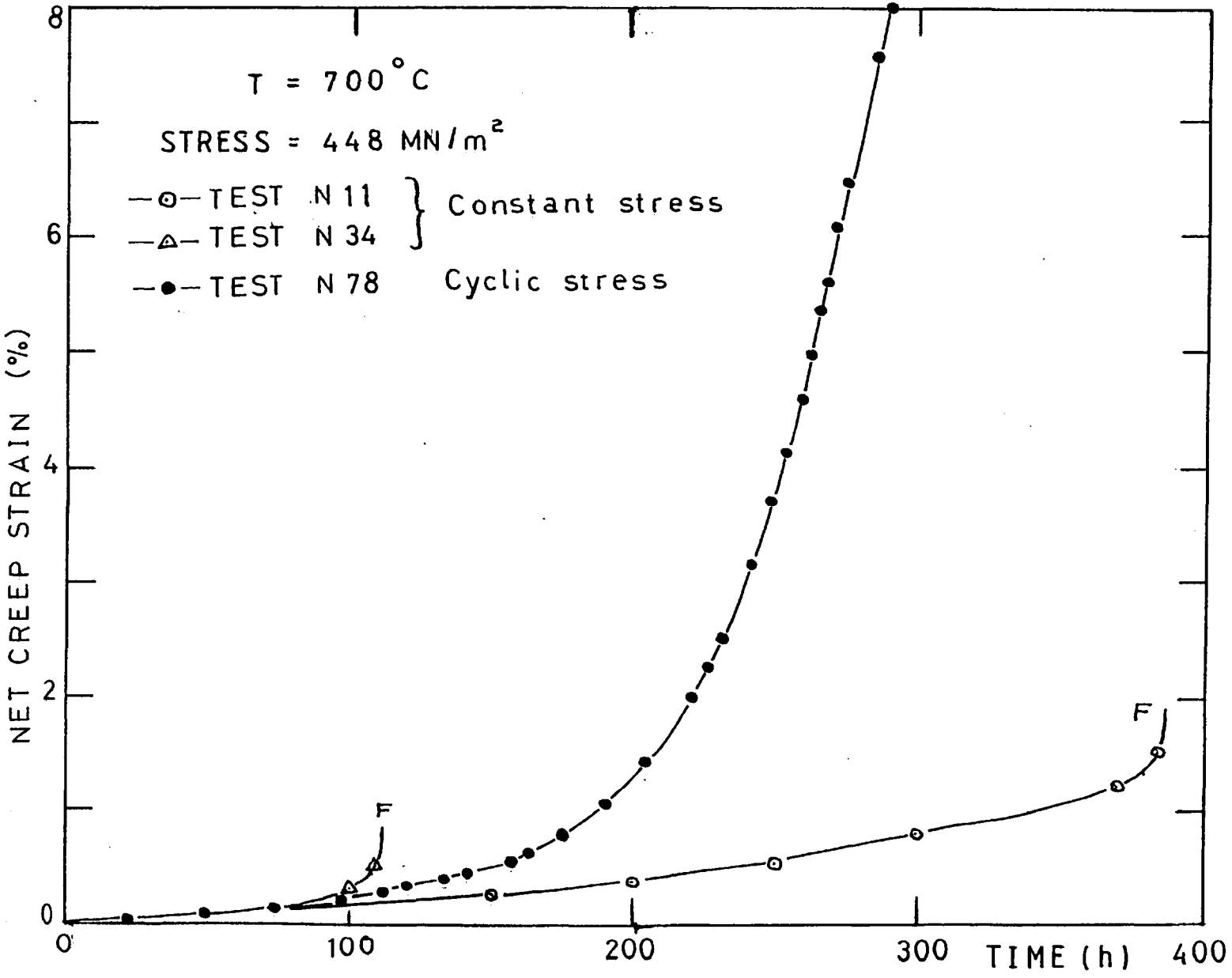

Figure 6.8: Net creep strain versus time at temperature for a stress of 448 MN/m^2

strain-time under stress basis, where the cyclic stress test lies between the two constant stress tests. The cyclic stress test has an apparent constant net strain rate after 240 h under load with no indication of approaching fracture. The shape of this curve is very similar to that of the long time constant stress creep test, N13, at 414 MN/m^2 where a ductility of approximately 10% was achieved after 2683 h (see Figure A.13).

The apparent constant net strain rate for the cyclic stress test is not found when the strain rates for each cycle are plotted on a time at temperature or time under load basis (Figure 6.9). Here, it is seen that the strain rate is gradually increasing with no particular relationship with the time at temperature. The dual points for the latter loading cycles were for tests where there was a very short recovery time (less than 0.1 h) and a corresponding small amount of strain recovered (approximately 0.01% compared with 0.04% for full recovery).

The main characteristic of the fractures for the constant stress creep tests at 700°C was shown in Section 4.2.2 to be short transverse interdendritic cracks on the longitudinal grain boundary. For the cyclic stress test, the stress concentrations induced at these short cracks were relieved, totally or partially, during the off load recovery periods. This could account for the higher strain, without fracture, obtained in the cyclic stress test. The increase in strain rate then being partially due to the effects of the cracks on the reduction in the load carrying area of the specimen, and partially due to the unrecovered structure providing a source of mobile dislocations. Inspection of the surfaces of the unbroken cyclic stress test specimen after the completion of the test showed several transverse cracks at different sections of the gauge length, a feature which was completely absent from the cyclic tests at 800°C.

The increase in steady-state creep rate for the cyclic stress test at 700°C was only of the order of two decades compared with over four

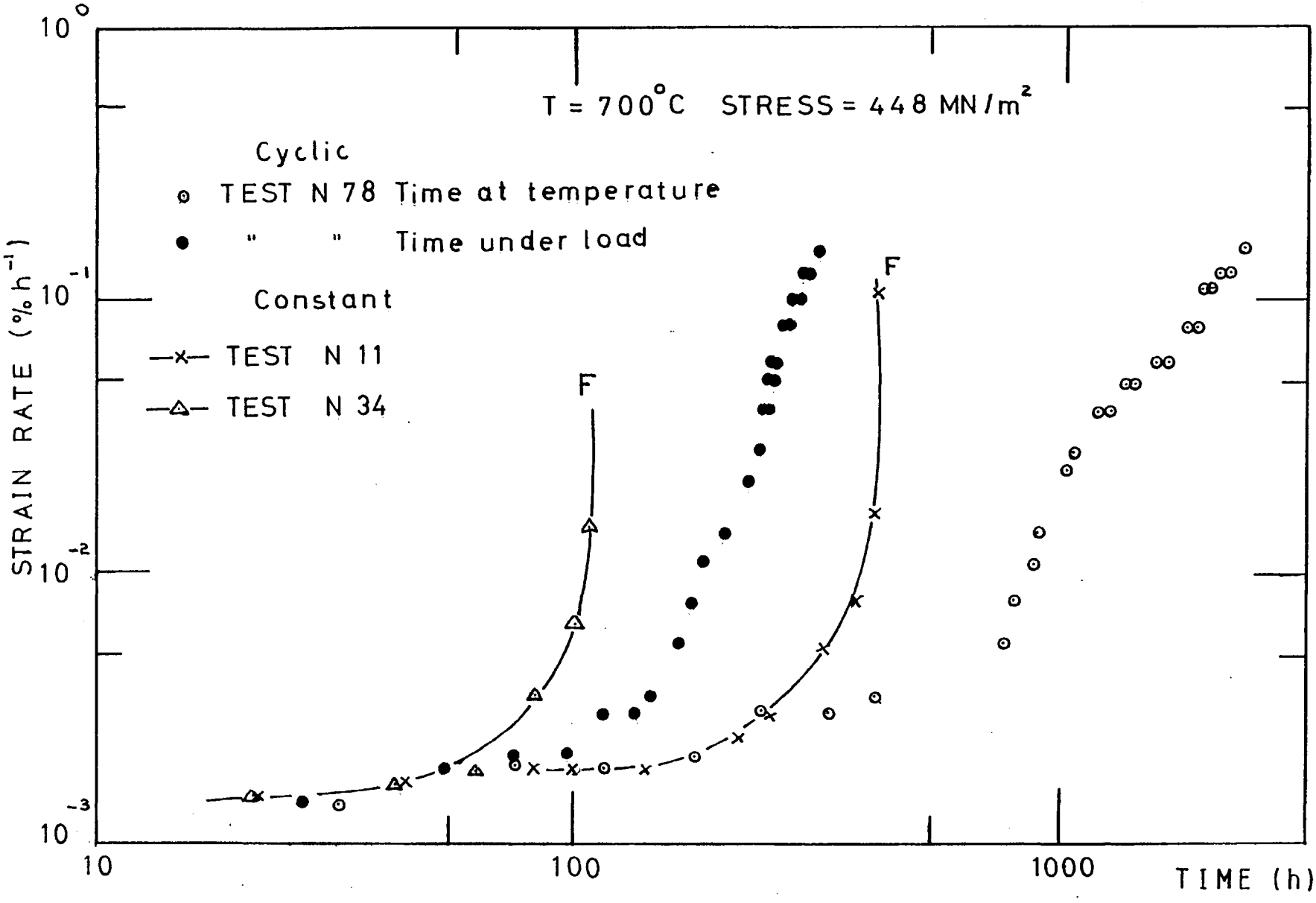

Figure 6.9: Strain rates for a creep stress of 448 MN/m² at 700°C

decades for the cyclic stress tests at 800°C over the same period of time. Hardness measurements on the unstressed ends of the specimen tested at 700°C showed an increase in value from the initial condition, whereas for the tests at 800°C the hardness values were considerably reduced after the exposure at temperature. It was also found that for test N78 after 1500 h at a temperature of 800°C, the specimen yielded on application of the load (for a stress of 276 MN/m^2), whereas the initial stress chosen was well below the yield stress obtained for short exposure times.

Thus, accumulated strain, cracks and a low recovery rate would characterise the creep properties at 700°C, whilst at 800°C the internal weakening of the structure could be responsible for the large increase in strain rate with exposure at temperature.

A series of tests were then made to investigate more fully this latter possibility by measuring the macroscopic yield stress as a function of time at temperature.

6.4 RELATIONSHIPS BETWEEN THE MACROSCOPIC YIELD STRESS AND THE γ' PARTICLE SIZE FOR THE OVERAGED STATE

The relationship between second phase dispersed particles and the bulk yield stress of the material is governed by the form of the dislocation-precipitate particle interaction, as was described in Section 1.4.2. The graphical representation between the increase in yield stress due to the precipitate particles and the particle diameter (or ageing time) was shown in Figure 1.5.

Once the critical particle size is reached, there is a decrease in the bulk yield stress and the material is said to be overaged. The critical particle size was shown to be dependent on the volume fraction of the γ' but for alloys of similar composition to the experimental alloy, the range of critical size was experimentally observed to be 100 Å to 300 Å

(0.01 to 0.03 μm) [5].

For the experimental alloy, a particle size of 300 Å (0.03 μm) can be predicted, from Figure 6.2, as being reached after 4 h exposure at 800°C and 0.9 h at 850°C for a fully aged specimen.

Some confirmation that the material will be in the overaged state after the above exposures to temperature can be found in the macroscopic hardness measurements (Figure 6.10). It is seen that at the test temperature of 800°C, the Vickers hardness continually decreased with time at temperature, the shortest exposure time being almost 20 h. At the test temperature of 850°C, there is a rapid decrease in Vickers hardness, from the as-aged range of 320 Hv to 380 Hv, with exposure time.

Thus, it will be expected that the experimental measurements of yield stress made at 800°C and 850°C, as reported in Section 4.2.4.3, will be for the material in the overaged condition.

The predominant mechanism of dislocation motion for the overaged condition is the Orowan dislocation looping by-pass mechanism [90]. For the original model derived by Orowan [80], the configuration of dislocations is as shown below, and it is assumed that the particles are non-coherent,

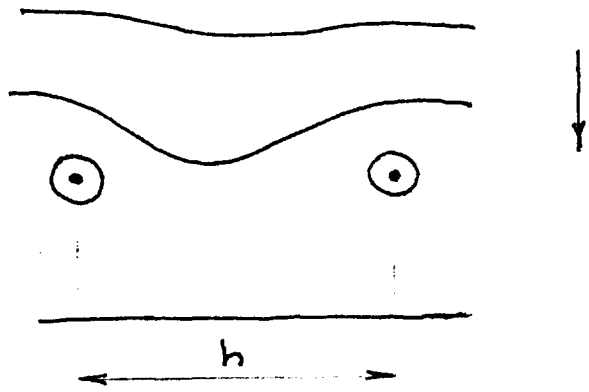

not deformed and that their flaw stress is large compared with the flow stress of the matrix. The additional strength due to the particles is then the force required to bend a dislocation to a radius $h/2$ which gives:

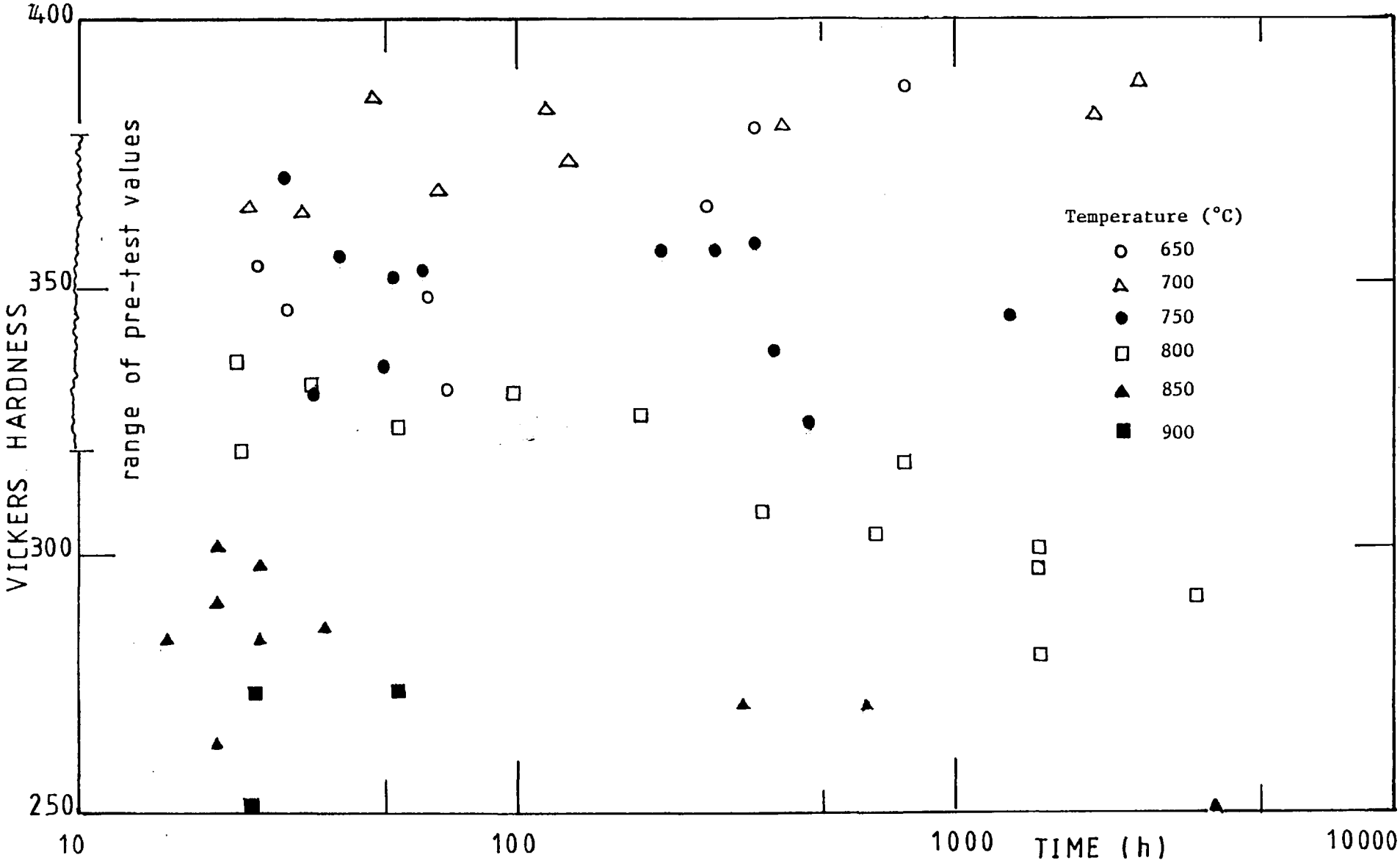

Figure 6.10: Vickers hardness of unstressed areas of test pieces

$$\Delta\tau = \frac{2Gb}{h} \tag{6.7}$$

where $\Delta\tau$ = increase in shear stress due to particles

G = shear modulus

h = spacing of obstacles

b = Burger's vector

The above equation assumes a very simple form for the line tension and it is this term that has been concentrated on in improving equation (6.7). Kelly & Nicholson [38] have averaged the values of line tension for screw and edge dislocations to give:

$$\Delta\tau = \frac{G\,b}{4\pi}\,\phi\,ln\left\{\frac{h-2r}{2b}\right\}\frac{1}{(h-2r)/2} \tag{6.8}$$

where r = particle radius

ϕ = mean factor in the line tension for screw and edge dislocations

h = centre to centre separation of particles

Ashby [74] has performed a similar analysis with different particle parameters, based on planar analysis, but derives an equivalent form of equation to (6.8).

The most common parameter experimentally measured is the precipitate particle size and for a constant volume fracture, f, there is a relationship between the parameters h and r (or d, particle diameter). For planar particles in a simple cubic lattice, Ashby gives:

$$h = \sqrt{\pi/f}\,r \tag{6.9}$$

but for a random distribution of particles:

$$h = 0.5 \sqrt{\pi/f}\, r \tag{6.10}$$

For the experimental alloy, of γ' volume fraction 20%, the relationship becomes, from (6.9), $h = 3.96\ r$ and, from (6.10), $h = 1.98\ r$.

A simple analysis for spherical particles at the edges of a cube, dimension h, shows that:

$$h = \sqrt[3]{\frac{4}{3}\frac{\pi}{f}}\, r \tag{6.11}$$

which gives for the experimental alloy, $h = 2.76\ r$. Another relationship is given by Clauer & Wilcox [81] as:

$$h = \frac{8}{3}\, r\, f^{\frac{1}{2}} + 2r \tag{6.12}$$

which gives $h = 3.19\ r$. Thus, all the above give a different constant in the proportionality but all have a linear relationship between h and r for a constant value of f. Equation (6.8) also appears in Decker's review article [5] but in the form:

$$\Delta\tau_L = 0.2\ G\ B\ \phi\ \frac{2}{\lambda}\ ln\ \frac{d}{2b} \tag{6.13}$$

where λ = mean planar interparticle separation

ϕ = f (angle between Burgers vector and the tangent to the dislocation)

$\Delta\tau_L$ = increase in critical resolved shear stress

Again, planar analysis has been used and λ can be related to r or d.

Both equations (6.8) and (6.13) have been derived for the increase in shear stress due to precipitate particles but, by application of suitable constants, the equations may be transformed to apply for tensile yield stresses.

It is thus proposed that for the experimental alloy in the overaged state that a relationship between the tensile yield stress and the precipitate particle diameter, d, exists in the form:

$$\sigma_y = \sigma_m + A \frac{1}{d} \ln \frac{d}{2b} \qquad (6.14)$$

where σ_y = tensile yield stress

σ_m = tensile yield stress of matrix

A = a parameter dependent on the elastic modulus and the volume fraction of γ'

As was previously mentioned in Section 4.2.4.3, the exact value of the tensile yield stress is difficult to determine and the value of the 0.01% proof stress was obtained experimentally. With no sudden yield effects at the test temperatures, 800°C and 850°C, there will only be a small numerical difference between the absolute yield stress and the 0.01% proof stress and it may be expected that equation (6.14) will still apply. for the 0.01% proof stress values.

For the various times at test temperatures, the particle diameter was predicted using the experimental data in Figure 6.2 and equation (6.5).

The parameter $(1/d) \ln (d/2b)$ was then calculated using a value for b of 2.530 Å [40,82]. The experimental 0.01% proof stress data, given in Table C.1, has been plotted against the calculated values of the parameter in Figure 6.11.

It is seen that at the test temperature of 850°C, a linear relationship

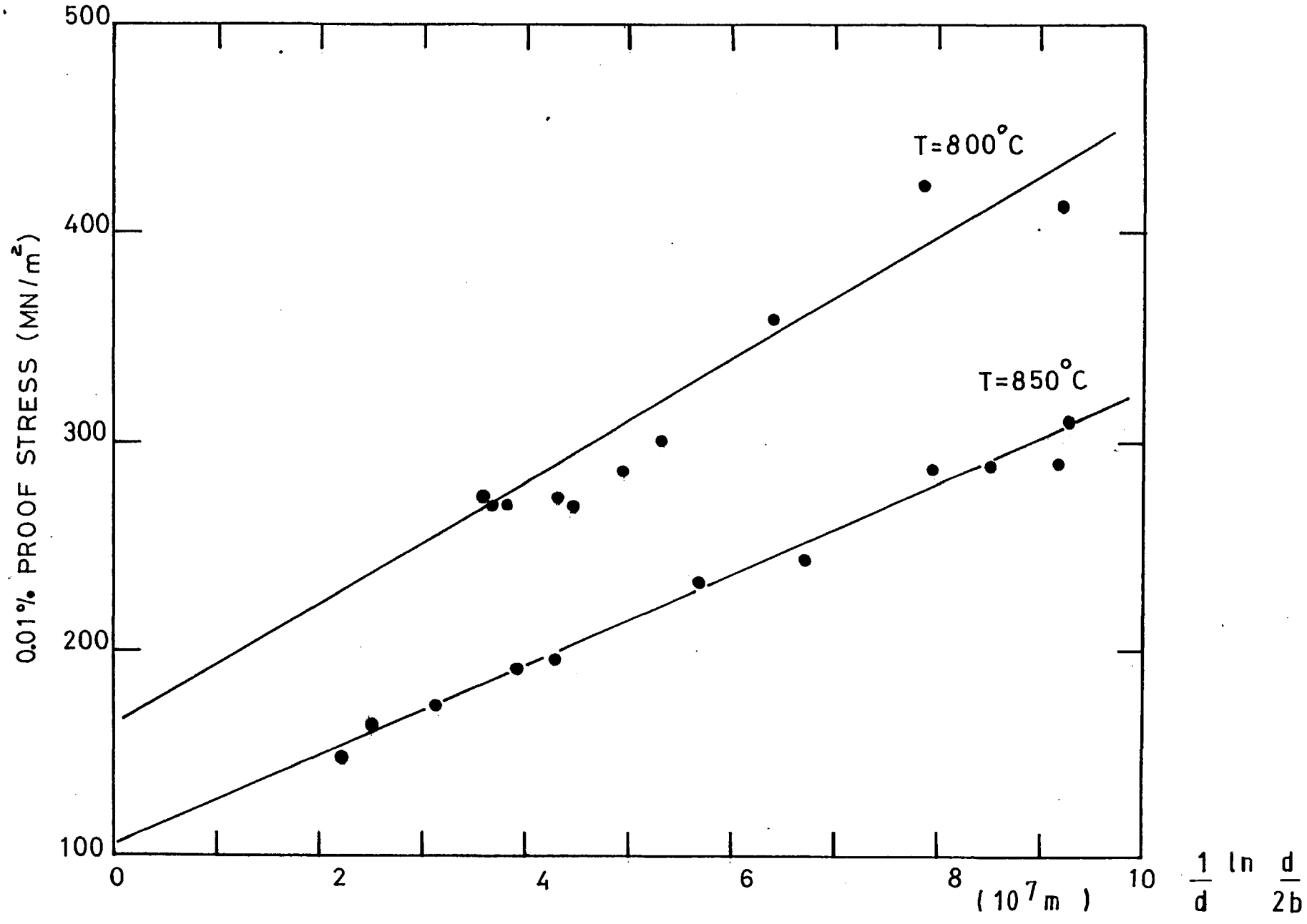

Figure 6.11: Proof stress-γ′ particle diameter relationship as proposed in equation (6.14)

exists but at 800°C there is some scatter and only the general trend is shown. From Figure 6.11, the value of the matrix 0.01% proof stress may be predicted as 160 MN/m^2 at 800°C and 105 MN/m^2 at 850°C. The values given by Beardmore et al [82] for the 0.2% flow stress of the matrix γ are approximately 145 MN/m^2 at 800°C and 117 MN/m^2 at 850°C. The values for 850°C agree closely, the values at 0.2% proof stress being predictably higher, but at 800°C the experimental results predict a too high value. This difference could well be due to the scatter in the data at this temperature causing an error in the prediction. More experimental evidence is needed.

Justification for the linear dependence of the elastic modulus on the constant A, proposed in equation (6.14), may be obtained by considering the ratio of the slopes in Figure 6.11. This gives a value of A_{800}/A_{850} of 1.13, whilst the ratio of mean elastic modulus from Table C.1 gives a ratio of E_{800}/E_{850} of 1.10. The latter value is also that obtained from the average values of elastic modulus taken during the loading periods of the constant stress creep tests. The agreement between the experimental ratios would indicate that the yield stress could be replaced by the rationalised parameter, σ_y/E.

The above analysis has concentrated on the properties of the experimental alloy at the temperatures 800°C and 850°C. For the test temperatures below 800°C, it was not considered that any serious overageing had taken place. In Figure 6.10, it is seen that the macroscopic hardness values at 650°C and 700°C marginally increased with time at temperature, whilst values at 750°C remained essentially constant. These values indicate that the material was at its near maximum hardness after the initial ageing of 16 h at 700°C but no significant overageing occurred at the temperatures 650°C, 700°C and 750°C for the maximum duration of the creep tests; 750 h at 650°C, 2700 h at 700°C, and 1350 h at 750°C.

6.5 CORRELATION OF THE γ' EFFECTS ON MECHANICAL PROPERTIES

Together with Section 4.2.3, this chapter has so far considered the γ' precipitate phase of the experimental nickel base alloy and its relationship with various individual mechanical properties and the external parameters of stress, time and temperature.

In Section 4.2.3, the interaction of the γ' particles with dislocations under creep conditions was observed to have two distinct regimes. Single linear dislocations were only observed with small particle sizes and low total dislocation density. The expected dislocation/particle interaction of particles being cut by dislocations in pairs was not found from the sections studied but this mechanism cannot be ruled out. For larger particle diameters, the dislocations were more often observed as loops around the particles. The transition to the looping interaction was in the range of particle diameters from 200 Å to 500 Å (0.02 μm to 0.05 μm). In Section 6.4, the dislocation/particle interaction of the climb of dislocation loops was also associated with the yielding of the material and a simple relationship was shown to exist between the macroscopic yield stress and the γ' precipitate particle size.

Relationships between the precipitate particle size and creep properties, mainly the creep rate, $\dot{\varepsilon}$, are more complex and varied. Some of the proposed theories were reviewed in Section 1.5. Of possible relevance are the models of Ansell & Weertman relating to the climb of dislocations, as a line, over particles. Assuming that the applied stress and temperature are constant and that the volume fraction of the precipitate phase is constant (hence, $\lambda \propto d$) equations (1.9) and (1.10) may be rewritten as:

$$\text{low stress region} \quad , \quad \dot{\varepsilon} \propto \frac{1}{d^2} \tag{6.15}$$

$$\text{high stress region} \quad , \quad \dot{\varepsilon} \propto \frac{\lambda^2}{d} \propto d \tag{6.16}$$

In Section 6.2, the growth law for the γ' precipitate particle diameter with time was experimentally formulated as:

$$d^3 - d_o^3 \propto t \tag{6.5}$$

For the experimental alloy in the overageing state, $d >> d_o$ and the above relationship may be simplified to $d \propto t^{1/3}$, the approximate relationship proposed by equation (1.1). Substitution in equations (6.15) and (6.16) then gives a time exponent for the creep rate of -2/3 and 1/3 for the low and high stress regions, respectively.

The division of the stress region was at a value of applied stress of $(\mu b)/\lambda$ which is similar in form to the increase in shear stress due to particles, related to the particle spacing by equation (6.7). The calculated value of the above stress is in the region 70 MN/m^2 to 100 MN/m^2 for the test conditions being considered at 800°C and thus the applied stress for the cyclic stress tests falls in the high stress region.

In Section 6.3, the experimental relationship between steady-state creep rate and time presented in Figure 6.6 was shown to have a time exponent of between 1.5 and 5 in the overageing region which is clearly above that proposed by the Ansell & Weertman theories represented by equation (6.16). Figure 6.6 does have a similar form to that proposed by McLean and presented in Figure 1.9. However, for the main area of interest (region 3), no specific time exponent was given for when the climb of dislocation loops was the main deformation mechanism. Thus, the explicit creep rate-time relationship shown in Figure 6.6 cannot be accounted for purely from the growth rate time dependent of the γ'

precipitate under a constant stress.

The dramatic increase in creep strain rate, of over three decades, was also associated with a reduction in the basic tensile yield stress, which was then linked to the Orowan looping mechanism of dislocations in Section 6.4. With the similarity of dislocation deformation mechanisms shown to be operating for both creep and tensile yielding, it is reasonable to propose that for creep of the experimental alloy in the overaged state, an effective stress parameter, σ_e, may take the form of:

$$\sigma_e = \frac{\text{applied tensile creep stress}}{\text{current material yield stress}} \qquad (6.17)$$

As was explained in Section 6.4, the exact yield stress is difficult to determine experimentally and the value of the 0.01% proof stress is thus substituted to give:

$$\sigma_e = \frac{\text{applied tensile creep stress}}{\text{current material 0.01\% proof stress}} \qquad (6.18)$$

This parameter was the first proposed to incorporate the direct driving force for creep, the applied tensile stress, and a measure of the internal weakening of the material due to the growth of the γ' precipitate phase, the current material 0.01% proof stress [93].

To determine values of the 0.01% proof stress for the experimental alloy, a value of the γ' precipitate particle size was first predicted by equation (6.5). Figure 6.11 was then used to find the value of the proof stress and the effective stress parameter given by equation (6.18). Figure 6.12 shows the relationship found between the effective stress parameter and the creep strain rate for the test temperature of 800°C, under conditions of constant and cyclic stresses. Also included is some constant stress creep rate data at 789°C [95]. The relationship for a

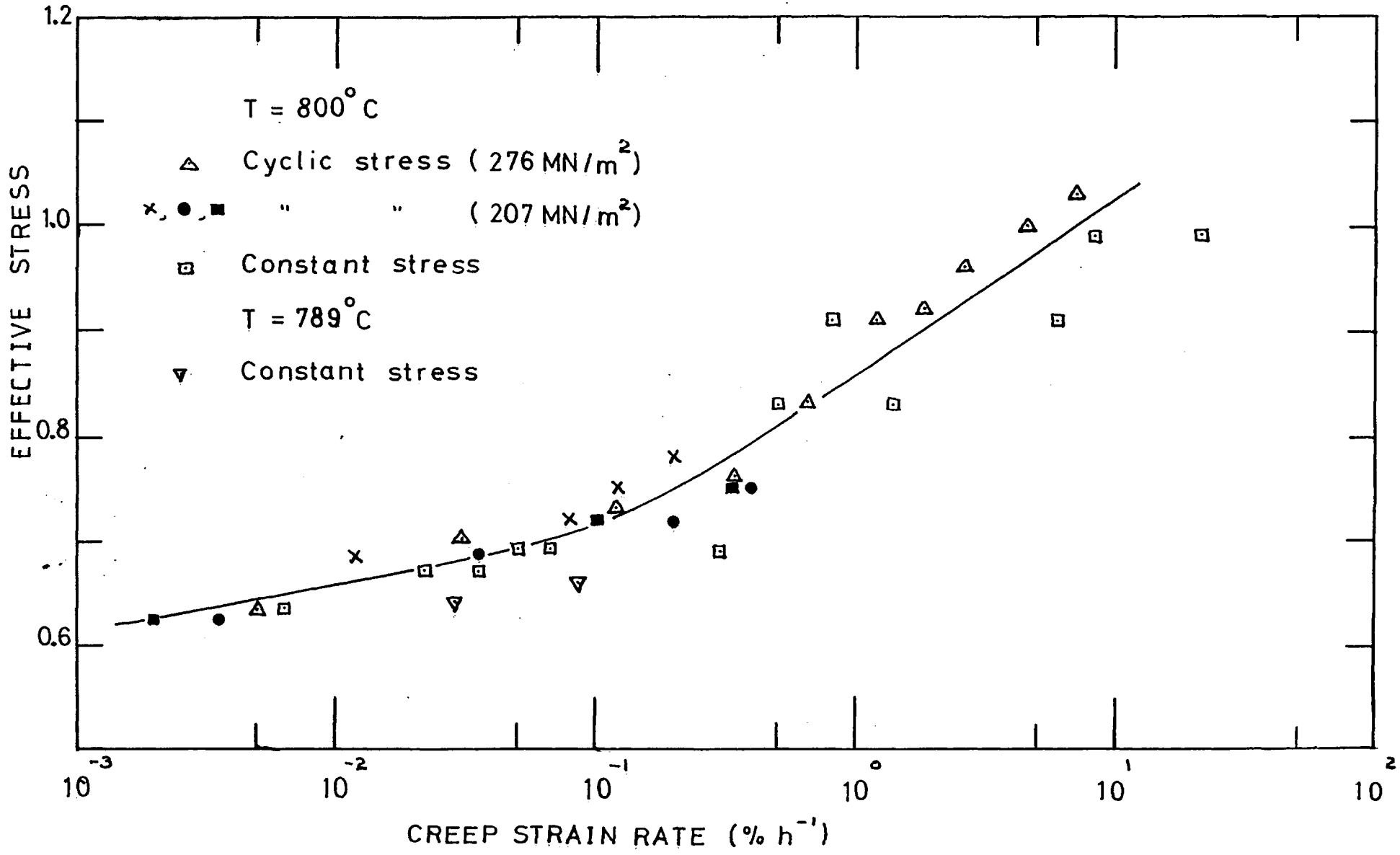

Figure 6.12: Effective stress versus creep strain rate at temperatures 789°C and 800°C

temperature of 850°C is shown in Figure 6.13. In both figures, data for the creep strain rate is only included for when the γ' precipitate particle diameter was greater than 500 Å (0.05 μm).

It is now seen that there is a unique relationship between the effective stress parameter and the creep strain rate at each test temperature. The effective stress parameter derived has thus described fully the creep strain rate, independent of time at temperature, in the range of stresses and temperatures tested.

If a simple power law relationship is expected between the creep strain rate and the effective stress, then for the limited range of conditions tested, a stress exponent of between 11 and 26 exists, the higher value occurring at the lower values of effective stress. The effective stress range covered was from 0.6 to 1.2. The effective stress functions shown in Figures 6.12 and 6.13 are very similar with the curves being translated on the effective stress axis. This would suggest that temperature is still a relevant variable and the final relationship for the creep strain rate should be of the form:

$$\dot{\varepsilon} = f(\sigma_e, T) \tag{6.19}$$

or in a more useful way:

$$\dot{\varepsilon} = f(\sigma_e)\, g(T). \tag{6.20}$$

In Section 5.3, it was shown that over a wide range of conditions that a relationship between the steady-state creep strain rate and the time to rupture existed in the form:

$$\dot{\varepsilon}_s \times t_R = constant = f(T) \tag{5.16}$$

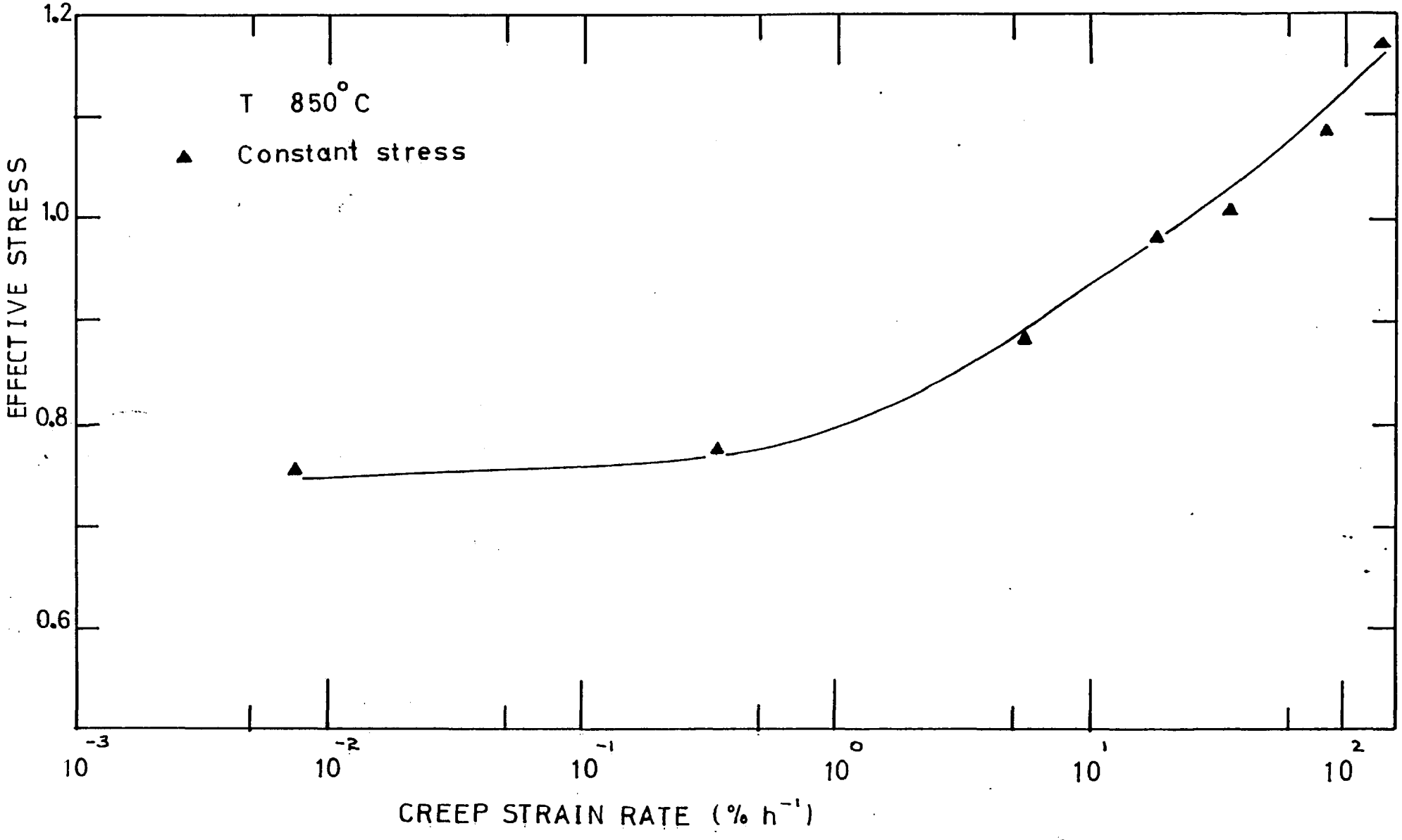

Figure 6.13: Effective stress versus creep strain rate at 850°C

It may then be possible to combine equations (5.16) and (6.20) to give:

$$f(\sigma_e) \times t_R = constant = h(T) \qquad (6.21)$$

which could then be used to estimate the remaining life of engineering components which had suffered overageing, or were operating in such conditions permanently. The measure used to characterise the overageing has been the 0.01% proof stress. For a material which did not have the full experimental data, this could be obtained from the relationship postulated by equation (6.14). Another possible method may be to relate the macroscopic hardness to the yield stress, a relationship which exists closely for steels but for which there is no published data for nickel base alloys.

CHAPTER 7

GENERAL DISCUSSION

The main aims of this research project were:

(a) to describe the creep properties of a gas turbine alloy in the practical operating range of stresses and temperatures;
(b) to explain the results in empirical, physical and theoretical terms.

To minimise the metallurgical complications of modern nickel base alloys one of the most basic precipitation hardened alloys was chosen, based on the commercial alloy Nimonic 80A. The experimental alloy contained only four chemical additions to the base nickel; chromium for solid solution strengthening, titanium and aluminium for the γ' precipitate hardening particles, and carbon. The latter constituent was in a lower concentration than normal in order to minimise possible complications from grain boundary carbides. The carbides formed did not influence any grain boundary deformation or denuded areas of γ' precipitate.

The predominant use of the experimental alloy in the directionally solidified grain form was hoped to eliminate many of the effects of the transverse grain boundaries which can be critical under creep conditions (see Section 1.3). This was only successful in the higher range of test temperatures, greater than 750°C, where creep ductilities and reduction in area at fracture were high. However, as a result of the short areas of transverse grain boundaries in the interdendritic regions, creep ductilities and life in the lower temperature range were influenced by failure which initiated at these transverse grain boundaries.

The poor performance of the equi-axed grain form of the material in

terms of creep life and ductility could be partly explained by the large grain size in comparison to the test specimen diameter but the main conclusion is that grain boundaries transverse to the stress axis are a major source of creep failure.

On a commercial basis, there are many cast components used in high stressed regions of gas turbines, including complete blade/disc units. However, for these cases, there is rigid control of the grain size in critical load bearing areas. In many cases, individual test pieces are machined from these areas to determine the relevant creep strengths and properties.

It is also noted that for the directionally solidified grain form only the exothermic mould produced material was tested, whereas Northwood & Homewood showed that by using a moving furnace technique, the creep life could be further improved. Thus, it cannot be claimed that the ultimate improvement in creep life and ductility over the equi-axed grain form through directional solidification has been found. It was the basic properties of the alloy which were more relevant than the ultimate strength and/or creep resistance.

Tests performed on the experimental alloy have taken both the mechanical and metallurgical forms. They may be summarised by:

Mechanical
- constant stress creep tests
- cyclic stress creep tests
- tensile yield stress as a function of time and temperature

Metallurgical
- macroscopic aspects of deformation and fracture
- study of the γ' phase morphology
- dislocation/particle interactions

From the constant stress creep tests, no simple picture of creep deformation emerged. The shape of the creep strain-time plots was a function of both stress and temperature. In the analysis of Section 4.2.1, the shapes of the plots were characterised into five groups, together with a new definition of $\dot{\varepsilon}_s$, the secondary creep rate. This is usually defined as the minimum creep rate but for the directionally solidified grain form, the minimum creep rate was not necessarily the secondary creep rate. In Figure 1.1, the secondary state, C, was shown as a period of reduced constant strain rate but, as was shown in Figure 4.5, under certain conditions, at temperatures at and above 800°C, the constant strain rate stage had a significantly greater value than the initial and second stages of creep.

All the five shapes of curves, however, could be said to be part of the unified creep strain-time curve shown in Figure 1.1.

It is noted that the form of the data used in the above analysis was a linear plot of creep strain versus time. The logarithmic plot of creep strain versus time may be considered to be more relevant if a total analysis of the creep strain-time relationship is desired. For many engineering applications, it is the steady-state creep rate and rupture parameters which are more relevant and these are more readily available from the linear plot. The material used was a nickel base alloy which is commonly used at high temperatures and high stresses in gas turbines. Creep lives of components can be based on either the rupture life or on a creep strain.

This is in comparison to the steel based alloys used in the electric power generation areas, where only very small strains can be tolerated over times of the order of 100,000 h.

With some degree of uniformity amongst the experimental creep strain versus time data, the empirical approach to the analysis may have been

expected to produce a reasonable set of parameters. The activation energy approach used in Section 5.3 is not the only method available, as was reviewed in Section 1.6, but is one which can have physical significance. However, no single value of activation energy could be found for the creep parameters fitted, ranging from the time to 0.1% creep strain to the time to fracture and the steady-state creep rate. The values of activation energy for creep were in the range 480 kJ/mol to 630 kJ/mol which is of the order of twice that for the self-diffusion of nickel. This was the first indication that more than one microstructural process was occurring during the creep tests and that the material could not be considered to have a constant structure. Also, significantly, it was not possible to find a single stress function that would fit for all the parameters. It would have been expected that with the difficulties experienced with the simple power-law and exponential law functions, that the combined terms of equation (5.15) would fit, but this was shown in Section 5.3.1 to be not the case.

A physical basis was also used in Section 5.2, where the creep strain-time equations based on dislocation dynamics were fitted to the data. The five-parameter model (equation (5.1)) is capable of fitting all sections of the creep curve shown in Figure 1.1, but not necessarily all at once. Thus, some discretion had to be made in the area of experimental creep data fitted, e.g. whether to consider the 'tertiary' stage, D, in Figure 1.1, as corresponding to the steady-state creep rate stage. With the three-parameter model (equation (5.2)), this is not such a serious problem as the incubation period cannot be accommodated in this form. If gross errors had been made in the selection of experimental data to be covered, it would be expected that this would become evident in the values of the parameters found from the analysis. This was not the case as meaningful relationships between the applied stress and A, ϕ and α were

found and the parameters B and B' followed a general trend. The relationships between A and ϕ confirmed that, for the material, the first order reaction rate theory of Webster, Cox & Dorn applied.

The dislocation dynamics approach was expected to provide some physical insight into the creep strain-time relationships investigated but, as was discussed in Section 5.2.1, difficulties arose in relating the parameters in the three- and five-term models to the experimental dislocation density and geometry. No exact dislocation densities could be measured once the particles reached 400 Å to 500 Å (0.04 μm to 0.05 μm) due to the complex meshes formed and the interactions with the particles.

The five-parameter model is based on sound dislocation dynamics theory but some modification is required to improve the prediction of the initial creep strain and strain rate on the completion of loading. It may be that some creep is occurring during the loading time and that this must be taken into account.

There is also a great need to accurately measure the mobile dislocation density for the duration of the creep test. The advent of the high power 1 MV electron microscope may lead to full tests being carried out *in situ*, although the complex interactions between grain boundaries, second phase particles and dislocations may not be all seen in the thin sections used.

The growth of the γ' precipitate particles was one of the main metallurgical features of the microstructural changes found in the experimental alloy with exposure to temperature and stress. The growth of the γ' particles was found:

i) to be independent of strain and applied stress;

ii) to have, in general, a constant spherical shape;

iii) to have a diameter, time and temperature dependence of the form:

$$d^3 - d_o^3 = A\ (exp - Q/RT)\ t$$

These findings do not all agree with previous studies on nickel base alloys. As was discussed in Section 1.4.2, the influence of stress on morphology is to some degree dependent on the volume fraction of the precipitate and the elastic constants of the matrix and precipitate. For the experimental alloy, the expected misfit between the γ' precipitate and matrix lattice parameters is 0.5%. According to previous work, this would suggest that the precipitate would be cubic and have a shape which was stress dependent. However, these effects were not observed in any section and the experimental alloy behaved in a similar manner to the commercial alloy Nimonic 80A as far as growth laws and morphology of the γ' phase are concerned. Despite the expected high misfit parameter, no coherency strains were observed.

It is noted that all the observations of γ' precipitate morphology and dislocation structure were taken from sections cut in a transverse plane to the stress axis. It was not thought that the main findings would be influenced by the angle of the crystal plane to the stress axis but if exact values of dislocation densities are to be determined for the experimental alloy, then other planes should be considered.

Because of the complex changes, and influences, of the microstructure, it is not to be totally unexpected that the empirical and physical approaches had limited validity. Thus, further tests were made to resolve and quantify the effects of time and temperature on the structure. Two independent sets of data were obtained, the yield stress and interrupted stress creep data. The yield stress as a function of time at temperature was resolved with the help of the γ' particle growth

analysis and the observations of the γ' particle/dislocation analysis. The latter showed that there was a change in dislocation deformation mechanism, from cutting to looping, at a γ' particle diameter in the area of 500 Å (0.05 μm).

A relationship between the yield stress and the γ' particle diameter for when the particle diameter was greater than 0.05 μm was confirmed by the equation:

$$\sigma_{0.01\%PS} = \sigma_{matrix} + A \frac{1}{d} ln \frac{d}{2b}$$

The need to substitute the proof stress for the yield stress was explained in Section 6.4. The above relationship only covers part of the total relationship between particle diameter and yield stress, as was shown in Figure 1.5, for the experimental alloy. However, there should be a general application of the above relationship to many precipitation hardened alloys, provided the condition of a constant volume fraction of the precipitate and a dislocation looping mechanism is met. The above relationship has been shown to apply for a nickel-thoria dispersion hardened alloy by Durber & Davies [96] where the particle size was kept constant but the spacing parameter, λ, varied. It is surprising that no observations were made on any growth of the second phase particles during the creep tests which were at temperatures of 0.7 T_m and 0.8 T_m.

From the proof stress-time relationship, the behaviour of the experimental alloy in the constant stress tests, at 800°C and above, and the interrupted creep tests became clearer. It was reasoned that the effective stress for creep was not purely the applied stress but a proportion of it. The empirical parameter, applied stress/yield stress (or 0.01% proof stress), was thus evolved and found to be in good agreement with the experimental data as a stress parameter.

In Section 1.6, some of the internal stress theories relating to creep

deformation which followed the work presented in this thesis were reviewed. In the early work of Sidey & Wilshire [47], the reduction in the driving force for creep by an internal stress, σ_o, was only single valued and experimentally found over a narrow range of conditions. Since then internal stress measurements by the progressive stress reduction method have indicated that the internal stress is a function of the material, the applied creep stress, the test temperature and of the time under load.

All the internal stress studies presented have been from an experimental basis, although Harrison & Evans [97] have indicated that the internal stress has two components, an inherent friction stress related to the minimum stress for dislocations to by-pass particles and a stress function related to the build up of non-active dislocation substructure during primary creep.

The internal stresses measured have, in general, had a linear dependence on the applied creep stress up to a point where the internal stress is then at a constant value. No significance has been placed on the steady-state value, although Wilshire & Threadgill [59] indicated that for several alloys, it was similar in value to the yield stress. This has not been reported by other authors.

Despite the unknown exact origin of the internal stress, the steady-state creep rates for many alloys and single-phase materials have been represented by:

$$\dot{\varepsilon}_s \propto (\sigma - \sigma_o)^n \exp\left(-\frac{Q}{RT}\right)$$

where the value of n is either 3.5 or 4. Similar reasoning to that presented in Section 6.5 was then used by Harrison [69] and Evans & Harrison [95] to normalise the effective stress, $(\sigma - \sigma_o)$, by dividing by the 0.05% proof stress. When this was done, then the secondary creep

rates were related by a simple form of:

$$\dot{\varepsilon}_s = B \left(\frac{\sigma - \sigma_o}{\sigma_{0.05\%PS}}\right)^{3.5}$$

which superimposed data for many single-phase and two-phase alloys, i.e. the constant B was independent of material, crystal lattice, microstructure and also temperature. This is to some extent surprising in that the initial reasoning is based on similar dislocation dynamics for each material but in the case of single-phase alloys, there are no second-phase particles to form the common dislocation/particle interaction expected.

In the above analysis by Harrison, constant values of the 0.05% proof stress were used and no allowance was made for any change in microstructure and its subsequent effect on yielding, as was clearly shown for the experimental alloy in Section 6.4. It was also proposed that the temperature function normally associated with secondary creep rate theories was fully incorporated in the temperature dependence of the 0.05% proof stress. This is not strictly the case as the internal stress, σ_o, was also shown to be a function of temperature.

The temperature dependence of an internal stress function would also explain why there was still a temperature function for the effective stress parameter presented in this work, i.e.

$$\dot{\varepsilon} = f(\sigma_e)\, g(T)$$

The evaluation of this temperature dependence would be a useful complement to the above internal stress theories and may extend their range to the higher creep rates and creep strains found for the experimental alloy.

The final use of the effective stress theory presented in Section 6.5 was the proposal of the relationship:

$$f(\sigma_e) \times t_R = constant = h(T)$$

which could be a useful tool for predicting rupture properties of gas turbine components, and other highly stressed engineering components operating in the high temperature regime greater than 0.5 T_m.

Thus, a possible creep life prediction method for practical applications has been found using mechanical and metallurgical tests, together with physical and phenomenological analysis. This was one of the main aims of this work. The data have been presented in individual sections on mechanical tests and microscopic observations, but at all times a general viewpoint was being made on the interaction between structure and properties.

CHAPTER 8

CONCLUSIONS

1. The creep properties of time to rupture and rupture strain for the basic nickel base alloy of composition (wt%) 19.5 Cr, 2.6 Ti, 1.4 Al, 0.06 C, balance Ni are enhanced over the cast equi-axed grain form when the material is tested in the directionally solidified cast form with the tensile creep stress axis in the <001> direction. Below a test temperature of 800°C, the short transverse interdendritic grain boundaries of the directionally solidified form have some influence on creep strain and fracture.

All further conclusions are related to the directionally solidified form of the alloy.

2. Empirical analysis of time to 0.1% creep strain, time to 2% creep strain, time to rupture, and the steady-state creep rate has not produced unique stress and temperature functions.

The stress functions σ^n and $exp\ b\sigma$ can both be used to represent the data over certain ranges of stress. The value of n varies from 4 to 20 and that of b from 0.028 $(MN/m^2)^{-1}$ to 0.033 $(MN/m^2)^{-1}$. The combined function $\sigma^{n-1}\ sinh\ b\sigma$ was not found to be applicable.

The temperature function can be represented from an activation energy approach, the value being between 480 kJ/mol and 630 kJ/mol. This is the range of twice the value for the activation energy for the self-diffusion of nickel.

3. The creep strain-time relations, based on dislocation dynamics, of:

$$\varepsilon = A\ t + D\ ln\ [B + (1-B)\ exp\ -\phi t] + \frac{C\ (1-B)(1-exp-\phi t)}{B + (1-B)\ exp\ -\phi t}$$

and:

$$\varepsilon = A' \alpha t + A' \ln [B' + (1-B') \exp - \alpha t]$$

are both valid for the experimental alloy. Of the 27 constant stress tests, creep data fitted to the second of the relationships gave a better least squared error fit for 17 cases.

No definite stress and temperature functions were found for the parameters B, C, D and B'. The values of A and the product $A'\alpha$ were similar to the steady-state creep rates found experimentally. There was a form of linear relationship between A, equivalent to the steady-state creep rate, and ϕ, the rate of exhaustion of primary creep, which follows the first order reaction rate theory of Webster, Cox & Dorn (Appendix G).

No direct link could be made between all of the parameters and dislocation densities from the mathematical viewpoint and the measurement of dislocation densities from electron micrographs was not possible.

4. The morphology of the γ' precipitate particle phase was found to be essentially spherical for all temperature tests and to have a constant volume fraction of 19%.

The γ' precipitate particle diameter was found to have a growth law of the form:

$$d^3 - d_o^3 = A \left(\exp - \frac{Q}{RT}\right) t$$

where d_o = 0.01 μm

A = 9.3×10^{-10} m^3/h

Q = 302 kJ/mol

for particles growing from the standard heat treated condition of the commercial alloy Nimonic 80A.

Observations of the dislocations in creep tested specimens indicated that above a particle size of between 0.02 μm and 0.05 μm, the dislocations by-passed the γ′ precipitate particles by a looping mechanism.

5. At temperatures of 800°C and above, the decrease in macroscopic yield stress associated with the increase in γ′ precipitate particle size could be represented by:

$$\sigma_{0.01\%PS} = \sigma_{\substack{0.01\%PS \\ matrix}} + A \frac{1}{d} \ln \frac{d}{2b}$$

where A is a function of temperature.

6. Under creep conditions where the dislocation deformation mechanism is by the by-passing of particles by loops, the creep strain rate is a function of an effective stress parameter:

$$\sigma_e = \frac{applied\ creep\ stress}{current\ material\ 0.01\%\ proof\ stress}$$

and temperature only. The relationship may be of the form:

$$\dot{\varepsilon} = f(\sigma_e)\, g(T)$$

Provided that the above holds, then a useful method of predicting life of gas turbine components may be found from:

$$f(\sigma_e)\, t_R = constant = h(T)$$

7. Future work indicated by the work presented in this thesis is:

i) Verifying and formulating the exact stress and temperature functions in the above two equations.

ii) Means of measuring the mobile dislocation density as a function of stress, temperature and time which can then be used to confirm the parameters of the dislocation dynamics models.

iii) Correlating the effective stress parameter derived with other internal and friction stress theories.

REFERENCES

[1] WEBSTER, G.A.

Phil. Mag., 14 (1966) 775.

[2] WEERTMAN, J.

Trans. ASM, 61 (1968) 681.

[3] KLAHN, D., MUKHERJEE, A.K., & DORN, J.E.

"Strain-rate effects",

Paper presented at 2nd Int. Conf. on the Strength of Metals and Alloys, ASM, Asilomar, California (1970).

[4] CONRAD, H.

Joint Int. Conf. on Creep, I Mech E, London (1963) 1-9.

[5] DECKER, R.F.

"Strengthening mechanisms in nickel base superalloys",

Paper presented at Symp. on Steel Strengthening Mechanisms, Zürich (May 1969); published by Climax Molybdenum Company.

[6] DECKER, R.F., & SIMS, C.T.

in The Superalloys, (ed. C.T. Sims & W.C. Hagel), John Wiley & Sons (USA) (1972) 42.

[7] NIMONIC ALLOYS: PHYSICAL AND MECHANICAL PROPERTIES

Henry Wiggin Publication (January 1970).

[8] VER SNYDER, F.L., & GUARD, R.W.

Trans. ASM, 52 (1960) 485.

[9] PIEARCEY, B.J., & TERKELSEN, B.E.

Trans. Met. Soc., AIME, 239 (1967) 1143.

[10] PIEARCEY, B.J., & VER SNYDER, F.L.

J. Aircraft, 3 (1966) 390.

[11] KEAR, B.H., & PIEARCEY, B.J.

Trans. Met. Soc., AIME, 239 (1967) 1209

[12] LEVERANT, G.R., & GELL, M.

Trans. Met. Soc., AIME, 245 (1969) 1167.

[13] NORTHWOOD, J.E., & HOMEWOOD, T.

Paper No. 25, 9th Int. Commonwealth Mining and Metallurgical Conf., London (1969).

[14] VER SNYDER, F.L.

"Basic problems underlying high temperature material development", Paper presented at 2nd Int. Conf. on the Strength of Metals and Alloys, ASM, Asilomar, California (1970).

[15] LUND, C.H.

Foundry Trade Journal (May 1970) 815.

[16] LEVY, I.S.

"Unique thermomechanical process techniques to improve elevated temperature properties in austenitic stainless steels and nickel base alloys",

Battelle Northwest Publication.

[17] VARIN, J.E.

in The Superalloys, (ed. C.T. Sims & W.C. Hagel), John Wiley & Sons (USA) (1972) 255.

[18] RAYMOND, L., & DORN, J.E.

Trans. Met. Soc., AIME, 230 (1964) 560.

[19] MUKHERJEE, A.K., BIRD, J.E., & DORN, J.E.

Trans. ASM, 61 (1968) 697.

[20] BARRET, C.R., NIX, W.D., & SHERBY, O.D.

Trans. ASM, 59 (1966) 3.

[21] GAROFALO, F., RICHMOND, O., DORMIS, W.F., & VON GEMMINGEN, F.

Joint Int. Conf. on Creep, I Mech E, London (1963) 1-31.

[22] McLEAN, D., & GIFKINS, J.

J. Inst. Met., 89 (1960-61) 29.

[23] THREADGILL, P.L. & WILSHIRE, B.

Met. Sci. J., 8 (1974) 117.

[24] McLEAN, D.

Mechanical Properties of Metals, John Wiley & Sons, New York (1962).

[25] PIEARCEY, B.J., KEAR, B.H., & SMASHEY, R.W.

Trans. ASM, 60 (1967) 634.

[26] DYSON, B.F., & McLEAN, D.

Met. Sci. J., 6 (1972) 220.

[27] HAGEL, W.C., & BEATTIE, H.J.

"Precipitation processes in steel",

Iron & Steel Institute (1959) 98.

[28] HESLOP, J.

Cobalt, 24 (September 1964) 128.

[29] MITCHELL, W.I.

Zeitschrift für Metallkunde, 57 (1966) 586.

[30] ROWE, J.P., & FREEMAN, J.W.

Joint Int. Conf. on Creep, I Mech E, London (1963) 1-65.

[31] TIEN, J.K., & COPLEY, S.M.

Metall. Trans., 2 (January 1971) 215.

[32] TIEN, J.K., & COPLEY, S.M.

Metall. Trans., 2 (January 1971) 543.

[33] WAGNER, C.

Z. Elektrochem., 65 (1961) 581.

[34] ORIANI, R.A.

Acta Met., 12 (1964) 1399.

[35] ARDELL, A.J., & NICHOLSON, R.B.

Acta Met., 14 (1966) 1295.

[36] BILSBY, C.F.

PhD Thesis, Cambridge (1967).

[37] ROWE, J.P., & FREEMAN, J.W.

Proc. I Mech E, 178 (3A) (1963-64) 1-65.

[38] KELLY, A., & NICHOLSON, R.B.

Progr. Mat. Sci., 10 (1963) 379.

[39] GLEITER, H., & HORNBOGEN, E.

Mat. Sci. & Eng., 2 (1967-68) 285.

[40] COPLEY, S.M., & KEAR, B.H.

Trans. Met. Soc., AIME, 239 (1967) 984.

[41] JOHNSON, W.G., & GILMAN, J.J.

J. Appl. Phys., 30 (1959) 127.

[42] GILMAN, J.J.

Trans. ASM, 59 (1966) 597.

[43] ANSELL, G.S., & WEERTMAN, J.

Trans. Met. Soc., AIME, 215 (1959) 840

[44] SHERBY, O.D., & BURKE, P.M.

"Mechanical behaviour of crystalline solids at elevated temperatures", Materials Science Department Report SU-DMS No. 67-33, Stanford University, Stanford, California.

[45] McLEAN, D.

Metall. Revs., 7 (1962) 481.

[46] EVANS, W.J., & WILSHIRE, B.

Trans. Met. Soc., AIME, 242 (1968) 2514.

[47] SIDEY, D., & WILSHIRE, B.

Met. Sci. J., 3 (1969) 56.

[48] EVANS, H.E., & WILLIAMS, K.R.

Phil. Mag., 25 (January-June 1972) 1399.

[49] AMIN, K.E., MUKHERJEE, A.K., & DORN, J.E.

J. Mech. Phys. Solids, 18 (1970) 413.

[50] LI, J.C.M.

Acta Met., 11 (1963) 1269.

[51] LAGNEBORG, R.

Met. Sci. J., 3 (1969) 18.

[52] MODÉER, B., & LAGNEBORG, R.

Jernkont. Ann., 155 (1971) 363.

[53] LAGNEBORG, R., FORSÉN, B.-H., & WIBERG, J.

Jernkont. Ann., 155 (1971) 322.

[54] KENNEDY, A.J.

Processes of Creep and Fatigue in Metals, Oliver & Boyd, Edinburgh (1962) 131.

[55] GRAHAM, A.

The Engineer, 198 (1952) 234.

[56] DORN, J.E.

"The spectrum of activation energies for creep",

Paper presented at Symp. on Creep and Recovery, ASM, Cleveland, Ohio (1956).

[57] GOLDHOFF, R.M.

Trans. ASME, J. Basic Eng., (December 1959) 629.

[58] LUBHAN, J.D., & FELGAR, R.P.

Plasticity and Creep of Metals, John Wiley & Sons, New York (1961) 205.

[59] WILSHIRE, B., & THREADGILL, P.L.

Conf. on Creep Strength in Steel and High Temperature Alloys, Iron & Steel Institute, Sheffield (September 1972).

[60] PENNY, R.K., ELLISON, E.G., & WEBSTER, G.A.

Mat. Res. Stand., 6 (1966) 77.

[61] TISHLER, D.N., & WELLS, C.H.

Mat. Res. Stand., 6 (1966) 20.

[62] RICHARDS, E.G.

J. Inst. Met., 96 (1968) 365.

[63] COTTRELL, A.H.

Dislocations and Plastic Flow in Crystals, Oxford University Press (1952) 18.

[64] WEBSTER, G.A., & PIEARCEY, B.J.

Met. Sci. J., 1 (1967) 97.

[65] GAROFALO, F.

Fundamentals of Creep and Creep Rupture in Metals, McMillan, New York (1965).

[66] NIX, W.D., & BARRETT, C.R.

Trans. ASM, 61 (1968) 695.

[67] GRAHAM, A., & WALLES, K.F.A.

J. Iron & Steel Inst., 179 (1955) 105.

[68] LLOYD, C.J., & McELROY, R.J.

Acta Met., 22 (1974) 339.

[69] HARRISON, G.F.

PhD Thesis, University of London (May 1975).

[70] WALLES, K.F.A.

"A quantitative presentation of the creep of Nimonic alloys", N G T E Note No. NT386.

[71] DAVIES, P.W., NELMES, G., WILLIAMS, K.R., & WILSHIRE, B.

Met. Sci. J., 7 (1973) 87.

[72] WILLIAMS, K.R., & WILSHIRE, B.

Met. Sci. J., 7 (1973) 176.

[73] INTRODUCTION TO THE STRUCTURE OF NIMONIC ALLOYS

Henry Wiggin Company Limited, Publication No. 3563 (May 1971).

[74] ASHBY, M.F.

Z. Metall., 55 (1964) 5.

[75] FULLMAN, R.L.

Trans. AIME, 197 (1953) 447.

[76] GREENWOOD, G.W.

Acta Met., 4 (1956) 243.

[77] STRUCTURES OF NIMONIC ALLOYS

Henry Wiggin Publication No. 3563 (September 1974).

[78] MITCHELL, W.I., & WAKEMAN, D.W.

"Origins of resistance to creep and rupture of some commercial high temperature alloys",

International Nickel Publication.

[79] PROBERT, K.S.

PhD Thesis, University of Cambridge (1968).

[80] OROWAN, E.

Symp. on Internal Stress in Metals and Alloys, Institute of Metals (1948) 451.

[81] CLAUER, A.H., & WILCOX, B.A.

Met. Sci. J., 1 (1967) 984.

[82] BEARDMORE, P., DAVIES, R.G., & JOHNSTON, R.L.

Trans. Met. Soc., AIME, 245 (1969) 1537.

[83] DYSON, B.F., & RODGERS, M.J.

Met. Sci. J., 8 (1974) 26.

[84] LARSON, F.R., & MILLER, J.

Trans. ASME, 74 (1952) 765.

[85] NIMONIC ALLOYS: PHYSICAL AND MECHANICAL PROPERTIES

Henry Wiggin Publication No. 3270 (January 1970).

[86] NIMONIC ALLOY 80A

Henry Wiggin Publication No. 3663 (April 1975).

[87] DYSON, B.F., & McLEAN, D.

"Predicting and prolonging creep life",

NPL IMS Internal Report No. 44, Project 14 (August 1971).

[88] BETTERIDGE, W.

The Nimonic Alloys, Edward & Arnold Limited, London (1959).

[89] SCARBOROUGH, J.B.

Numerical Mathematical Analysis, John Hopkins Press, Oxford (1950) 478.

[90] BROWN, L.M., & HAM, R.K.

in Strengthening Methods in Crystals, (ed. A. Kelly & R.D. Nicholson), Applied Science Publishers, London (1971) Chapter 2.

[91] TOUGH, E.

Private communication, Rolls-Royce Small Engine Division, Leavesdon.

[92] EVANS, W.J., & HARRISON, G.F.

Met. Sci. J., 13 (1979) 641.

[93] COX, A.P.D.

"The influence of material structure on creep in a nickel base alloy", Paper presented at Symp. on Forecasting the Mechanical Performance of a Material, Imperial College, 28-29 March 1972.

[94] EVANS, W.J., & HARRISON, G.F.

"The development of a universal equation for secondary creep rates in pure metals and engineering alloys",
N G T E Report No. R340 (January 1976).

[95] ABDUL HAMEED, M.

Private communication.

[96] DURBER, G.L.R., & DAVIES, T.J.

Met. Sci. J., 8 (1974) 225.

[97] HARRISON, G.F., & EVANS, W.J.

in Strength of Metals and Alloys, (ed. P. Haasen et al), Pergamon Press (1979) 239.

APPENDIX A

CONSTANT STRESS CREEP DATA FOR DIRECTIONALLY SOLIDIFIED GRAIN FORM

Test Number N	Cast Number	Stress (MN/m^2)		Rupture Time (h)	Rupture Strain (%)	Reduction in Area (%)	Hardness, H_v		Elastic Modulus (GN/m^2)	
		Nominal	Actual				Initial	Final	At Room Temperature	At Test Temperature
47	66B2	-	517	736.1	≈5	23	-	387	136	97
26	67B4	552	563	336.0	(2.0)	(3)	378	380	133	108
29	73B4	552	554	44.6	(0.7)	(3)	-	348	-	115
50	64A3	586	598	253.9	8.6	19	349	365	139	117
24	67B2	655	683	47.0	14.7	37	329	332	126	108
35	71A1	689	721	6.7	(3.1)	(16)	333	354	139	108
48	64A4	689	736	9.1	12.4	22	328	346	130	99

( ) Unbroken specimen

Figure A.1: Constant stress creep tests at 650°C

Test Number	Cast Number	Stress (MN/m^2)		Rupture Time (h)	Rupture Strain (%)	Reduction in Area (%)	Hardness, H_v		Elastic Modulus (GN/m^2)	
N		Nominal	Actual				Initial	Final	At Room Temperature	At Test Temperature
13	68A3	-	414	2682.7	≈10	44	360	388	131	123
34	73B5	-	448	111.7	≈0.5	17	337	373	-	112
11	68A1	-	448	386.1	≈1.6	23	363	380	130	-
15	68B2	-	483	95.2	(0.4)	(0)	343	383	115	107
14	68B1	-	517	14.7	0.3	7	328	-	120	100
18	68B5	-	517	40.3	3.3	20	340	368	125	103
56	69B1	-	517	24.3*	(0.9)	(1)	-	353	138	106
16	68B3	-	552	0.2	0.2	19	360	365	126	110
17	68B4	-	552	32.3	7.2	9	326	-	116	99
12	68A2	586	596	5.5	5.9	18	340	385	100	102
55	75A4	621	641	5.9	13.4	39	-	364	130	95

( ) Unbroken specimen ; * Interrupted test

Figure A.2: Constant stress creep tests at 700°C

Test Number N	Cast Number	Stress (MN/m^2) Nominal	Stress (MN/m^2) Actual	Rupture Time (h)	Rupture Strain (%)	Reduction in Area (%)	Hardness, H_v Initial	Hardness, H_v Final	Elastic Modulus (GN/m^2) At Room Temperature	Elastic Modulus (GN/m^2) At Test Temperature
8	73A	-	241	1322.0	(0.1)	(0)	345	343	128	100
4	69A	-	276	364.0	(0.1)	(0)	315	350	151	134
32	73B3	-	310	334.0	2.6	25	340	358	132	-
36	71A2	-	310	436.4	(3.2)	(4)	336	324	-	-
9	75A	-	345	164.2	(0.2)	(0)	326	356	114	97
37	71A3	-	345	351.1	12.1	54	340	350	135	-
31	73A2	-	379	266.6	11.7	21	-	356	-	108
30	73A1	-	414	38.6	2.9	9	-	353	141	109
10	66B	-	448	8.0	7.4	30	343	352	107	94
33	73A4	-	483	17.9	15.0	44	344	356	130	93
6	71B	552	570	0.5	(13.4)	-	-	335	129	97
49	64B3	552	553	3.8	18.5	61	342	370	132	100
5	69B	621	650	0.7	(11.4)	-	325	329	117	-

( ) Unbroken specimen

Figure A.3: Constant stress creep tests at 750°C

Test Number N	Cast Number	Stress (MN/m^2)		Rupture Time (h)	Rupture Strain (%)	Reduction in Area (%)	Hardness, H_v		Elastic Modulus (GN/m^2)	
		Nominal	Actual				Initial	Final	At Room Temperature	At Test Temperature
23	67B1	-	207	855.0	(17.7)	(25)	333	300	120	94
22	67A4	-	276	71.3	8.7	36	352	330	114	108
21	67A3	-	310	29.1	9.0	41	327	324	112	81
25	67B3	-	379	10.1	18.3	50	325	332	128	94
27	73A3	-	414	1.8	11.6	33	347	320	134	92
28	73B1	-	448	0.7	(16.7)	(16)	316	346	135	81

( ) Unbroken specimen

Figure A.4: Constant stress creep tests at 800°C

	Test Number N	Cast Number	Stress (MN/m^2) Nominal	Stress (MN/m^2) Actual	Rupture Time (h)	Rupture Strain (%)	Reduction in Area (%)	Hardness, H_v Initial	Hardness, H_v Final	Elastic Modulus (GN/m^2) At Room Temperature	Elastic Modulus (GN/m^2) At Test Temperature
850°C	42	73B2	-	138	312.6	≈5	20	354	270	131	89
	40	71A6	-	207	13.4	(3.5)	(3)	336	286	118	82
	41	64A1	-	276	2.1	16	39	339	301	129	83
	39	71B5	-	310	0.2	≈38	87	319	291	121	-
	44	66A4	-	310	0.7	22	83	-	264	137	86
	45	64B1	-	345	0.5	25	83	354	284	129	79
	46	64A2	-	345	0.1	30	79	342	297	130	80
	38	71B4	414*	-	-	-	91	369	284	137	-
900°C	52	68A2	-	138	29.4	25.5	84	331	273	122	75
	54	66A3	-	138	4.4	35.3	87	342	274	133	77
	51	71A7	-	207	0.4	41.2	95	359	252	122	70

( ) Unbroken specimen ; * Fractured on loading

Figure A.5: Constant stress creep tests at 850°C and 900°C

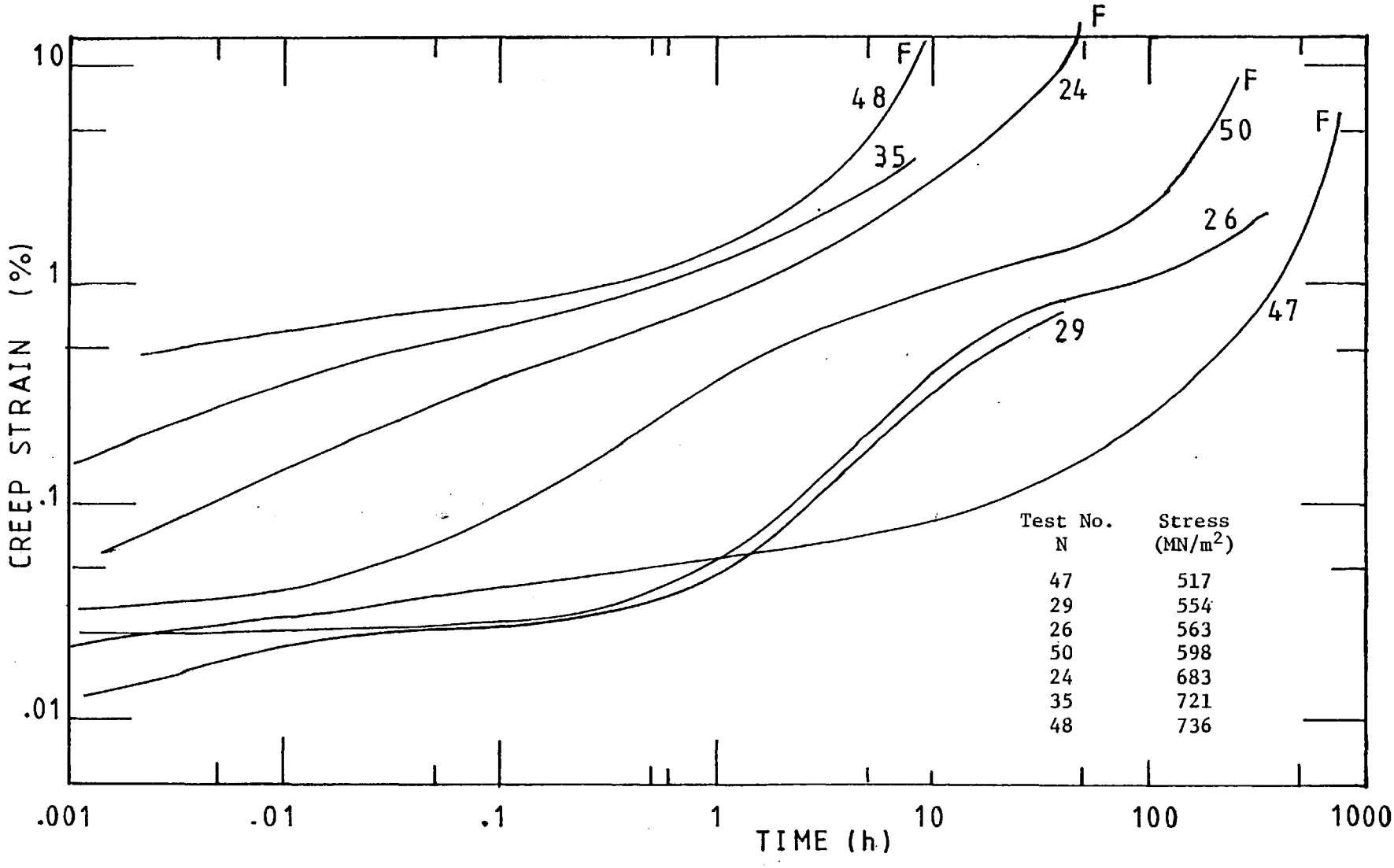

Figure A.6: Log creep strain versus log time under constant stress at 650°C

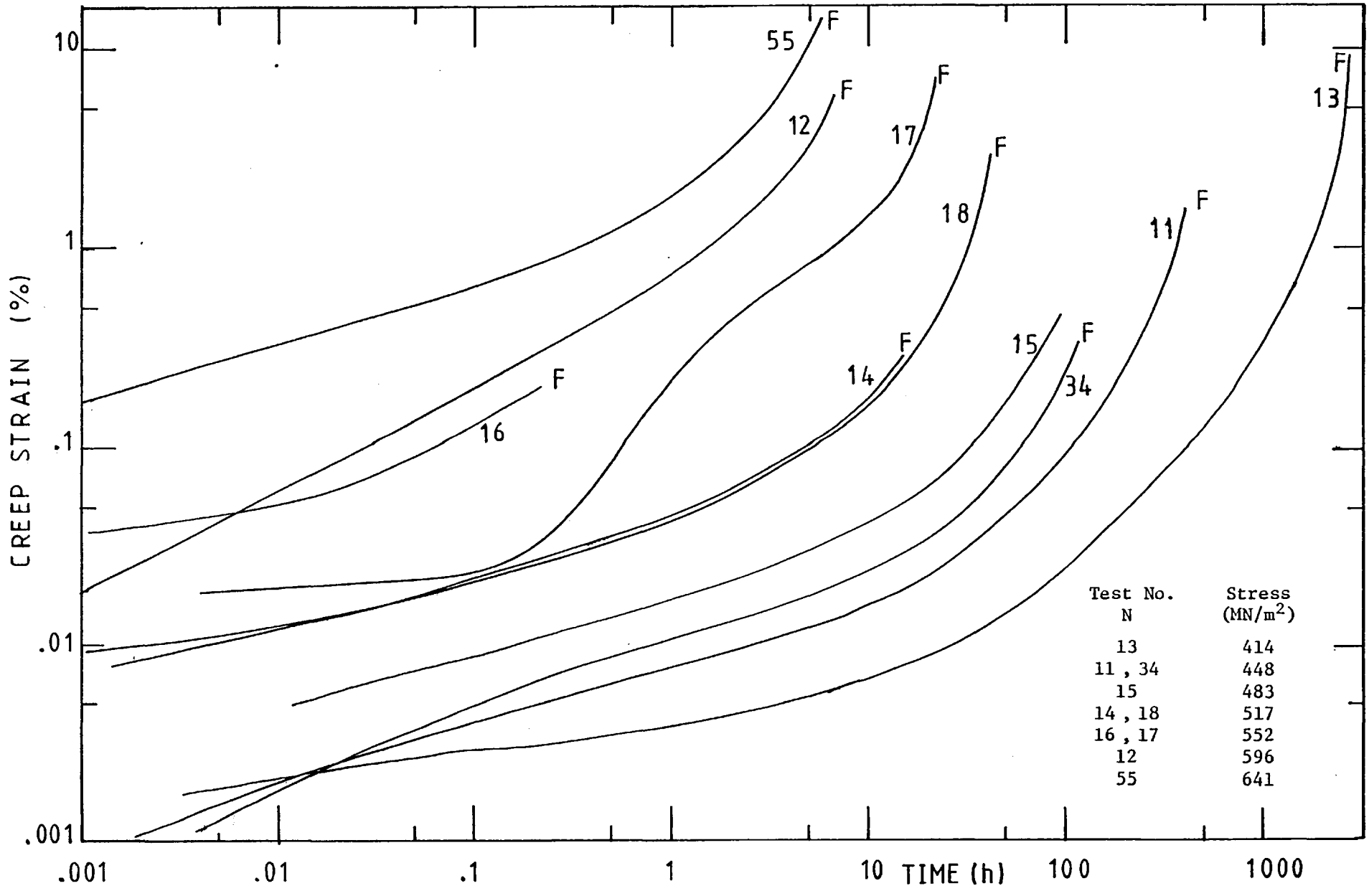

Figure A.7: Log creep strain versus log time under constant stress at 700°C

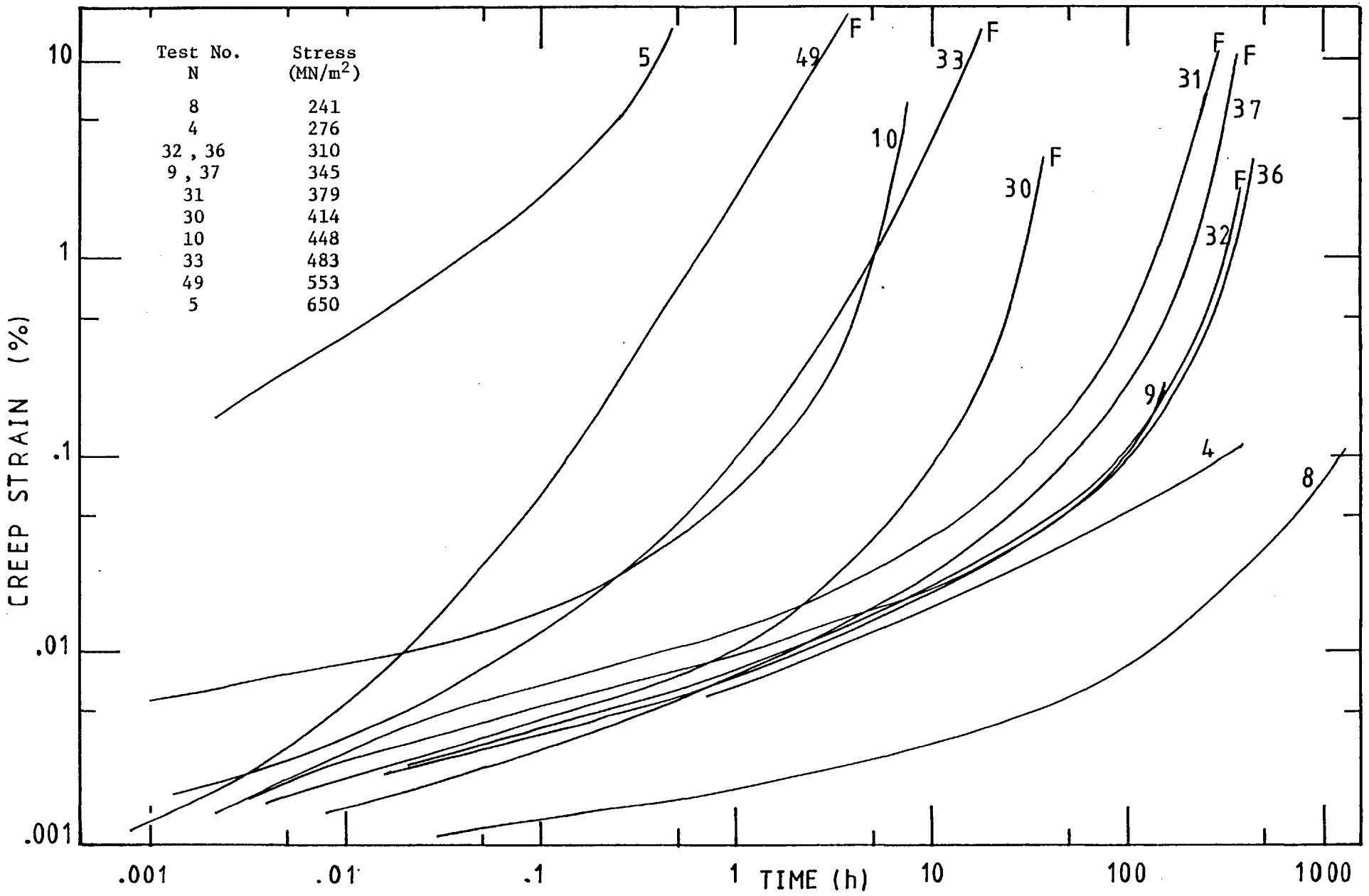

Figure A.8: Log creep strain versus log time under constant stress at 750°C

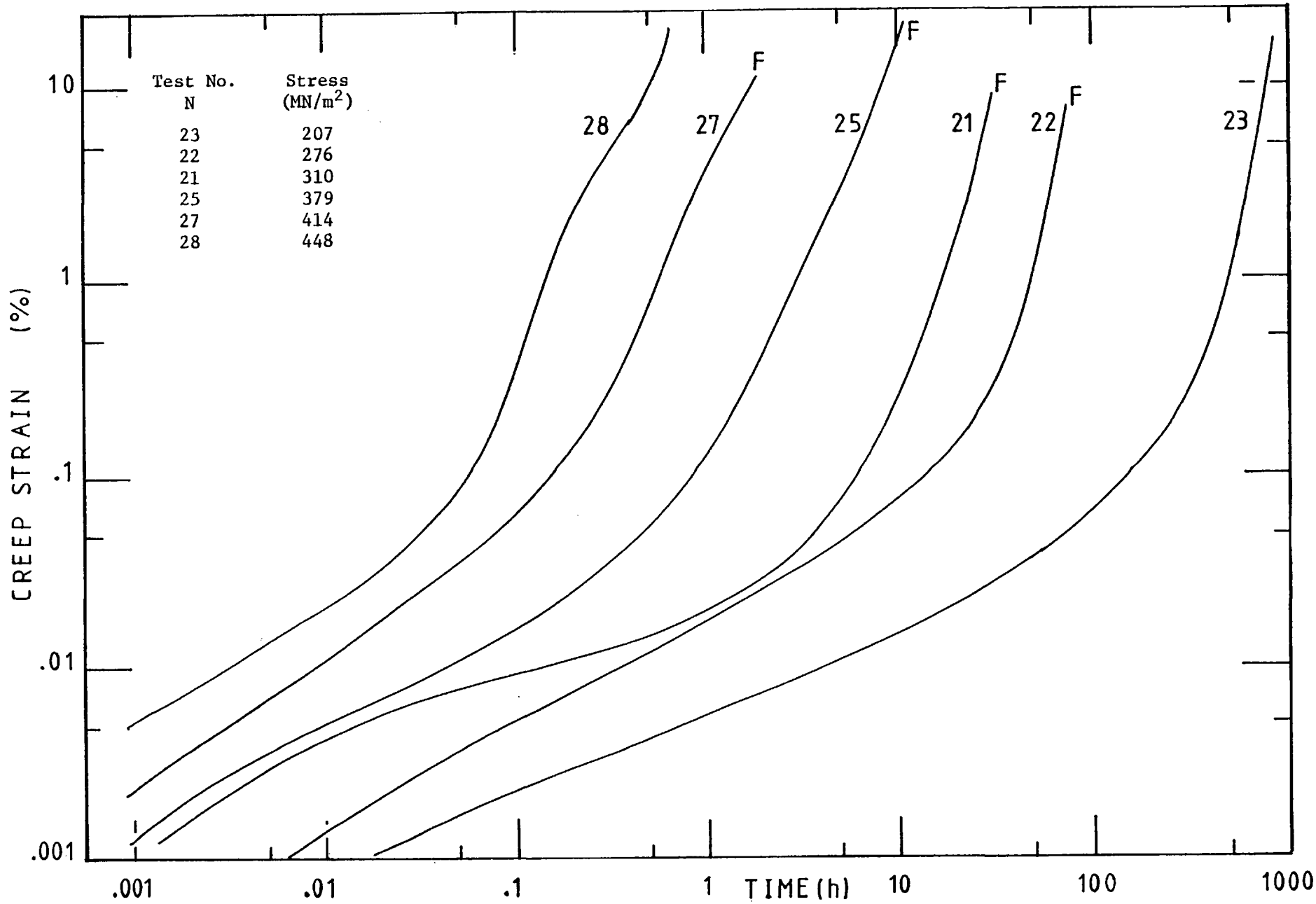

Figure A.9: Log creep strain versus log time under constant stress at 800°C

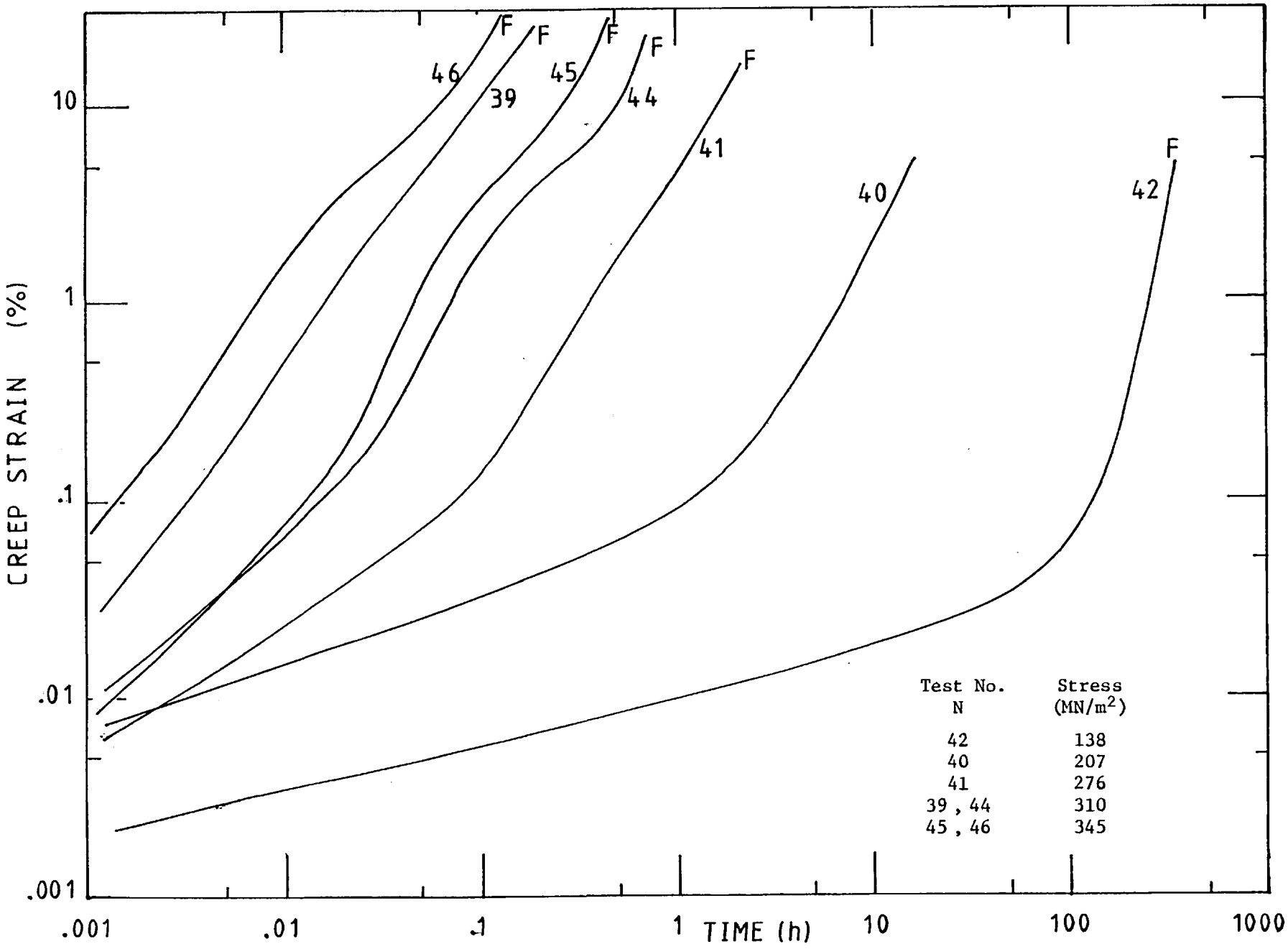

Figure A.10: Log creep strain versus log time under constant stress at 850°C

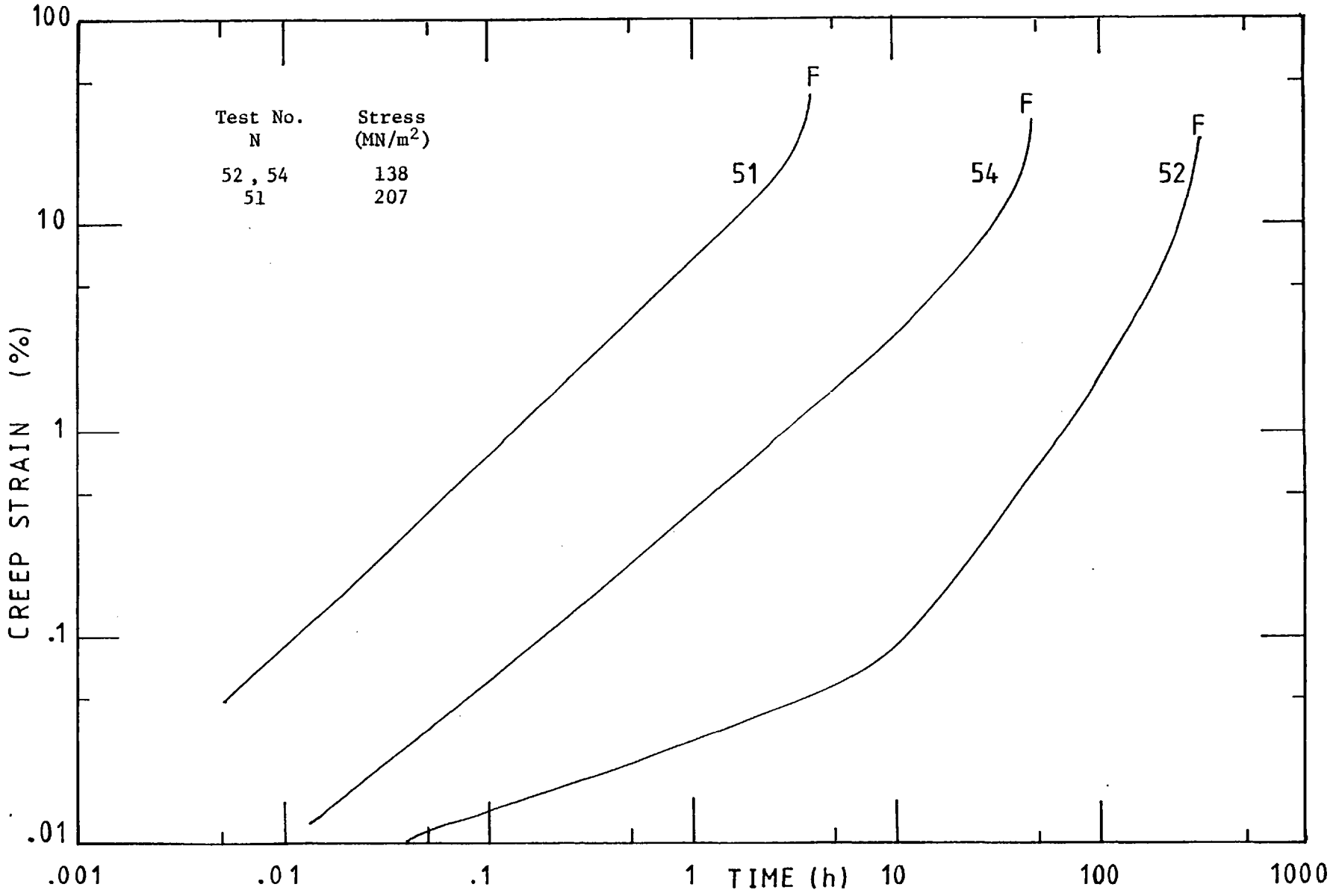

Figure A.11: Log creep strain versus log time under constant stress at 900°C

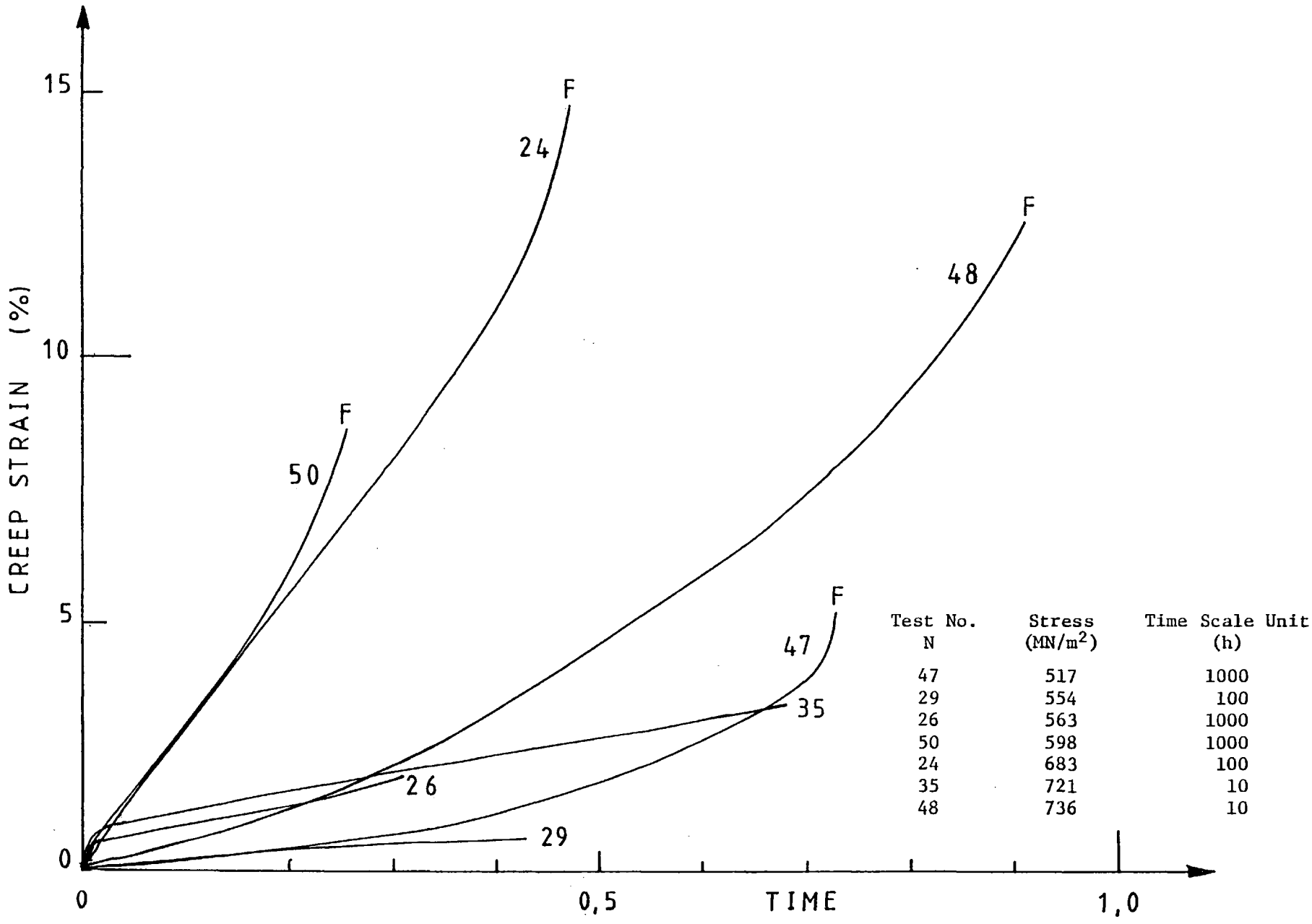

Figure A.12: Creep strain versus time under constant stress at 650°C

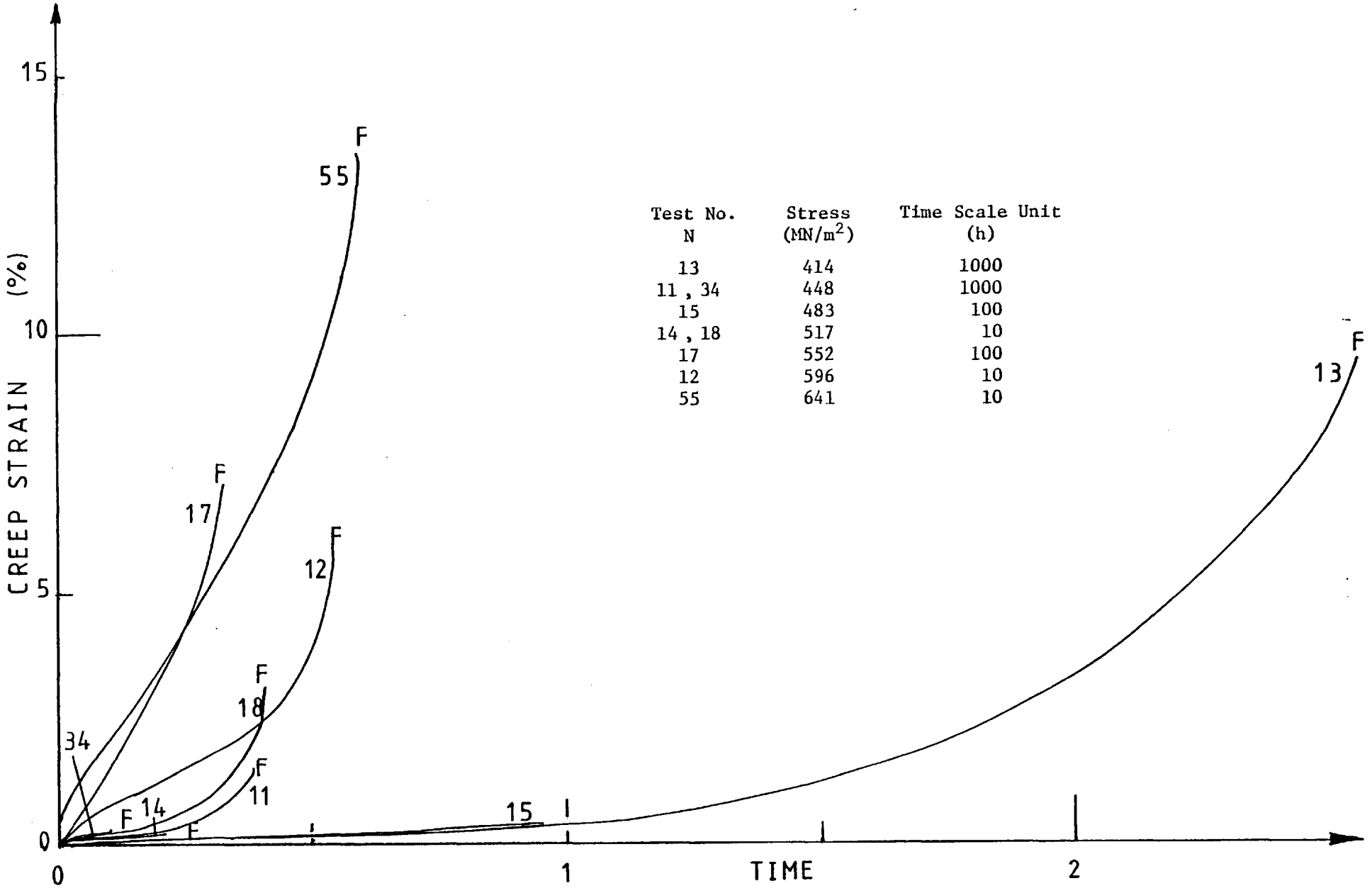

Test No. N	Stress (MN/m^2)	Time Scale Unit (h)
13	414	1000
11 , 34	448	1000
15	483	100
14 , 18	517	10
17	552	100
12	596	10
55	641	10

Figure A.13: Creep strain versus time under constant stress at 700°C

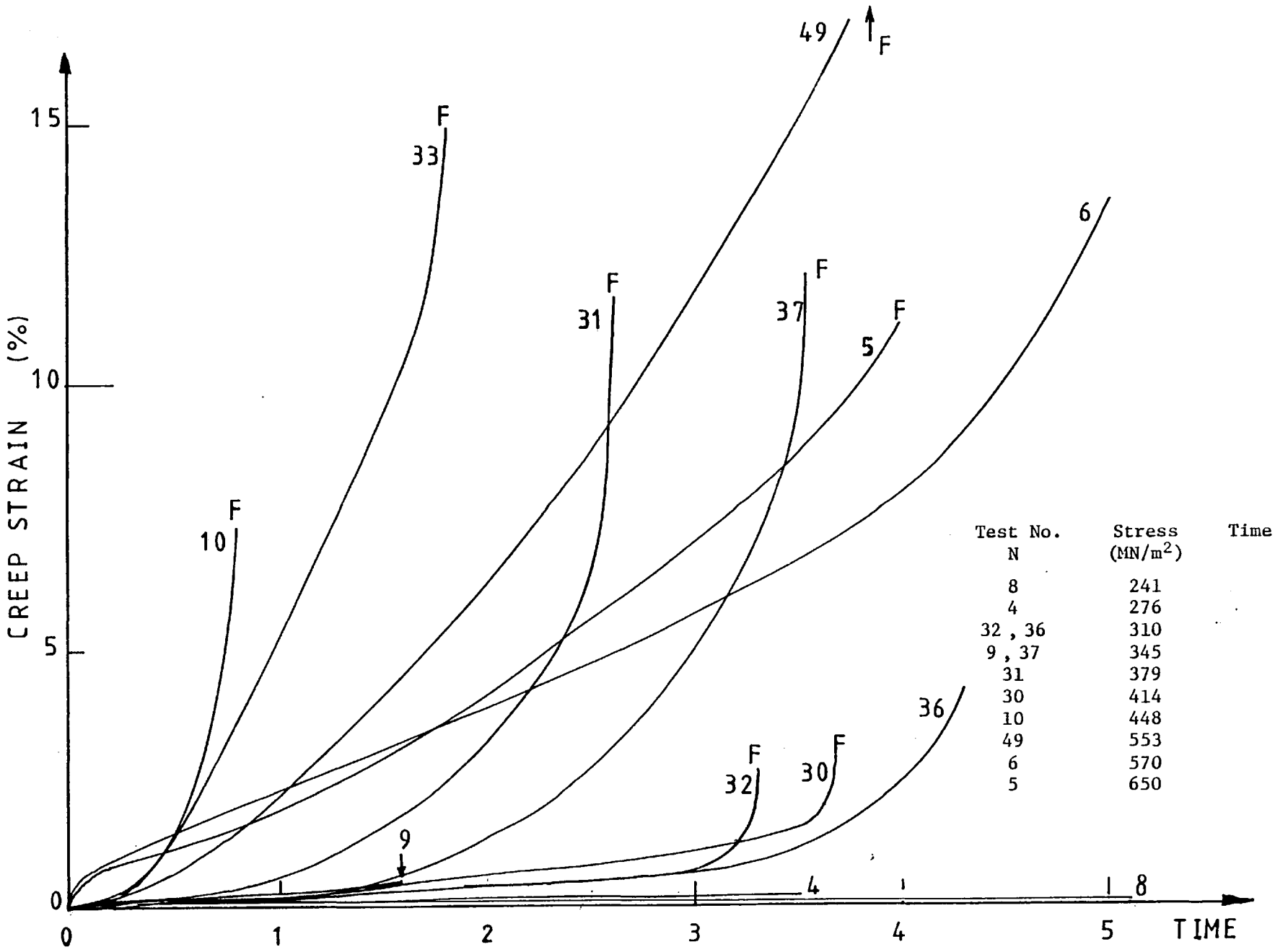

Test No. N	Stress (MN/m^2)	Time Scale Unit (h)
8	241	100
4	276	100
32 , 36	310	100
9 , 37	345	100
31	379	100
30	414	10
10	448	10
49	553	1
6	570	0.1
5	650	0.1

Figure A.14: Creep strain versus time under constant stress at 750°C

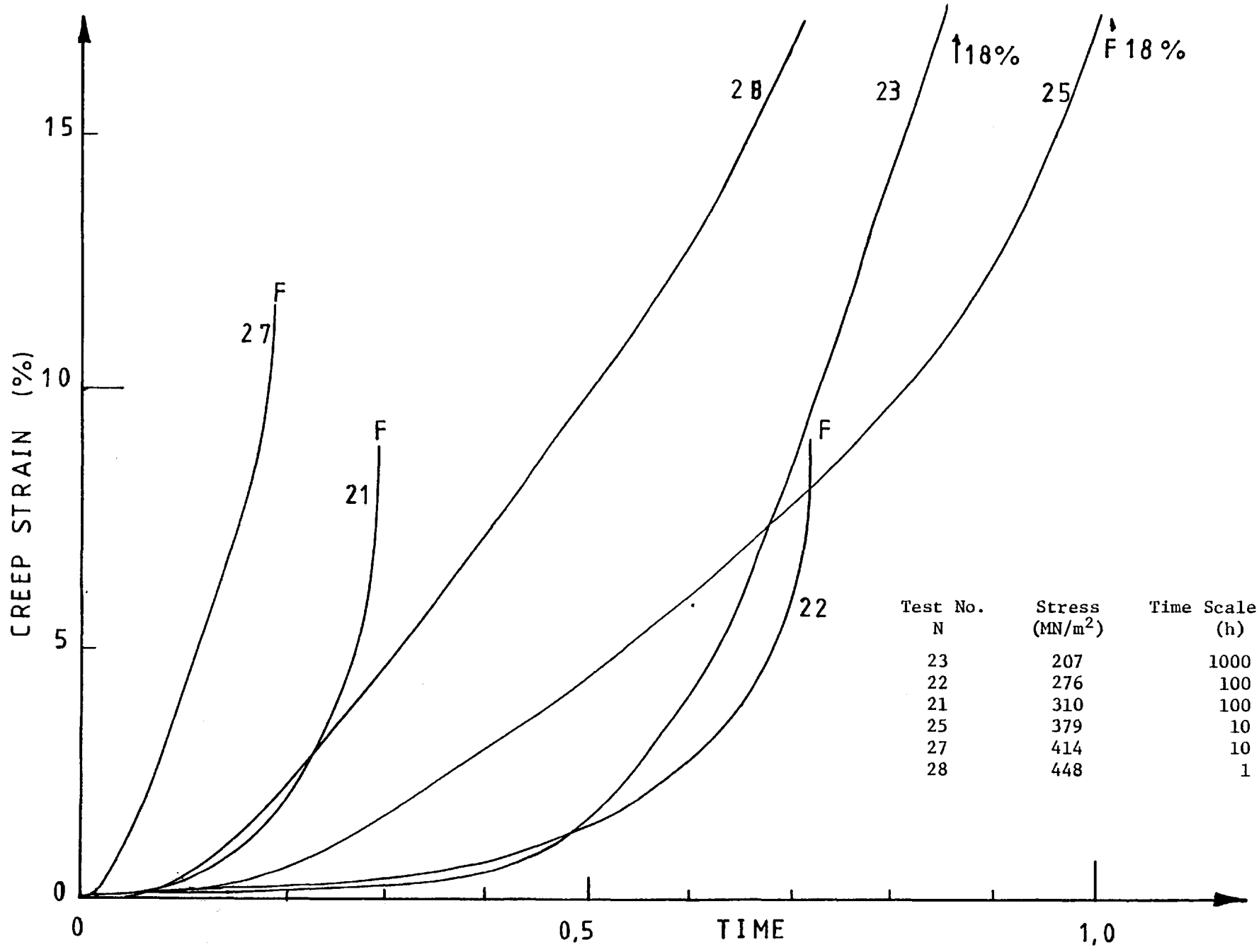

Test No. N	Stress (MN/m^2)	Time Scale Unit (h)
23	207	1000
22	276	100
21	310	100
25	379	10
27	414	10
28	448	1

Figure A.15: *Creep strain versus time under constant stress at 800°C*

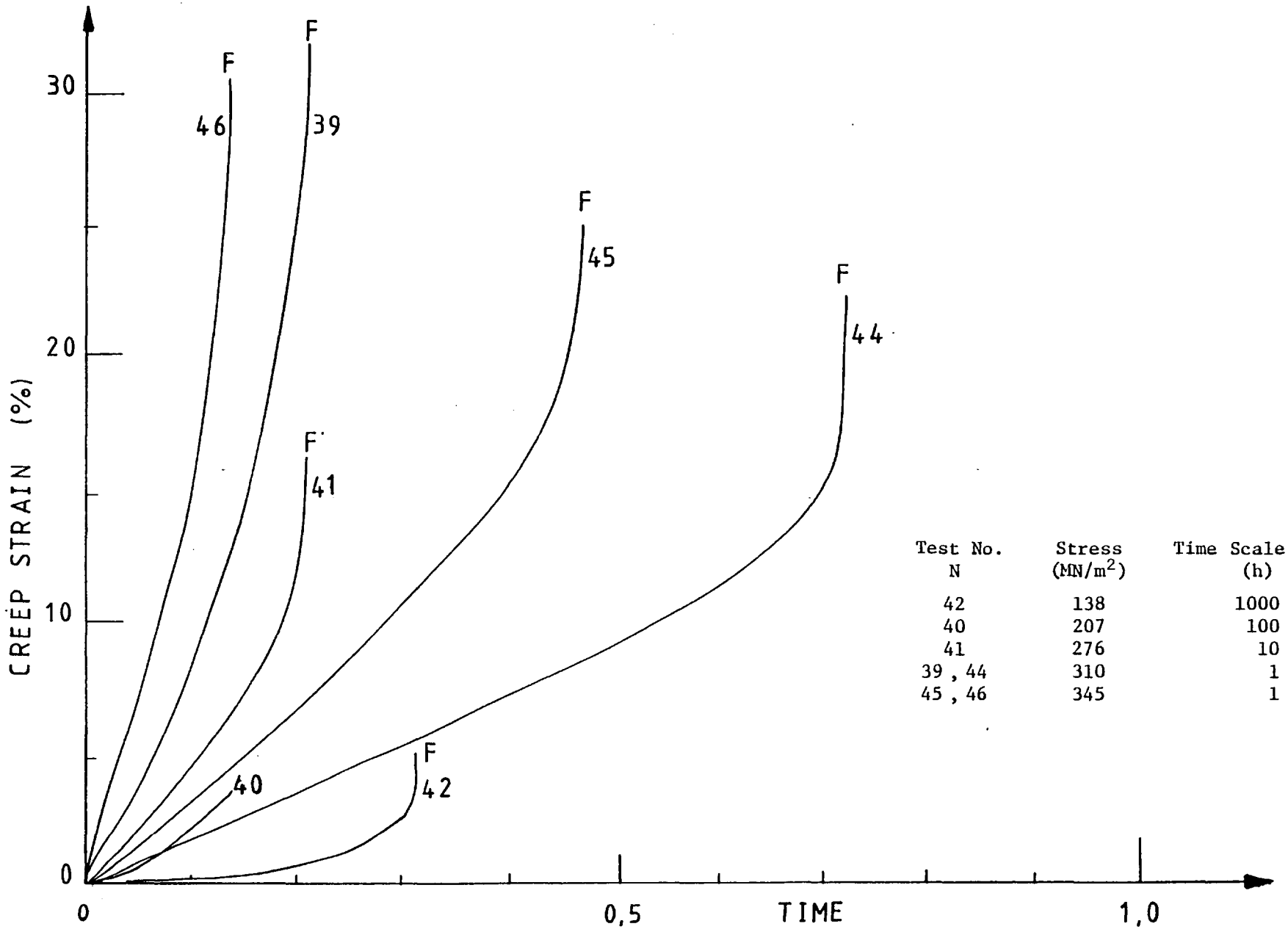

Figure A.16: Creep strain versus time under constant stress at 850°C

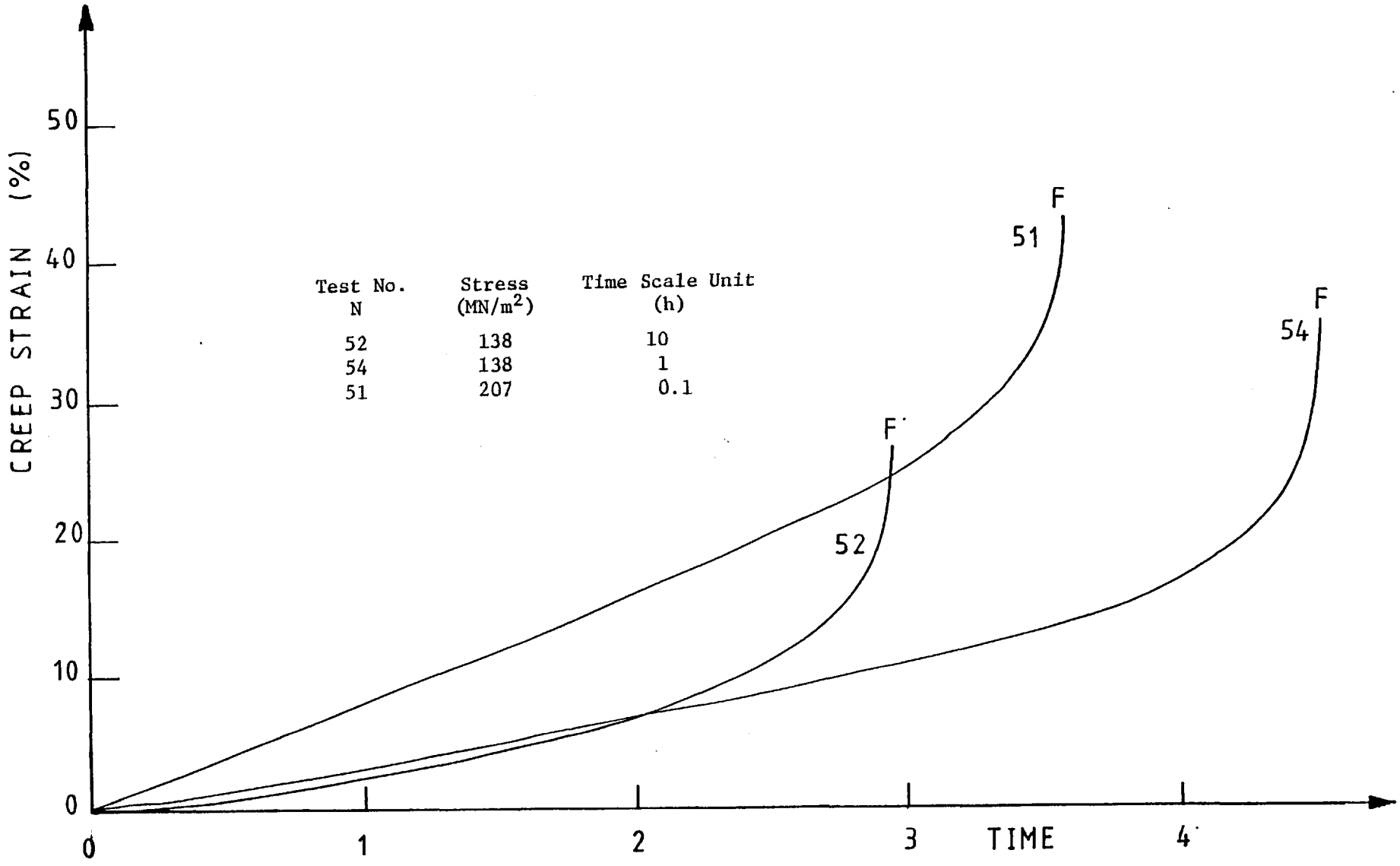

Figure A.17: Creep strain versus time under constant stress at 900°C

APPENDIX B

CYCLIC STRESS CREEP AND ELASTIC DATA FOR DIRECTIONALLY SOLIDIFIED GRAIN FORM

ε_c : forwards creep strain

ε_r : recovered creep strain

t_c : time under load per cycle

t_r : recovery time following loading for that cycle

Cycle Number	Time at 800°C (h)	ε_c (%)	t_c (h)	ε_r (%)	t_r (h)	Elastic Strain (%)	
						Loading	Unloading
1	42	0.0260	24.5	0.0243	74.0	0.2120	0.2140
2	139	0.0222	24.5	0.0225	53.5	0.2188	0.2025
3	217	0.0213	25.5	0.0080	71.1	0.2355	0.2329
4	315	0.0297	21.2	0.0066	73.5	0.2276	0.2245
5	409	0.0610	26.7	0.0100	70.3	0.2295	0.2355
6	506	0.0664	16.2	0.0166	103.0	0.2310	0.2334
7	625	0.3567	17.9	0.0150	72.0	0.2035	0.2190
8	714	0.1297	1.98	0.0115	118.3	0.2041	0.2059
9	835	0.1798	1.52	0.0123	95.7	0.2033	0.2060
10	931	0.2074	1.46	0.0103	97.1	0.2038	0.2080
11	1029	0.2718	1.65	0.0112	120.0	0.2055	0.2114
12	1152	0.2734	1.11	0.0120	73.4	0.2444	0.2541
13	1227	0.2780	1.10	0.0141	162.1	0.2492	0.2538
14	1390	0.3387	0.68	0.0040	160.9	0.2317	0.2560
15	1552	0.4685	0.95	-	-	0.2495	-

TABLE B.1

Cyclic Stress Data for Test N68

Stress = 207 MN/m^2, Temperature = 800°C

Cycle Number	Time at 800°C (h)	ε_c (%)	t_c (h)	ε_r (%)	t_r (h)	Elastic Strain (%)	
						Loading	Unloading
1	26	0.0334	40.0	0.0093	131.1	-	0.2103
2	200	0.0274	18.9	0.0135	65.2	0.1903	0.1908
3	284	0.0374	24.1	0.0086	119.8	0.1969	0.2004
4	427	0.1502	24.0	0.0112	98.0	0.1998	0.2029
5	550	0.2704	8.7	0.0131	116.5	0.1933	0.2210
6	674	0.2850	2.3	>0.0072	140.6	0.2348	0.2447
7	818	0.3270	1.5	0.0140	121.1	0.2452	0.2492
8	940	0.3065	1.4	0.0094	159.0	0.2230	0.2358
9	1101	0.4124	2.1	0.0168	165.8	0.2255	0.2325
10	1267	0.5323	1.6	0.0148	214.4	0.2218	0.2337
11	1484	0.5092	0.8	0.0151	96.5	0.2293	-

TABLE B.2

Cyclic Stress Data for Test N74

Stress = 207 MN/m^2, Temperature = 800°C

Cycle Number	Time at 800°C (h)	ε_c (%)	t_c (h)	ε_r (%)	t_r (h)	Elastic Strain (%)	
						Loading	Unloading
1	11	0.0158	12.3	-	10.5	0.2139	0.2249
2	34	0.0152	13.5	-	10.0	0.2107	0.1868
3	57	0.0178	24.8	-	14.1	0.1966	0.1845
4	97	0.0126	12.9	0.0047	11.4	0.1874	0.1812
5	117	0.0083	8.2	0.0051	17.0	0.1796	-
6	143	0.0130	11.7	0.0019	12.6	0.1814	0.1834
7	167	0.0081	12.0	-	84.1	0.1809	0.1820
8	263	0.0281	24.3	0.0066	7.0	0.1873	0.1877
9	293	0.0284	25.1	0.0028	16.8	0.1866	0.1888
10	336	0.0322	24.1	0.0034	72.0	0.1878	0.1872
11	432	0.0709	21.6	0.0088	26.2	0.1900	0.1935
12	479	0.1124	24.2	0.0080	21.7	0.1920	0.1996
13	525	0.2052	24.7	0.0118	26.0	0.1989	0.2245
14	576	0.2670	21.7	0.0169	33.0	0.2078	0.2020
15	630	0.2690	15.0	0.0140	38.5	0.2137	0.2020
16	684	0.2703	9.4	0.0175	86.4	0.2444	0.2419
17	789	0.3187	6.4	0.0180	188.9	0.2477	0.2491
18	985	0.3395	5.1	0.0150	203.6	0.2510	0.2510
19	1154	0.3758	2.9	0.0145	188.9	0.2447	0.2450
20	1345	0.4484	2.9	0.0144	621.4	0.2444	0.2553
21	1970	0.6950	3.0	0.0185	328.3	0.2450	0.2532
22	2301	0.6307	1.9	0.0155	338.5	0.2553	0.2625
23	2642	0.7650	1.7	0.0210	191.0	0.2310	0.2460
24	2834	0.7271	1.4	0.0183	382.8	0.2567	0.2652
25	3218	0.8835	1.4	0.0245	286.2	0.2650	0.2705

TABLE B.3

Cyclic Stress Data for Test N75

Stress = 207 MN/m^2, Temperature = 800°C

Cycle Number	Time at 800°C (h)	ε_c (%)	t_c (h)	ε_r (%)	t_r (h)	Elastic Strain (%)	
						Loading	Unloading
1	49.0	0.0383	8.7	0.0060	14.1	0.2668	0.2533
2	74.2	0.0514	10.1	0.0137	13.5	0.2544	0.2540
3	97.8	0.0557	10.2	0.0123	14.7	0.2525	0.2552
4	117.6	0.1072	8.8	0.0179	40.4	0.3092	0.3099
5	166.8	0.3105	5.4	0.0217	16.5	0.3135	0.3232
6	188.8	0.3327	2.6	0.0229	22.0	0.3220	0.3276
7	213.4	0.3940	1.8	0.0205	23.6	0.3270	0.3322
8	238.8	0.3842	1.0	0.0230	26.7	0.3345	0.3352
9	266.8	0.3315	0.62	0.0199	50.8	-	0.3300
10	318.2	0.5093	0.66	0.0170	18.4	0.3345	0.3327
11	337.5	0.5103	0.86	0.0213	21.6	0.3330	0.3321
12	360.2	0.5990	0.88	0.0215	48.1	0.3368	0.3351
13	409.3	0.5379	0.53	0.0189 (0.0242)	25.6	0.3345	0.3334
14	434.5	0.7037	0.74	0.0190 (0.0285)	70.9	0.3370	0.3425
15	506.2	1.2210	0.99	0.0252 (0.0302)	95.2	0.3420	0.3440
16	602.5	1.2427	0.78	0.0151 (0.0266)	95.2	0.3155	0.3434
17	698.6	1.0073	0.39	0.0103 (0.0243)	148.2	0.3245	0.3600
18	837.2	1.3089	0.47	0.0145 (0.0280)	191.2	0.3279	0.3606
19	1028.9	1.4283	0.39	0.0119 (0.0274)	338.0	0.3685	0.3661
20	1367.2	1.6793	0.28	0.0212 (0.0340)	76.4	0.3975*	0.3924
21	1443.9	1.7777	0.36	0.0200 (0.0352)	144.1	0.4044*	0.3998
22	1588.2	1.3041	0.18	-	-	0.3795*	-

Figures in brackets indicate maximum recovered strain before forwards creep under minimum load. * indicates plastic yielding.

TABLE B.4

Cyclic Stress Data for Test N76

Stress = 276 MN/m^2, Temperature = 800°C

Cycle Number	Total Time at 700°C (h)	ε_c (%)	t_c (h)	ε_r (%)	t_r (h)	Elastic Strain (%)	
						Loading	Unloading
1	20.3	0.0455	25.3	0.0050	19.3	0.4089	0.4492
2	65.5	0.0565	25.2	0.0140	24.7	0.4331	0.4324
3	115.5	0.0552	25.3	0.0117	25.2	0.4352	0.4420
4	166.1	0.0605	22.3	0.0121	28.8	0.4430	0.4350
5	216.3	0.0695	16.8	0.0163	24.6	0.4455	0.4432
6	257.8	0.0362	6.6	0.0149	50.1	0.4467	0.4411
7	314.7	0.0580	13.8	0.0152	49.1	0.4410	0.4487
8	377.6	0.0455	8.1	0.0135	312.4	0.4430	0.4505
9	698.1	0.1202	14.7	0.0198	47.8	0.4473	0.4582
10	760.7	0.0667	5.2	0.0178	101.6	0.4550	0.4602
11	867.6	0.1765	12.9	0.0196	9.6	0.4532	0.4720
12	890.0	0.2510	15.0	0.0370	154.8	0.4705	0.4820
13	1059.8	0.3943	13.5	0.0350	29.7	0.4665	0.4785
13a	1102.1	0.016	1 min	0.007	2.0	-	-
14	1104.2	0.5431	16.9	0.0360	95.8	0.4630	0.4845
15	1217.1	0.2756	5.0	0.0426	18.7	0.4920	0.4959
16	1240.9	0.2535	5.1	0.0449	162.6	0.4984	0.4950
17	1408.6	0.3898	6.2	0.0380	18.6	0.5141	0.5089
18	1433.6	0.2777	4.5	0.0425	147.0	0.5035	0.4922
19	1578.5	0.5370	6.6	0.0423	16.0	0.5125	0.5032
20	1601.1	0.3988	5.3	0.0417	138.0	0.4980	0.5030
21	1744.4	0.4670	4.6	0.0208	0.08	0.4984	0.4992
22	1749.2	0.3871	4.2	0.0430	162.2	0.5000	0.5020
23	1915.6	0.3547	2.4	0.0087	0.008	0.5170	0.5235
24	1918.0	0.2678	2.4	0.0432	88.9	0.5214	0.5078
25	2009.3	0.4578	3.3	0.0020	0.00025	0.5275	-
25a	2012.6	0.0060	0.013	0.0063	0.0025	-	0.4975
26	2012.6	0.3884	3.7	0.0425	66.6	0.4930	0.5025
27	2083.1	1.3748	10.5	0.0470	84.8	0.4964	0.5120
28	2178.4	0.9143	5.5	-	-	0.5130	-

TABLE B.5

Cyclic Stress Data for Test N78

Stress = 448 MN/m^2, Temperature = 700°C

APPENDIX C

YIELD STRESS DATA FOR EXPOSURE AT TEMPERATURE

FOR DIRECTIONALLY SOLIDIFIED GRAIN FORM

	Temperature (°C)	Time at Temperature (h)	0.01% PS (MN/m^2)	Plastic Strain (%)	Elastic Modulus (GN/m^2)
Test N81T	20	-	-	-	130
	800	27.5	405	0.1000	103
		47.6	407	0.1210	96
		119.5	359	0.1580	83
		214.7	304	0.0790	91
		290.8	286	0.1270	94
		397.3	260	0.0436	91
		456.3	272	0.0980	90
		698.0	236	0.0267	92
		724.3	273	0.0400	88
		796.5	274	0.0897	83
	20	-	-	-	121
Test N82T	20	-	-	-	121
	850	44.9	242	0.0121	86
		44.9	242	0.0165	86
		70.8	232	0.0800	83
		139.4	194	0.0850	83
		184.3	192	0.1285	79
		304.9	174	0.0558	81
		547.7	167	0.0558	82
		646.3	146	0.1571	84
	20	-	-	-	131

TABLE C.1

Yield Stress Parameters for Tests N81T and N82T

APPENDIX D

CONSTANT STRESS CREEP DATA FOR EQUI-AXED GRAIN FORM

Temperature (°C)	Test Number N	Specimen Cast Number	Stress (MN/m^2)	Condition at End of Test			Elastic Modulus (GN/m^2)	
					Time (h)	Strain (%)	At Room Temperature	At Test Temperature
650	73E	B8	414	U	8.1	0.004	174	150
	69E	A6	552	F	0.12	0.870	-	175
700	65E	A5	345	F	4.9	0.300	186	141
	66E	B3	345	U	30.6	0.030	178	145
	59E	B4	414	F	15.3	0.030	-	145
	58E	B6	483	U	3.8	0.060	193	161
	57E	A3	552	F	0.2	0.100	190	147
750	60E	A3	414	U	2.6	0.040	185	150
	61E	A11	414	U	5.7	0.110	194	149
	62E	C3	414	F	4.9	0.110	192	-
	63E	A8	483	U	0.03	0.040	179	140
	64E	A4	483	F	0.13	0.580	192	145
800	70E	A2	207	U	63.5	0.060	-	116
	71E	B5	345	U	1.8	0.090	200	-
	72E	A7	414	U	0.3	0.470	165	141

U = fracture outside gauge length ; F = fracture inside gauge length

TABLE D.1

Constant Stress Creep Tests for Equi-Axed Grain Alloy

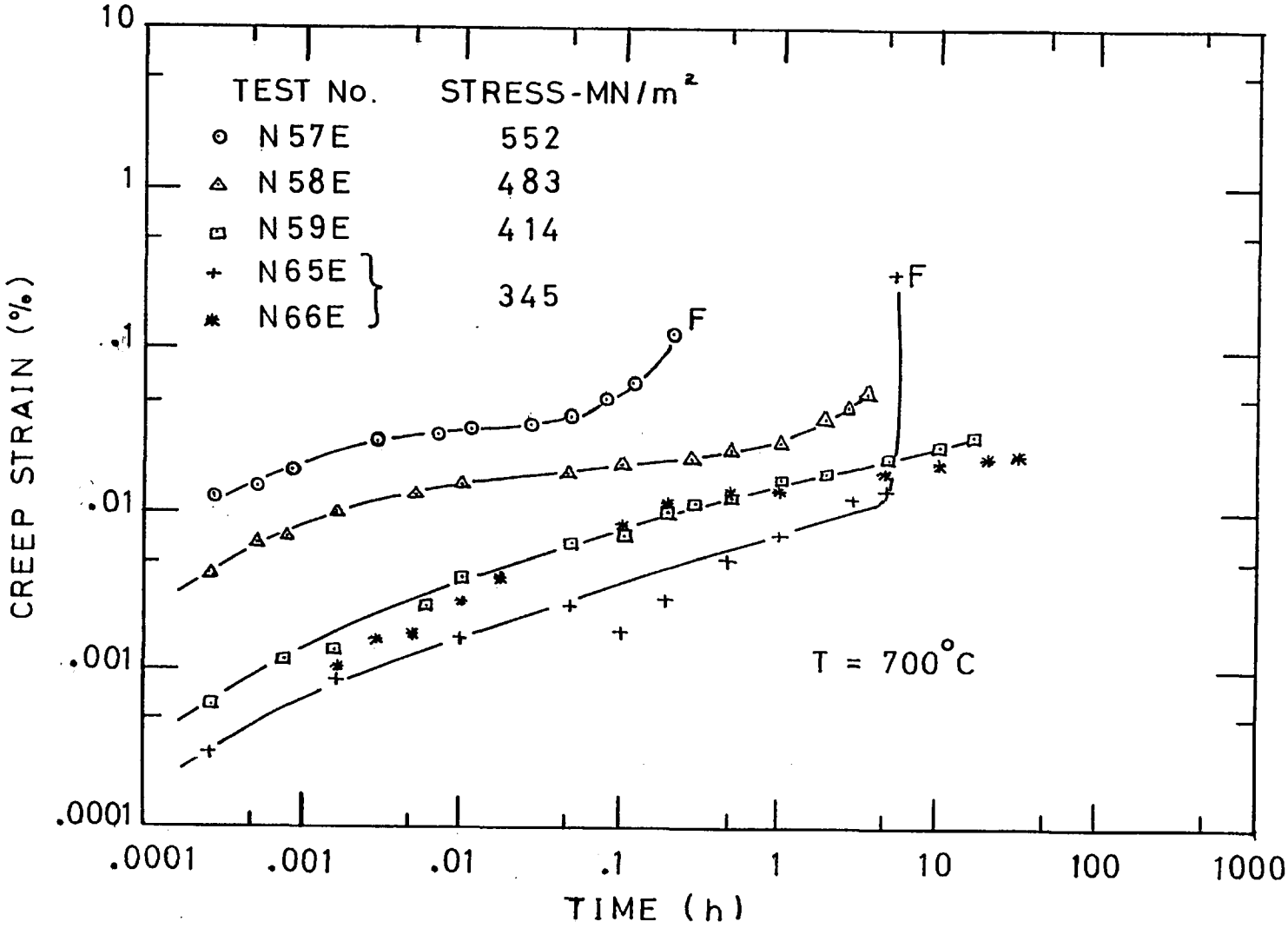

Figure D.2: Log creep strain versus log time for constant stress creep tests at 700°C

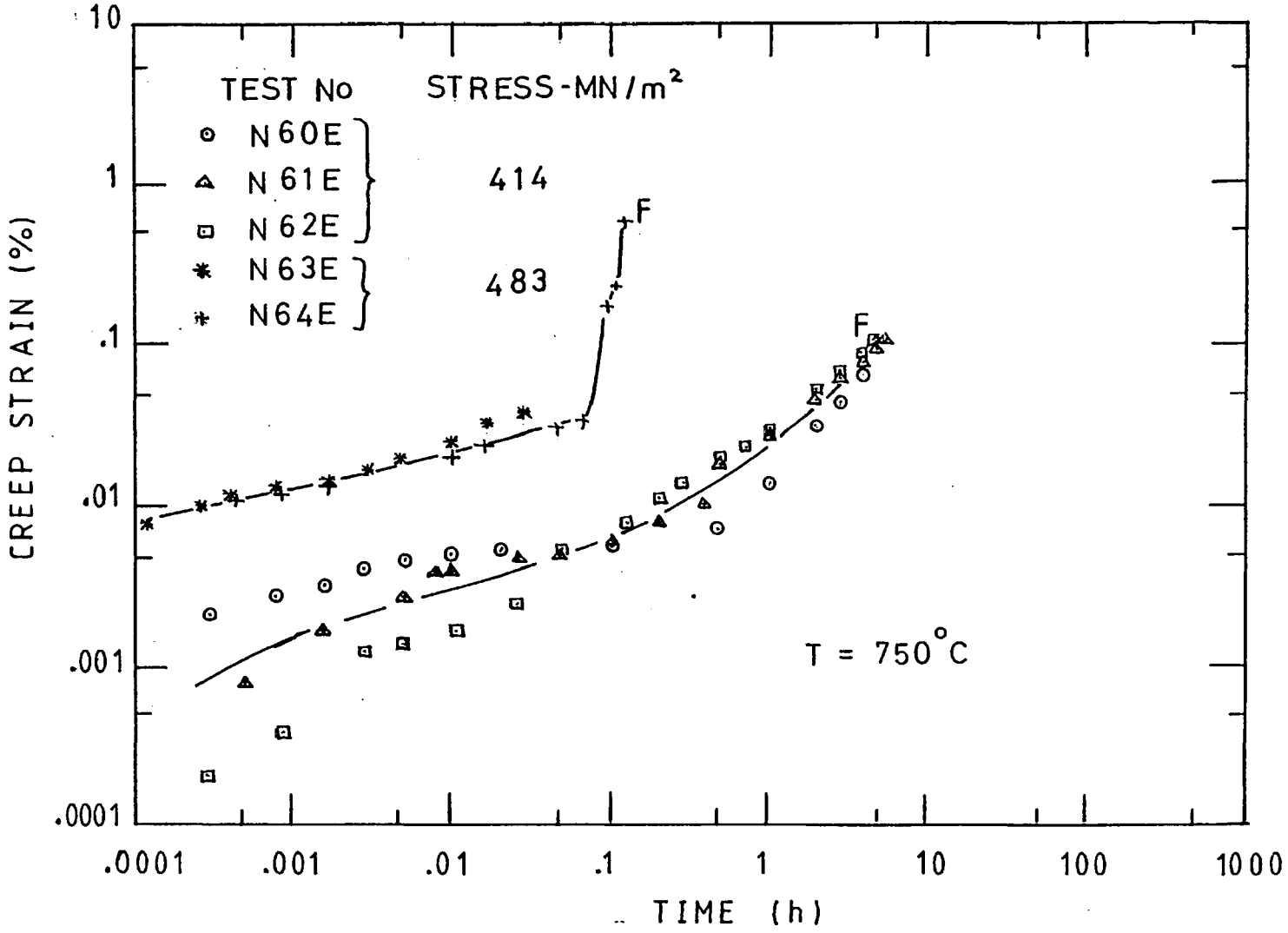

Figure D.3: Log creep strain versus log time for constant stress creep tests at 750°C

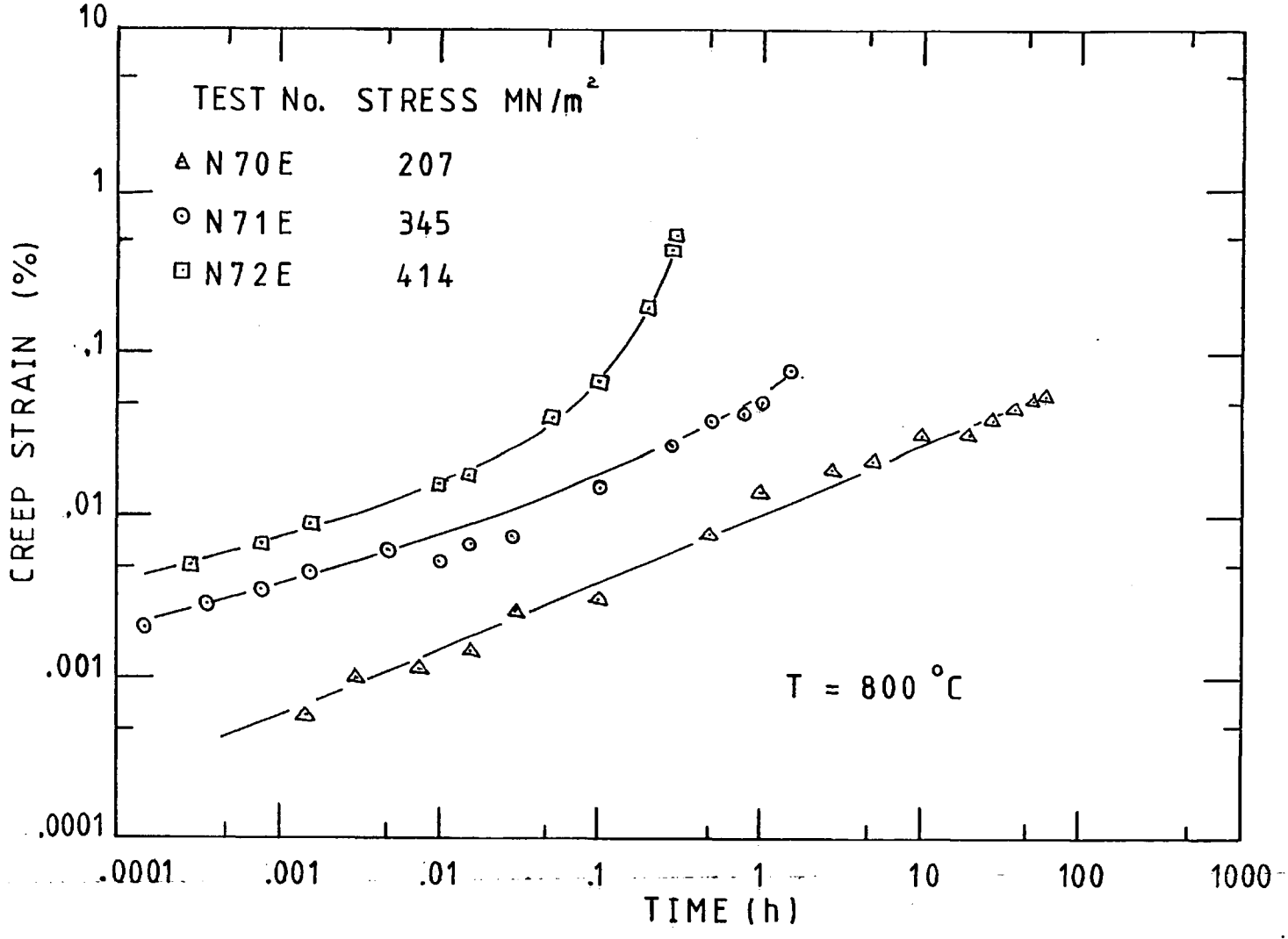

Figure D.4: Log creep strain versus log time for constant stress creep tests at 800°C

APPENDIX E

CONVERGENCE CRITERIA AND SUBROUTINES FOR COMPUTER PROGRAM

APPENDIX E

Convergence criteria used for the best fit to experimental data by Share Program No. SDA 3094 01.

(a) Epsilon Test (ε): Passed whenever:

$$\frac{|\delta_j|}{r + |b_j|} < \varepsilon \quad , \quad \text{for all } j$$

where b_j = value of jth parameter

δ_j = proportion $(1/k)$ of the increment to b_j

r = constant

ε = convergence criterion

Values assigned were:

$r = 10^{-3}$

$\varepsilon = 5 \times 10^{-5}$

$k = 5$

(b) Gamma-Lambda Test (γ-λ): Passed if λ becomes greater than 1.0 when γ is greater than 90°, the functions λ and γ being values used in the confidence region calculations. When this criterion is passed, rather than the standard "ε test", the computed parameter corrections are dependent only on unusually large rounding error, almost certainly due to very high correlations among the parameter estimates.

(c) Gamma-Epsilon Test (γ-ε): Passed if all parameter increments become small enough to pass the "ε test" as a result of successive halving of the increments, when γ < GAMCR (set to $\pi/4$). When this criterion is passed, rather than the standard "ε test", the value of ϕ (the sum

of the errors squared) is presumed minimised within the limits of rounding error.

(d) Force-Off (F): This was used to limit the number of iterations carried out on one set of data. Minimum value set = 200, maximum = 700.

```
$IEFTC SUBC

SUBC        -  EFN    SOURCE STATEMENT  -  IFN(S)   -

      SUBROUTINE FCODE(Y,X,B,PRNT,F,I,RES)
      DIMENSION Y(50),X(50,5),B(50),PRNT(5),P(50)
      COMMON /BLK1/ N
      IF ( B(5).LT.0.0 ) GO TO 10
      GO TO 11
   10 B(5) = 12.0/X(N,1)
      WRITE (6,1002) B(5)
 1002 FORMAT (6X,29H, B(5) NEGATIVE , NEW VALUE = ,E18.8)
   11 IF ( B(2).LT.0.0 ) GO TO 1
      GO TO 2
    1 B(2) = 0.5
      WRITE (6,1000)
 1000 FORMAT (15H, B(2) NEGATIVE )
    2 BEXP = B(5)*X(N,1)
      IF ( BEXP.GT.86.0 ) GO TO 3
      GO TO 4
    3 B(5) = 12.0/X(N,1)
      WRITE (6,1001) B(5)
 1001 FORMAT ( 6X,33H EXP LARGE , NEW VALUE OF B(5) = ,E18.8)
    4 COE = EXP(-B(5)*X(I,1))
      COX=B(2)+(1.0-B(2))*COE
      PRNT(1)=B(1)*X(I,1)
      PRNT(2)=B(4)*ALOG(COX)
      PRNT(3)=B(3)*(1.0-B(2))*(1.0-COE)/COX
      PRNT(4)=X(I,1)
      F=PRNT(1)+PRNT(2)+PRNT(3)
      RES = Y(I) - F
      RETURN
      END
```

```
$IEFTC SUBD

SUBD        -  EFN    SOURCE STATEMENT  -  IFN(S)   -

      SUBROUTINE PCODE(P,X,B,PRNT,F,I)
      DIMENSION Y(50),X(50,5),B(50),PRNT(5),P(50)
      COE=EXP(-B(5)*X(I,1))
      COX=B(2)+(1.0-B(2))*COE
      P(1)=X(I,1)
      P(2)=(1.0-COE)*(COX*(B(4)-B(3))-B(3)*(1.0-B(2))*COE)/COE**2
      P(3)=(1.0-B(2))*(1.0-COE)/COX
      P(4)=ALOG(COX)
      P(5)=-(1.0-B(2))*X(I,1)*COE*(COX+(B(3)+B(4))-B(3)*(1.0-B(2))*
     1(1.0-COE))/COE**2
      RETURN
      END
```

Subroutines for five-parameter model

```
$IBFTC SUBC

SUBC        -  LEVEL  SOURCE STATEMENT  -  IFN(S)  -

      SUBROUTINE FCODE(Y,X,B,PRINT,F,I,RES)
      DIMENSION Y(50),X(50,5),B(50),PRINT(5),P(50)
      IF(B(2).LT.0.0) B(2) = 0.5
      COXM = B(3)*X(I,1)
      IF(ABS(COXM).GT.88.0) B(3) = 0.1
      COX = B(3)*X(I,1)
      PRINT(1) = B(1)*COX
      PRINT(2) = B(1)*ALOG(B(2)+(1.0-B(2))*EXP(-COX))
      PRINT(3) = X(I,1)
      F = PRINT(1) + PRINT(2)
      RES = Y(I) - F
      RETURN
      END
```

```
$IBFTC SUBD

SUBD        -  LEVEL  SOURCE STATEMENT  -  IFN(S)  -

      SUBROUTINE PCODE(P,X,B,PRNT,F,I)
      DIMENSION Y(50),X(50,5),B(50),PRNT(5),P(50)
      IF(B(2).LT.0.0) B(2) = 0.5
      COXM = B(3)*X(I,1)
      IF(ABS(COXM).GT.88.0) B(3) = 0.1
      COX = B(3)*X(I,1)
      COX1 = EXP(-COX)
      COE = B(2)+(1.0-B(2))*COX1
      P(1) = COX+ALOG(COE)
      P(2) = (1.0-COX1)*B(1)/COE
      P(3) = COX+B(1)*(-X(I,1))*(1.0-B(2))*COX1/COE
      RETURN
      END
```

Subroutines for three-parameter model

APPENDIX F

COMPUTER DERIVED PARAMETERS AND COMPARISONS BETWEEN FITTED AND EXPERIMENTAL DATA

Test No N	Temp (°C)	Stress (MN/m^2)	N	$\hat{\varepsilon}$ (%)	Five-Parameter Model							Three-Parameter Model				
					A	B	C	D	ϕ	ΣR^2	FIT	A'	B'	α	ΣR^2	FIT
47	650	517	25	2.0	0.00405	0.01	-0.00319	0.0370	0.026	9.3×10^{-2}	ε	29.46	0.0279	0.00223	6.5×10^{-2}	F
26	650	563	35	2.0	0.00169	0.925	3.874	-10.27	0.0189	7.9×10^{-1}	F	0.151	53.18	0.0260	1.2×10^{-1}	γ-ε
50	650	598	25	1.9	0.0125	200.0*	0.135	0.198	0.06*	2.4×10^{-2}	F	0.189	95.88	0.0713	2.3×10^{-2}	γ-ε
24	650	683	20	3.9	0.291	19.72	-2.408	-0.935	0.102	7.3×10^{-1}	ε	0.0803	1709.7	2.636	5.4×10^{-2}	F
35	650	721	20	3.1	0.315	8000.0*	-0.0266	0.122	0.3*	8.2×10^{-3}	ε	0.141	493.7	2.473	1.7×10^{-2}	ε
13	700	414	30	4.6	0.0033	1.826	-17.68	-20.65	0.0010	2.9×10^{0}	γ-ε	16.98	0.0040	0.0020	1.9×10^{-1}	F
34	700	448	20	0.4	0.00068	0.467	-1.541	-2.520	0.00486	3.3×10^{-2}	γ-ε	4.767	0.0433	0.00861	1.5×10^{-2}	F
15	700	483	25	0.4	0.0046	0.800*	-4.128	-4.454	0.10*	5.2×10^{-3}	ε	10.04	0.0519	0.00653	3.0×10^{-3}	γ-ε
18	700	517	25	1.9	0.134	0.336	-0.995	2.390	0.055	2.0×10^{-1}	γ-ε	7.102	0.0139	0.0838	2.7×10^{-2}	F
17	700	552	25	4.4	0.206	0.693	-4.460	-3.210	0.133	2.1×10^{-1}	γ-ε	1.567	0.722	0.1248	2.7×10^{-1}	ε
12	700	595	25	2.0	0.511	10.0*	2.8×10^{7}	-6.2×10^{6}	4.91	4.0×10^{-3}	ε	0.1801	4.865	2.763	1.1×10^{-2}	ε
55	700	640	25	4.2	1.359	20.0*	-0.639	0.0053	5.0*	1.3×10^{-1}	F	0.2339	23.87	5.569	2.6×10^{-1}	F

N = number of points fitted

$\hat{\varepsilon}$ = maximum value of experimental strain

ΣR^2 = sum of squared errors

FIT = criteria for final solution (as listed in Appendix E)

* = initial estimate unchanged

Table F.1: Parameters for Dislocation Dynamics Models

Test No N	Temp (°C)	Stress (MN/m^2)	N	$\hat{\varepsilon}$ (%)	Five-Parameter Model							Three-Parameter Model				
					A	B	C	D	ϕ	ΣR^2	FIT	A'	B'	α	ΣR^2	FIT
4	750	276	20	0.1	0.00019	2.0*	-0.177	-0.0699	0.0159	1.8×10^{-4}	ε	0.0139	18.86	0.0137	1.4×10^{-4}	γ-ε
30	750	414	20	1.4	0.0748	0.0511	-0.0174	0.3269	0.1960	1.1×10^{-2}	F	1.495	0.0465	0.102	6.7×10^{-4}	ε
10	750	448	20	1.3	0.485	0.100	-0.0775	0.2140	1.440	7.3×10^{-3}	γ-ε	0.830	0.0396	0.912	5.2×10^{-3}	ε
33	750	483	20	2.7	0.796	0.0485	-0.0433	0.6905	0.9762	2.3×10^{-3}	ε	1.940	0.0518	0.584	7.3×10^{-3}	γ-ε
23	800	207	25	9.3	0.0716	0.0191	-0.218	8.059	0.0086	3.4×10^{-1}	γ-ε	7.927	0.00082	0.01137	1.4×10^{-1}	ε
22	800	276	25	4.8	0.0652	1.019	35.29	-28.93	0.177	6.9×10^{0}	F	11.95	0.00319	0.0739	3.9×10^{-2}	ε
21	800	310	25	3.7	0.155	1.0	584.7	-579.5	0.319	1.7×10^{0}	F	1.802	0.0175	0.2410	6.6×10^{-3}	ε
25	800	379	20	4.1	1.326	0.0198	0.0274	0.911	1.5*	5.3×10^{-3}	γ-ε	0.984	0.0422	1.543	2.4×10^{-2}	ε
27	800	448	20	5.3	6.446	0.090*	-0.0438	0.815	8.0*	3.9×10^{-2}	γ-ε	0.816	0.0506	7.906	3.5×10^{-2}	ε
28	800	483	20	5.4	19.69	0.118	0.612	2.576	13.37	2.9×10^{-2}	ε	2.696	0.1104	12.45	5.4×10^{-1}	ε
42	850	138	20	0.6	0.0166	0.6895	-5.672	4.510	0.00644	8.6×10^{-2}	ε	7.880	0.00098	0.0211	6.8×10^{-3}	γ-ε
40	850	207	20	3.5	0.418	0.5186	-1.767	1.150	0.2749	1.5×10^{-2}	ε	0.854	0.1120	0.4514	1.2×10^{-2}	ε
41	850	276	20	9.5	5.749	0.90*	-6.887	3.614	4.80*	2.3×10^{-1}	ε	0.921	0.281	6.271	2.4×10^{-1}	ε
44	850	310	20	9.1	18.71	0.90*	81.94	90.16	19.98	4.3×10^{-2}	γ-ε	1.029	0.5835	18.65	1.2×10^{-1}	ε

Notation as for Table F.1

Table F.2: Parameters for Dislocation Dynamics Models

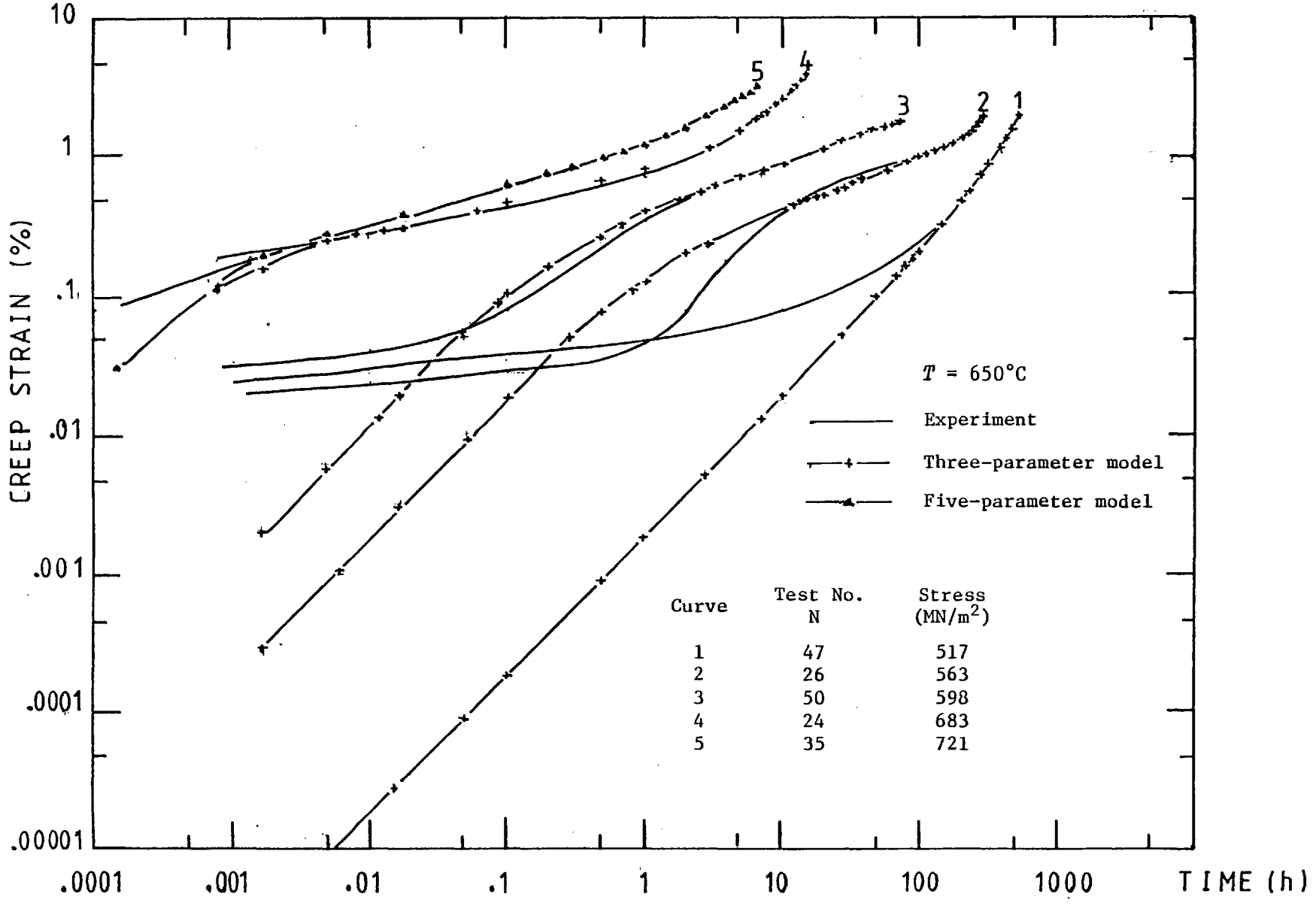

Figure F.1: Comparison between fitted and experimental creep strain versus time at 650°C

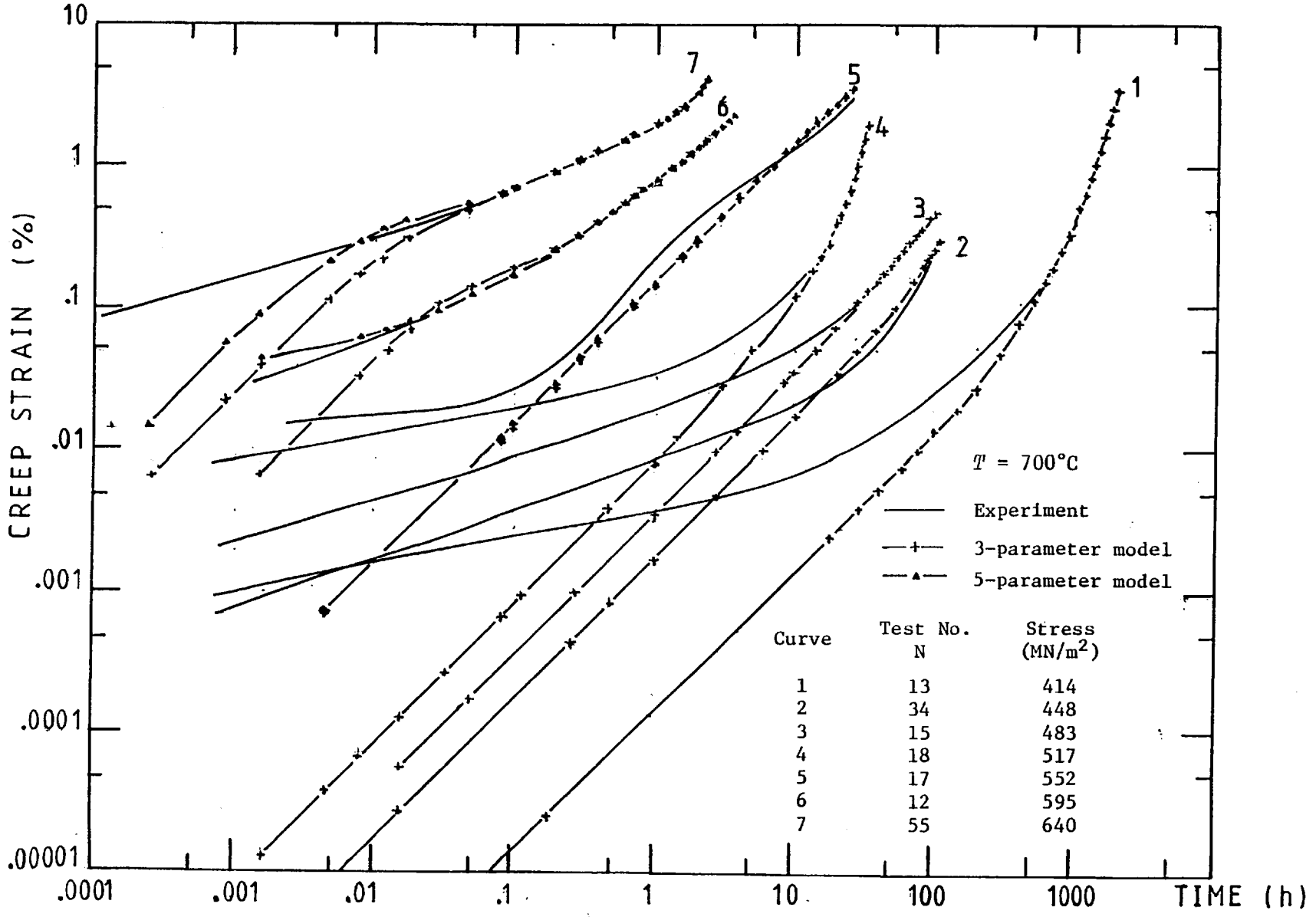

Figure F.2: Comparison between fitted and experimental creep strain versus time at 700°C

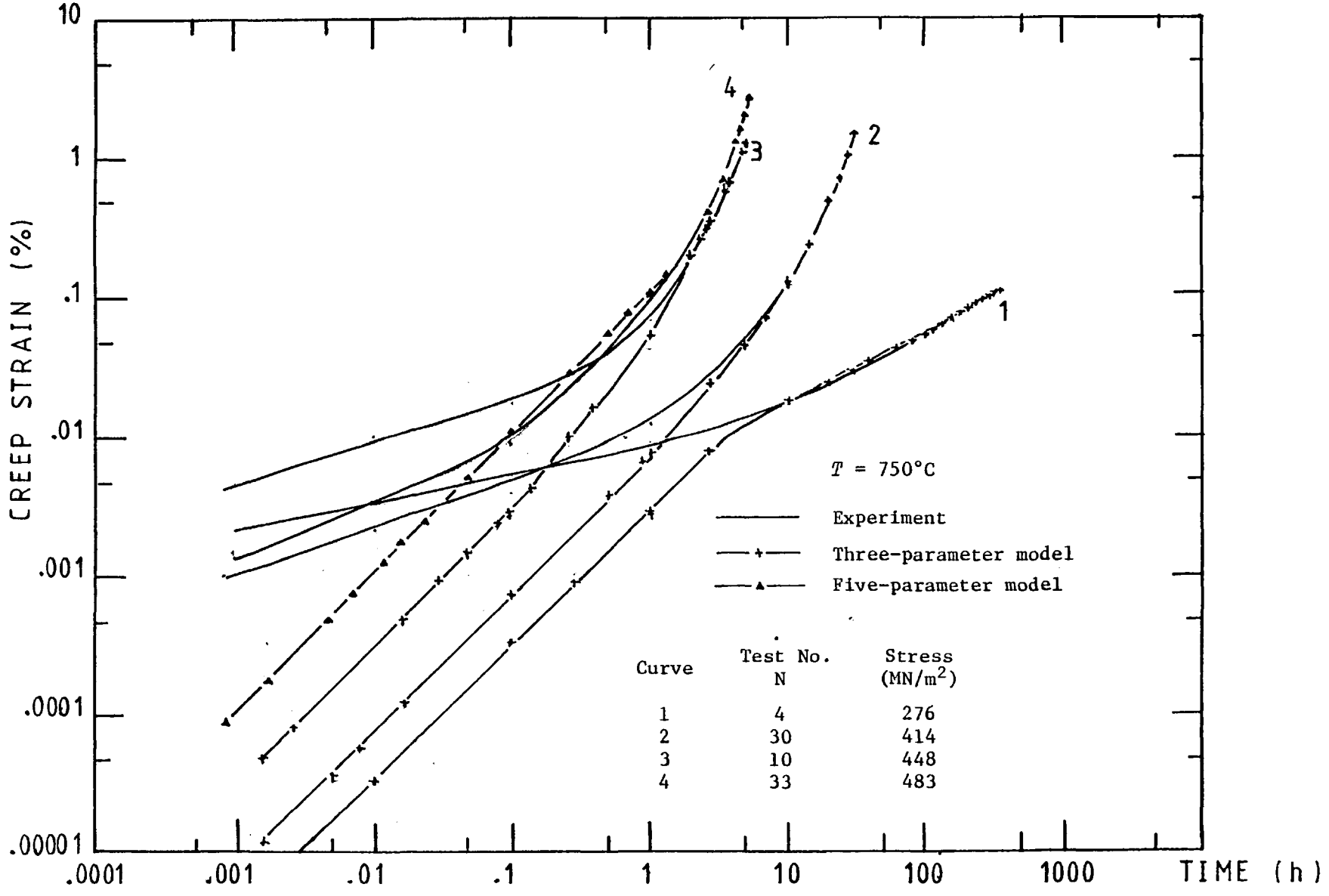

Figure F.3: Comparison between fitted and experimental creep strain versus time at 750°C

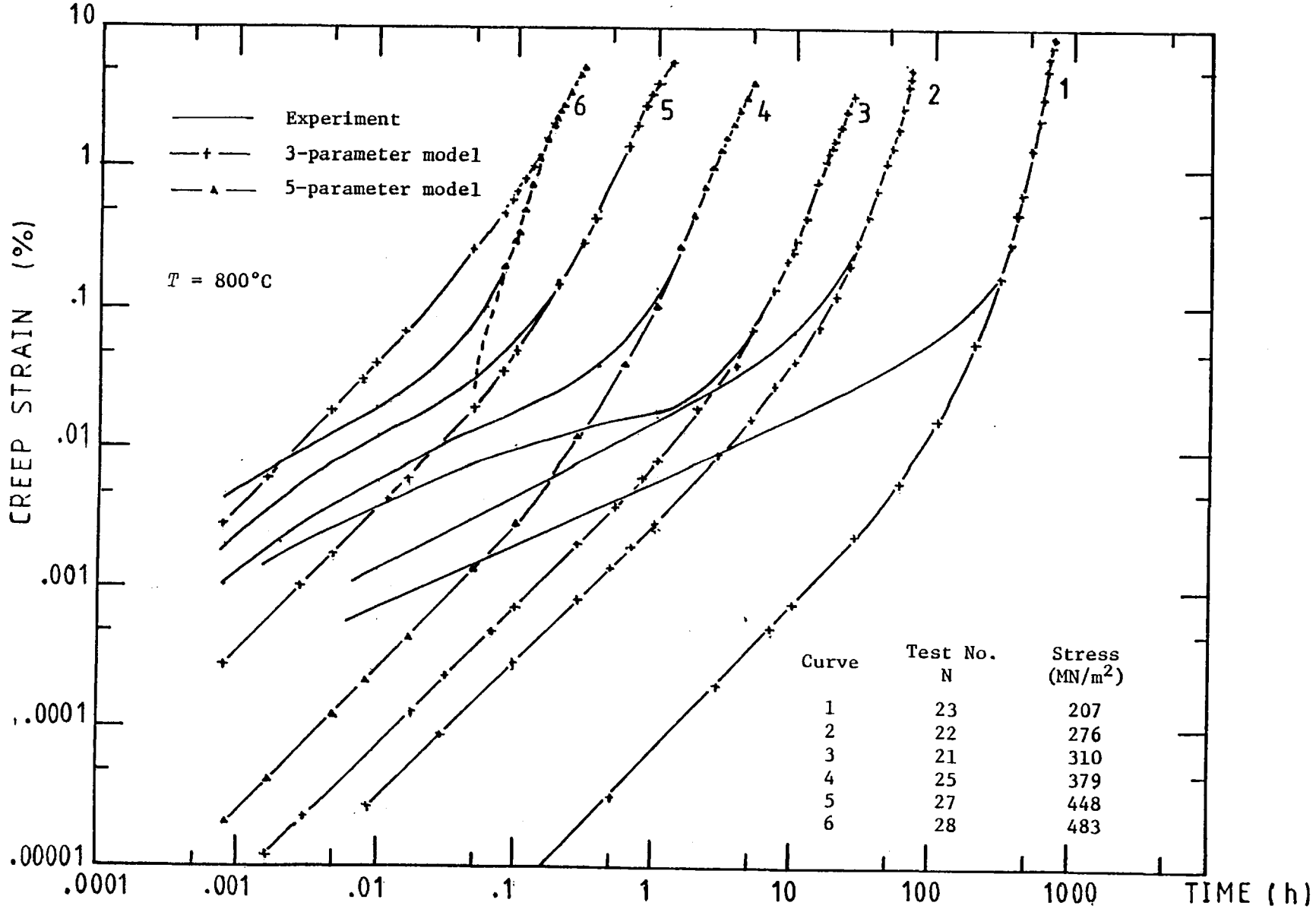

Figure F.4: Comparison between fitted and experimental creep strain versus time at 800°C

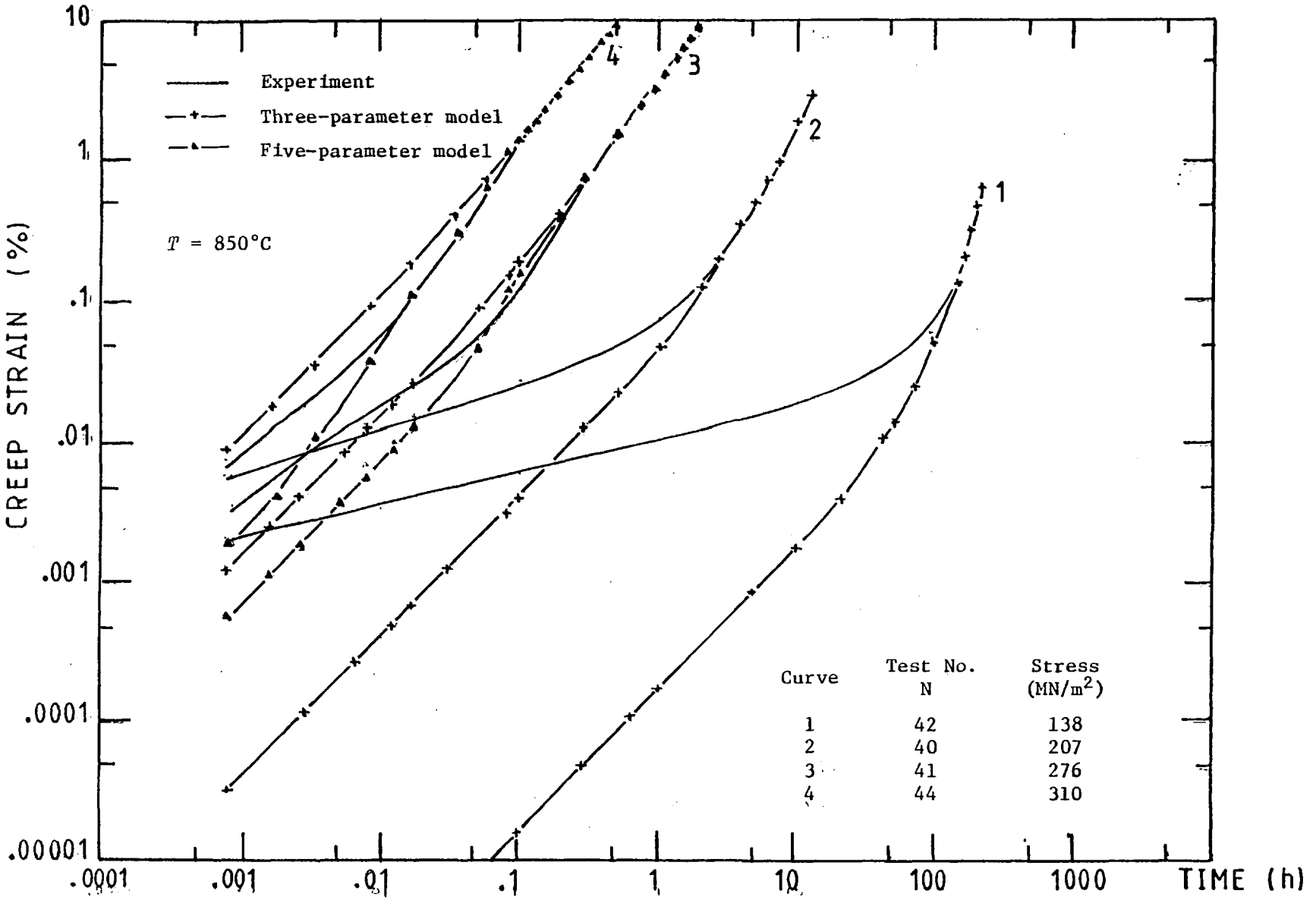

Figure F.5: Comparison between fitted and experimental creep strain versus time at 850°C

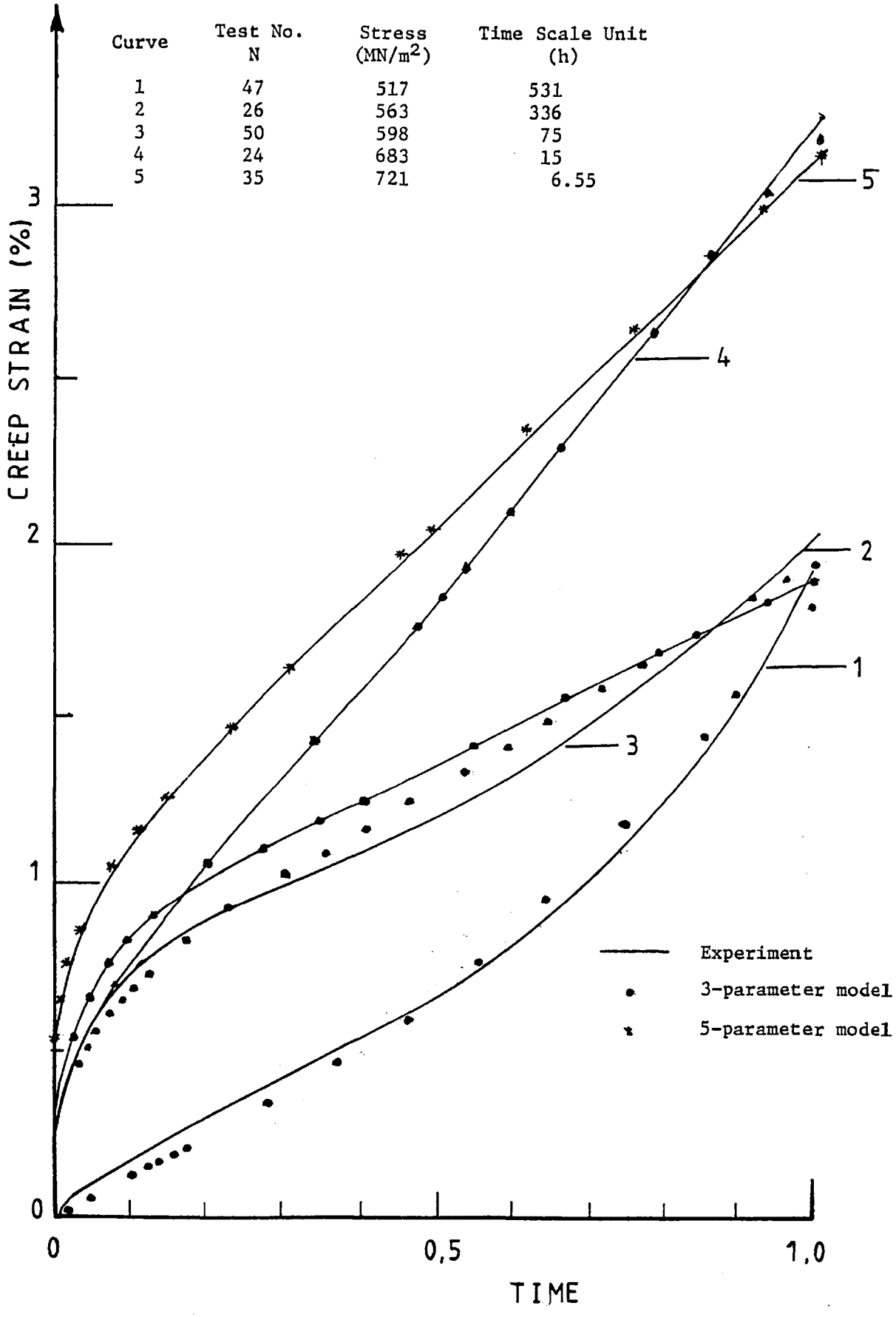

Figure F.6: Comparison between fitted and experimental creep data at 650°C

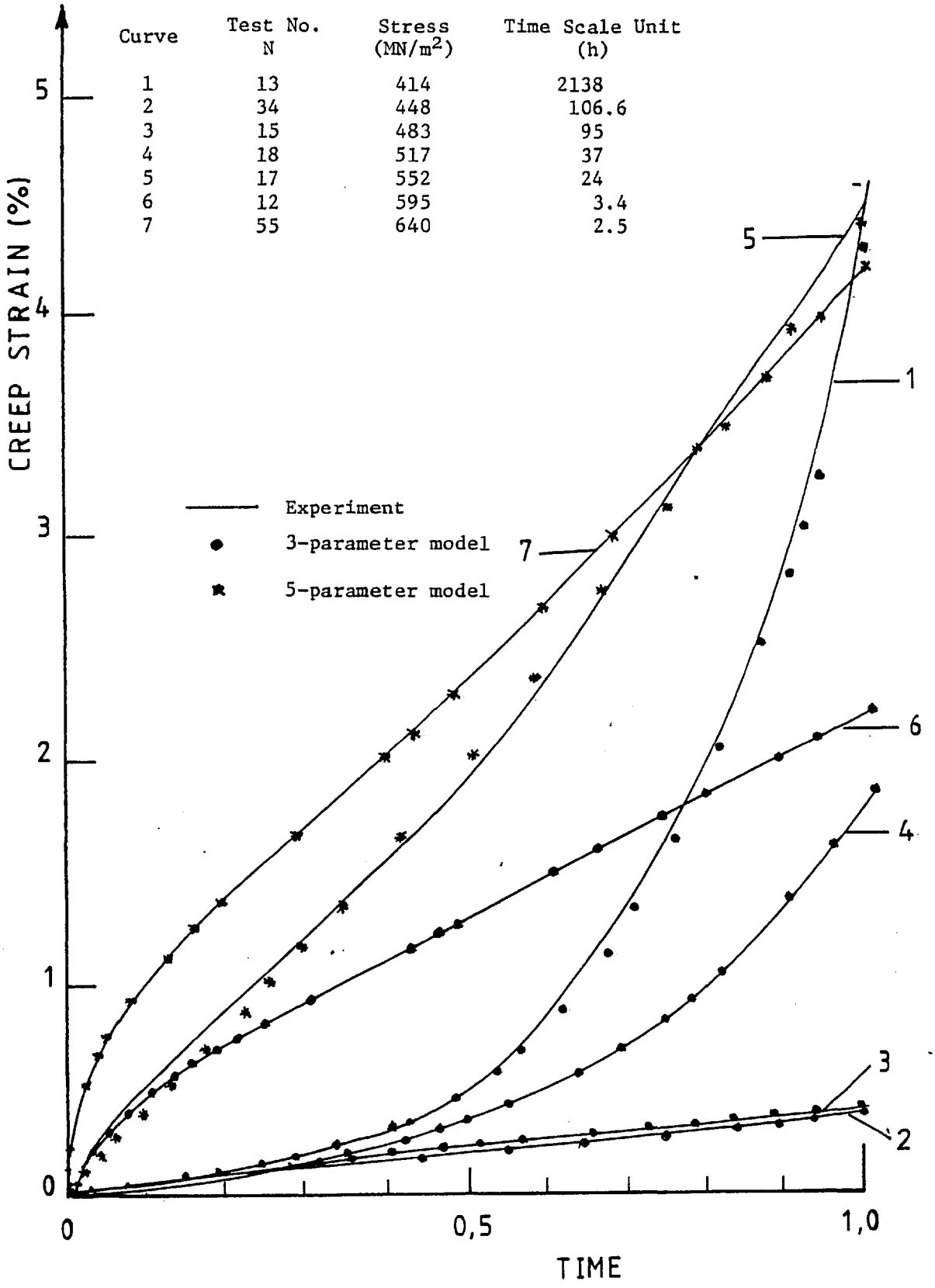

Figure F.7: Comparison between fitted and experimental creep data at 700°C

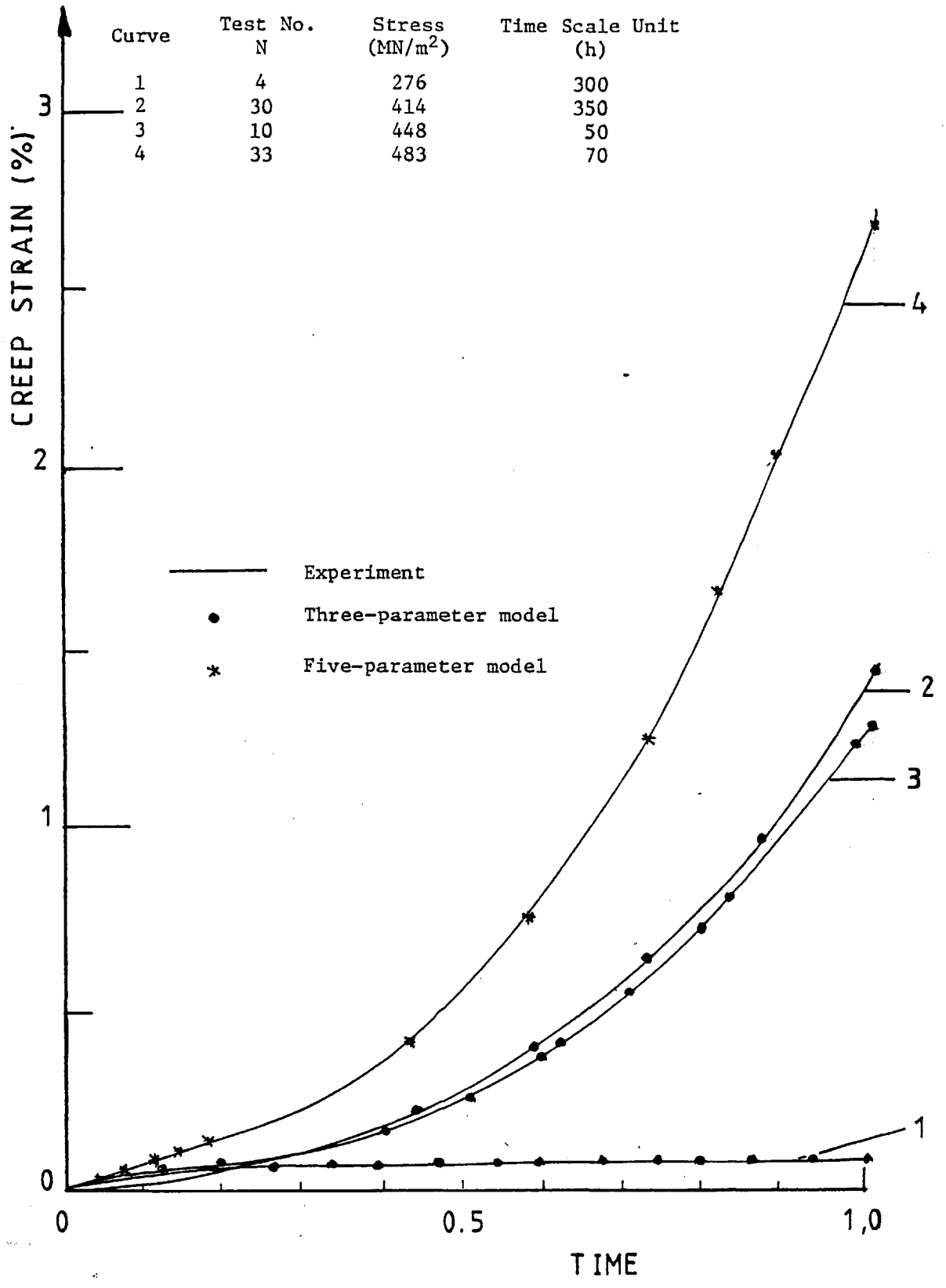

Figure F.8: Comparison between fitted and experimental creep data at 750°C

Curve	Test No. N	Stress (MN/m^2)	Time Scale Unit (h)	Strain Scale Unit (%)
1	23	207	698	9
2	22	276	68	5
3	21	310	24.7	5
4	25	379	4.8	5
5	27	448	1.2	5
6	28	483	0.33	5

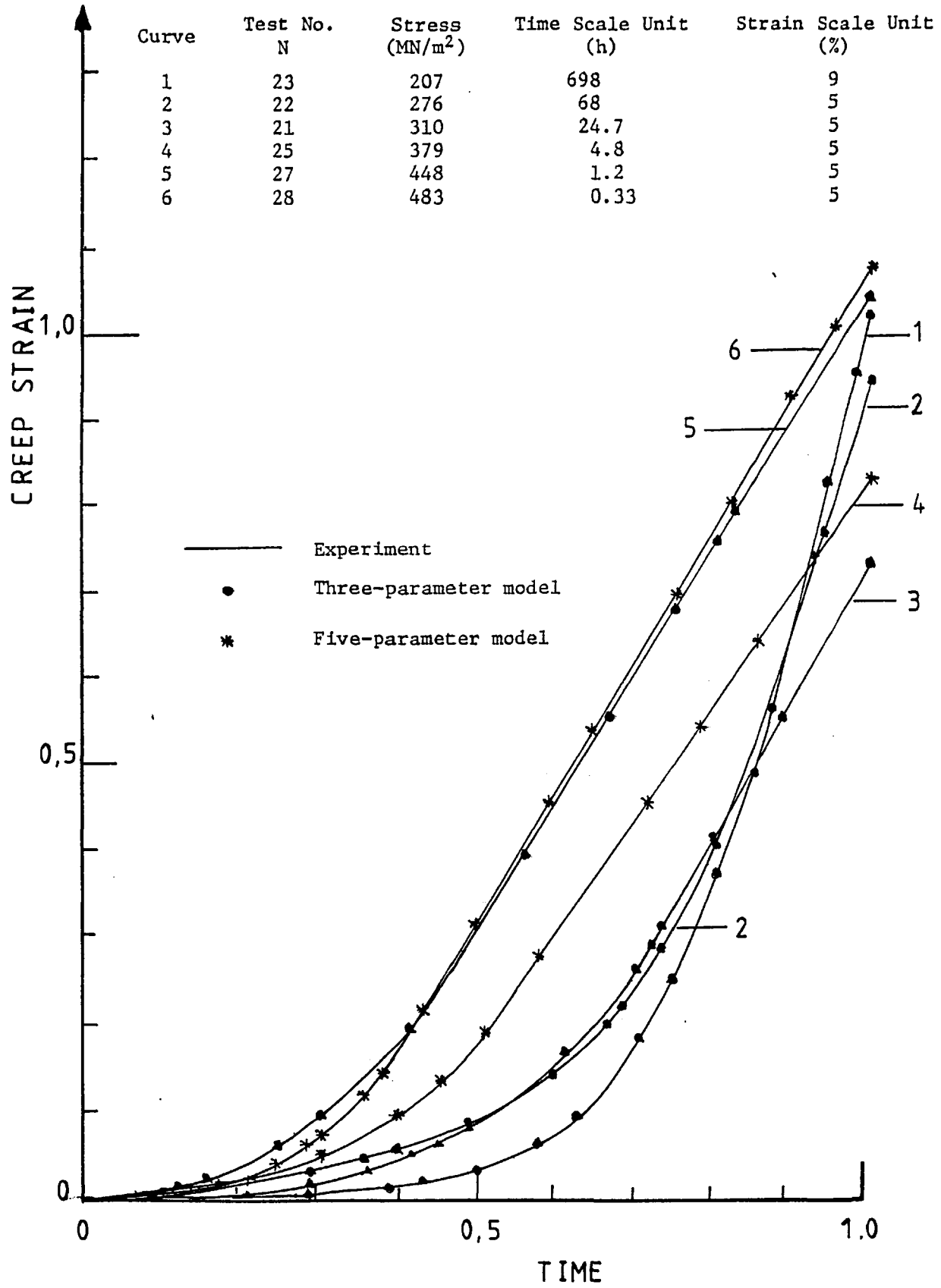

Figure F.9: Comparison between fitted and experimental creep data at 800°C

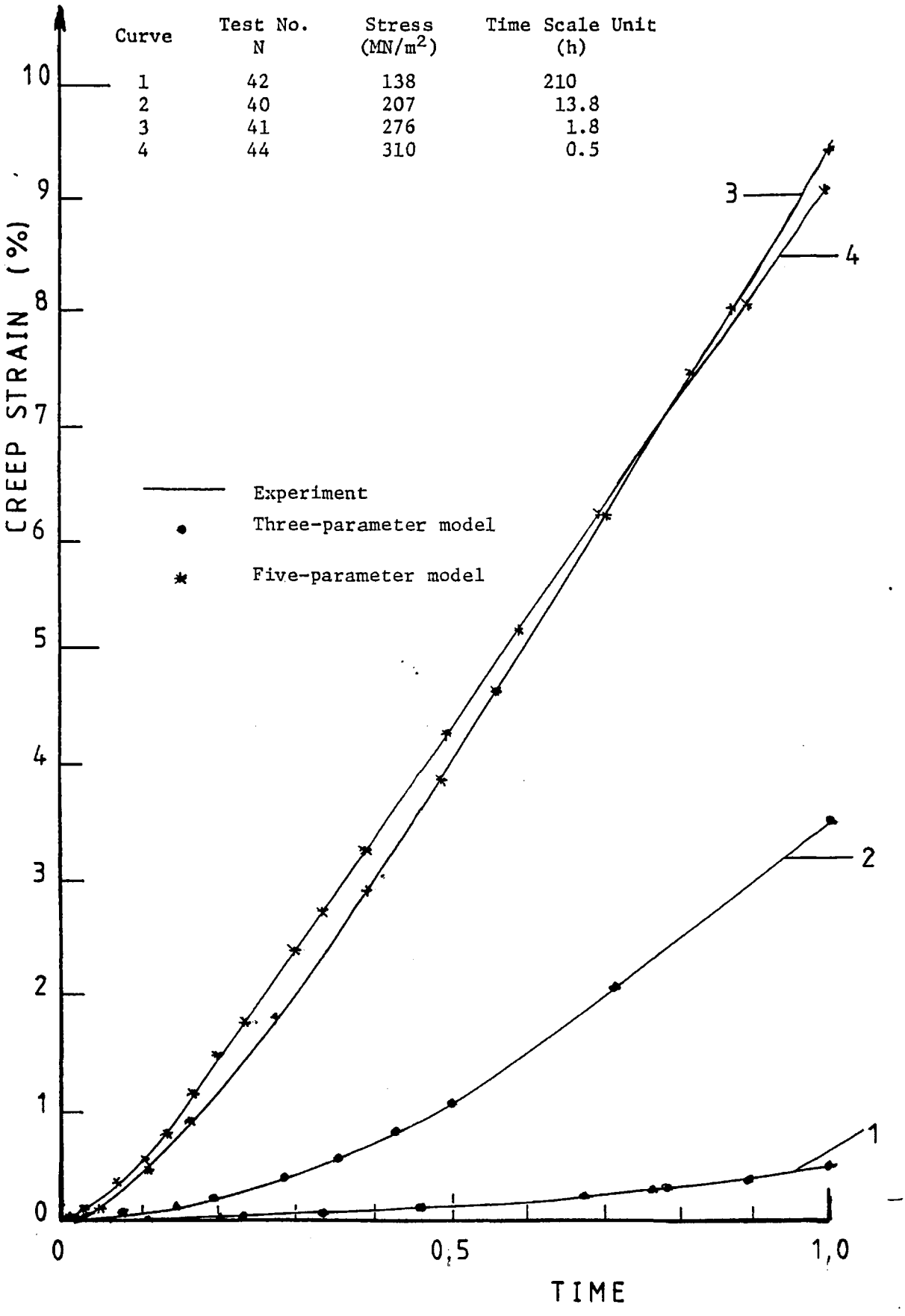

Figure F.10: Comparison between fitted and experimental creep data at 850°C

APPENDIX G

A RELATIONSHIP BETWEEN TRANSIENT AND STEADY-STATE CREEP AT ELEVATED TEMPERATURES

Paper by G.A. Webster, A.P.D. Cox, & J.E. Dorn

Published in *Metal Science Journal*, 3 (1969) 221

A Relationship between Transient and Steady-State Creep at Elevated Temperatures

G. A. Webster, A. P. D. Cox, and J. E. Dorn

An analysis is presented which shows that the strain (ε)/time (t) relation

$$\varepsilon = \varepsilon_0 + \varepsilon_T\{1 - \exp(-t/\tau)\} + \dot{\varepsilon}_s t$$

where ε_0 is the instantaneous strain on loading, ε_T the magnitude of transient creep, τ the relaxation time of transient creep, and $\dot{\varepsilon}_s$ the steady-state strain rate, can be derived by assuming that transient and steady-state creep obey first-order reaction-rate theory. The assumption is considered to be reasonable at temperatures greater than about one half of the melting temperature where creep is diffusion-controlled, provided that one diffusion-controlled process only is governing deformation. When these conditions are satisfied, the proportionality observed experimentally, for a number of materials over a range of stresses and temperatures, between the initial strain rate $\dot{\varepsilon}_i$, steady-state strain rate $\dot{\varepsilon}_s$, and the relaxation frequency $1/\tau$ is expected from the analysis. Departure from proportionality between $1/\tau$ and $\dot{\varepsilon}_s$ for type-316 stainless steel at low stresses is shown to be caused by the intrusion of a second process, in this case grain-boundary sliding, which contributes increasingly to deformation as stress is reduced. Evidence is also presented which shows that the above equation is an adequate description of creep strain after stress has been reduced during a test, indicating that dislocation structures formed at one stress can rearrange at another stress according to first-order kinetics. Finally, it is suggested that the product, $\dot{\varepsilon}_s t$, can be regarded as a stress/time/temperature parameter that can be used to correlate both creep strain and time to rupture of materials over the ranges of stress and temperature where the analysis applies.

Good quantitative correlations have been established between the steady-state creep rates at high temperatures (above $\sim 0{\cdot}5\ T_m$, where T_m is the melting temperature in degrees absolute) and the various factors on which they depend. Largely by default, however, correspondingly definitive rationalizations of transient-creep behaviour have not yet matured. The equations applied most frequently to describe the time-dependence of creep at high temperatures are

$$\varepsilon = \varepsilon_0 + at^{\frac{1}{3}} + \dot{\varepsilon}_s t \qquad \ldots(1)$$

and

$$\varepsilon = \varepsilon_0 + \varepsilon_T\{1 - \exp(-t/\tau)\} + \dot{\varepsilon}_s t \qquad \ldots(2)$$

where ε is strain at time t, ε_0 the instantaneous strain at $t = 0$, arising from application of the stress, and the remaining quantities a, $\dot{\varepsilon}_s$, ε_T, and τ are material parameters that depend on the stress and temperature as well.

The two above-quoted equations were originally presented as empirical relations.[1,2] The parameters of equation (1) can satisfactorily be adjusted to fit most of the high-temperature creep data spanning the transient and steady-state ranges.

Paper No. MS 148. Manuscript received 1 April 1969; accepted 5 June 1969. G. A. Webster, Ph.D., is a Lecturer and A. P. D. Cox, B.Sc.(Eng.), is a Research Student in the Department of Mechanical Engineering, Imperial College, London, where the work was carried out. J. E. Dorn, B.S., M.S., Ph.D., is Professor of Materials Science, Department of Mineral Technology, and Senior Research Metallurgist, Inorganic Materials Research Division, Lawrence Radiation Laboratory, University of California, Berkeley, Cal., U.S.A.

Similarly, as shown originally by McVetty[2] and later confirmed by Garofalo,[3] equation (2) also permits a good fit of experimental data. Consequently, any preference for one equation over the other must be based on other departures between them. Whereas equation (1) suggests that the initial creep rate is infinite, equation (2) leads to the physically more acceptable prediction of a finite creep rate immediately after loading. In some instances the initial creep rates are so high and changing so rapidly with time that it is not possible to decide whether they are infinite or finite. In a large number of examples, however, the initial creep rates are clearly finite and equation (2) must be preferred. Also several authors[4-6] have arrived at expressions analogous to equation (2) from detailed considerations of specialized dislocation models for the rates of multiplication and annihilation of dislocations during high-temperature creep.

Despite the apparent virtues of equation (2), the only parameter in it that has been studied in any detail is the steady-state creep rate $\dot{\varepsilon}_s$. The remaining rate-determining parameters, ε_T and τ, have been extracted from experimental data[7-9] but the origin and nature of their functional dependence on stress, temperature, &c., have not been discussed. In this paper simple reaction-rate concepts are invoked to relate the stress- and temperature-dependences of the parameters ε_T, τ, and $\dot{\varepsilon}_s$ to the rate-controlling mechanisms of high-temperature creep.

Analysis

The creep curve is separated into the distinct regions: primary (transient), secondary (steady-state), and later (tertiary) creep, merely for convenience of description. There are no experimental observations to suggest that creep is controlled by unique processes in each region. Indeed, the available evidence is to the contrary; it suggests that the same processes, while not necessarily always contributing in the same proportion, are active along the entire creep curve.

Simple relations have been obtained relating the different stages of creep. For example, Dorn[10] has shown that transient and steady-state creep can often be described by the same time/temperature parameter and other results[3,11] indicate that steady-state creep rate and time to rupture, t_r, can frequently be related by

$$\dot{\varepsilon}_s t_r = C \qquad \ldots (3)$$

where C is a constant for many materials. There would seem, therefore, to be grounds for believing that transient and steady-state creep can be correlated.

Excluding the case of fine-grained material under low stresses where Herring–Nabarro creep predominates, creep deformation usually proceeds by a combination of dislocation motion within grains and grain-boundary sliding accompanied by grain-boundary rotation and grain-boundary migration. Nevertheless situations do exist where a single process predominates. For instance at temperatures above $\sim 0{\cdot}5\ T_m$ creep is diffusion-controlled,[3,12] often with the major contribution to strain coming from dislocation motion.

Attention will be confined here to the simple case when only one process is controlling creep. When dislocation motion dominates, creep strain rate, $\dot{\varepsilon}$, is given by

$$\dot{\varepsilon} = \varphi b v \rho \qquad \ldots (4)$$

where φ is an orientation factor, b the Burgers vector, v the mean mobile dislocation velocity, and ρ is the mobile dislocation density. Transmission electron microscopy has revealed that dislocation structures change during creep.[2,3,7,13] Immediately following the initial plastic strain ε_0 (resulting from application of the stress) most of the dislocations are present in entanglements forming cell walls that appear in hedge-like arrangement wherever slip has taken place; this substructure is completely analogous to that obtained after cold work at room temperature. During transient creep, however, the entangelements disperse until, when steady-state creep is reached, the substructure consists of subgrains, having complex dislocation tilt and twist boundaries, within which are individual dislocations.

Exactly how the dislocation rearrangements occur will depend on the actual process controlling creep. If, for example, deformation is governed by dislocation climb, the average dislocation glide velocity will be represented by a term of the form $v = A_0/L\tau_c$, where L is the mean segment length of a climbing dislocation, τ_c the average time it takes a pair of segments of opposite sign to annihilate each other or for a pair of the same sign to climb out of their interaction field, and A_0 is the area swept out as a dislocation enters unoccupied volume of the crystal. When entanglements are prevalent A_0 will be relatively large and L small, but as subgrains form A_0 will become smaller and the dislocation segments longer so that the strain rate will decrease until steady-state creep is reached.

Other dislocation processes will produce similar effects and it is clear that, irrespective of the mechanism controlling creep, the product $v\rho$, which represents the rate at which area is being swept out by dislocations, will change as deformation proceeds and the dislocations rearrange themselves from their initial configuration after loading to the equilibrium substructure formed during steady-state creep. Consequently, before equation (4) can be integrated, a quantitative estimate of how this rearrangement takes place is required.

Consider the motion of individual dislocation segments. When this is controlled by vacancy diffusion, the speed of the dislocations will depend on the flux of vacancies to and from suitable sites on dislocations. This flux is given by simple first-order chemical kinetics. Furthermore, since the rearrangement of dislocations must also proceed by the motion of individual dislocations, and since Dorn[10] has shown that transient and steady-state creep can be described by the same time/temperature parameter, it is consistent to assume that this rearrangement will itself obey first-order chemical kinetics. Hence, in these circumstances the rate of change of the product $v\rho$ should be proportional to the difference between its current and steady-state values, or expressed in terms of strain rates

$$\frac{d\dot{\varepsilon}}{dt} = -(\dot{\varepsilon} - \dot{\varepsilon}_s)/\tau \qquad \ldots (5)$$

where τ is the relaxation time for rearrangement of dislocations during transient creep. When dislocation climb is controlling, τ will depend on τ_c.[14]

Whereas equation (5) is always valid when the deviation from the steady state, namely $\dot{\varepsilon} - \dot{\varepsilon}_s$, is small, regardless of the order of the reaction, the implication here is that it is valid also for large differences between $\dot{\varepsilon}$ and $\dot{\varepsilon}_s$.

Integration of equation (5) gives the required creep expression

$$\varepsilon = \varepsilon_0 + \varepsilon_T\{1 - \exp(-t/\tau)\} + \dot{\varepsilon}_s t \qquad \ldots (2)$$

where

$$\varepsilon_T = (\dot{\varepsilon}_i - \dot{\varepsilon}_s)\,\tau \qquad \ldots(6)$$

and $\dot{\varepsilon}_i$ is the creep rate at $t = 0$. In addition, because the same process is assumed to be controlling the cooperative rearrangement of the dislocations as is controlling their individual motion, it follows that the coefficient $\dot{\varepsilon}_s$ and the relaxation frequency $1/\tau$ should have the same stress- and temperature-dependence, i.e.

$$1/\tau = A\dot{\varepsilon}_s \qquad \ldots(7)$$

where A is a dimensionless constant of proportionality. A similar relation may also be determined between $\dot{\varepsilon}_i$ and $\dot{\varepsilon}_s$. It has been shown[13,15,16] that the same form of relationship exists between stress and dislocation density measured from tensile tests as exists between stress and dislocation density measured during steady-state creep, i.e.

$$\sigma = \alpha Gb\sqrt{\rho} \qquad \ldots(8)$$

where σ is the applied stress relative to glide on the slip planes and α is a proportionality factor in the range 0·1–2. This observation suggests that equivalent dislocation structures, which have the same functional dependence on stress and temperature, are produced immediately after loading as are produced during steady-state creep. Consequently, it is reasonable (from equation (4)) to expect $\dot{\varepsilon}_i$ and $\dot{\varepsilon}_s$ also to have the same stress- and temperature-dependence, i.e.

$$\dot{\varepsilon}_i = B\dot{\varepsilon}_s \qquad \ldots(9)$$

where B is another proportionality factor.

The actual functional forms of $\dot{\varepsilon}_i$, $\dot{\varepsilon}_s$, and τ will be determined by the process controlling creep. For diffusion-controlled processes the experimentally determined steady-state creep rate can usually be expressed by a relationship of the form[13]

$$\dot{\varepsilon}_s = A_s \left(\frac{\sigma}{G}\right)^n \frac{DGb}{kT} \qquad \ldots(10)$$

where G is the shear modulus, D the self-diffusivity, A_s a proportionality factor, kT the Boltzmann constant times absolute temperature, and n is usually in the range 4–8.

Equations (7), (9) and (10) will now be compared with some experimental results of Evans and Wilshire[9] on zinc, nickel, and iron, and those of Garofalo *et al.*[7,8] on type-316 stainless steel and an austenitic iron-base alloy.

Comparison with Experimental Data

Equation (2) was found to describe adequately the creep data for all the materials examined. The numerical values of the coefficients $\dot{\varepsilon}_i$, $\dot{\varepsilon}_s$, ε_T, and τ, which were obtained by the respective authors from computer calculations, are not included in this paper for the sake of brevity. However, the relationships between them are described in some detail.

In all cases the results confirm the proportionality between $\dot{\varepsilon}_i$ and $\dot{\varepsilon}_s$ over the range of stresses and temperatures investigated. Where sufficient data are available the stress- and temperature-dependence of steady-state creep rate is also in reasonable agreement with equation (10).

The relationship between $1/\tau$ and $\dot{\varepsilon}_s$ bears closer inspection.

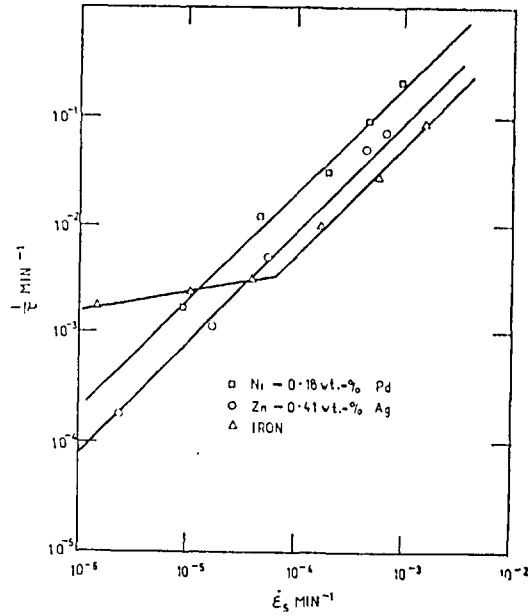

Fig. 1 The relationship between the steady-state creep rate, $\dot{\varepsilon}_s$, and the relaxation frequency, $1/\tau$, over a range of stress. (Evans and Wilshire.[9])

Fig. 1 is a plot of data obtained by Evans and Wilshire[9] from experiments carried out on nickel, zinc, and iron at different stresses but at a constant temperature (close to 0·5 T_m) for each material. The results demonstrate the proportionality between $1/\tau$ and $\dot{\varepsilon}_s$, except at low stresses for the iron. The departure from linearity for iron was caused by a sudden change in the stress-dependence of $1/\tau$ at low stresses, while that of $\dot{\varepsilon}_s$ remained the same. No reasons for this were ascertained at the time.

Fig. 2 shows a similar plot for an austenitic iron-base alloy[8] over a range of stresses at 704° C. It again demonstrates the proportionality between $1/\tau$ and $\dot{\varepsilon}_s$. Furthermore, it indicates that the ratio is essentially independent of grain size for the extent of grain diameters considered (namely 9–190 μm).

Fig. 3 relates to the results obtained for type-316 stainless steel.[7] The significance of these is that they confirm the proportionality between $1/\tau$ and $\dot{\varepsilon}_s$ over a range of temperature as well as stress, although there is some deviation from linearity at low stresses, (i.e. low strain rates). Just as with the iron (Fig. 1) this was caused by a change in the functional form of $1/\tau$, while that of $\dot{\varepsilon}_s$ remained unchanged. A possible explanation of this may be gathered from some measurements of the relative contribution of grain-boundary sliding to total creep strain obtained by Garofalo *et al.*[7] during the course of their investigation. The results are presented in Fig. 4 as a function of stress. They show that the contribution made by grain-boundary sliding is small ($< \sim 10\%$) above a stress of $\sim 13\,000$ lbf/in^2. Below this value grain-boundary sliding becomes progressively more important with decreasing stress, until at the lowest stress it amounts to almost half the total strain.

For type-316 stainless steel at low stresses, therefore, dislocation motion within the grains and grain-boundary sliding both contribute significantly to creep deformation. Under these circumstances equation (4) does not predict the total amount of creep strain. In addition, simple first-order chemical kinetics will not be obeyed because two processes with different stress-dependences are occurring together. This

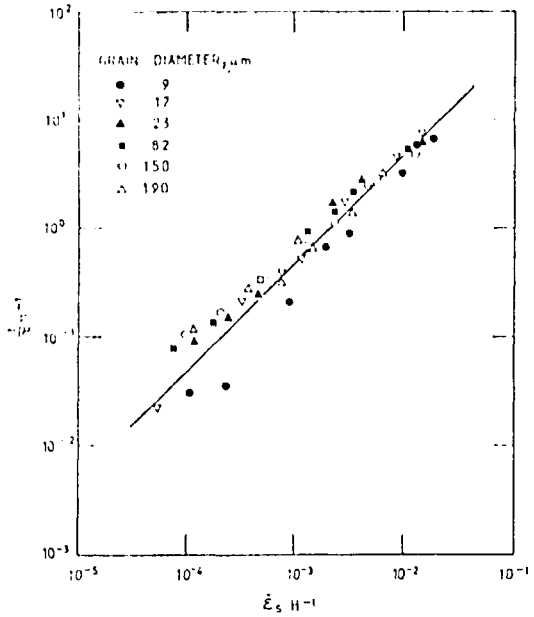

Fig. 2 Relationship between steady-state creep rate, $\dot{\varepsilon}_s$, and the relaxation frequency, $1/\tau$, for an austenitic iron-based alloy[8] over a range of stresses and grain sizes at 704° C (0·55 T_m).

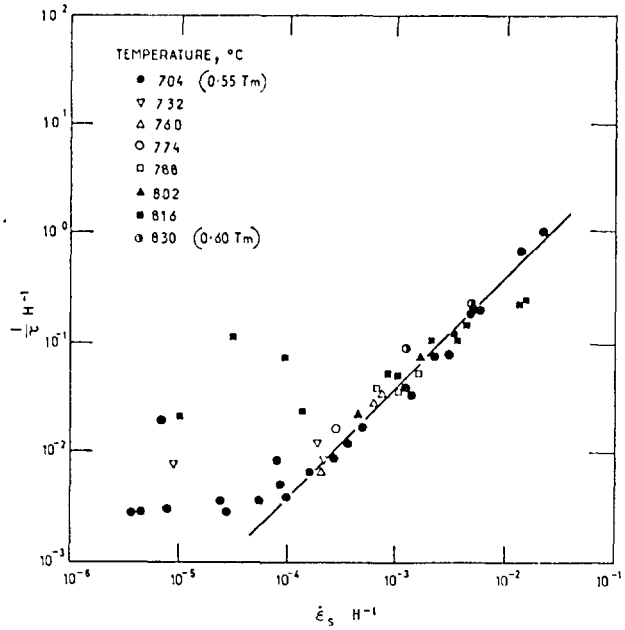

Fig. 3 Relationship between steady-state creep rate, $\dot{\varepsilon}_s$, and relaxation frequency, $1/\tau$, for type-316 stainless steel[7] over a range of stresses and temperatures.

argument applies irrespective of whether or not the two processes operate independently. Consequently, the loss of proportionality between $1/\tau$ and $\dot{\varepsilon}_s$ is to be expected at low stresses for this material.

If all the data below 13 000 lbf/in^2 are eliminated from Fig. 3, Fig. 5 is obtained. The latter figure indicates proportionality between $1/\tau$ and $\dot{\varepsilon}_s$ over the whole range where deformation occurs chiefly by dislocation motion within the grains, thus demonstrating effectively that the deviation from proportionality at low stresses was caused by the complication of grain-boundary sliding contributing appreciably to creep.

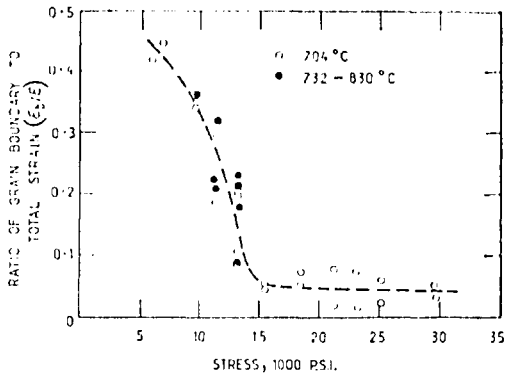

Fig. 4 The contribution of grain-boundary sliding to total creep strain as a function of stress for type-316 stainless steel.[7]

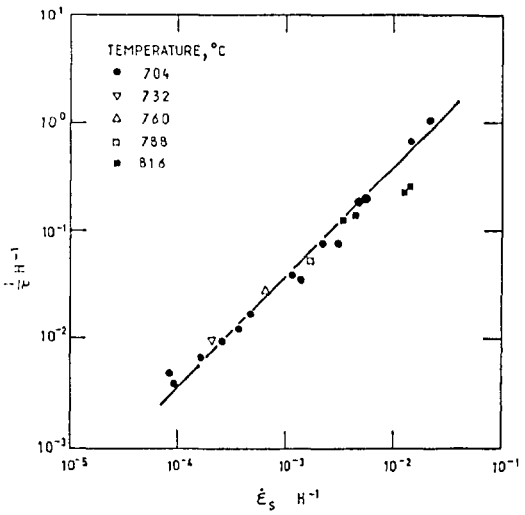

Fig. 5 Relaxation frequency, $1/\tau$, as a function of steady-state creep rate, $\dot{\varepsilon}_s$, at stresses > 13 000 lbf/in^2 for type-316 stainless steel.

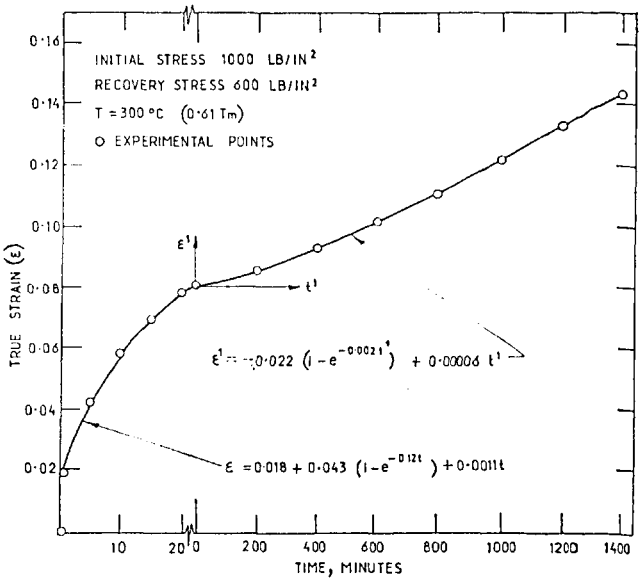

Fig. 6 Fit of the creep equation (2) to data of Raymond and Dorn[17] on pure aluminium, before and after a stress change.

An analysis by the present authors of some constant-stress creep data at temperatures in the neighbourhood of 0·5 T_m for pure aluminium, previously published by Raymond and Dorn,[17] again showed the adequacy of equation (2) although insufficient results were available to draw any conclusions about the relationship between $\dot{\varepsilon}_i$, $\dot{\varepsilon}_s$, and τ. Fig. 6 illustrates, however, that equation (2) is still applicable after stress is reduced by a moderate amount part way through a creep test, suggesting that a dislocation substructure formed at one stress also relaxes according to first-order chemical kinetics when rearranging to form a steady-state substructure at a lower stress.

Discussion

The good agreement obtained between theory and experiment at elevated temperatures shows that, when one diffusion-controlled process only is governing deformation, transient and steady-state creep can be related, to a first approximation, by simple first-order reaction-rate theory. When deformation obeys first-order chemical kinetics, proportionality between the initial strain rate $\dot{\varepsilon}_i$, steady-state strain rate $\dot{\varepsilon}_s$, and relaxation frequency $1/\tau$ is expected. This is demonstrated by the experimental data except at low stresses for iron and type-316 stainless steel. The deviation from proportionality for stainless steel was shown to be caused by the occurrence of appreciable grain-boundary sliding at the lower stresses. It is a general observation that the relative contribution of grain-boundary sliding to total strain increases with decreasing stress, so that it is quite possible that departure from linearity at low stresses for the iron was also caused by the introduction of significant grain-boundary sliding.

Table 1 summarizes the calculated values obtained for the ratios $1/\dot{\varepsilon}_s\tau$ and $\dot{\varepsilon}_i/\dot{\varepsilon}_s$, together with the magnitudes of ε_T for the materials considered. It must be mentioned, however, that significant deviations were sometimes obtained[9] between the experimental and calculated values of $\dot{\varepsilon}_i$, suggesting that simple first-order reaction-rate theory is not always obeyed immediately after loading. Nevertheless, even in these instances it affords a good approximation over the remainder of the creep curve. From Table 1 it will be seen that $\dot{\varepsilon}_i/\dot{\varepsilon}_s$ varies very little with material and that $1/\dot{\varepsilon}_s\tau$ changes by less than an order of magnitude. The constancy of $1/\dot{\varepsilon}_s\tau$ with grain size for the austenitic iron-based alloy is significant and provides further substantiation of the link between τ and $\dot{\varepsilon}_s$, particularly as both $1/\tau$ and $\dot{\varepsilon}_s$ were, themselves, found to be grain-size-dependent.[8]

Because of the proportionality between $\dot{\varepsilon}_i$, $\dot{\varepsilon}_s$, and $1/\tau$, the magnitude of transient creep ε_T is a constant (from equation (6)) independent of stress and temperature for a given material. By making use of equation (7), the creep equation (2), neglecting the instantaneous strain on loading, can be written in the form

$$\varepsilon = \varepsilon_T\{1 - \exp(-A\dot{\varepsilon}_s t)\} + \dot{\varepsilon}_s t \quad \ldots(11)$$

where the steady-state creep rate $\dot{\varepsilon}_s$ is the only coefficient in the expression that depends on stress and temperature. The rate of relaxation of transient creep is given by the exponential term in equation (11) and is, therefore, determined directly by the steady-state creep rate. Furthermore the product $\dot{\varepsilon}_s t = \theta$, say, can be regarded as a stress/time/temperature parameter which can be used to construct a master creep curve to correlate creep data over a range of stresses and temperatures for a given material, i.e.

TABLE 1

Summary of the Relationships between the Coefficients $\dot{\varepsilon}_i$, $\dot{\varepsilon}_s$, τ, and ε_T for the Materials Examined

Material	$1/\dot{\varepsilon}_s\tau = A$	$\dot{\varepsilon}_i/\dot{\varepsilon}_s = B$	ε_T,%
Iron	45	3·3	5·1
Nickel	73	3·3	3·15
Zinc	190	3·3	1·2
Austenitic iron-base alloy	50	3–6·4*	4–11*
Type-316 stainless steel	38	3·3	6·0

* Varies to some extent with grain size

$$\varepsilon = \varepsilon_T\{1 - \exp(-A\theta)\} + \theta \quad \ldots(12)$$

where this expression is the equation of the master curve. Equation (3) further states that rupture occurs at a limiting value of this stress/time/temperature parameter, namely $\theta = C$. Consequently, equation (12) indicates that this rupture criterion can be thought of either as a constant total-strain criterion or as a constant steady-state creep-strain criterion.

The limited evidence suggesting that creep after a stress change also obeys equation (2) indicates that a dislocation structure formed at one stress relaxes at another stress according to first-order chemical kinetics. So long as a stress change does not cause a change in the rate-controlling process of creep, such a result would be expected from the analysis. This evidence, therefore, provides further support for the approach.

Acknowledgements

The authors wish to express their grateful thanks to the Science Research Council for providing funds to enable Professor Dorn to visit Imperial College for eight weeks in 1968, during which time this work was initiated, to Rolls-Royce for giving financial support to one of them (A.P.D.C.), and to Dr. Newey for helpful comments.

References

1. E. N. da C. Andrade, *Proc. Roy. Soc.*, 1910, [A], **84**, 1.
2. P. G. McVetty, *Mech. Eng.*, 1934, **56**, 149.
3. F. Garofalo, "Fundamentals of Creep and Creep-Rupture in Metals". **1965:** New York, &c. (Macmillan).
4. N. S. Akulov, *Acta Met.*, 1964, **12**, 1195.
5. J. C. M. Li, *ibid.*, 1963, **11**, 1269.
6. G. A. Webster, *Phil. Mag.*, 1966, **14**, 775.
7. F. Garofalo, O. Richmond, W. F. Domis, and F. von Gemmingen, "Joint International Conference on Creep", p. 1/31. **1963:** London (Inst. Mech. Eng.).
8. F. Garofalo, W. F. Domis, and F. von Gemmingen, *Trans. Met. Soc. A.I.M.E.*, 1964, **230**, 1460.
9. W. J. Evans and B. Wilshire, *ibid.*, 1968, **242**, 1303.
10. J. E. Dorn, "Creep and Fracture of Metals at High Temperatures", p. 89. **1956:** London (H.M. Stationery Office).
11. P. W. Davies, J. D. Richards, and B. Wilshire, *J. Inst. Metals*, 1961–62, **90**, 431.
12. J. E. Dorn, "Creep and Recovery", p. 255. **1957:** Cleveland, Ohio (Amer. Soc. Metals).
13. A. K. Mukherjee, J. E. Bird, and J. E. Dorn, *Univ. California Rep.* **(UCRL 18526)**, 1968.
14. J. E. Bird and J. E. Dorn, private communication, to be published.
15. D. McLean, "Mechanical Properties of Metals". **1962:** New York and London (John Wiley).
16. D. McLean, *Trans. Met. Soc. A.I.M.E.*, 1968, **242**, 1193.
17. L. Raymond and J. E. Dorn, *ibid.*, 1964, **230**, 560.

APPENDIX H

SOME EFFECTS OF GRAIN STRUCTURE ON THE CREEP PROPERTIES OF A CAST NICKEL BASE ALLOY

Paper by A.P.D. Cox & G.A. Webster

Published in *Jernkontorets Annaler*, 155 (1971) 349

SOME EFFECTS OF GRAIN STRUCTURE ON THE CREEP PROPERTIES OF A CAST NICKEL-BASE ALLOY

A. P. D. Cox[1] and G. A. Webster[1]

539.434:669.245-14

INTRODUCTION

For many years one of the main concerns of engineers and metallurgists working in the creep field has been to develop materials with improved elevated temperature properties. As with room temperature properties, an improvement in creep rupture strength is generally accompanied by a decrease in ductility. For practical applications a reasonable balance must be achieved between the two, as too low a ductility could result in premature failure of a component at stress concentrations.

The nickel base alloys, which are currently used in many high temperature applications, are examples of materials where alloying additions and heat treatments have been suitably blended to provide improved creep rupture strength, whilst still maintaining adequate rupture ductility when used in both the cast and wrought forms.

Failure in long time creep tests in nickel-base alloys is predominantly intercrystalline and along grain boundaries transverse to the applied stress axis. These transverse boundaries can be eliminated by directional solidification. Directional solidification in nickel base alloys results in a columnar grained structure with a preferred [001] orientation. First VerSnyder and Guard [1] and then others [2–5] have shown that the elimination of transverse grain bounderies in these materials removes an early source of failure. In addition, the preferred orientation gives added creep strength [4] so that directional solidification can improve both the creep lives and ductilities of nickel-base alloys.

The structural processes occurring during the elevated temperature deformation of directionally solidified nickel-base alloys have been investigated by a number of authors [4, 6, 7]. Webster and Piearcey [8] found, in contrast to conventionally cast nickel-base alloys, that a directionally solidified alloy, containing 60% by volume of γ', exhibited an incubation period prior to the onset of normal primary, secondary and tertiary creep. Structural changes accompanying the creep deformation showed γ' precipitate agglomeration, a build up of dislocations at the γ/γ' interface and growth of the carbide particles. Because these processes were occurring simultaneously, it was not possible to assess their relative efforts. This complication also arose when stress and/or temperature were cycled [9]. However, some specimens were specially heat-treated to promote the growth of γ' precipitate or M_6C carbides, and it was found that the more significant changes in the creep rupture time were due to the M_6C growth, which considerably reduced the rupture time. In the present investigation a simpler nickel base alloy containing a much lower fraction of γ' precipitate and fewer carbides is examined.

MATERIAL AND SPECIMENS

The alloy chosen for this investigation is basically a simplified form of the commercial nickel-base alloy Nimonic 80A[2]. It has the composition 19.5% chromium, 2.5% titanium, 1.5% aluminium, 0.06% carbon and balance nickel. The material was cast in both the conventional and directionally solidified forms. Directionally solidified ingots, 50 mm in diameter, 80 mm long, were produced with an [001] oriented grain structure by the exothermic mould technique. The conventionally cast material was produced in ingots 130 mm in diameter and 130 mm long, the true equiaxed grain structure being limited to the inner 60 mm diameter.

In each case rough specimen blanks were removed from the ingots, solution treated in air at 1 080 ± 5°C for 8 h and air cooled. The blanks were then finish machined before ageing in air at 700 ± 2°C for 16 h and air cooling. This heat-treatment produced a uniform dispersion of fine $Ni_3(Al,Ti)$ γ' precipitate

[1] Department of Mechanical Engineering, City and Guilds College, London.

[2] Trade name of Henry Wiggin Ltd.

particles, approximately 100 Å in diameter, in a γ solid solution matrix, and no large carbide particles.

The specimens used were of a size and shape previously [10] found to reduce misalignment in creep tests. Each specimen had a gauge section with a diameter of 6.4 mm and a length of 38 mm. Initially the orientation of the [001] axis of the columnar grained specimens was checked by the Laue x-ray back-reflection method. However, subsequently it was found satisfactory to etch the gauge section, to reveal the columnar grain stucture, as shown in Fig. 1.

EXPERIMENTAL PROCEDURE

Uni-axial tensile creep experiments were carried out in lever-type testing machines, following the procedures recommended by Penny et al. [10], and using an extensometer arrangement described by Tishler and Wells [11]. In each case the initial elastic and plastic strains on loading and the subsequent creep strains were recorded automatically, with an estimated accuracy of $\pm 0.002\%$, using linear variable differential transducers.

All experiments were carried out as near as possible at a constant stress. For long time tests a constant stress condition was approximated by removing $\frac{1}{2}\%$ of the load from the loading arm every $\frac{1}{2}\%$ of strain, to allow for reduction in area of the cross section. In short time tests, high ductilities (in excess of 20%) in the columnar grained material made this method impractical. In these experiments automatic stress compensation was adopted. This was achieved by using the signal from the extensometer transducer to traverse a jockey weight progressively along the lever arm to keep the load proportional to the strain in the gauge length.

Experiments were carried out over the stress range from 140 to 700 MN/m² and over the temperature range from 650 to 900°C (approximately 0.55 to 0.75 T_m, the melting temperature in degrees absolute) to give rupture lives in the region 0.1 to 1 000 h. Hardness measurements were made on each specimen before and after creep. Most specimens were tested to failure, but a number were interrupted in various stages of creep. When experiments were interrupted, the specimens were cooled rapidly under load to preserve, as far as possible, the dislocation substructures formed during creep.

Samples for thin-foil electron microscopy were taken from 0.3 mm thick slices cut transversely from the gauge lengths of tested specimens. Each sample was mechanically thinned to 0.1 mm, polished by a jet of 50% HCl, and finally thinned in either a solution of 80% acetic acid and 20% perchloric acid at −5°C and 14 V, or in a solution of 10% perchloric acid and 90% ethanol at −40°C and 25 V.

EXPERIMENTAL RESULTS

Mechanical data

Creep curves to rupture have been obtained for both the conventionally cast and the directionally solidified material. Figures 2 and 3 show the range of shapes of curves obtained for the directionally solidified material. Curve (a) on Fig. 2 is typical of the shape observed at 650 and 700°C at creep stresses in excess of the yield stress (approximately 500 MN/m²), whereas curve (b) is typical of tests carried out at temperatures above 700°C at low stresses. Curve (a) exhibits the normal primary, secondary and tertiary stages of creep, but curve (b) initially shows a very low creep rate which increases gradually until a constant high creep rate is obtained. Not all low stress tests exhibited this constant high creep rate, however: in some tests the creep rate continued to increase until failure. Figure 3 shows a curve typical of a test carried out at

Fig. 1. Creep specimen showing oriented grain structure of directionally solidified material.

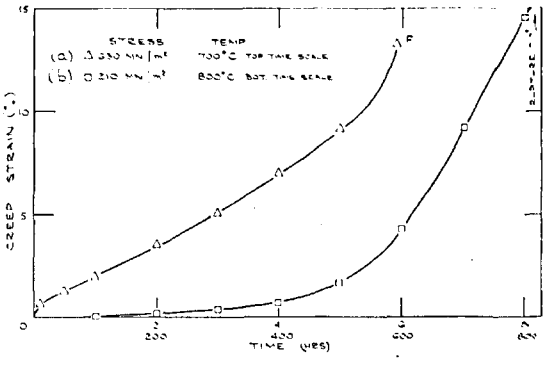

Fig. 2. Typical high and low stress creep curves of directionally solidified material.

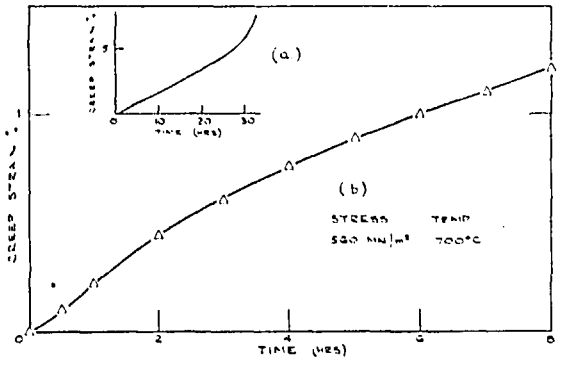

Fig. 3. Typical intermediate stress creep curve of directionally solidified material.

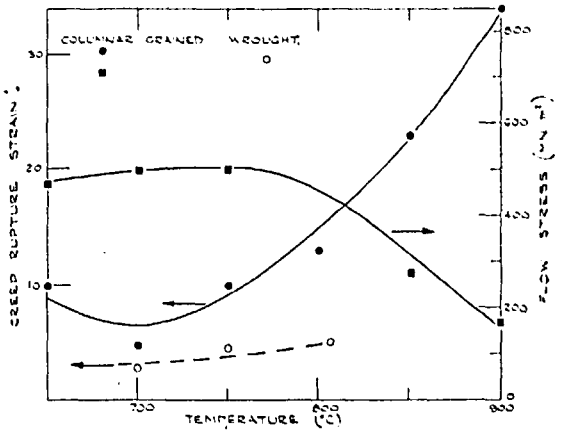

Fig. 5. Temperature dependence of ductility and flow stress of directionally solidified material.

a stress in the region of the yield stress. The curve shows a slight tendency towards a reduced creep rate and an incubation period prior to the onset of normal primary, secondary and tertiary creep.

No evidence of a low initial creep rate has been observed in any of the experiments carried out on the conventionally cast material. A comparison between creep curves obtained at the same stress and temperature for the conventionally cast and the directionally solidified materials is shown in Fig. 4. It will be observed that the creep rate in the conventionally cast material is always greater and that this material failed with a ductility of approximately 0.1% strain. In no cases have ductilities in excess of 1% strain been obtained with the conventionally cast material at test temperatures of 700°C and 750°C.

The temperature dependences of the rupture ductility and of the yield stress of the directionally solidified material are shown in Fig. 5. It will be observed that the minimum ductility of approximately 5% strain occurs at 700°C, where the yield stress is a maximum. As the yield stress decreases above 750°C, ductility progressively increases to a value in excess of 30% at 900°C. There was some spread in the ductilities of individual specimens, which was attributed to the relatively large grain size (approximately 4 mm in some instances) of the material and to slight misalignments in grain orientations. At the large ductilities appreciable necking, sometimes in more than one place in the same specimen, occurred prior to fracture.

Hardness measurements taken on the unstressed ends of tested specimens showed that at 650 and 700°C there is a continuing slight increase in hardness with increasing time and temperature; at 750 and 800°C very little change, and at 850 and 900°C a rapid fall to almost the solution treated value.

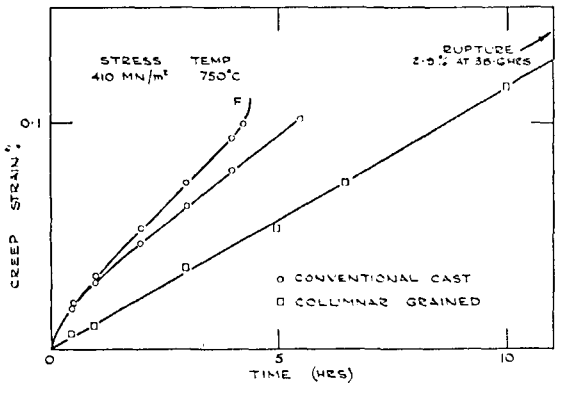

Fig. 4. Comparison between creep curves of directionally solidified and conventionally cast material.

STRUCTURAL OBSERVATIONS

As expected, failure in the conventionally cast material was initiated along grain boundaries predominantly transverse to the stress axis. Also in some instances porosity, during the casting process, was observed, which may have contributed to the very low ductilities obtained with this material. In the columnar grained material cracks were found to initiate (as shown in Fig. 6) from short, almost transverse, interdendritic regions in the longitudinal grain boundaries. Final failure was transcrystalline in either a shear or a direct tensile mode (Fig. 7). In addition, some separation of longitudinal grain

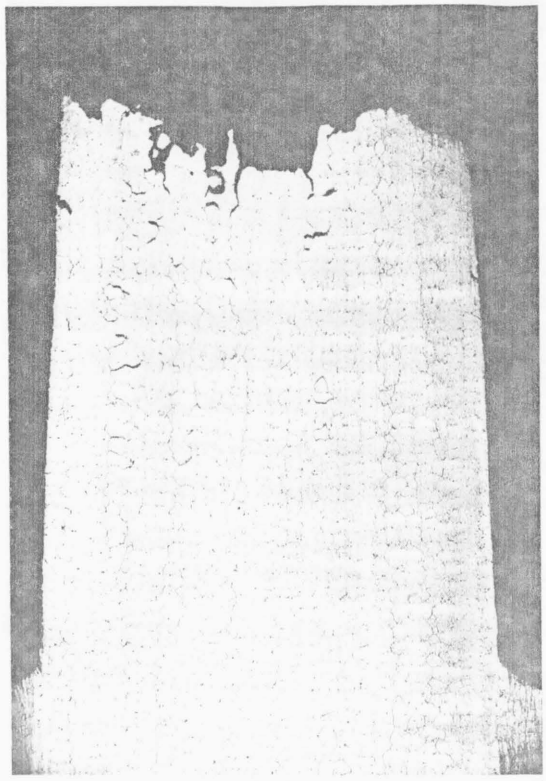

×10

Fig. 6. Longitudinal section of typical creep fracture of directionally solidified material.

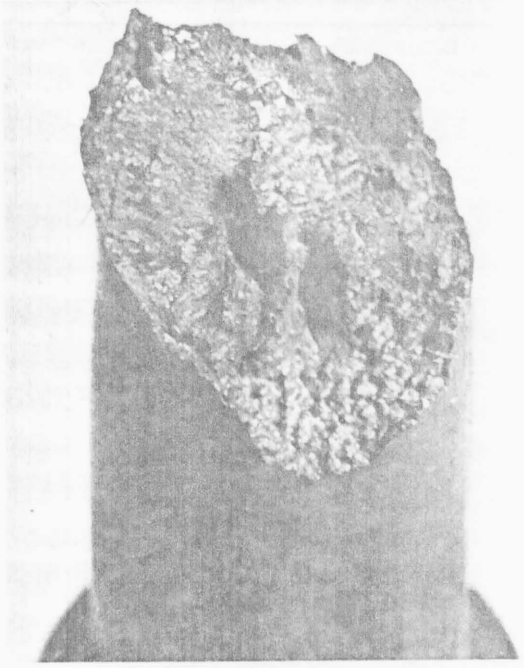

Fig. 7. Fracture surface of directionally solidified material.

boundaries has been observed, indicating considerable deformation of individual grains after separation had occurred. No significant differences in rupture ductilities or fracture characteristics were observed between short-time and long-time creep tests.

Dislocation substructures characteristic of different stages of creep, and γ' particle size changes are shown in Fig. 8. In the initial condition very few dislocations were observed. Fig. 8(a) shows the low dislocation density associated with the low strain rate region of creep curve (b) in Fig. 2, where there is little interaction between γ' particles and dislocations. Fig. 8(b) is taken from a specimen near failure after a creep curve of type (a) and shows an increase in dislocation density but still little interaction, the strain in this case being approximately 5%. Fig. 8(c) shows a much higher dislocation density with the particles surrounded by dislocations and is typical of low stress conditions at a well advanced tertiary stage. (8% strain after 2,633 h). Fig. 8(d) shows much the same type of structure as Fig. 8(c) but has been reached after only 20 h at 850 C, and at a strain of approximately 11%, which corresponds to the end of the secondary creep section of curve (b) in Fig. 2. The γ' particle size for both Figs. 8(c) and 8(d) is of comparable size, which indicates the high temperature of dependence of particle growth rate and is in general agreement with the $t^{\frac{1}{3}}$ power growth law as proposed by Oriani [12] and confirmed for nickel-base alloys by Mitchell [13].

DISCUSSION OF RESULTS

The directionally solidified material shows unusual shapes of creep curves, which are not shown by the conventionally cast material. Compared with previous work on a more complex alloy [8], an incubation period is only observed at stresses in the region of the flow stress, and the very low initial strain rate followed by an increased secondary rate is a phenomenon which has not been observed before. The incubation period and low initial strain rates are attributed to a low initial dislocation density after loading, which only builds up slowly as deformation proceeds. Large initial plastic strains are required to introduce enough dislocations initially for sufficient work hardening to occur for primary creep of any magnitude to be observed. In the low stress

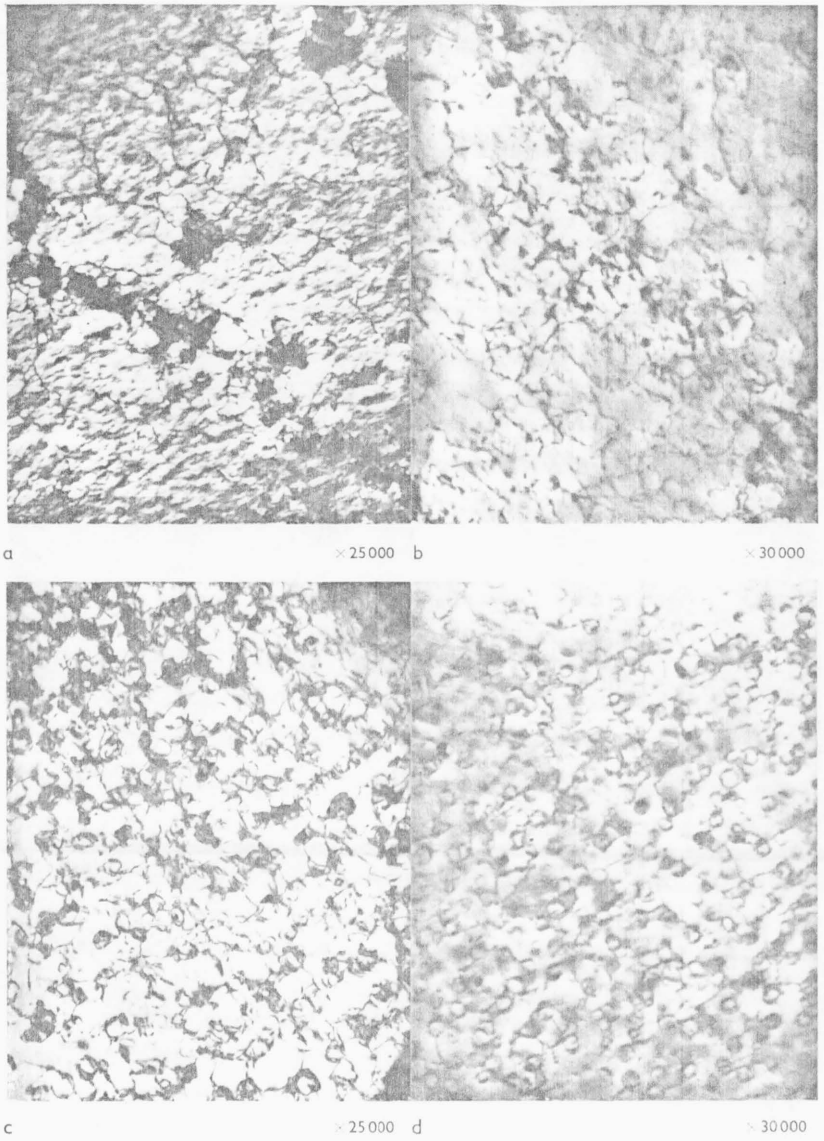

Fig. 8. Transmission electron micrographs of directionally solidified material tested to:
(a) 0.4% strain after 95 h at 480 MN/m² and 700°C.
(b) 5% strain after 6 h at 590 MN/m² and 700°C.
(c) 8% strain after 2,683 h at 410 MN/m² and 700°C.
(d) 11% strain after 0.5 h at 340 MN/m² and 850°C.

tests, dislocation density is seen to increase with creep strain, causing an increase in strain rate, and no primary creep. Thermal recovery in this material, which has a much lower volume fraction of γ' (approximately 15%), compared with 60% for the more complex alloy [8], must therefore be sufficiently rapid to overcome work-hardening, except when large initial plastic strains are introduced.

Tertiary creep in the directionally solidified material is attributed to three main causes: γ' agglomeration, cracking, and necking of the specimens. Of these, the latter two are thought to be the most important, as hardness measurements indicated that only at temperatures in excess of 750°C did coarsening of the γ' precipitate result in appreciable softening. Constant stress compensation in the creep tests was based on the assumption of uniform deformation within the gauge length and constant volume being maintained. Both necking and cracking prevent these conditions from being satisfied, and in view of the high stress dependence of creep of this material (as will be discussed later), once these conditions occur, the local stress will rise and an accelerated creep rate will result. Since it has not been

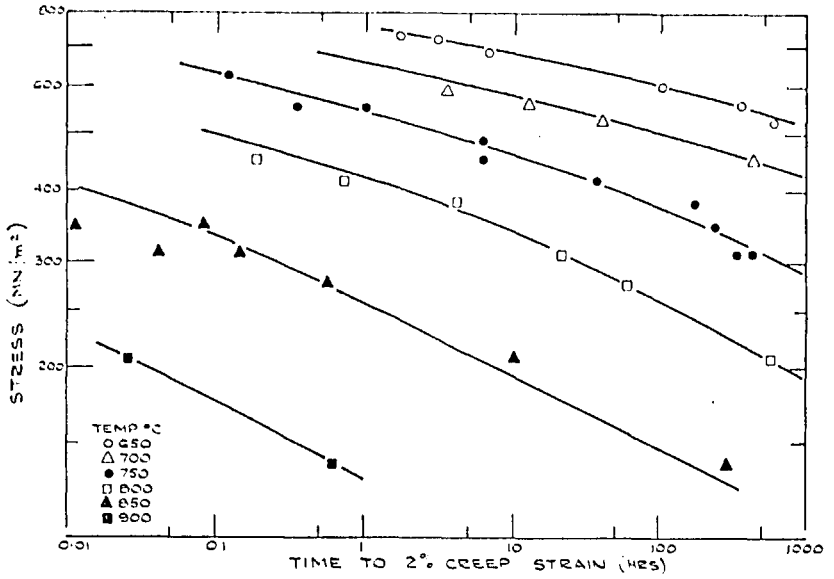

Fig. 9. Stress and temperature dependence of the time to 2% creep strain for the directionally solidified material.

found possible to estimate when necking first occurs in individual specimens, the onset of tertiary creep is difficult to predict.

In order to overcome the difficulty of defining a secondary creep rate for the directionally solidified material, and to make correlations with other published data on nickel base alloys, the temperature and stress dependences for creep have been obtained by plotting the time to a specific strain, or rupture, against stress for each temperature. An example of the former for time for 2% creep strain is shown in Fig. 9, and Fig. 10 shows the corresponding rupture data. The somewhat more pronounced scatter in the rupture data is caused by variations in the fracture ductilities of the individual specimens.

At stresses in excess of 350 MN/m² the stress dependence of both the time to 2% creep strain and to rupture is exponential, whereas at the lower stresses a power law dependence with a stress index of approximately 8 is obtained. These are both in agreement with the dependences observed in the more complex alloy [8].

The curves in Figs. 9 and 10 can be superimposed onto one "master" curve by using an activation energy form of time–temperature parameter. For temperatures below 800°C a constant activation energy for creep of approximately 150 kcal/mol is obtained, which is in agreement with values obtained for other nickel-base alloys [6], but which is appreciably higher than the activation energy for self-diffusion of nickel, 66 kcal/mol [14]. It is possible to explain this difference by including the activation energy for growth of the γ' precipitate, 86 kcal/mol [13]. Since the γ' precipitates provide obstacles to the motion of dislocations, any change in their size and spacing will affect creep properties. As coarsening of the γ' precipitate is temperature dependent, it is thought not unreasonable that the change in γ' precipitate size with temperature will add to the temperature sensitivity of creep and cause the high activation energy of 150 kcal/mol. This high activation energy is also obtained for secondary creep rates where they are measurable. A deviation from this temperature dependence was, however, observed for creep at 850 and 900°C. At these temperatures resolution of the γ' precipitate occurs, causing a loss of precipitation hardening and a lower resistance to deformation, as indicated by the hardness measurements. Consequently, the material is weaker at these temperatures than predicted by the above temperature dependence.

Figure 11 shows a comparison of the rupture data for both the conventionally cast and directionally solidified materials at the temperatures where minimum ductilities are observed in both. Generally, the stress dependence of the equiaxed material is less than that of the directionally solidified material, indicating that the latter material becomes progressively stronger with increasing time of test, in agreement with the results obtained on another nickel base

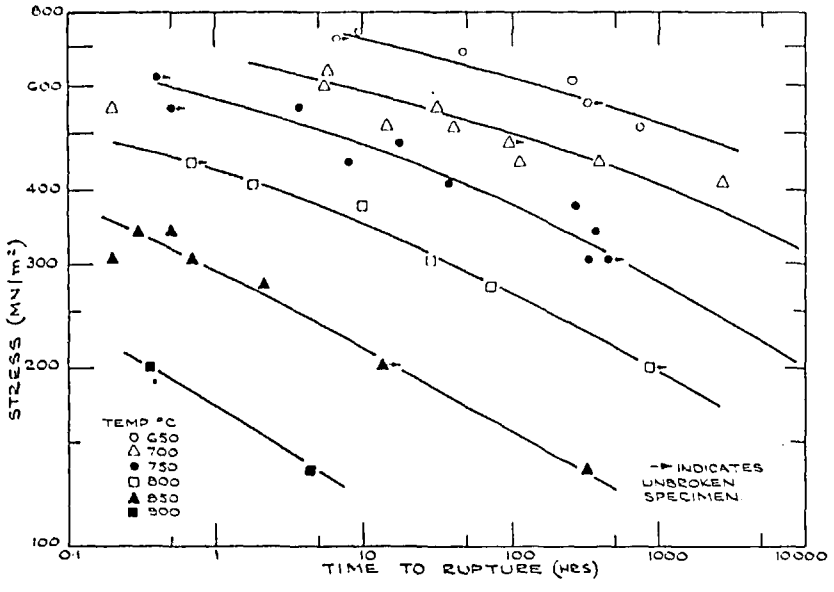

Fig. 10. Stress and temperature dependence of the time to rupture for the directionally solidified material.

alloy, by Northwood and Homewood [5]. The difference in creep strength between the two materials is attributed to the considerably lower ductility at fracture of the conventionally cast material and to its lower flow stress of 440 MN/m² at 700 and 750°C. This is approximately 15% lower than that of the columnar grained material at the same temperature.

SUMMARY

Creep data are presented over the range from 650 to 900°C for a nickel-base alloy which was cast in two forms. In one form the alloy was directionally solidified to give a columnar grained material with a preferred [001] orientation; in the other form it was conventionally cast. The results indicate that the oriented material exhibits greater creep strength and rupture ductility than the conventionally cast material. The improvement in properties is attributed to an increase in flow stress and to an absence of transverse grain boundaries in the oriented material. An incubation period and low initial creep rates observed in the oriented material are explained by low initial dislocation densities, which gradually

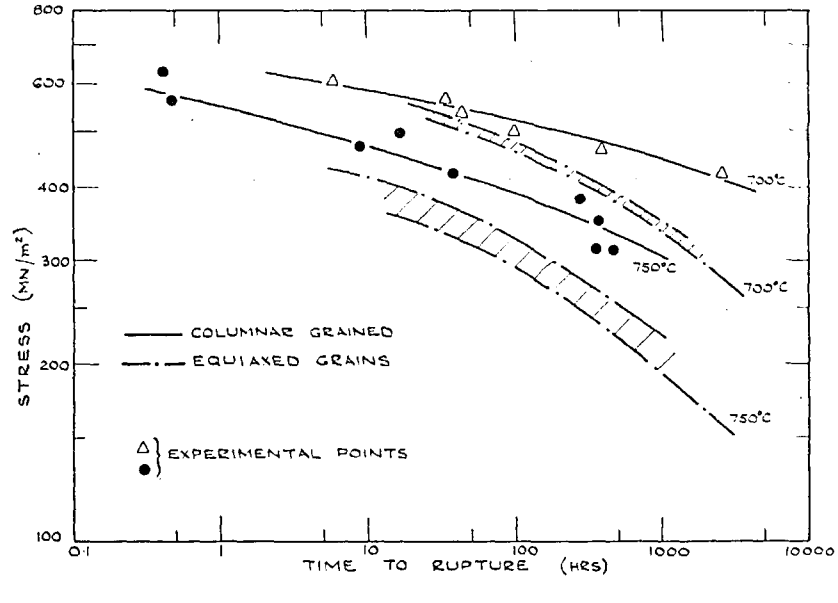

Fig. 11. Comparison of the time to rupture for directionally solidified and conventionally cast materials.

build up with increasing strain and result in an increasing creep rate. At high stresses, the stress dependence of creep is exponential, but at low stresses it tends to a power law dependence with a stress index of eight. A constant activation energy for creep of 150 kcal/mol is obtained at 800 C and below.

REFERENCES

1. F. L. VerSnyder & R. W. Guard, Directional grain structures for high temperature strength. *Trans. Am. Soc. Metals 52 (1960) pp. 485–493.*
2. B. J. Piearcey & F. L. VerSnyder, Single crystal alloy extends turbine blade service life four times. *SAE J. 74 (1966) pp. 36–43.*
3. B. J. Piearcey & B. E. Terkelsen, The effect of unidirectional solidification on the properties of cast nickel-base superalloys. *Trans. Met. Soc. AIME 239 (1967) pp. 1143–1150.*
4. B. H. Kear & B. J. Piearcey, Tensile and creep properties of single crystals of the nickel-base superalloy Mar-M200. *Trans. Met. Soc. AIME 239 (1967) pp. 1209–1215.*
5. J. E. Northwood & T. Homewood, Experiments on the unidirectional solidification of the nickel-base alloy 713 C. Paper 25, Ninth Commonwealth Mining and Metallurgical Congress, London 1969.
6. G. R. Leverant & B. H. Kear, The mechanism of creep in gamma prime precipitation-hardened nickel-base alloys at intermediate temperatures. *Met. Trans. 1 (1970) pp. 491–498.*
7. G. R. Leverant, M. Gell & S. W. Hopkins, The influence of the γ' precipitate on the elevated temperature strength deformation characteristics of a nickel base alloy. 2nd Int. Conf. on Strength of Metals and Alloys, Asilomar, Calif., Sept. 1970.
8. G. A. Webster & B. J. Piearcey, An interpretation of the effects of stress and temperature on the creep properties of a nickel-base superalloy. *Metal Sci. J. 1 (1967) pp. 97–104.*
9. G. A. Webster & B. J. Piearcey, The effects of load and temperature cycling on the creep behaviour of a nickel-base alloy. *Trans. Am. Soc. Metals 59 (1966) pp. 847–859.*
10. R. K. Penny, E. G. Ellison & G. A. Webster, Specimen alignment and strain measurement in axial creep tests. *Mat. Res. & Standards 6 (1966) pp. 76–84.*
11. D. N. Tishler & C. H. Wells, Improved high-temperature extensometer. *Mat. Res. & Standards 6 (1966) pp. 20–22.*
12. R. A. Oriani, Ostwald ripening of precipitation in solid matrices. *Acta Metallurg. 12 (1964) pp. 1399–1409.*
13. W. I. Mitchell, Ausscheidungshärtung von Hochtemperaturlegierungen auf Nickel-basis. *Z. Metallkunde 57 (1966) pp. 586 589.*
14. J. E. Dorn, The spectrum of activation energies for creep. Creep and recovery Am. Soc. Metals, Cleveland, Ohio 1957, *pp. 255–283.*